Implementation & Optimization of Parallel Imaging and Compressed Sensing Techniques for Faster Acquisition of Multi-Channel Magnetic Resonance Spectroscopic Imaging for Brain Tumor Patients

by

Maryam Vareth

A dissertation submitted in partial satisfaction of the

requirements for the degree of

Joint Doctor of Philosophy
with University of California, San Francisco

in

Bioengineering

in the

Graduate Division

of the

University of California, Berkeley

Committee in charge:

Professor Sarah Nelson, Co-chair
Professor Steve Conolly, Co-chair
Associate Professor Peder Larson
Associate Professor Laura Waller
Assistant Professor Janine Lupo

Fall 2016

Implementation & Optimization of Parallel Imaging and Compressed Sensing Techniques for Faster Acquisition of Multi-Channel Magnetic Resonance Spectroscopic Imaging for Brain Tumor Patients

by

Maryam Vareth

Abstract

Implementation & Optimization of Parallel Imaging and Compressed Sensing Techniques for Faster Acquisition of Multi-Channel Magnetic Resonance Spectroscopic Imaging for Brain Tumor Patients

by

Maryam Vareth

Doctor of Philosophy in Bioengineering

University of California, Berkeley

Professor Sarah Nelson, Co-chair

Professor Steve Conolly, Co-chair

Primary brain tumors are typically aggressive lesions that are difficult to treat and have a relatively poor prognosis for many patients. Magnetic resonance imaging (MRI) tools have been commonly utilized in the management of patients diagnosed with gliomas. Functional and metabolic MRI techniques have been proposed to add information regarding the tissue characteristics and biochemistry for better tumor localization, treatment planning and follow up of the disease.

Magnetic resonance spectroscopic imaging (MRSI) is a metabolic imaging technique used to analyze brain tissue chemistry. By showing metabolically active infiltrative tumor that can look similar to surrounding tissues on conventional MR images, MRSI allows for a more accurate definition of the extent of the disease. Despite those benefits, MRSI has not been widely used to care for patients with brain tumors.

Three major difficulties encountered in using MRSI in a clinical setting are limited coverage, coarse spatial resolution and long data acquisition time. The possibility of combining compressed sensing and parallel imaging techniques to accelerate the acquisition time, increase coverage of the brain or resolution while ensuring high quality data without loss of information was the primary goal of this dissertation.

Several new techniques have been developed to accelerate MRSI acquisition in addition to reconstruct and optimally combine the accelerated multi-channel whole-brain 3D-MRSI data accurately and robustly. These techniques were validated on healthy volunteers and patients with brain tumors. They allowed the acquisition of MRSI data from a much larger brain

volumes and finer spatial resolution than the conventional methods. The proposed AVD-GRAPPA technique reduced the $20min$ acquisition to $< 5min$ with clinically interpretable spectra (high correlation to the full sampling). The improved coverage and spatial resolution will be useful for evaluating heterogeneous and infiltrative tumors, which are difficult to evaluate with current protocols. This advancement should make possible a more accurate assessment of the progression of tumors in serial studies.

The result of this dissertation suggests that magnetic resonance spectroscopic imaging is an important technique for spatially characterizing brain tumors that can be acquired in a shorter time to obtain equivalent disease related information. It is expected that shorter scan times will result in less patient discomfort, motion artifacts and will increase the scanner throughput and the usage of MRSI data in treatment management of the patients with brain tumor.

In the loving memory of Nosrat Iranzadi

Dedicated to my parents

Ali and Behdokht Vareth

and my sibilings

Matin and Mina Vareth

So many signals around *Fortunate those who decode*

Plenty points to be found *Where does the secret abode?* [1]

[1] Adopted from Hafez, one of the greatest Persian Poets (14th century)

Contents

List of Figures

List of Tables

Acknowledgments

First and foremost, I owe a tremendous portion of my success in graduate school to my advisor, and mentor, **Dr. Sarah Nelson**, whose endless guidance, encouragement, knowledge and support over the years allowed me to grow as both a scientist and an individual. It's been my privilege to watch and learn from her about what it means to be a true collaborator, a courageous thinker, and above all, an authentic leader. She has been a superb role model whose positive outlook, exemplary leadership and mentorship will continue to impact my life in years to come. It's been an honor working under Sarah's supervision. I suspect my problematic procrastination at times came from a fear of submitting work to Sarah that was undeserving of her brilliance.

Second and foremost, I am deeply indebted to my academic advisor and mentor, **Dr. Steve Connolly**, whose unwavering support and encouragement along with his formidable knowledge and insight will forever inspire me to keep learning and growing as a scholar. I would like to express my sincere gratitude to him for introducing me to the wonders and frustrations of scientific research and for being my guiding beacon during all these years. I am truly thankful for his steadfast integrity, and selfless dedication to both my personal and academic development. Over the years, the sage advice of Steve would keep me grounded through my happiest moments and afloat during the most turbulent times.

I had the extreme good fortune to have many more supportive mentors, colleagues and friends. While I have countless individuals to thank, I will undoubtedly forget some here and so I apologize in advance for those inadvertently leave out.

My most sincere and profound thanks is owed to my dissertation committee, **Dr. Peder Larson**, **Dr. Janine Lupo** and **Dr. Laura Waller** and qualifying exam committee, **Dr. Sue Noworolski** whose tremendous time and energy spent helping me refining this project which will never be forgotten. Your discussions, ideas, and feedbacks have been absolutely invaluable to guide and shape my research throughout the years. I feel a tremendous gratitude for having the phenomenal **Janine** as a "speak-to" person and truly grateful to have her as a friend. My academic family extends well beyond my committee, as such I must acknowledge a number of people who encouraged me to continue on this path despite various hurdles and setbacks. I would like to express my gratitude to **John Kurhanewicz**, **Dr. Dan Vigneron**, **Dr. Miki Lustig**, and **Dr. John Pauly** for their much needed advice and insight at various stages and valuable discussions. I would like to thank, **Dr. Susan Chang** and **Dr. Soonmee Cha** for keeping us focus on the clinical impact of our work, and for taking the time to teach us about clinically interpreting MRI exams. The flaws in this dissertation are mine but its strengths are largely due to the knowledge these incredible mentors bequeathed.

One of the best parts of this journey has been the amazing group of people I've been able to work with. I am always in awe of the amount of talent and enthusiasm that permeates the Brain Group and Surbeck Labs. To **Yan Li**, **Qiuting Wen**, **Wei Bian**, **Emma Essock-Burns**, **Ilwoo Park**, **Eugene Ozhinsky**, **Trey Jalbert**, and **Adam Elkhaled** for useful discussions about research and their friendship. To **Angela Jakary** for always being willing to help in scanning, for her vibrant spirit and warm greetings everyday. To **Jason Crane** and **Beck Olson** for their ingenuity in building the software tools, their patience and helping hands in debugging software with me throughout these projects. To **Chris Williams**, **Sana Vaziri**, **Marisa Lafontaine**, **Evan Neill**, **Manisha Dayal**, **Wendy Ma** and **Shauna O'Donnell** for their help with patient scans, post-processing and patient consenting.

I would like to thank the Margaret Hart Surbeck Foundation and the Board of Directors, who wrap the research done here in the human element of hope and keep us focused on the true value of the work. I would like to deeply thank the patients and volunteers who participate in these studies. Volunteering their time to participate in biomedical research so that the future care of others may be improved is of the noblest character. The work presented here is a testament to their generosity.

Last but not least, my most heartfelt thanks goes to my beloved family. My family has been an incredible source of strength for me as I forged my way through life and graduate school. I would like to express my eternal gratitude to my amazing parents **Behdokht** and **Ali Vareth** for their unconditional love, patience, support, guidance and wisdom. You were always my voice of reason. Thank you for letting me dream, for making me believe in the impossible, for letting me fly, for letting me fall, and for continuously reminding me the glass is ALWAYS half full. I'm blessed and forever grateful to be your daughter. It is your shining example that I try to emulate in all that I do. To my dear brother and sister, **Matin** and **Mina Vareth**, for always being there, keeping me sane and making me laugh. Thanks for volunteering and tolerating many hours of MRI scanning so I could test and validate my algorithms to put forth in this dissertation.

Grant funding of this dissertation project provided by: UC Discovery Grant ITL-BIO04-10148 in conjunction with GE Healthcare, NIH Grant R01 CA127612, NIH Grant P01 CA118816 and NIH Grant P41EB013598.

Chapter 1

Introduction

Medical Imaging is becoming an increasingly important tool in both research applications and clinical care. A range of imaging technologies now provide unprecedented sensitivity for visualizing brain structure and function from the level of individual molecules to the entire brain. Different types of imaging are used to reveal brain structure, function, and metabolism (biochemical reactions of individual molecules). These three main categories are often referred to as anatomical, physiological and metabolic or molecular imaging.

Magnetic Resonance Imaging (MRI) is uniquely suited to provide invaluable information about brain tumors. While X-rays and computed tomography (CT) are good at imaging bones and large organs, they are not able to provide the exquisite contrast between different types of soft tissues. They also require significant doses of ionizing radiation, which if performed too often, provides a risk factor for causing cancer. Ultrasound is safe and inexpensive so that is widely used for imaging internal organs but it suffers from attenuation in the skull so it is not employed for clinical brain imaging. Positron emission tomography (PET) and single photon emission computed tomography (SPECT) are able to monitor specific molecular process but require injection of radioactive isotopes. They can be used to image brain tumors but must be applied in combination with anatomical images obtained from MRI and/or CT. MRI is non-invasive with non-ionizing radiation, exquisite soft-tissue contrast, multi-dimensional imaging capability, and accurate presentation of structural, functional and molecular characteristic of healthy and diseased tissues. It has therefore became the method of choice for diagnosis, treatment planning and assessment of response to therapy for patients with brain tumors.

Gliomas are the most common type of primary brain tumors in adults and are typically aggressive lesions that are difficult to treat and have a relatively poor prognosis (1, 2). They are highly infiltrative and exhibit substantial variation in appearance on conventional MR imaging. Defining the spatial extent of the tumor and optimizing treatment is complicated by heterogeneity within and between lesions, as well as by temporal changes associated with

Biological Process	MR Techniques	MR Parameters
invasion	DTI, 1H MRSI	Reduced NAA, reduced FA, increased ADC.
Tumor Celluarity	DTI, 1H MRSI	Decreased ADC, increased Cho, increased CNI.
Proliferation	1H MRSI	Increased Cho, increased CNI.
Apoptosis/necrosis	1H MRSI	Increased lipid.
Hypoxia	Lac-edited 1H MRSI, hyperpolarized 13C.	Increased lactate.
Gliosis	DTI, 1H MRSI	Increased myo-inositol/Cho.
Edema	1H MRSI	Highly increased ADC, reduced FA.
Angiogenesis	1H MRSI	Increased rCBV or fBV, changes in K_{trans} or %REC.
Late RT effects	SWI	Appearance of micro-hemorrhages.

ADC, apparent diffusion coefficient; Cho, choline-containing compounds; CNI, choline to N-acetylaspartate index; DCE, dynamic contrast-enhanced; DSC, dynamic susceptibility-weighted contrast; DTI, diffusion tensor imaging; FA, fractional anisotropy; fBV, fractional blood volume; Ktrans, fitted constant describing leakage of the contrast agent into the interstitial space; NAA, N-acetylaspartate; rCBV, relative cerebral blood volume; %REC, percentage recovery of the DSC signal to baseline; RT, radiation therapy; SWI, susceptibility weighted imaging.

Table 1.1: Relationship between MR parameters and biological properties of the tumor that can be obtained by quantitative analysis of multiparametric imaging examination for patients with glioma. *Courtesy Dr. S.J. Nelson*

tumor progression and treatment induced damage (3). Patients classified as having low-grade histology have a median overall survival of 7 years or more, but need to be monitored carefully to make sure that their tumor does not upgrade to a more malignant phenotype. Patients with the most aggressive grade IV histology (4) who are treated with the current standard of care of 6 week radiotherapy and 6 cycle of temozolomide (5), have a median overall survival of 15 months and often undergo multiple surgeries and adjuvant therapies in an attempt to control their disease. Finding therapies that are effective in defeating brain tumors or in at least postponing their growth requires an advance indication of whether the treatment is working or not without having to wait months or years until the patient succumbs to the disease. The hope is that MR imaging can help to select treatments that are most effective for subgroups of patients.

The true power of MRI is in its flexibility to manipulate the image intensities by changing machine parameters in a way that exploits the differences in the magnetic properties of tissues. Many types of MR acquisition techniques have been developed that take advantage of variations in contrast mechanisms to give clinicians a more comprehensive insight into tumor cellularity, hypoxia, disruption of normal tissue architecture, changes in vascular density and vessel permeability of diseased tissues. While conventional MRI is used for visualization of the anatomy and for measuring changes in the volume of enhancing and non-enchancing lesions, other advanced techniques such as diffusion, perfusion, and spectroscopic imaging have provided crucial additional features for treatment planning and the assessment of response to therapy (6–8). Table 1.1 shows MR parameters that have been used in recent studies and are relevant for evaluating the biological properties of the tumor.

Although MRI is routinely used for monitoring response to therapy, there is increasing concern about the interpretation of the changes in the appearance of the lesions observed on T_1 and T_2 weighted images (6, 9, 10), because they are not specific for tumor and can therefore provide ambiguous results. This leads to one of the most important challenges which is facing neuroncologists today, namely the definition of criteria for differentiating between tumor recurrence and treatment-related changes (11). Metabolic imaging may be particularly useful in characterizing regions of suspected recurrence, because it reflects changes in cellular properties associated with biological function.

Magnetic Resonance Spectroscopy (MRS) uses similar physical principles as MRI, but instead of showing anatomical images, it allows for the detection of relative concentrations of certain chemical compounds in the tissue. Variations in levels of such compounds provide a mechanism for distinguishing between tumor and normal brain. Magnetic Resonance Spectroscopic Imaging or MRSI combines the principles of spatial localization used in MRI with MRS technology to estimate relative concentrations of metabolites from an array of voxels throughout the brain. The data can be displayed as a grid of spectra or as metabolite maps, overlaid on top of anatomic MR images. By showing metabolically active tumor that can look similar to surrounding tissues on conventional MR images, MRSI has the potential for distinguishing between infiltrating tumor cells, solid tumor, necrosis (dead tissue), edema (swelling) and gliosis (scarring). MRSI parameters have been used as biomarkers of malignancy and aggressiveness of the tumor and have been successfully applied for planning surgery and radiation therapy (6).

The metabolic imaging technique that has been used at UCSF over the past two decades to evaluate patients with brain tumors is proton (H-1) MRSI. This can be used to monitor changes in endogenous signals within the brain and has shown that tumor is characterized by an increase in Cho and decrease in NAA relative to normal brain (12–16). A complementary MR metabolic imaging technology that is able to track dynamic changes in the signal intensity of C13 lactate following intravenous injection of hyperpolarized C-13 pyruvate. This is of particular interest for the management of patients with glioma because the presence of lactate is a characteristic of high-grade glioma and is a prognostic factor for poor overall survival.

Despite those benefits, MRSI has not been widely used to care for patients with brain tumors. This is largely due to the difficulty in obtaining good quality MRSI data in a routine clinical setting as opposed to specialized research centers. Among the challenges faced when applying spectroscopic imaging techniques are reducing acquisition times, improving the spatial resolution and coverage of the brain, and reducing interfering signals from fat tissues.

The unifying goal of the projects in this dissertation was to address challenges associated with making MRSI more practical in a clinical setting by developming novel techniques for accelerated MRSI acquisition and reconstruction. To accomplish this I have developed k-

space sampling methods with parallel data reconstruction strategies to allow rapid acquisition of large matrices of spectroscopic data to increase coverage of the brain and/or resolution and ensure high quality data. I have developed techniques to automate MRSI coil combination and post-processing pipelines. The ultimate goal is to provide a fast and reliable method for obtaining metabolic data as part of the standard clinical MR examination in order to make informed decisions about the management of patients with glioma.

Chapter 2 describes the necessary clinical background and provides the reader with a brief overview of brain tumors and treatments in addition to the fundamental principles of MRI and MRSI and their applications to brain tumor patients.

Chapter 3 covers the physics background and the theoretical simulation of surface and array coils as a means to provide improved coil designs for optimal parallel imaging reconstructions. It also briefly describes a development of a simple new design for a two-channel quadrature traveling wave antenna for MR experiments at 7T scanner (17).

Chapter 4 describes several strategies to find the most robust and accurate algorithm for producing phase sensitive coil combination of multi-channel, multi-voxel 3D-MRSI data acquired from the brain for clinical purposes in an acquisition time of 5-10 minutes. The automated pipeline for reconstruction and post-processing are presented (18, 19). Methods that are considered include first point phasing, unsuppressed/suppressed water referencing, whitened singular value decomposition and generalized least squared. Each technique is tested on large population: 6 volunteers and 55 patients with brain tumor (105 exams).

Chapter 5 explains the theory behind compressed sensing in MRI and MRSI applications. A detailed comparison of three different non-linear reconstruction algorithms is presented: (1) Non-Linear Conjugate Gradient (2) Stagewise Orthogonal Matching Pursuit and (3) Projection Over Convex Set. Based on their performance on the brain images, the best algorithm was chosen to be extended to an MRSI application; to reduce the acquisition time of the water reference dataset that is used for phase, frequency correction and coherently combining multi-channel MRSI data (20). Furthermore, an enhanced k-space trajectory scheme was introduced and incorporated into the pulse sequence of the 3D spectroscopic imaging for flexible CS-MRSI acquisition.

Chapter 6 details the novel approaches of parallel imaging techniques such as GRAPPA, SPIRiT and ℓ_1-SPIRiT in MRI and MRSI applications. The objective of this chapter was to find the most robust and accurate algorithm for phase sensitive reconstruction of accelerated MRSI data acquired from the brain for clinical purposes in an acquisition time of $\approx$5 minutes and to automate the reconstruction and processing (17, 21–23). A new approach called AVD-GRAPPA enabled EPSI is introduced for most robust and accurate PI-MRSI.

1.1 References

1. E. Lopci, C. Franzese, M. Grimaldi, P. A. Zucali, P. Navarria, M. Simonelli, L. Bello, M. Scorsetti, and A. Chiti, "Imaging biomarkers in primary brain tumours," *European Journal of Nuclear Medicine and Molecular Imaging*, vol. 42, pp. 597–612, Dec. 2014.

2. P. Y. Wen and S. Kesari, "Malignant gliomas in adults," *New England Journal of Medicine*, vol. 359, no. 5, pp. 492–507, 2008.

3. J. W. Henson, S. Ulmer, and G. J. Harris, "Brain Tumor Imaging in Clinical Trials," *American Journal of Neuroradiology*, vol. 29, pp. 419–424, Mar. 2008.

4. S. Kesari, "Understanding Glioblastoma Tumor Biology: The Potential to Improve Current Diagnosis and Treatments," *Seminars in Oncology*, vol. 38, pp. S2–S10, Dec. 2011.

5. R. Stupp, M. E. Hegi, M. R. Gilbert, and A. Chakravarti, "Chemoradiotherapy in Malignant Glioma: Standard of Care and Future Directions," *Journal of Clinical Oncology*, vol. 25, pp. 4127–4136, Sept. 2007.

6. S. J. Nelson, "Assessment of therapeutic response and treatment planning for brain tumors using metabolic and physiological MRI," *NMR in Biomedicine*, Apr. 2011.

7. S. Cha, "Update on brain tumor imaging: From anatomy to physiology," *American Journal of Neuroradiology*, vol. 27, no. 3, pp. 475–487, 2006.

8. W. Hollingworth, L. S. Medina, R. E. Lenkinski, D. K. Shibata, B. Bernal, D. Zurakowski, B. Comstock, and J. G. Jarvik, "A systematic literature review of magnetic resonance spectroscopy for the characterization of brain tumors.," *American Journal of Neuroradiology*, vol. 27, pp. 1404–1411, Aug. 2006.

9. L. C. Hygino da Cruz, I. Rodriguez, R. C. Domingues, E. L. Gasparetto, and A. G. Sorensen, "Pseudoprogression and Pseudoresponse: Imaging Challenges in the Assessment of Posttreatment Glioma," *American Journal of Neuroradiology*, vol. 32, pp. 1978–1985, Dec. 2011.

10. J. L. Clarke and S. Chang, "Pseudoprogression and pseudoresponse: challenges in brain tumor imaging.," *Current neurology and neuroscience reports*, vol. 9, pp. 241–246, May 2009.

11. P. C. Sundgren, "MR Spectroscopy in Radiation Injury," *American Journal of Neuroradiology*, vol. 30, pp. 1469–1476, Sept. 2009.

12. S. J. Nelson, "Magnetic resonance spectroscopic imaging," *Engineering in Medicine and Biology Magazine, IEEE*, vol. 23, no. 5, pp. 30–39, 2004.

13. S. J. Nelson, "Multivoxel magnetic resonance spectroscopy of brain tumors.," *Molecular cancer therapeutics*, vol. 2, pp. 497–507, May 2003.

14. y. Li, J. M. Lupo, R. Parvataneni, K. R. Lamborn, S. Cha, S. M. Chang, and S. J. Nelson, "Survival analysis in patients with newly diagnosed glioblastoma using pre- and postradiotherapy MR spectroscopic imaging," *Neuro Oncology*, vol. 15, pp. 607–617, Apr. 2013.

15. L. Yaan, I. Park, and S. J. Nelson, "Imaging Tumor Metabolism Using In Vivo Magnetic Resonance Spectroscopy," *The Cancer Journal*, vol. 21, no. 2, pp. 123–128, 2015.

16. L. Yan, P. Larson, A. P. Chen, J. M. Lupo, E. Ozhinsky, D. Kelley, S. M. Chang, and S. J. Nelson, "Short-echo three-dimensional H-1 MR spectroscopic imaging of patients with glioma at 7 tesla for characterization of differences in metabolite levels," *Journal of Magnetic Resonance Imaging*, vol. 41, pp. 1332–1341, June 2014.

17. M. Vareth, A. Flynn, B. Wei, Y. Li, D. B. Vigneron, S. J. Nelson, and X. Zhang, "Accelerated Parallel Traveling Wave MR and Compressed Sensing Using a 2-Channel Transceiver Array," *Proceeding of the 21st Annual Scientific Meeting of the ISMRM*, pp. 1–1, Nov. 2013.

18. M. Vareth, L. Yaan, J. M. Lupo, and S. Nelson, "Comparison of Several Coil Combination Techniques in Multi-Channel 3D MRSI for Brain Tumor Patients ," *Proceeding of the 23rd Annual Scientific Meeting of the ISMRM*, Dec. 2015.

19. M. Vareth, y. Li, J. Lupo, P. E. Z. Larson, and S. J. Nelson, "Coil Combination Strategies for 3D Multi-Channel H-1 PRESS localized EPSI Data for Patients with Brain Tumors," *Magnetic Resonance in Medicine (under revision).*

20. M. Vareth, E. Ozhinsky, and S. J. Nelson, "Multi-Channel Spectroscopic Imagin Reconstruction Using Water-Referencing with Compressed Sensing ," *Proceeding of the 19th Annual Scientific Meeting of the ISMRM*, pp. 1–1, Nov. 2011.

21. M. Vareth, y. Li, J. Lupo, and S. J. Nelson, "2D-SPIRiT accelerated MRSI of the brain using different calibration regions at 7T," *Proceeding of the 22nd Annual Scientific Meeting of the ISMRM*, pp. 1–1, Mar. 2014.

22. M. Vareth, y. Li, and S. J. Nelson, "Reconstruction of Arbitrary Variable Density Cartesian Sampling Strategies Using Robust 2D-GRAPPA-EPSI for the Short-Echo 3D-MRSI of the Brain at 3T," Mar. 2016.

23. M. Vareth, y. Li, J. Lupo, P. E. Z. Larson, and S. J. Nelson, "Arbitrary Variable Density AVD-GRAPPA enabled EPSI of short-echo 3D-MRSI of whole brain at 3T," *Magnetic Resonance in Medicine (under preparation).*

Chapter 2

Background

2.1 Brain Tumor

2.1.1 Brain Cell Types and Functions

The brain is primarily composed of two classes of cells: nerve and glial cells. The nerve cells, or neurons, are the structural and functional unit of the nervous system. They contain a cell body, soma and processes which are called axon and dendrites. The axon and dendrites take part in the conduction of electric impulses via ion movement between neurons and hence supply the communication network. The four main functions of glial cells are to surround neurons and hold them in place, to supply nutrients and oxygen to neurons, to insulate one neuron from another, and to destroy and remove the carcasses of dead neurons (clean up). Glia are grouped into four types, the astrocytes, oligodendrocytes, ependymal cells and microglia.

- **astrocytes** are star-shaped and have long processes that connect them to the outside of capillary walls and the pia mater. They regulate the transmission of electrical impulses within the brain in addition to controlling the microenvironment of neurons and maintaining the integrity of the blood-brain barrier (BBB). The latter is a barrier between the brain tissue and the blood capillaries that protects the brain by restricting the entry of all molecules except glucose and amino acid that cross the cell membrane by means of diffusion and active transportation.
- **oligodendrocytes** play a role in the production of a lipoprotein called "myelin" that covers the axons in some nerve cells. The myelin functions as an electrical insulator and ensures efficient nerve conduction. The parts of the brain that have myelinated nerve cells appear white and are called the "white matter". The cortex of the brain contains mostly the neuron bodies without myelination and appears gray which are called the "gray matter".
- **ependymal** cells line the central canal of the spinal cord and the ventricles of the brain. These cells are involved in the production of cerebrospinal fluid (CSF) which is a

colorless acellular fluid that protects the central nervous system (CNS) from concussive injuries, transports hormones and removes the wastes.
- **microglia** are the resident macrophage-like cells of the brain and spinal cord and they get activated in the event of a destructive lesion to clean the cell debris.

2.1.2 Brain Tumor Classification

Brain tumors are classified as either being primary or metastatic in origin. Primary tumors originate from the cells in the brain, while their metastatic counterparts originate from other organs and eventually migrate to the brain. While both types of lesions are difficult to treat, the primary brain tumors are typically more invasive and do not exhibit a defined boundary relative to healthy tissues. They are classified by the type of brain cells that they arise from and include:

- **neurons** (neuroblastoma, ganglioneuroblastoma and ganglioneuroma)
- **glia** (astrocytoma (originating from astrocytes), oligodendroglioma (originating from oligodendrocytes), ependymoma (originating from ependymal cells) and mixed type (exhibiting characteristics of more than one type of glial cell))
- **myelin producing schwann cells** (schwannoma)
- **meninges** (meningioma)
- **pituitary gland** (pituitary tumors)
- **pineal gland** (pineal tumors)

Primary brain tumors that originate from glia are referred to as gliomas. Astrocytomas are the most common type of gliomas. Oligodendrogliomas are another common type of glioma which have better prognosis because they are more sensitive to chemotherapy. Gilomas can be further divided into a four-tiered scale according to the World Health Organization (WHO) based upon histological criteria that include the level of invasiveness, growth rate, similarity to normal cells, and presence of abnormal vascularity:

- **Grade I:** tumors are slow growing and their borders are well defined. They most often occur in children and are considered benign.
- **Grade II:** tumors (low grade) are characterized by invasive cells and the presence of nuclear atypia. They are treatable and have relatively good prognosis with treatment: median survival is 5-10 years. These tumors progress to higher grade.
- **Grade III:** tumors (anaplastic) exhibit nuclear atypia and increased mitosis. Median survival for anaplastic tumors is around 3 years.
- **Grade IV:** tumors, called glioblastoma multiforme (GBM), exhibit signs of necrosis or endothelial proliferation in addition to the rest of the features above. Median survival for patients with GBM is only 12-15 months. They are, unfortunately, the most common type of primary brain tumors.

Pathologists define the severity or grade of the lesions on the degree of malignancy or aggressiveness that is observed in microscopic analysis of biopsy or surgical samples, which are not always accurate. Samples from the same patient may correspond to more than one grade. In

such cases, the diagnosis corresponding to the highest observed grade is the one that is used. Although grade II glioma have a better overall prognosis, they often undergo transformation to a higher grade at the time of recurrence and require more aggressive treatment.

2.1.3 Brain Tumor Epidemiology

In 2015, American Cancer Society expected approximately 1.7 million new diagnosis of cancer in the United States with 590,000 death (1). In the US this will translate to approximately 23,000 new cases of brain and CNS cancer this year, with almost 15,000 deaths. During 2006-2010 years, 326,711 brain and CNS tumors were reported for all ages (112,458 malignant, 214,253 non-malignant) (2). The incidence rate of all primary brain and CNS tumors was 21.03 cases per 100,000 person.

The broad category of glioma represents approximately 28% of all brain tumors and 80% of primary malignant tumors (2). Glioblastoma is the worst common gliomas, while astrocytoma and glioblastoma combined accounting for about three-fourths of all gliomas as defined by the Central Brain Tumor Registry of the United States (CBTRUS). Despite their relatively low incidence, brain tumors are very deadly, the estimated 5- and 10-year relative survival rates for malignant brain and CNS tumors are 33.8% and 18.1%, respectively. However, these is a large variation in survival estimates depending upon tumor histology with the 5-year survival rates for astrocytoma being 94.4% and only 5% for glioblastoma.

2.1.4 Brain Tumor Diagnosis and Treatment Strategies

There is no screening system available for diagnosing early stage brain tumors. They are typically diagnosed after the patient presents some symptoms involving headache, seizures, cognitive or neurological deficits, such as hemiparesis (weakness on one side of the body), aphasia (impairment of language), or sensory abnormalities, personality changes, nausea or vomiting. Age, histological grade and tumor location are prognostic factors for survival.

Imaging modalities such as MRI or CT are used to determine the presence of a mass lesion and its suitability for surgical resection. Histological diagnosis of tumor grade depends upon the analysis of the tissue samples obtained during biopsy and surgery. Neuro-oncologists use a combination of factors, including tumor grade and location to select treatment.

Surgical resection is the primary treatment for gliomas, followed by adjuvant radiation (RT) and chemotherapy. The goal of surgery is to perform a maximal safe resection that reduces tumor burden and minimizes symptoms while preserving brain functions. Unfortunately the infiltrative nature of gliomas may make it impossible to remove the entire tumor due to proximity to critical cortical areas and difficulty in defining the location of the margin. Following resection, pathologists define the severity or grade of the lesions on the degree

of malignancy or aggressiveness based upon the microscopic analysis of biopsy or surgical samples.

Directly after surgery, radiation therapy is used to kill residual tumor cells by inflicting DNA damage. The target area is planned based on MRI images with the goal of delivering the highest does to the tumor and minimizing damage to normal tissue. Stereotactic radiosurgery or gamma knife is used to treat tumors in locations that are impossible to reach surgically.

Chemotherapic agents are used to further suppress disease progression by targeting rapidly dividing cells in the body. The number of chemotherapy agents effective in the brain is limited due to the presence of BBB, which prevents large molecules from entering the brain tissue from the bloodstream. Temozolomide (TMZ) is one of the few agents that can easily cross the BBB and is the current standard of care for patients with high grade glioma.

In the recent years there has been a significant interest in using anti-angiogenic drugs, such as bevacizumab (Avastin) for treatment of GBMs which are highly vascular and rich in protein known as vascular endothelial growth factor (VEGF) which promotes new blood vessels. Traditionally it was thought that these drugs prevent tumor growth by inhibiting the formation of new blood vessels and promoting regression of existing vessels. However, there is still no consensus on the mechanism of these drugs and, while reducing inflammation around the lesion and delaying progression have been shown to make them more infiltrative and, their effectiveness in improving overall survival is still under debate. Selecting the most effective treatment protocol, parameters and timing of individual therapies for different types of tumors remains unknown and is an active area of medical research.

Patients receive serial scans to capture the extent of resection, presence of residual tumor, and to monitor treatment, response to therapy and disease progression. Since it is often impossible to completely kill all the tumor cells, the disease will eventually recur at or near the location of the original lesion. At that point another cycle of treatment may be prescribed, unfortunately mutation and natural selection of cells that are resistant to therapy means that the recurrent tumor is often more malignant than the primary one.

2.2 Fundamentals of Magnetic Resonance Imaging (MRI)

MRI is the leading diagnostic imaging modality used for evaluation of brain tumors due to its non-invasiveness, use of non-ionizing radiation, exquisite soft-tissue contrast, multi-dimensional imaging capability, and accurate presentation of structural, functional and molecular characteristic of healthy and diseased tissues. The property of Nuclear Magnetic Resonance (NMR) was first described by Isidor Rabi in 1938. Edward Mills Purcell and Felix

Bloch further extend this concept into the use on liquids and solids in 1946 and received the Nobel Prize in Physics for their work in 1952. Since then, NMR has become a powerful tool for chemical and structural analysis of different molecules. Paul Lauterbur and Peter Mansfield used the principles of NMR to produce non-invasive images of the body and were awarded the Nobel Prize in Medicine or Physiology in 2003. Over the past 40 years, MRI has become a widely available technology and been applied to address many biomedical problems. In this section the basic phenomenon of NMR is considered. After establishing the Larmor resonance condition with combination of classical and quantum mechanical arguments, the NMR signal generation and detection, and MR image formation is briefly discussed. Following an introduction to the k-space formalism, which provides a quantitative description of any MRI sequence, the principles of fast MRI methods are discussed.

2.2.1 Spin, Magnetic Moment, and Magnetization Dynamics

NMR is based on the interaction between atom and an external magnetic field. The atom is the smallest unit of matter and is comprised of a cloud of electrons and a nucleus that consists of protons and neutrons. In quantum mechanics, an individual unpaired elementary particle (e.g., proton, electron, or neutron) have a property of angular momentum called spin. The spin quantum number takes on values in multiples of $\frac{1}{2}$ that can either be positive or negative. Nuclei with an odd number of protons and/or neutrons has a non-zero spin and is therefore NMR active. The most important nuclei with $I = \frac{1}{2}$ are ^{1}H, ^{13}C, ^{15}N and ^{31}P, however, due to the abundance of the hydrogen atoms in the human body, ^{1}H is widely used to obtain signals for imaging.

A nuclear moment spins around its own axis creating a microscopic magnetic field called a nuclear magnetic dipole moment, μ. In resting state, the spins of the nuclei in the tissue are oriented randomly, making combined magnetization zero. However, in the presence of a static external magnetic field, 1/2-spins tend to orient in two possible directions, parallel or anti-parallel to the $\mathbf{B_0}$ field as demonstrated in Figure 2.1. The lower energy level (α spin state) corresponds to magnetic moments parallel with $\mathbf{B_0}$, while spins in the higher energy level (β spin state) have an antiparallel alignment with $\mathbf{B_0}$. Because of the spin angular momentum, the external magnetic field will generate a torque on the magnetic moment, μ, and create a rotational movement called procession, which can be described as:

$$\frac{d\mu}{dt} = \gamma\, \mu \times \mathbf{B_0} \tag{2.1}$$

where μ is the net magnetic moment of a single nucleus and $\mathbf{B_0}$ is the external magnetic field. In the Cartesian coordinate system, assuming the direction of external magnetic field $\mathbf{B_0}$ is along z-axis, the solution of this differential equation is:

$$\omega_0 = \gamma\, \mathbf{B_0} \tag{2.2}$$

where γ is gyromagnetic ratio. This solution implies that the nuclear magnetic moment rotates around z-axis with an angular frequency of ω_0 which is called Larmor frequency and

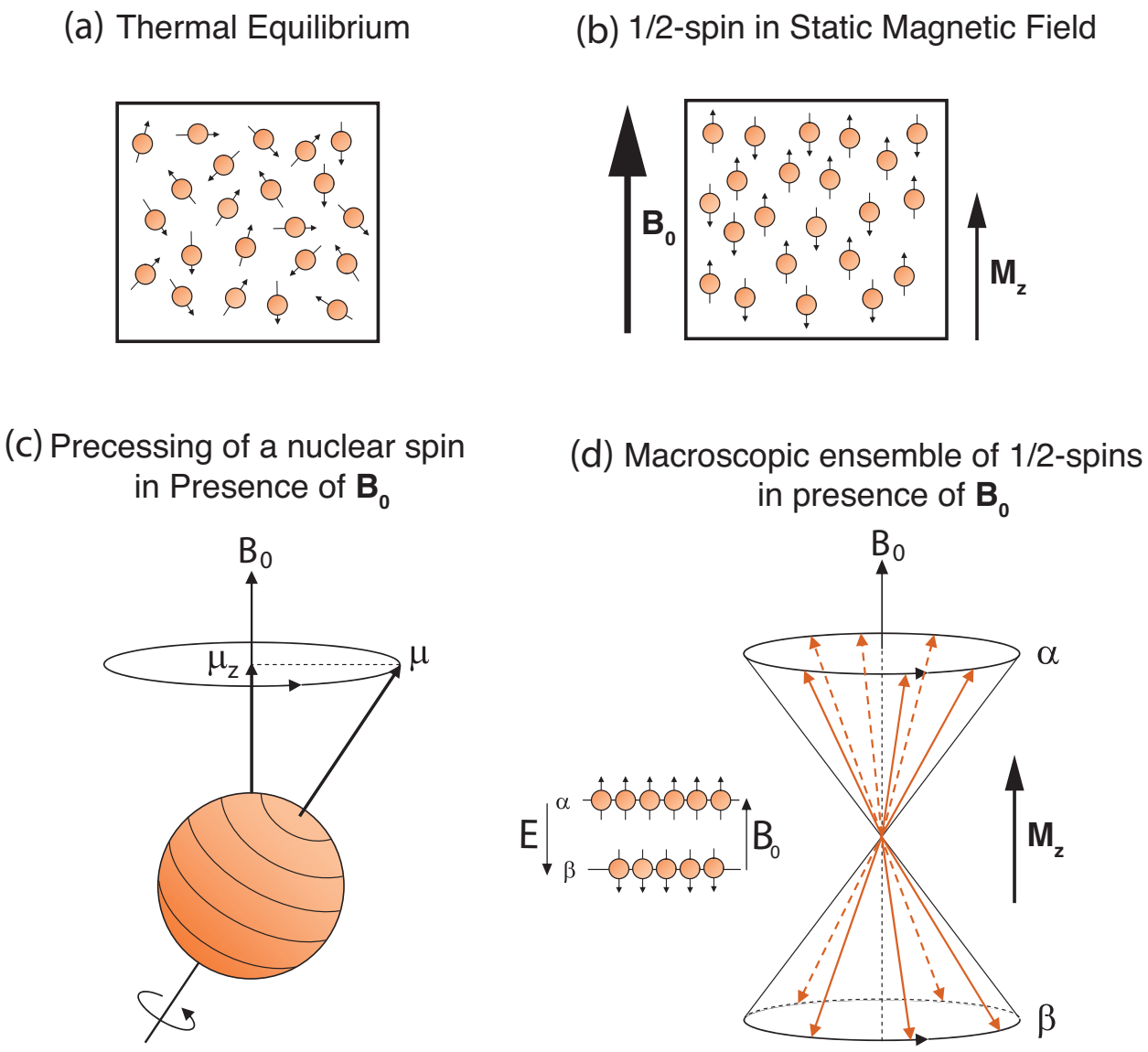

Figure 2.1: (a) Spins are oriented randomly at thermal equilibrium. (b) When a static magnetic field is applied, there is a net magnetization vector $\mathbf{M_z}$. (c) A nuclear spin precesses in the presence of an external magnetic field about $\mathbf{B_0}$. (d) In a macroscopic level the 1/2-spins distribute themselves among two possible orientations according to the Boltzmann equation with net magnetization $\mathbf{M_z}$.

the magnitude of the magnetic moment and its angle with z-axis remains unchanged during procession.

Figure 2.1(b) shows a sample containing many spins, which are randomly distributed on the cones and due to the small energy difference between two states, there will be small difference in the population of these spin states. This energy difference between these two states can be calculated by:

$$\Delta E = \frac{\gamma\, h}{2\pi}\, \mathbf{B_0} \tag{2.3}$$

where h is the Planck's constant. Furthermore, the population difference can be calculated using the Boltzmann equations as follows:

$$\frac{n_\alpha}{b_\beta} = \exp\left(\frac{\Delta E}{k\, T}\right) \tag{2.4}$$

where n_α is the number of spins in the (low energy) state, n_β is the number of spins in the (high energy state), k is the Boltzmann constant and T is the absolute temperature. Furthermore, the detectable magnetization, $\mathbf{M}$, can be estimated as:

$$\mathbf{M} \approx \frac{\gamma^2\, h^2\, \mathbf{B_0}\, \rho}{4\, k\, T} \tag{2.5}$$

where ρ is the total number of spins, h is the Planck's constant, k is the Boltzmam constant and T is the absolute temparture. The amplitude of the magnetization is directly proportional to the spin density and the strength of the external magnetic field.

2.2.2 RF Excitation and Signal Formation

In order to observe nuclear magnetization $\mathbf{M}$, the precessional motion needs to be detected by the scanner but at thermal equilibrium the spins have no phase coherence in the transverse plane and the net longitudinal magnetization is a static vector. $\mathbf{M}$ can only be observed by rotating the net longitudinal magnetization towards the transverse plane. This can be accomplished by using a second magnetic field that is oscillating in the transverse plane.

The oscillating magnetic field, $\mathbf{B_1(t)}$ needs to rotate in the same manner as the precessing spins and can be generated by an RF coil to excite the spins and establish a coherent phase among these randomly precessing spins. The radiation energy must be equal to the energy difference between the spin states to create a coherent transition of spins from one state to another. For all currently available magnets, the energy level difference between the two spin states corresponds to electromagnetic radiation in the RF range. Thus $\mathbf{B_1(t)}$ needs to have a carrier frequency equal to Larmor frequency and in a direction that is perpendicular to $\mathbf{B_0}$ since this field is applied only for a short time, it is usually referred as an RF pulse.

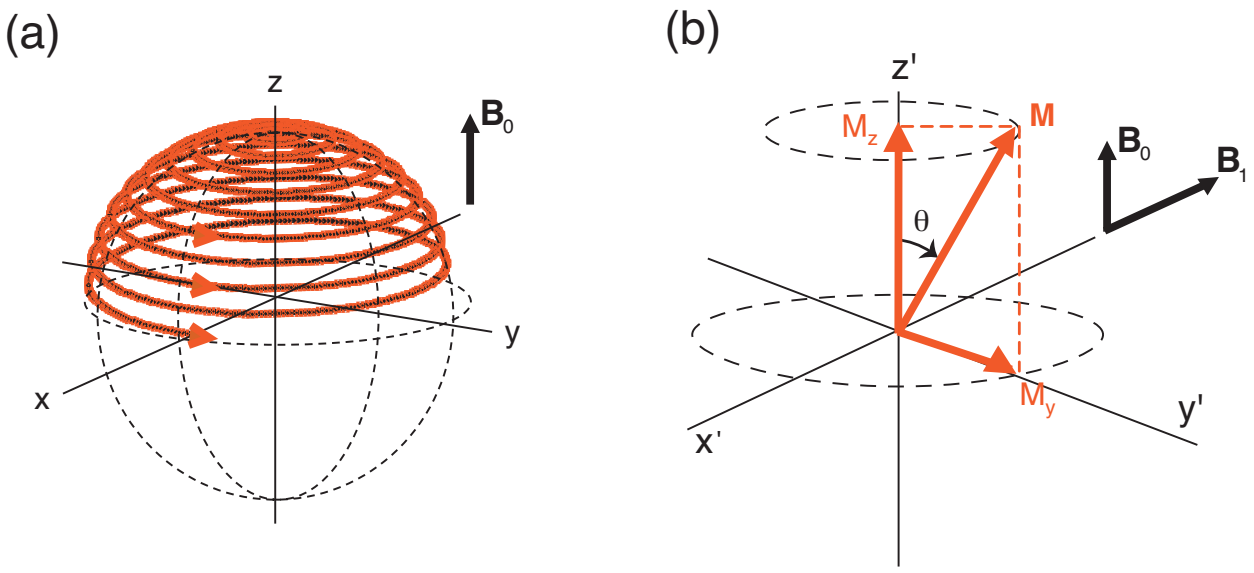

Figure 2.2: (a) Excitation of magnetization in the nonrotating, laboratory frame xyz. (b) Excitation of magnetization in the rotating frequency frame x′y′z′

During the RF pulse, the longitudinal magnetization will precess about both $\mathbf{B_0}$ and $\mathbf{B_1}$ experiencing a torque from the applied $\mathbf{B_1}$ field, which results in a rotation of $\mathbf{M}$ towards the transverse plane. Due to the simultaneous effect of these two external magnetic fields, the rotation of $\mathbf{M}$ is rather complex. Figure 2.2 illustrates the excitation of magnetization in both, the non-ratoting laboratory frame xyz and rotating frame x′y′z′; the latter is considerably simplifies the rotation concept.

In non-rotating frame, the longitudinal magnetization $\mathbf{M}$ is initially aligned with the z-axis and precesses about both the static magnetic field $\mathbf{B_0}$ and the irradiating RF field $\mathbf{B_1}$ in the transverse plane. This results in a rotation towards the transverse plane due to $\mathbf{B_1}$ and a simultaneous precession at the Larmor frequency about $\mathbf{B_0}$. In the rotating frame, the RF pulse becomes a static field since it is rotating at the same speed as the rotating frame (Larmor frequency). Initially at thermal equilibrium the Boltzmann distribution of individual spins creates a net magnetization vector along z′-axis. Since the individual spins have no phase coherence, there is no net magnetization in the transverse plane. Applying $\mathbf{B_1}$ along -x′-axis rotates the magnetization towards +y′-axis which is equivalent to creating phase coherence between spins. When the magnetic field $\mathbf{B_1}$ is set to give complete excitation, the spins have reached complete phase coherence resulting in a net magnetization vector along +y′-axis and no magnetization remains along z′-axis.

The angle between $\mathbf{B_0}$ and $\mathbf{M}$ is called flip angle, and is determined by:

$$\theta = \gamma \, \mathbf{B_1} \, \tau \tag{2.6}$$

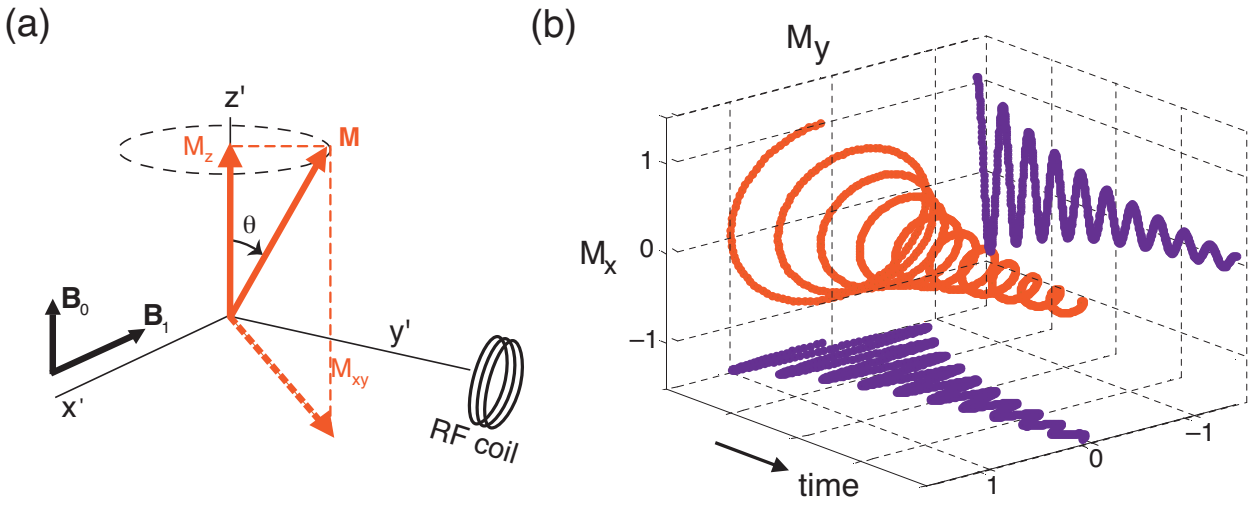

Figure 2.3: (a) Following an excitation pulse, the NMR signal is detected by the RF receiver coil surrounding the sample. (b) The free induction decay (FID) of nuclear magnetization.

where τ represents the RF pulse duration. Immediately after applying the RF pulse, the transverse magnetization starts to precess at its Larmor frequency and decays with a time constant which is discussed in details in the section 2.2.5. Based on the Faraday's Law of electromagnetic induction and the principle of reciprocity, this rotating magnetization could be detected as a weak oscillating voltage by a receiver coil surrounding the sample which is shown in Figure 2.3(a). The sum of the precessing transverse magnetization over the volume of the object is recorded as the MR signal and it is called "free induction decay" (FID) as shown in Figure 2.3(b).

2.2.3 Spatial Localization

To distinguish between the signals coming from different parts of the object, the resonance frequency ω_0 is made position-dependent, such that after Fourier Transform (FT), the different frequencies correspond to spatial position. This is accomplished by making the external magnetic field position-dependent with a help of three orthogonal magnetic field gradients, (G_x, G_y, G_z), which their amplitude varies linearly with position as illustrated in Figure 2.4.

These magnetic field gradients are generated by electrical currents in specially shaped coils within the bore of the magnet and with addition of the static magnetic field $\mathbf{B_0}$ generate a

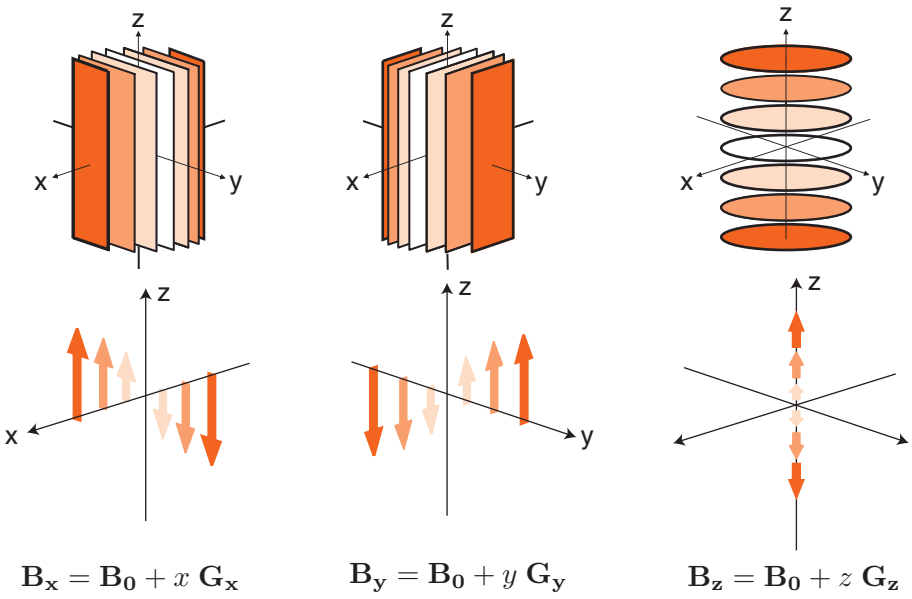

Figure 2.4: The magnetic field strength generated by each gradient in x,y,z direction increases linearly with position, as illustrated by the arrows amplitudes and the color of the planes.The isocenter, the middle plane with white color, has a magnetic field strength of zero.

slightly different magnetic field at each position $\mathbf{r}$ which can be described as:

$$\mathbf{B}(\mathbf{r}) = \mathbf{B_0} + \mathbf{rG} \tag{2.7}$$
$$\omega(\mathbf{r}) = \gamma\mathbf{B_0} + \gamma\mathbf{rG} \tag{2.8}$$
$$\omega(\mathbf{r}) = \omega_0 + \Delta\omega(\mathbf{r}) \tag{2.9}$$

Using Equation 2.9, all three dimensions of a 3D object can be encoded using either frequency or the phase of the signal to obtain spatial information.

Using the gradients to establish a relationship between the position of spins and their precessional frequency is called "frequency encoding". If a gradient field is applied for certain duration and then turned off to result in a phase variation across the object, it is called "phase encoding" of the spins. The time integral of a gradient field multiplied by γ/π is called the spatial frequency variable "k" along that direction. A collection of varying gradient strengths result in different k values that are collectively referred to as the "k-space".

2.2.4 k-space Description of Signal Reception

MRI can be described as an expensive Fourier Transform machine, i.e. it is a modality where the raw data are collected in the spatial frequency domain a.k.a "k-space" and must be transformed to recover signals in the spatial domain.

One must transverse k-space to acquire the data, therefore, the key idea for the acquisition in MRI is that the operator manipulates gradient fields over time to control the collection of data in spatial frequency domain.

Taking few steps back, as mentioned previously, only the $\mathbf{M_{xy}}$ component of magnetization $\mathbf{M}$ is detected by MRI scanners. The received signal is the summation over the volume as follows:

$$p(t) = \int_x \int_y \int_z \mathbf{M_{xy}}(\mathbf{x}, \mathbf{y}, \mathbf{z}, \mathbf{t})\, dx\, dy\, dz \tag{2.10}$$

Equation 2.10 does not include the time varying precession factor which is normally expressed by a complex number $e^{(-j\omega_0 t)}$ because it assumes that the magnetization signal is demodulated to baseband before detection. In order to capture spatial images, gradient magnetic fields are used on top of the main $\mathbf{B_0}$ field to create intentional spatial variations in magnetic field as illustrated in Figure 2.4 to achieve spatial localization and this local spatial distribution is not reflected in Equation 2.10 yet. The signal received from a spatial image is the superposition of magnetization density multiplied by the phase that depends on spatial location and Equation 2.10 can be rewritten accordingly:

$$p(t) = \int_x \int_y \mathbf{M_{xy}}(\mathbf{x}, \mathbf{y})\; e^{-j\,(\gamma\, G_x\, x + \gamma\, G_y\, y)\; t}\, dx\, dy \tag{2.11}$$

$$where \quad k_x(t) = \int_0^t \frac{\gamma}{2\pi} G_x(\tau)\, d\tau \qquad and \tag{2.12}$$

$$k_y(t) = \int_0^t \frac{\gamma}{2\pi} G_y(\tau)\, d\tau \qquad then \tag{2.13}$$

$$p(t) = \int_x \int_y \mathbf{M_{xy}}(\mathbf{x}, \mathbf{y})\; e^{\left(-j2\pi \left[k_x(t)x + k_y(t)y\right]\right)}\, dx\, dy \tag{2.14}$$

In summary, the received signal $p(t)$ is the 2D Fourier transform of the magnetization $\mathbf{M_{xy}}$.

Figure 2.5 illustrates the graphical interpretation of the signal equation with a Cartesian k-space readout trajectory. As presented by Equations (2.12 , 2.13) and illustrated in Figure 2.5 (a,b), the integral of the gradients determines the region of k-space covered. In Figure 2.5 (a), the $\mathbf{G_y}$ gradient is used for phase encoding; it moves the acquisition to a specific k_y position, after which the $\mathbf{G_x}$ gradient, "frequency encode", accomplishes traversal of a horizontal line in k-space. During the traversal of the k-space line, the detection circuitry is activated and data are collected. The phase encode can then be repeated with different gradient amplitude to cover different lines in k-space. Figure 2.5 (c) shows lines being readout in the 2D k-space, but this can be easily extended to 3D lines if the k_z dimension were added.

Figure 2.5 (c,d) shows that the extend to which k-space is covered determines resolution in the object domain. Higher resolution can be achieved by going out further in k-space and

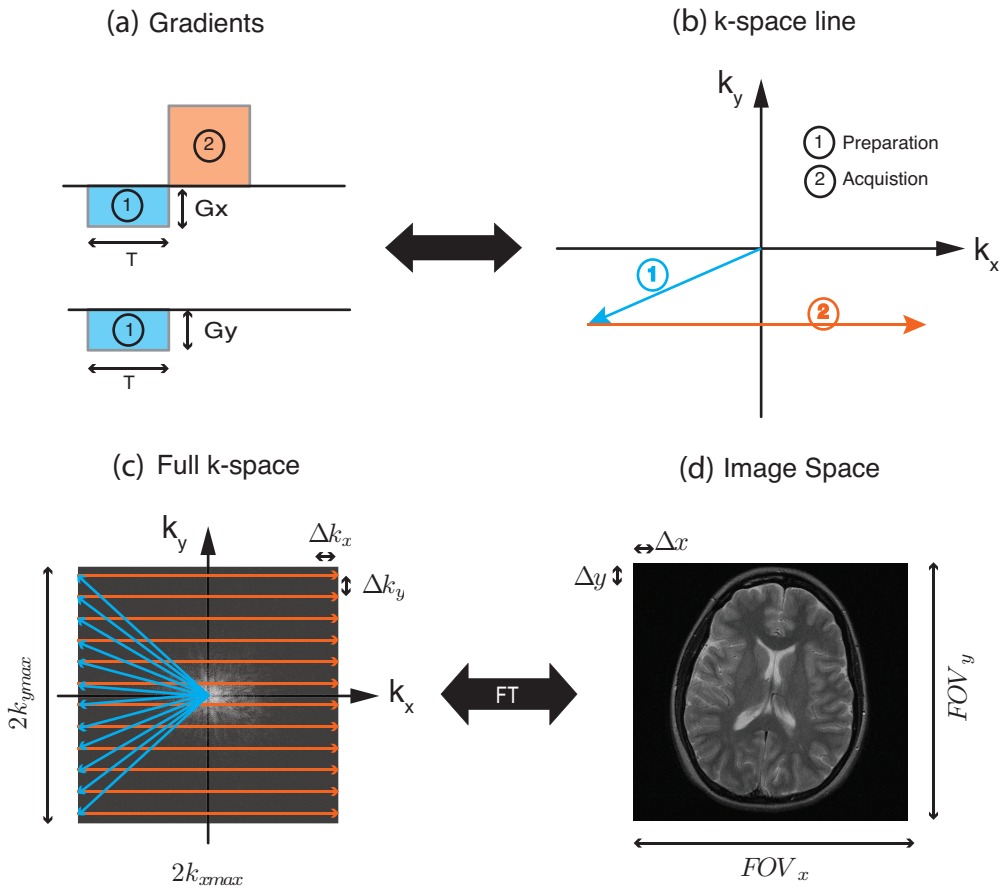

Figure 2.5: Coverage of k-space. (a) Time course of gradients. (b) Corresponding k-space traversal. (c) The gradients in (a) are repeated with different phase encode amplitude $\mathbf{G_y}$ to cover the entire k-space. (d) The k-space data are inverse Fourier Transformed to create the original image.

capturing the higher spatial frequency components, to accomplish this, the product $\frac{\gamma}{2\pi}\mathbf{G}\ t$ has to increase.

$$\Delta_x = \frac{1}{2k_{(x,max)}} \tag{2.15}$$

$$\Delta_y = \frac{1}{2k_{(y,max)}} \tag{2.16}$$

Figure 2.5 (c,d) shows that k-space sampling determines the coverage in the object domain. The Field of View (FOV) can be increased by sampling k-space more finely, which is limited in the k_y direction by the number of lines collected and is related to the phase encoding step

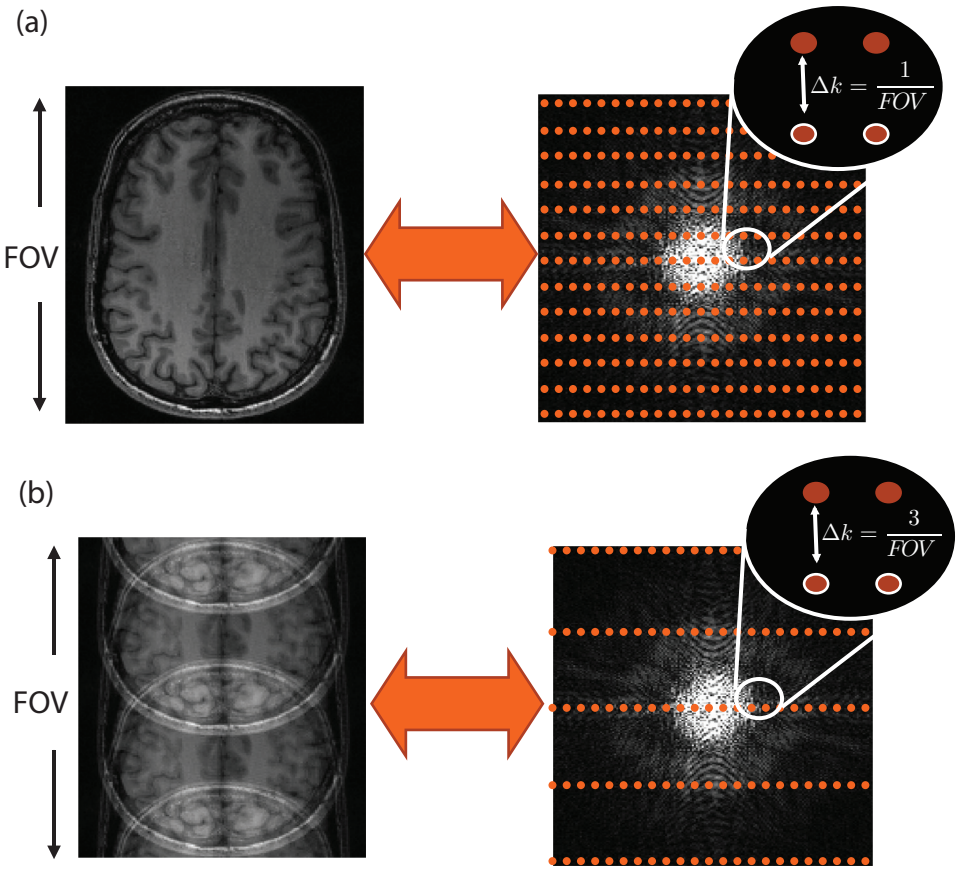

Figure 2.6: Original Image vs Aliased Image. (a) Acquired at or above Nyquist sampling rate. (b) Acquired below Nyquist sampling rate.

size.

$$FOV_x = \frac{1}{\Delta k_x} \tag{2.17}$$

$$FOV_y = \frac{1}{\Delta k_y} \tag{2.18}$$

The FOV chosen should be larger than the size of object images, i.e. Δk needs to be sufficiently small (Nyquist Criterion); otherwise, ghosting (aliasing) would occur as illustrated in 2.6. To obtain an image with a specific resolution and FOV, the number of samples required may be very time consuming because the raw data are typically acquired line by line, and the pulse sequence must be repeated for each of these lines in order to build up a full data set in k-space. Approaches for accelerating the data acquisitions are introduced and discussed in section 2.2.6.

2.2.5 Relaxation and Image Contrast

Following the excitation of the spins using an RF pulse, they gradually loose their phase coherence and return to their thermal equilibrium. Decay of the magnetization along the $xy-axis$ and a simultaneous regrowth of the magnetization along the z-axis can be described by the Bloch equation:

$$\frac{d\mathbf{M}}{dt} = \gamma\ \mathbf{M} \times \mathbf{B} - \frac{\mathbf{M_x}i + \mathbf{M_y}j}{T_2} - \frac{(\mathbf{M_z} - \mathbf{M_z^0})k}{T_1} \tag{2.19}$$

where $\mathbf{M_z^0}$ is the magnetization value at the presence of $\mathbf{B_0}$ only.

T_1 or spin-lattice relaxation time constant measures the time for the magnetization to grow back to 63% of its original value along the z-axis. Longitudinal relaxation is the process by which spins release energy into the surrounding lattice environment allowing the longitudinal magnetization $\mathbf{M_z}$ to recover to equilibrium $\mathbf{M_0}$. After a 90° pulse,

$$\mathbf{M_z(t)} = \mathbf{M_0}\ (1 - \exp(-\frac{t}{T_1})) \tag{2.20}$$

T_2 or spin-spin relaxation time constant measures the time for the transverse magnetization to decay to 37% of its value after RF excitation pulse. Transverse relaxation is the process by which spins lose their coherence through spin-spin interactions and the transverse magnetization $\mathbf{M_{xy}}$ returns to zero.

$$\mathbf{M_{xy}}(t) = \mathbf{M_0}\ \exp(-\frac{t}{T_2}) \tag{2.21}$$

In practice, $\mathbf{M_{xy}}$ decreases even faster since magnetic field inhomogeneity and susceptibility effects cause spin to dephase as well. T_2^* takes into the account the relaxation due to inhomogeneity of the magnetic field T_{2i} in addition to spin-spin interactions T_2:

$$\frac{1}{T_2^*} = \frac{1}{T_2} + \frac{1}{T_{2i}} \tag{2.22}$$

The relaxation constants T_1 and T_2 vary depending on the tissue types, which generating different contrast between biological tissues as illustrated in Figure 2.7 and Table 2.1. In general, T_2 values are much less dependent on $\mathbf{B_0}$ than T_1. Both of the them are strongly influenced by the water content of the tissue and vary significantly in abnormal tissues, which is one of the reason why MRI is highly sensitive tool for imaging brain. The intensity of the MR signal, p, depends on parameters such as TR, TE, T_1, T_2 and the spin population ρ as described by:

$$p = \rho\ (1 - \exp(-\frac{TR}{T_1}))\ \exp(-\frac{TE}{T_2}) \tag{2.23}$$

Image-Weighting	TE	TR
T_1 weighted	short	short
T_2 weighted	long	long.
Proton density-weighted	short	long

Table 2.1: Relationship between TE, TR and various image-weighting

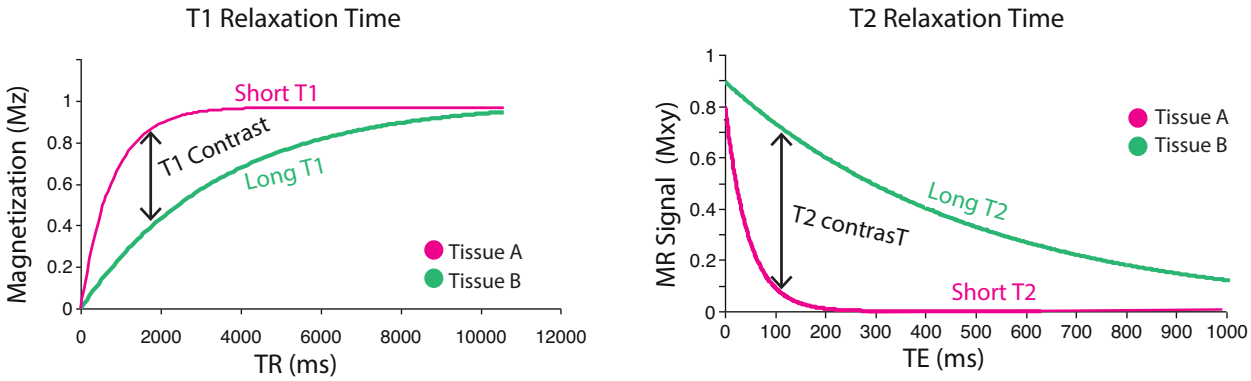

Figure 2.7: T_1-T_2 Relaxation Contrast Mechanism

2.2.6 Accelerated MRI

The k-space formalism is necessary to understand the principles behind the accelerated MRI which can be divided into three main categories. One method that has been applied uses modified or non-cartesian k-space sampling strategies such as echo planar, spiral or radial scanning. These trajectories acquire data at arbitrary positions in k-space due to the variable gradient waveform, whereas cartesian sampling acquires data at regular positions, due to the constant readout gradient. In the most extreme case, Ultra-fast MRI sequences lead to single shot scans, in which the entire k-space is acquired in a single acquisition and therefore require considerable more complex reconstruction algorithms than the simple Fourier Transform.

Another method to reduce k-space sampling are strategies such as compressed sensing. This method acquires less number of k-space samples (sub-nyquist) in a "randomly" fashion. Many signals are sparse in some domain, that is the same amount of information can be presented in smaller number of coefficients in that particular domain and compressed sensing takes advantage of that redundancy in the measurement domain. In this case, a more involved non-linear reconstruction method can accurately solve this under-determined (randomly undersampled) system of linear measurements by forcing the sparsity and data consistency constraints.

A third approach is to use multi-channel receiving coils and parallel imaging reconstruction techniques. This scheme utilizes spatially varying sensitivity from different channels of RF array to reduce the encoding time. This type of reduced k-space sampling produces coherent aliasing images in individual receivers however by much more demanding reconstruction methods and exploiting sensitivity profiles from each coil, one can unfold these aliased images. In general, there are two commercially available implementations of parallel reconstruction, image domain techniques and k-space domain techniques. All approaches aim for the best compromise between minimizing localized image artifacts on one hand and image noise on the other hand. The maximum reduction factor is limited by the number of independent coil elements and by the depth inside the body.

Rather than providing a complete overview of fast MRI methods, the discussion here is limited to the ultra fast echo planar imaging (EPI) based pulse sequences that initially was proposed by Mansfield. EPI is arguably the fastest method and forms the basis for a wide range of other fast MRI sequences and it is well suited to illustrate some of the consideration involved with fast MRI methodology. The compressed sensing (CS) and parallel Imaging (PI) methods will be introduced and discussed in the later chapters throughout this thesis.

The basic pulse sequence for gradient-echo EPI is shown in Figure 2.8 (a), with corresponding k-space trajectory shown in Figure 2.8 (b). The first two gradients (blue trapezoids) bring the start of k-space sampling to the edge of k-space at $(-k_{x,max}, -k_{y,max})$. The frequency-encoding gradient $\mathbf{G_x}$ (orange trapezoid) leads to the generation and acquisition of the first gradient-echo along the k-space line $k_y = k_{y,max}$ with $-k_{x,max} \leq k_x \leq +k_{x,max}$. A phase-encoding blip (blue triangle) brings the k-space position to $(+k_{x,max}, -k_{y,max} + \Delta k_y)$, after which sign-reversal of the frequency-encoding gradient $\mathbf{G_x}$ (yellow trapezoid) leads to the generation and acquisition of the second gradient-echo along the k-space line $k_y = -k_{y,max} + \Delta k_y$ with $+k_{x,max} \leq k_x \leq -k_x x, max$.

It is straightforward to see that all of the k-space can be sampled with a "back-and-forth" frequency encoding trajectory between $-k_{x,max}$ and $+k_{x,max}$ in which the second dimension evolves from $-k_{y,max}$ to $+k_{y,max}$ by constant-amplitude phase-encoding blips of Δk_y. Maximum echo formation is achieved when $k_y = 0$, which corresponds to the middle echo in k-space. The k-space sampling during spin-echo EPI is similar to that of gradient-echo EPI with the most noticeable difference that the application of a 180° pulse leads to refocusing of phase evolution due to magnetic field inhomogeneity for the echo in the center of k-space.

Direct Fourier transformation of the acquired EPI data does not result in a recognizable image due to differences between the odd and even echoes. The odd and even echoes are acquired in opposite directions in k-space and need to be time-reversed. Also eddy currents, gradient asymmetry and magnetic field inhomogeneity can all cause residual differences between even and odd echoes leading to ghosting in the image domain. The use of a reference dataset acquired without phase-encoding blips, is a robust method to significantly reduce

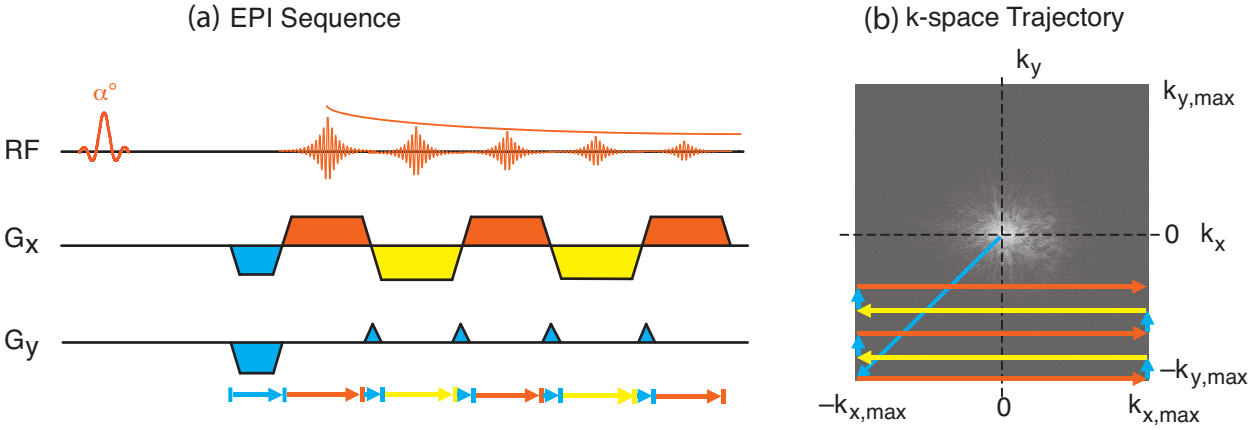

Figure 2.8: (a) Gradient-Echo EPI Sequence. (b) Corresponding (single-shot) k-space trajectory.

these ghosts. The reasoning being that without phase-encoding gradients all echoes in the reference data set should be identical (aside from T_2^* relaxation). Therefore any differences between echoes must be attributed to experimental imperfections and can be used to correct the phase-encoded EPI dataset resulting in reduction of ghosting.

EPI is exceptionally sensitive to experimental imperfections, like eddy currents, gradient asymmetry and magnetic field inhomogeneity. A pixel with a magnetic field inhomogeneity shifts in the frequency- and phase-encoding direction which become a significant problem specially at higher magnetic fields due to their encountered inhomogeneity. Besides improving the magnetic field homogeneity, the pixel shift can only be reduced by increasing the bandwidth (at the expense of a reduced SNR) or decreasing the number of phase-encoding increments per excitation. In the case when not all phase-encoding increments are acquired following a single excitation (multi-shot EPI), the geometric distortion in the phase-encoding direction reduces significantly. Furthermore, acquiring k-space over multiple excitations also allows a reduction of the minimum attainable echo-time, which can be an effective method to improve sensitivity or image contrast. The only downside of multi-shot EPI is that the experiment duration becomes multiple of TR, which can present an obstacle when very fast dynamic processes are studied such as cardiac MRI and fast functional responses.

2.2.7 MRI of Brain Tumor

Pre- and post-contrast T_1-weighted imaging and T_2-weighted fluid attenuated inversion recovery (FLAIR) are the two common types of MR imaging sequences used for tumor localization. The gadolinium (Gd) is a common contrast agent used in MR imaging. Figure 2.9 shows a post-contrast T_1-weighted and T_2-weighted images of several brain tumor patients.

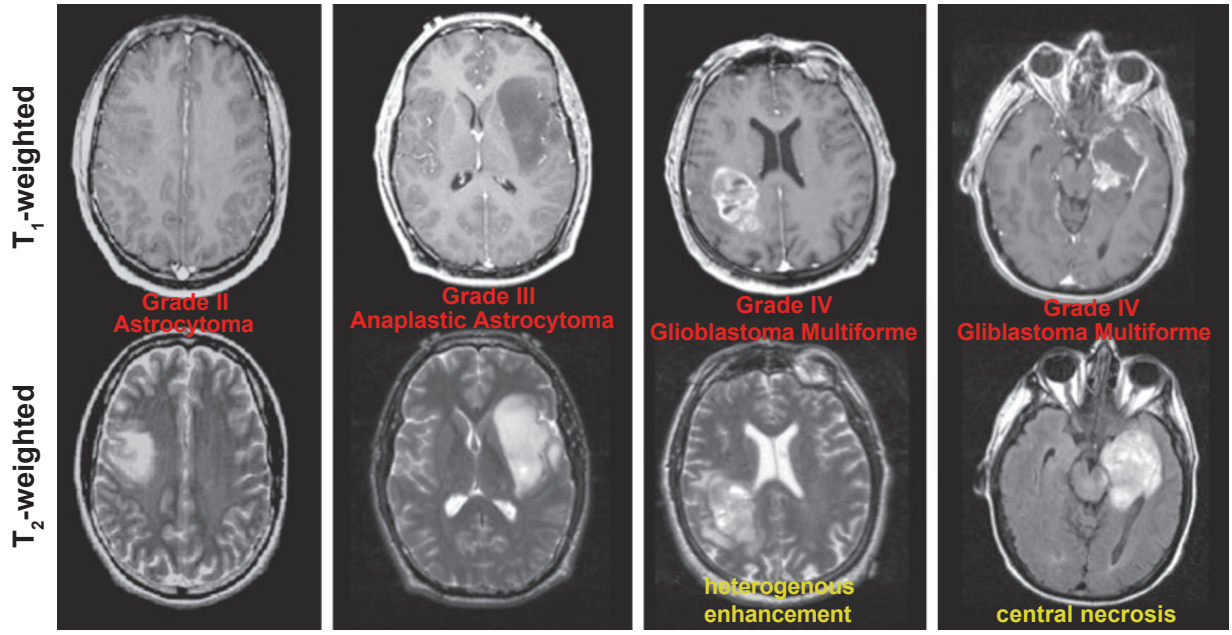

Figure 2.9: Post-gadolinium T_1-weighted and T_2-weighted images from patients with various tumors.

Tumor is usually seen as a hypointense area in the T_1-weighted images before Gd injection. After the contrast administration, Gd leaks into the areas of the brain where the BBB is disrupted, resulting in hyperintense regions due to the shortening of T_1.

T_2-weighted FLAIR images are acquired with an inversion recovery spin-echo sequence which starts with an additional 180° RF pulse tipping the magnetization into the z-axis. The magnetization starts relaxing back to its thermal equilibrium. After an inversion time (TI), the 90° RF pulse is applied followed by the regular spin echo sequence. The magnetization that is at z=0 at time TI does not experience the 90° RF pulse, and can not have a contribution at the resulting spin echo. This technique is commonly used to suppress the signal coming from the CSF in brain tumor imaging to allow for a better differentiation of edema. T_2-weighted FLAIR images show low intensity at the CSF locations, and hyperintensity in the areas of tumor, edema, and necrosis due to increased water content.

Although MRI is highly sensitive in tumor detection, the true margin of tumor border may be difficult to assess especially in infiltrative tumors such as glioma. This is in part due to infiltrative growth pattern of gliomas into adjacent normal brain tissue, and therefore they often do not have grossly or macroscopically definable margins. Physiological or metabolic MR imaging techniques like MR spectroscopic imaging, diffusion weighted imaging or perfusion weighted imaging are investigated to better the diagnostic capability of MRI and the

treatment planning and the prognosis of patients.

The combination of MRI and MRSI has been suggested to be more effective in tumor localization (3–8), directing tissue sampling (9, 10), assessment of progression and predicting outcome (5, 11–14), treatment planning (5, 9, 15), radiation therapy planning (16, 17), focal therapy (9, 10, 18, 19), and assessing response to therapy (5, 9, 10, 20–22) than MR imaging alone.

2.3 Fundamentals of Magnetic Resonance Spectroscopic Imaging (MRSI)

In-vivo MRSI is an important research tool and clinical imaging tool for providing biologically relevant information for assessing the underlying mechanisms of disease and for monitoring response to therapy (23). Both MRI and MRSI are applications of the NMR phenomenon: while MRI is primarily based on signal coming from protons in water, MRSI is obtained by differentiating the signals coming from proton in small metabolites. The resonance condition in NMR signal of MRI application is used to obtain the spatial information whereas, in MRSI is used to provide spectral information. The general schemes for MRI/MRSI data generation and subsequent data analysis are presented in Figure 2.10.

MRSI technology is built upon earlier work of localized single voxel spectroscopy (MRS) that was first described by Brown et al in 1982 (24) and further developed by Maudsley et al in 1983 (25). In recent years, MRSI has reached a remarkable degree of maturity and has attracted considerable amount of interest in clinical applications, however despite those interests, several technical challenges currently limit the widespread of clinical acceptance and usage of MRSI. The fundamental challenge with all MRSI is low concentration, ≈ 5 mM vs ≈ 55 mM water which is 10000 loss of SNR. MRSI historically has required a high degree of user training in exam prescription which makes its integration into clinical setting very difficult. Among the challenges faced in acquisition such as long acquisition times, low spatial resolution, poor coverage, interfering signal from fat tissues and sinuses, challenges in reconstruction, post-processing and quantification are also nontrivial. In our laboratory, robust techniques have been developed to automate MRSI prescription and acquisition and to improve the coverage of the brain while ensuring high quality data. These tools have been validated on healthy volunteers and patients with brain tumors and implemented in the hospital for routine clinical research examinations (**?**). The increasing availability of high field scanners and multichannel radio frequency coils has also provided the opportunity to acquire in-vivo data with significant improvements in sensitivity and signal to noise ratio. These capabilities may be used to shorten acquisition time and provide increased coverage. The ability to acquire rapid, volumetric MRSI data is critical for examining heterogeneity in metabolic profiles and for relating serial changes in metabolism within the same individual

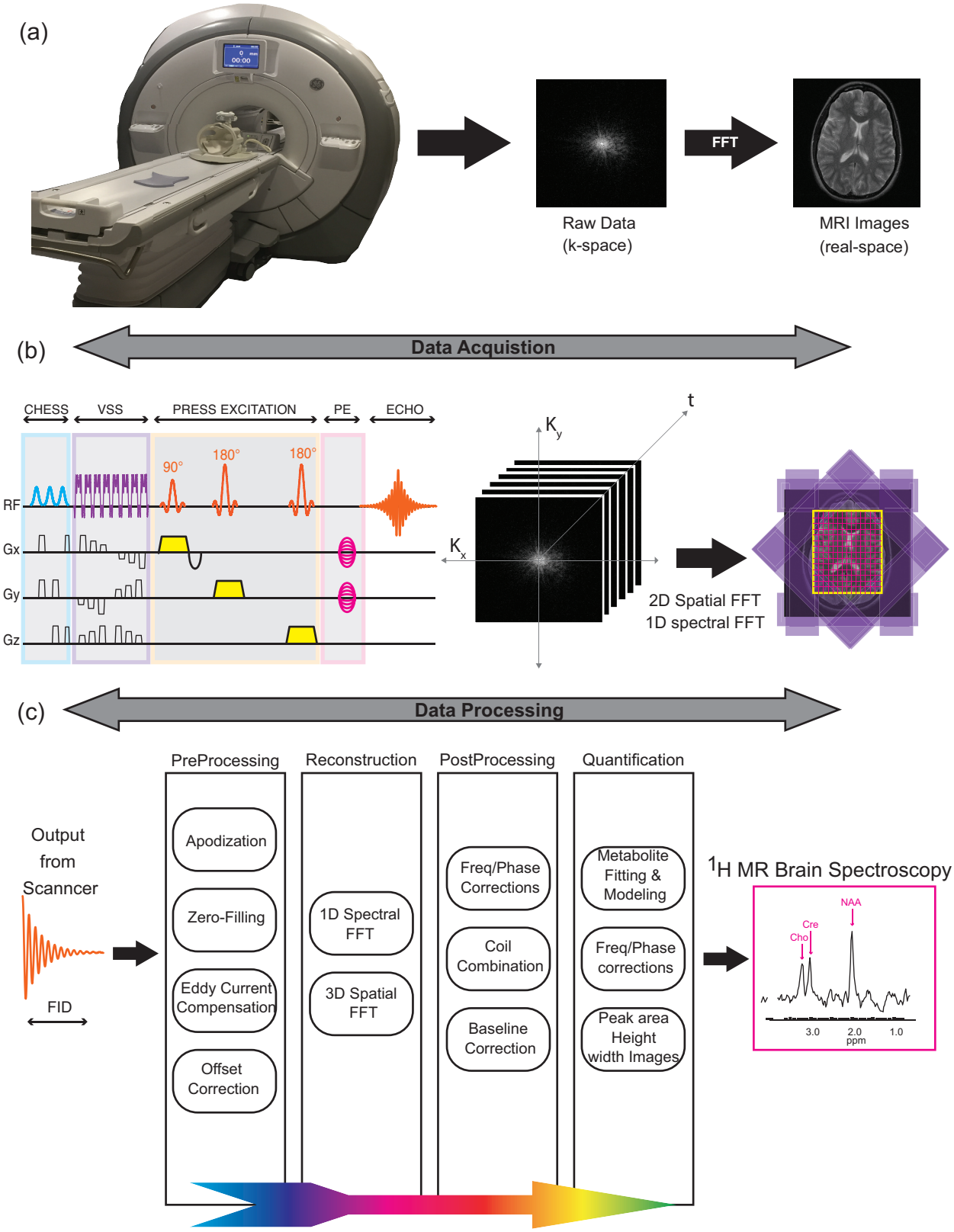

Figure 2.10: Diagrammatic representation of MRSI data generation and data processing in MRSI.

during the course of the disease. This section will describe the principles and data acquisition and reconstruction of spectroscopic imaging and its use for brain tumors. Throughout this thesis we discuss strategies and their implementations that use alternative k-space sampling trajectories and parallel imaging methods in order to speed up data acquisition for easier implementation in clinical settings.

Before explaining any advanced techniques that are developed here, one has to understand the basic of spectroscopy. In this section the basic phenomena in NMR signal of the MRSI application such as chemical shift and J-coupling will be described. The principles underlying MRI apply for many MRSI techniques, therefore, following sections concentrate on describing the challenges and concentrations of the MRSI pulse sequences. Some elementary data-processing of raw MRSI signals are presented. Additionally, a brief introduction to the k-t space formalism is given to provide a quantitative description of any MRSI sequence and the principles behind the fast MRSI methods.

2.3.1 Chemical Shift and J-Coupling

As seen previously, the essential concept of MRI is that the resonance frequency ω_0 is made position-dependent, such that after Fourier transformation the different frequencies correspond to spatial position rather than frequency shift as in MRSI. MR spectroscopic imaging is based on the principle that not all protons in a molecule have resonance at the same frequency (26). There are two main basic principles behind the formation of an MR spectroscopic signal, called a "spectrum". The "chemical shift" is the reason that multiple frequency components are observed within the signal from a single location. The "J-coupling" is the phenomenon that controls the multiplicity of the spectral peaks causing a split peak appearance. These two concepts will be briefly discussed here.

Chemical Shift:

The magnetic field experienced by a proton is influenced by multiple factors, i.e. the resonance frequency ω_0 not only depends on the gyromagnetic ratio (γ) and the external magnetic filed ($\mathbf{B_0}$) but is also highly sensitive to the chemical environment of the nucleus under investigation, which is referred to as the chemical shift (δ). Electron clouds around protons are known to create minimal magnetic fields opposing the primary applied static magnetic field ($\mathbf{B_0}$), reducing the magnetic field sensed by the protons. This effect is called "shielding" of electrons. Thus, the protons of the a molecule placed in a magnetic field experience slightly different field strengths due to the variation in their electron environment, leading to different resonance frequencies, ω, defined as,

$$\begin{aligned} \mathbf{B} &= \mathbf{B_0}(1-\sigma) \\ \omega &= \gamma \mathbf{B_0}(1-\sigma) \end{aligned} \tag{2.24}$$

where ω is the chemical shielding constant. Obviously, the frequency of a shielded proton is dependent on the strength of $\mathbf{B_0}$. To avoid the dependency and creating an absolute frequency scale, chemical shifts are expressed in terms of parts per million (ppm) rather than radians or Hertz (Hz). By convention the chemical shift δ is defined as:

$$\delta = \frac{\omega - \omega_{ref}}{\omega_{ref}} \times 10^6 \tag{2.25}$$

where ω and ω_{ref} are the frequencies of the compound under investigation and of reference compound, respectively. A widely accepted reference compound for ^1H and ^{13}C NMR is tetramethylsilane (TMZ) to which $\delta = 0$ has been assigned. For example, the resonant frequency of fat protons differ from water protons by 225 Hz at 1.5 T and 450 Hz at 3T, but this difference is 3.5 ppm in both cases. The normal way of displaying MR spectra is to plot high ppm values on the left, and low ppm values on the right.

J-Coupling:

The NMR resonance frequencies or chemical shifts give direct information about the chemical environment of nuclei and aid in detecting the compounds. An additional feature that can be observed in high-resolution NMR spectra is splitting of resonances into several peaks, a phenomenon called J-Coupling or spin-spin coupling. This is because the protons under investigation can be influenced by the electrons through the chemical bonds that are three or less bonds away in distance. J-coupling contains information about bond distance and angles and most importantly provides information on the connectivity of the molecules. Unlike chemical shift, the J-coupling is independent of the applied magnetic field and the frequency difference between the multiple peaks of a proton stays the same and depends on the coupling interaction between the spin groups and this constant frequency difference is called a "J-coupling constant".

For a 1/2-spin system such as protons, each neighboring spin can have one of two possible spin orientations in the presence of $\mathbf{B_0}$, either spin-up or spin-down. Thus the magnetic field sensed by the proton under investigation can be altered by $\pm\mathbf{\Delta B}$ resulting to process faster or slower than normal. This results in the observation that n protons will split the adjacent protons to $n + 1$ peaks and the intensities of these peaks are simply result of the possible spin orientations.

Thus, the spin-spin splitting can be explained by the $n + 1$ rule in its most simplistic form. This rule states that protons that have n neighboring protons have $n + 1$ peaks as a result of their interactions. However, the $n + 1$ rule only applies when the neighboring protons are chemically equivalent to each other. The mechanism in which the splitting patterns and intensities occur for other types can be rather complicated and beyond the scope of this introduction however more information can be found in (26).

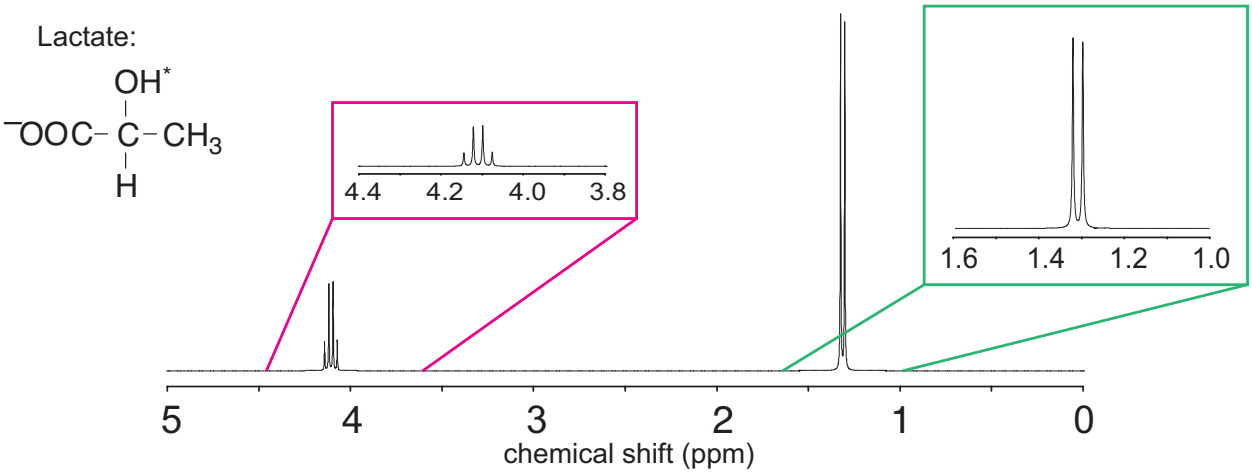

Figure 2.11: Chemical structure and simulated ^{1}H spectrum of Lactate.

As a simple example Figure 2.11 shows the NMR spectrum of lactic acid (lactate) which is the end-product of anaerobic glycolysis pathway and the major interest in cancer research. Based on $n + 1$ rule, as shown in Figure 2.11, lactate (Lac) would have 4 peaks (quartet) at 4.10 ppm for the single methine group (CH) because of the three protons on the methyl (CH3). Similarly, the three equivalent methyl group would have 2 peaks (doublet) at 1.31 ppm because of the one neighboring proton of methine group. Increased lactate concentration have been observed under a wide variety of conditions in which blood flow is restricted such as hypoxia and tumor. In these cases in the brain, Lac overlaps with macromolecular resonances and large subcutaneous lipid. However, lactate can be detected with adequate localization and spectral editing techniques which is discussed in later section.

2.3.2 MRSI Data Acquisition

MRSI pulse sequences use a combination of frequency and spatially selective pulses to suppress unwanted signals (such as water and fat) and localize metabolites of interest to specific regions of the anatomy. Given the accurate volume selection, then the next step is to perform spatial encoding in a manner that can be reconstructed to provide an array of spectral data. Figure 2.10 (b) illustrates conventional phase-encoded MRSI pulse sequence, in which the phase encoding gradient amplitude is incremented once per TR which is the most commonly used MRSI method and still represents the gold standard for sensitivity and localization performance. The next few sections briefly describe each module of the pulse sequence shown in Figure 2.10 (b) for brain MRSI acquisition.

MRSI acquisition cannot be portrayed without discussing point spread function (PSF), which describes the spread of signal from a point source into neighboring voxels as a result of the finite extent of the encoded k-space points (k-space sampling). For uniform k-space sampling,

the PSF is a $sinc = \frac{\sin x}{x}$ function which is the Fourier Transform of the rectangular sampling window. Meaning, for a point source in the center of the voxel the zero crossings of the PSF functions happens exactly in the centers of the neighboring voxels. In other words, there is no signal spread to adjacent voxels and the image of the point source is a single bright voxel. However, a point source located at the edge of a voxel leads to considerable spread of signals into neighboring voxels. The signal contamination of *sinc* function has positive and negative contributions depending on the distance from the origin of the PSF due to side-lopes of the *sinc* fucntion, which can lead to very complex signal interference. PSF is a direct consequence of the coarse spatial resolution of MRSI and this so-called Gibbs ringing phenomena is also present in conventional MRI, but it is less visible than in MRSI due to the considerably higher spatial resolution.

Brain metabolite levels are on the order of 10 mM or less, whereas water and lipid (fatty tissues under the skin) in brain are approximately 50-80M. Therefore, water and lipid suppression techniques are critical for proton spectroscopy in order to reliably observe the much smaller metabolite signals. Since both water and lipid resonances have shorter T_2 relaxation times than many metabolites, suppression factors are also usually better in long TE compared to short TE spectra, but use of a long TE alone is insufficient to obtain sufficient suppression and short TE spectrum are more desirable since they provide more information.

Water Suppression:

The quality of water suppression is often directly related to the magnetic field homogeneity, and the quality of spatial localization. Water suppression should achieve a reduction to a degree that water does not limit the dynamic range of the receiver, water does not significantly affect the spectral baseline and vibration-induced sidebands of the water are negligible. More important than the absolute degree of suppression is the shape of the water peak. Meaning, a relatively large but approximately Lorentzian shaped water peak is easily removed by post-processing methods. However, an incompletely dephased water peak, spread out over a wide frequency range will lead to a significant baseline distortion which is not easily removed by post-processing methods. Therefore, some of the criteria to evaluate different water suppression methods are but not limited to degree of suppression, insensitivity to RF imperfections, ease of phasing the spectra, and insensitivity to relaxation effect.

The most common approach to suppress the water is to pre-saturate the water signal using frequency selective pulses prior to the localization in the MRSI sequence. As shown in the Figure 2.10 (b), Chemical shift selective (CHESS) pulses (27) are 90° single frequency selective excitation pulses followed by big dephasing gradients. By using more than one pulse, and with a correct choice of flip angles (28), very good suppression factors can be obtained (>1000).

Since some T_1 relaxation will occur between the suppression pulse and the read-out pulse

of the localization sequence, a flip angle somewhat greater than 90° is required in order to catch the water longitudinal magnetization at its null point. By using more than one pulse, the sequence can be designed to give good suppression factors over a range of T_1 relaxation times and $\mathbf{B_1}$ field strengths (B1 inhomogeneity) (28).

This procedure leaves the spin system in a state where no net magnetization of the component resonating at the selected frequency is retained. The other components resonating at different frequencies than the selected frequency remain entirely unaffected in the form of z-magnetization. Then, subsequent 90° excitation pulse of the pulse sequence only excites the frequencies which have z-magnetization. Therefore, the resulting image or spectra contain minimal signal intensity for the suppressed frequency.

Lipid Suppression:

Interference from lipid signal has long been a major problem in MR spectroscopy. Very large lipid signals can be produced by tissues that have a large fraction of adipocytes and signals from those regions can be very problematic in spectroscopy in terms of bleeding into nearby voxels (Gibbs ringing) due to the coarse resolution of MRSI. Although subcutaneous lipid signal needs to be suppressed, the lipid within the lesion of brain is a valuable biomarker for tumor malignancy (29). So, while water signal can be successfully suppressed in brain using frequency selective techniques such as CHESS, subcutaneous lipid peaks are more difficult to suppress spectrally without precluding the lipid in brain lesions and the compounds such as Lactate and NAA which resonate in the same region of the spectrum. Alternatives techniques are pre-saturating the regions that would produce large lipid signal.

Currently the most commonly employed methods for lipid suppression, namely volume pre-localization, outer volume suppression (OVS) and very selective saturation pulses (VSS), utilize the difference in spatial origins of lipids and metabolites. Since the subcutaneous lipids are either not excited/refocused or excited but suppressed, they do not contribute to the detected signal.

Volume pre-localization methods use localization techniques such as STEAM and PRESS (described in details in the next section) to select a relatively large rectangular volume inside the brain. The human (or animal) brain is not rectangular in any orientation, and volume pre-localization destroys signal from cerebral tissues on the edge of the brain. This can be problematic when abnormalities are present at the brain periphery, such as encountered in stroke or tumors. Two other effects become especially pronounced during volume pre-localization, namely imperfect slice profiles and the chemical shift displacement (described in the following sections).

OVS is usually implemented with a number of saturation bands or sat bands with each sat band eliminating most of the MR signal from a slab of space. OVS works essentially oppo-

site to the strategy employed by volume pre-localization. Rather than avoiding the spatial selection of lipids, OVS excites narrow slices centered around the brain in lipid-rich regions. Following slice-selective excitation, the transverse magnetization is dephased ("spoiled") by a subsequent magnetic field crusher gradient. Following the OVS modules, the brain water and metabolites signals can be excited without lipid contamination. Conventional sinc-shaped pulses for OVS bands have relatively low bandwidth and high peak amplitude. These limitations result in poor edge profiles, $\mathbf{B_1}$ and T_1 sensitivity, chemical shift effect and long excitation times.

VSS pulses (30) are short quadratic-phase spatial suppression pulses. While conventional OVS pulses found to be suboptimal, short trains of VSS pulses per saturation band are used to provide improved spatial suppression with reduced dependence on $\mathbf{B_1}$ and T_1. VSS pulses have very sharp excitation profile. The passband of VSS pulses is very high on the order of 6 kHz, which results in reduced chemical shift artifact for MR spectroscopy. Figure 2.10 (b) shows a schematic representation of VSS pulses applied along with spectral spatial pulses.

MRSI Excitation & Localization :

Because the bleeding problem of lipid and water signal into neighboring voxels can be very significant in ^{1}H-MRSI, very precise spatial localization methods are required. Most ^{1}H-MRSI pulse sequences use volume excitation procedures to select a box shaped tissue region over which the field homogeneity is excellent and that does not contain adipose tissue. Therefore, first and foremost, spatial localization is used to remove unwanted signals from outside the region of interest (ROI), like extracranial lipids in MRSI applications of the brain. Additional benefits of spatial localization originate from the fact that variations in $\mathbf{B_0}$ and $\mathbf{B_1}$ magnetic fields are greatly reduced over the small localized volume, therefore providing narrower spectral lines and more uniform signal excitation and reception, respectively. While pre-localization of a box-shaped region inside the brain may improve the overall spectral quality, it can also result in considerable loss of volume coverage in peripheral regions of the brain. Brain can be segmented into gray-matter, white-matter and CSF, each of which has unique metabolic profiles. Careful positioning of the localized volume can minimize "partial volume effects" (contamination of signal from one compartment by signal from another compartment), and provide better tissue characterization.

MRSI acquisition is similar to MRI with an exception of not using the gradient magnetic field during signal readout, i.e. rather than using a frequency encoding in one dimension and phase encoding in other dimension, one uses phase encoding in all dimensions (hence the longer acquisition time). The use of phase encoding only to obtain location information ensures complete temporal separation of spatial encoding from spectral encoding. The recorded signal becomes a combination of the signals produced by spins that precess at different frequencies (spectral encoding) due to their chemical shift, i.e. chemical shift is independent of spatial encoding. Therefore, the reconstruction is straightforward using Fourier Transform

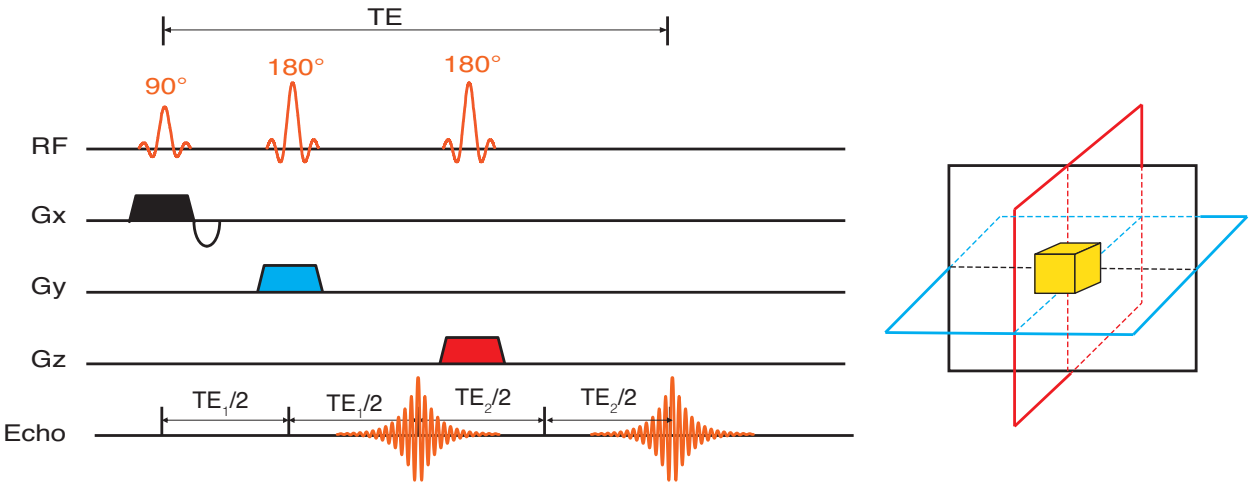

Figure 2.12: PRESS Localization.

along the orthogonal spatial and spectral dimension of raw data matrix. Phased encoding must be performed in all spatial dimensions, and is very time consuming. The number of phase encoding steps corresponds to the total number of voxels in the spectroscopic image. For example to acquire 16x16x16 three-dimensional (3D) matrix using $TR = 2(s)$ would require 2.3 hours of encoding which is unacceptable for human studies.

In the last two decades a wide variety of spatial localization techniques have been developed. The two most commonly used techniques for in-vivo ^1H spectroscopy acquisition are STEAM (31) (STimulated Echo Acquisition Mode) and PRESS (32) (Point RESolved Spectroscopy). Both of these sequences use three slice-selective RF pulses ($[90°, 90°, 90°]$,$[90°, 180°, 180°]$ respectively) with orthogonal magnetic field gradients where the intersection of the slices defines the Volume of Interest (VOI). STEAM and PRESS are generally similar but differ in few key aspects. For example, STEAM has a sharper slice profile because it is easier to produce the 90° pulse with a sharp slice profile than a 180°. Provided equal volumes of tissues using the same parameters (Repetition Time (TR), Echo Time (TE), number of averages, etc), PRESS should have approximately factor of 2 better SNR than STEAM, because the stimulated echo in STEAM is formed from only half the available equilibrium magnetization. STEAM should have a shorter minimum TE than PRESS, since it uses a Mixing Time (TM) period during which T_1 rather than T_2, relaxation occurs and shorter 90° than 180° pulses may be possible. STEAM is somewhat more susceptible to the effect of motion. Nevertheless, these differences are fairly subtle and STEAM and PRESS are generally comparable in clinical brain spectroscopy, and in practice, the choice of sequence often depends mainly on the availability form the MRI vender.

Majority of MRSI data acquired in this thesis are 2D/3D PRESS localized, therefore more detail is given for this sequence only. PRESS employs a double spin-echo excitation. PRESS

utilizes three consecutive 90°, 180° and 180° slice selective RF pulses applied along with gradient pulses in three orthogonal directions. Figure 2.12 shows a schematic representation of the PRESS pulse sequence.

The first 90° RF pulse and its gradient along x excites the spins resonating at a certain frequency within a slice of tissue. The first 180° RF pulse and its gradient along y are applied at a time $\frac{TE_1}{2}$ after the 90° pulse, and it excites the spins located within a slice along y, and rephases the spins located only at a column located at the intersection of the previously excited slice x and the current slice y. An echo is formed at a time TE_1 after the 90° pulse due to the effects of the 90° and 180° pulses, and it is not sampled. The second 180° pulse is applied at a time $\frac{TE_2}{2}$ after the first 180° pulse with its gradient along z. This pulse excites the spins located within a slice along z, and rephases the spins located only at the intersection of all three selected slices. The final echo is formed at a time $\frac{TE_2}{2}$ after the second 180° RF pulse. This echo is sampled and processed to form a spectral image of the voxel at the intersection of all three excited slices.

A serious limitation of the PRESS selection is that the selected volume has to resemble a rectangular prism. Techniques such as 2D RF excitation (33) have been proposed to overcome this by exciting an arbitrary shaped volume. They require very long RF excitation pulses and can have problems with chemical shift displacement due to the limited bandwidth of those pulses. A critical issue when using any form of spatially selective excitation at higher field strengths is to consider the bandwidth of the rf pulse and the frequency shift between the resonances that are being evaluated.

Chemical Shift displacement:

The spatial position of the localized volume obtained by a localization method that employs frequency selective RF pulses in the presence of magnetic field gradients will be linearly affected by the chemical shift of the compound under investigation. From Equation 2.9 it follows that the frequency of spins with Larmor frequency ω_0 in the presence of a magnetic field gradient $\mathbf{G_x}$ in the x direction is given by:

$$\omega(x) = \omega_0 + \gamma\, x\, \mathbf{G_x} \tag{2.26}$$

$$x = \frac{\omega(x) - \omega_0}{\gamma \mathbf{G_x}} \tag{2.27}$$

Therefore, a difference in Larmor frequency ω_0 between two different compounds results in a spatial displacement x of the localized volume for one compound relative to the other according to:

$$\Delta x = \frac{\Delta\omega}{\gamma\, \mathbf{G_x}} = \frac{\Delta\omega}{\Delta\omega_{max}} \mathbf{V_x} \tag{2.28}$$

where $\Delta\omega$ represents the difference in Larmor frequency. The right-hand equality is constructed based on the fact that the required gradient strength $\mathbf{G_x}$ to select a given voxel

size $\mathbf{V_x}$ in the x direction is proportional to the spectral bandwidth of the RF pulse $\Delta\omega_{max}$. Equation 2.28 reveals that the chemical shift displacement is more severer at higher fields and that the artifact can only be minimized by increasing the magnetic field gradient strength, which (for a constant voxel size) corresponds to an increase in spectral bandwidth of the RF pulse. Shortening the RF pulse length will increase the bandwidth, at the expense of an increased specific absorption rate (SAR).

The limited bandwidth of excitation pulses of the PRESS selection makes it difficult to obtain a sharp excitation profile. Moreover, because of the chemical shift effect, the volume of excitation for lactate and lipid is significantly shifted from that of choline. To overcome that, an overprescribed (OverPRESS) method was developed in which the PRESS volume is automatically enlarged by a factor of 1.2 - 1.5 over that prescribed (34). That ensures that all metabolites are excited within the prescribed volume. Outer-volume suppression is used to sharpen the profile of the excited area. Because of their much higher bandwidth, the saturation pulses are less susceptible to chemical shift.

In short, acquiring high quality MRSI data is a demanding task. Many ingredients and shortcomings of MRSI need to be considered and addressed in order to develop appropriate pulse sequences and protocols for clinical setting. Most of the features of the MRSI pulse sequences are interlaced, meaning improving one aspect of acquisition may require a compromise in another. Therefore achieving clinically acceptable data requires a tactful balance between these components. Some of the challenges of acquiring a good MRSI data lies within the following categories:

- **Voxel size or resolution:** In general MRSI uses the same phase encoding procedures that are used in MRI to map spatial information of the NMR signals, however in the case of proton spectroscopy, the signal is produced by the metabolites within the tissue that are at least 10000 times less in concentrations compared to water. To detect enough signal above noise for quantification purposes, MRSI must use much larger voxel sizes in comparison to MRI. The lower spatial resolution of MRSI makes the consideration of the blurring effect of spatial point spread function (PSF) more important. Voxel volumes are typically on the order of $1cc$ or smaller. Achieving higher spatial resolution is desirable since it allows better characterization of the extent of disease and its heterogeneity in addition to reducing the ringing artifact of the subcutaneous fat (due to PSF), however it adversely affects Signal to Noise Ratio and increase the acquisition time.

- **Signal to Noise Ratio (SNR):** SNR measures how the intensity of the acquired MR signal compares to the level of the noise. The motion of electrons within the body is the main factor causing noise in the data. To accurately quantified the metabolites for clinical application, their peaks need to be reliably detected above the noise floor. SNR is proportional to the volume of the voxel and to the square root of the total

acquisition time. Therefore, SNR can be improved using larger voxels or by averaging the multiple scans of the same tissue. On the other hand, accelerating the acquisition or increasing the spatial resolution that is desirable in clinical applications leads to loss in SNR. In recent years, another alternative for improving SNR is using multi-channel RF received coils.

- **Multi-channels RF received coils:** The use of phased array coils increases SNR and proposes additional capabilities in spatial encoding in a way that enables accelerated MRSI acquisition by reducing the number of required phased encoding steps. The acceleration offered by parallel imaging techniques can be used to reduce the total scan times and thus increase patient comfort and reduce sensitivity to motion, or can be exchanged for increased volumetric coverage and/or higher spatial resolution depending on the available SNR. However, new challenges due to variations in geometry, wiring, receive delays and electrical properties of the coil elements arise in combining the data from different receive channels in an efficient manner.

- **Acquisition time:** Acquiring high-resolution data with large field of view requires long acquisition time. Accelerated techniques, such as echo-planar spectroscopic imaging can robustly accelerate the acquisition, but result in lower SNR. A clinical exam consists of anatomical, functional and metabolic imaging sequences and must take into account the patient comfort and cost. Typical clinical exams are scheduled in 30 or 60 minute slots, while clinical research exams can be up to 90 minutes long during which the patient has to lie perfectly still. Any motion during the scan can significantly compromise the data quality.

- **Field strength of $\mathbf{B_0}$:** The SNR and spectral resolution of MRSI increase with field strength (due to increased chemical shift dispersion and reduced higher-order coupling effects) which can improve the performance of metabolite quantification, or can be traded for shorter acquisition times or higher spatial resolutions. However, there are many factors that may reduce the expected SNR and spectral resolution at higher field, such as longer T_1 relaxation times that lead to saturation-related signal losses, line broadening due to magnetic susceptibility effects, shorter T_2 relaxation times that require shorter echo time (TE) acquisition to maintain sensitivity, constrained RF power deposition and limitations in the design of homogeneous RF coils.

- **$\mathbf{B_0}$ inhomogeneity:** Variation of the main magnetic field (B0) within a voxel leads to peak widening and loss of SNR. The oral and nasal cavities, ear canals and sinuses cause significant nonlinear variations of the local magnetic field, especially in the anterior and inferior parts of the brain. The increase in $\mathbf{B_0}$ inhomogeneity at ultra-high field (i.e., at 7 Tesla and beyond) is a challenge for shimming that limits the sensitive volume.

- **$\mathbf{B_1}$ variation:** The power of RF from the excitation pulses varies due to the inhomogeneity of the transmit coil profile and attenuates within the tissue. This causes

variation of the achieved flip angles and results in sub-optimal SNR, water and lipid suppression. Due to increased $\mathbf{B_1}$ inhomogeneity and the constrains on RF pulse performances at higher fields, spatial pre-localization becomes a major challenge.

- **Specific Absorption Rate (SAR):**. The power deposited into biological tissues by RF pulses and ultimately dissipated as heat is reflected and quantified by SAR and expressed in units of watts per kilogram. Keeping SAR within the safe limits often requires limiting the number and power of RF pulses or increasing the repetition time (TR), which in turn, leads to longer total acquisition time. This is especially a problem on the ultra-high-field scanners and/or when using complex RF pulses for excitation or suppression of water and lipids.

- **Water and fat suppression:** Often artifacts from water and lipid signals that are related to field inhomogeneity and the PSF present themselves in ^{1}H-MRSI data sets. Water produces a much larger signal than the target metabolites and if not suppressed it causes baseline distortions and obscures small signals at other resonances. Lipid signals that are as much as 1000 times stronger than metabolite signals can be produced from the fatty tissues under the skin throughout the body, including the scalp. Lipid signals produced by such regions can be problematic in terms of bleeding into nearby voxels up to the point of making quantification of the metabolites of interest impossible if not suppressed effectively.

- **Phase sensitive data:** Phase of the signal varies between voxels within the brain due to variation in the magnetic field. It also varies between the signal from different channels of a multi-channel receive coil. Consistent phase is needed for interpretation and quantification of spectra, and, in case of multi-channel data, to avoid SNR loss due to the signals from different channels canceling each other.

- **Echo Time (TE):** TE is an important parameter of spin-echo-based pulse sequences. The major metabolites that are observed in the brain with 1^H-MRSI in long echo time (100 ms) include choline-containing compounds (Cho), creatine (Cr), N-acetyl aspartate (NAA), lactate (Lac) and lipid (Lip). Shorter TE sequences (35 ms) yield additional information from metabolites with short er$T2$, such as glutamate (Glu), glutamine (Gln), myo-Inositol (mI) and glycine (Gly). However, shorter TE also results in higher water and lipid signals and uneven baseline from the contributions of the macromolecule making the metabolite quantification more challenging. On the other hand the use of long TE results in substantially decreased sensitivity to the metabolite signals due to T_2 loss and J-modulation of multiplet resonances.

- **Brain Coverage:** The MRSI exam needs to cover the complete lesion and as much of the apparent healthy tissue as possible that may exhibit signs of metabolic abnormality. Increasing the field of view results in longer acquisition time and increases the risk of lipid contamination and problems due to the inhomogeneity of the main magnetic field

($\mathbf{B_0}$) and radio frequency excitation ($\mathbf{B_1}$). Achieving high brain coverage while using outer volume suppression (OVS) to suppress the lipid signal requires complex OVS configurations with a large number of saturation bands.

- **Automatic Prescription:** MRSI acquisition is controlled by dozens of parameters, including placement of the selected volume and Outer Volume Selection (OVS) bands, shimming currents, etc. Choosing optimal parameters that result in high quality data for a particular subject requires a skilled operator and can take a long time. Suboptimal prescription often results in poor data quality and incomplete coverage of the target lesion. Automating the prescription is important for clinical implementation, for optimizing coverage, for making comparison across populations and for using serial scans to evaluate response to therapy in the same subject. In our laboratory, Ozhinsky et al. (**?**), developed an automated method using sequence parameters that have been shown to provide robust spectral data at 3T. This included PRESS volume selection in conjunction with the BASING technique which not only improves water suppression but can also be employed for J-resolved spectral editing to separate resonances such as lactate and lipid.

2.3.3 MRSI Data Processing

The general schemes for MRSI data generation and subsequent data analysis are presented in Figure 2.10. MRS data analysis is divided into four stages: preprocessing, reconstruction, postprocessing and quantitation. Some of the processing steps can be applied in both frequency and time domains with similar outcome. There is a direct correspondence between the representative parameters involving FIDs in time domain and metabolite peaks of the spectrum in frequency domain. Hence, quantification of MR signal is performed from both the FID and the spectrum equivalently.

However, there are many differences between time and frequency- domain data analysis. In the time domain method, concentration of a metabolite component is proportional to the amplitude of the signal, whereas in the frequency domain, concentration of metabolites is proportional to the area under the metabolite peak. In time domain method, MRS data is analyzed within the "measurement domain". If the measured signal is ideally identified by high SNR, with no truncation and no baseline distortion, then both time and frequency domain methods give the same results within the error limits. Any imperfections in the measured signal, due to experimental conditions may create a difference in metabolite concentration between the frequency and the time-domain data. In time-domain data processing, a particular range of good data points can be used for analysis, whereas in the frequency domain, Fourier transformation is performed for all data set and separating the good data points is not possible in frequency domain. In the frequency domain, distortion of the spectrum may arise due to the receiver induced effect at the initial data point as well as due to truncation of the FID. This creates a rolling baseline. Immobile components due to short transverse

relaxation time (T_2) generate spectra with broad line widths. These broad lines create a "macromolecular baseline" or a baseline originating from short T_2 components, which makes the baseline approximation more demanding. The time-domain computations can be more memory and time consuming compared to frequency-domain. In general, time- domain methods do not rely on equally spaced sampling intervals, which may be attractive for the multidimensional MRSI techniques.

2.3.4 MRSI of Brain Tumor

An example of ^{1}H MRSI of in-vivo normal human brain from a 3T MR scanner is illustrated in Figure 2.13 (a). The major metabolites that are observed in long TE ($>100ms$) include choline-containing compounds (Cho), creatine (Cr), N-acetyl aspartate (NAA), lactate (Lac) and lipid (Lip). Cho is an essential nutrient for the synthesis of the neurotransmitter, a major constituent of the cell membrane. Cr reflects bioenergetics processes and represents the energetic status of the cell. NAA is the most abundant amino acid in brain that is synthesized in neurons and is an indicator of the neuronal viability. Figure 2.13 (b) shows the T_1-weighted MR image along with a typical normal and tumorous spectra of the patient with glioma. The elevation of Cho, due to increased membrane synthesis in neoplasms, and the reduction of the neuronal marker NAA have been used for distinguishing regions of tumor from normal brain tissue (13). Lac, which is a marker of anaerobic metabolism, overlaps with Lip signals that arise from necrosis or from contamination due to subcutaneous Lip. Spectral editing using J- difference methods have been applied to separate Lac from Lip for assessing the malignancy of tumors (35). High levels of Lac and Lip have been reported as a robust predictor of poor overall survival in patients with glioblastoma (36). An comprehensive example of a newly diagnosed glioblastoma patient is shown in Figure 2.14 with normal and tumorous voxels (37).

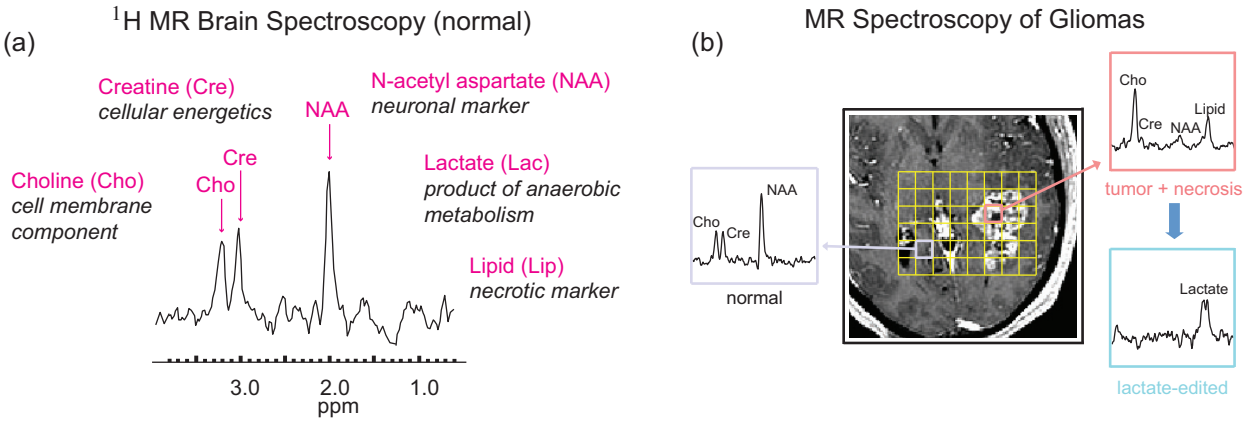

Figure 2.13: T_1-weighted MR image along with an examples of spectra located at the yellow grid for a glioma patient.

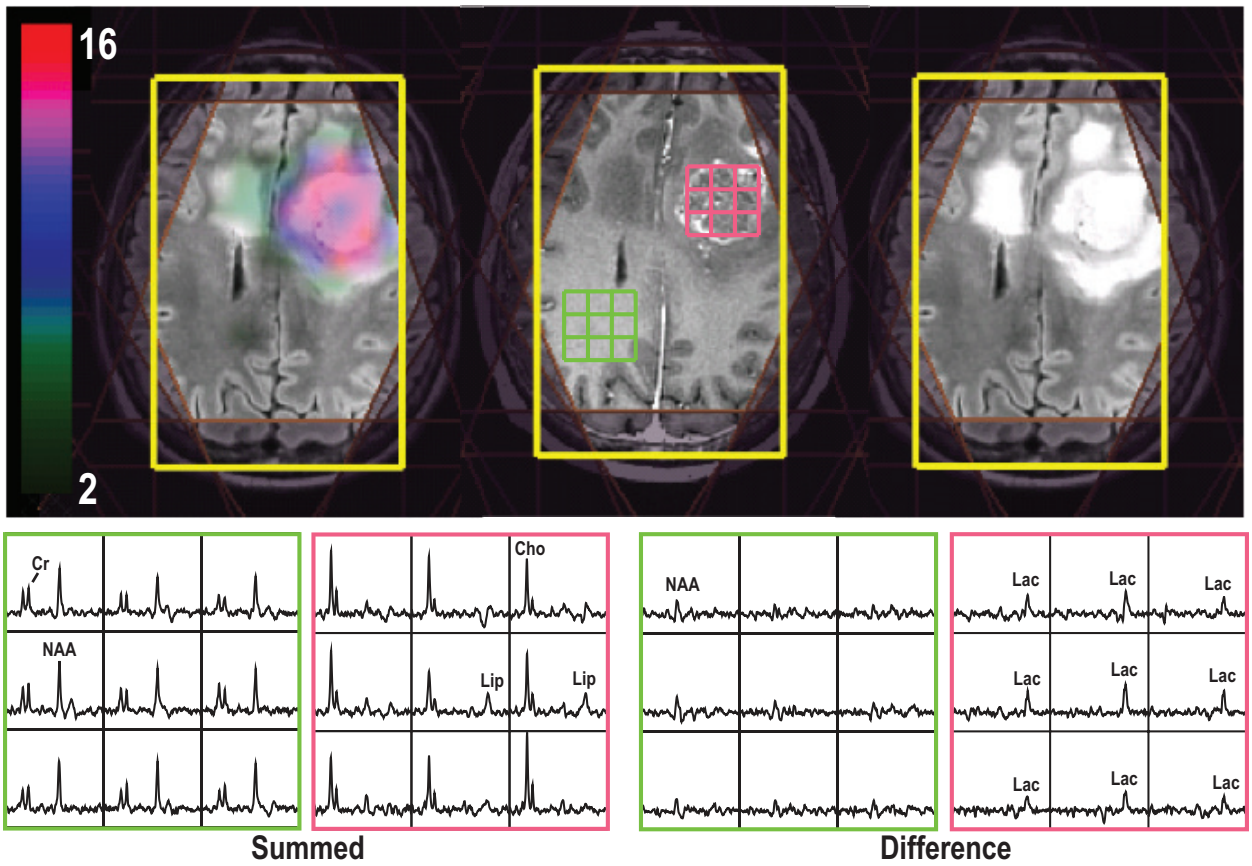

Figure 2.14: 3D lactate-edited ^{1}H MRSI acquired from a patient with a newly diagnosed glioblastoma (TE/TR=144/1500ms, matrix size $18 \times 18 \times 16$, flyback in S/I, nominal spatial resolution = 1 cm^3, T_{acq}=13min). Spectral array corresponds to summed and difference of the lactate-edited spectra. The Cho-to-NAA index overlaid on T_2weighted images shows abnormal metabolic lesions.

Shorter TE sequences (<40ms) yield additional information from metabolites with short T_2, such as glutamate (Glu), glutamine (Gln), myo-Inositol (mI) and glycine (Gly), in the spectrum. An example of spectra acquired using short echo MRSI at 3T is illustrated in Figure 2.15. The mI is predominately located within astrocytes, and often overlaps with the peak of glycine in spectrum. Elevations in mI and glycine were observed in low-grade but shown to decrease in high-grade brain tumor lesions. Glu and Gln also appear in the spectrum but the peak overlapping makes it difficult to isolate individual components at 3T, thus a combined index known as Glx that represents a combination of Glu and Gln is often used for comparative purpose. Glx participates in energy metabolism, macromolecular synthesis and signaling pathways, suggesting that it is a good target to treat or monitor patients.The complex roles of Glu, Gln, and GSH in tumors make it valuable for evaluation of patients with glioma.

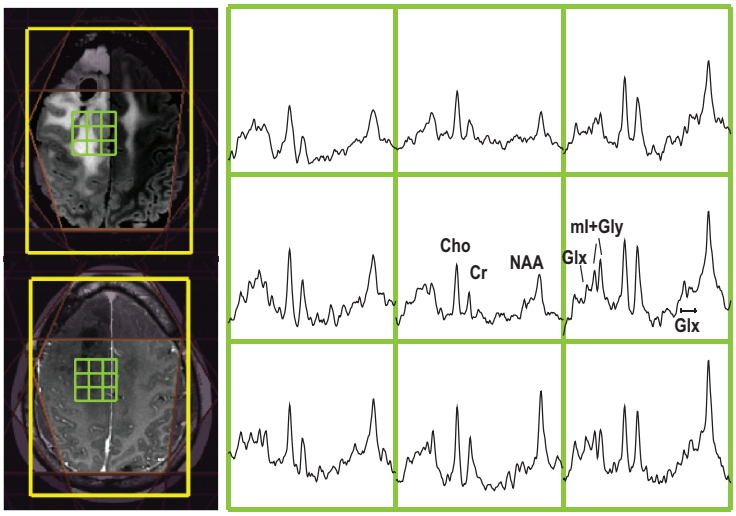

Figure 2.15: Example of short-echo ^{1}H MRSI acquired from a patient with grade II glioma at 3T (TE/TR-35/1500ms, matrix size $18 \times 18 \times 16$, flyback in S/I, nominal spatial resolution = 1 cm^3, T_{acq}=8min). Note the baseline has not been removed from the spectra that are shown.

2.3.5 Accelerated MRSI

The principles of fast MRI are often equally applicable to MRSI, which was discussed in section 2.2.6. MRSI methods based on EPI and Spiral sequences with their k-space trajectories are shown in Figure 2.16. The main difference with conventional MRSI sequences is that the fast MRSI sequences, just as the MRI methods, employ magnetic field gradients during signal acquisition. The main difference with a conventional EPI method (Figure 2.8) is that the phase-encoding blips in between the oscillating readout gradient lobes are missing. Therefore, rather than being encoded with information about the second spatial dimension, the echoes are encoded with chemical shift information. As time progresses, phase evolution due to chemical shifts increases. This can be expressed by a spectroscopic frequency k-space parameter $k_\omega = \omega t$.

Parallel MRSI is identical to parallel MRI in all but two important ways. Firstly, parallel MRSI has an additional spectral dimension. Secondly, MRSI acquisitions are inherently low to medium resolution experiments and as a consequence the PSF is only remotely resembling a Dirac function. As a result, a pixel in the aliased dataset is not only a sum of the corresponding unaliased signals, but through the PSF also contains contributions from many other spatial positions. Therefore the reconstruction of undersampled MRSI data become more complicated and complex.

Compressed Sensing MRSI is identical to compressed sensing MRI if 3D MRSI is undersampled in k_x and k_y. However, due to low resolution of spectroscopy that does not provide enough sparsity to exploit. A better strategy would be to attempt undersampling in the k_f and k_x dimensions and apply the sparsity in the spectral dimension.

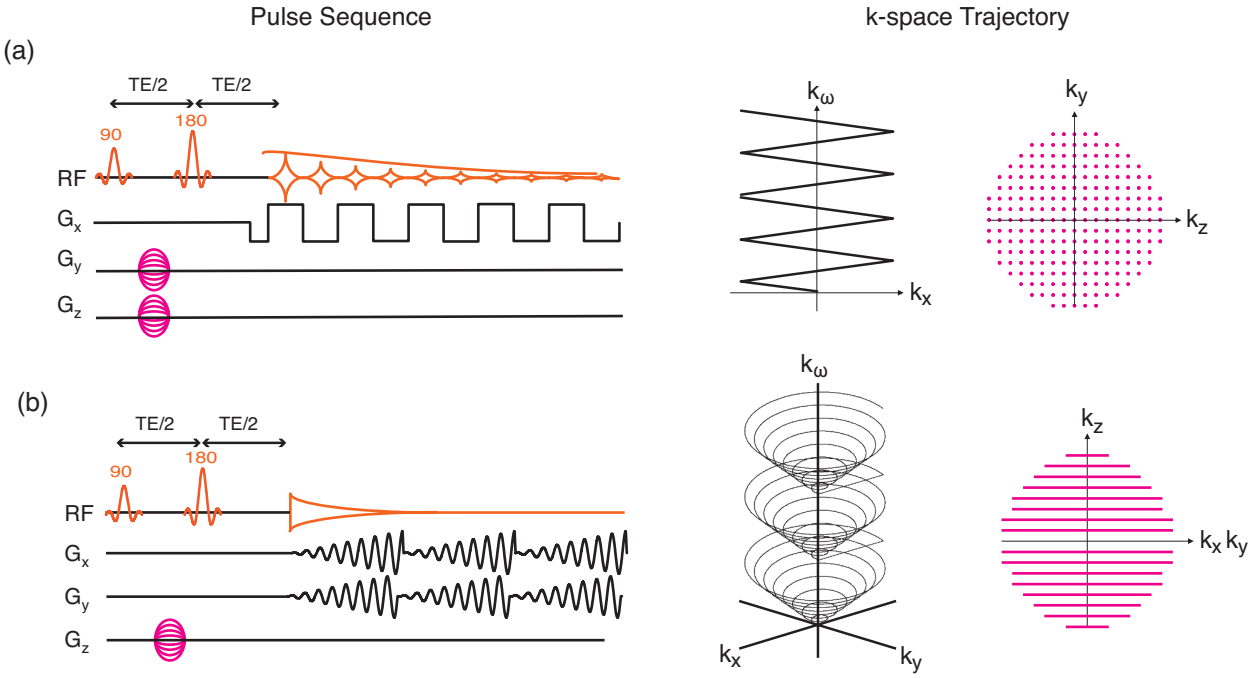

Figure 2.16: Pulse sequences for fast MRSI and their k-space sampling trajectories.

2.3.6 DNP Hyperpolarization

A fundamental reason for the low sensitivity of the NMR originates from low polarization of the nuclear spins at thermal equilibrium. One of the most straightforward and expensive methods to increase the spin polarization and consequently the sensitivity is to increase the external magnetic field. However, even at hight magnetic fields only about one out of 10^5 nuclear spins contributes to detectable signal. In proton MRSI, the low sensitivity of the proton is compensated by its high concentration in biological tissues, however, in 13C MRSI, the MR sensitivity of 13C is severely challenged by its low abundance in vivo and its low gyromagnetic ratio.

Another method to enhance the polarization is to fabricate an artificial nonequilibrium distribution of the nuclei in an external "polarizer system" . This method refers to as "hyperpolarization" and can provide a $\geq 50,000$ fold polarization enhancement. Dynamic Nuclear Polarization (DNP) is one way to achieve hyperpolarization by transferring spin polarization from electrons to nuclei in a strong magnetic filed at very low temperature ($1°K$) through microwaves irradiation. Using DNP, metabolic substrates can be hyperpolarized in solid state and then dissolved to liquid state for in vivo injection to monitor uptake and enzymatic conversion/activity in specific metabolic pathway.

An important characteristic of using hyperpolarized agent in MRI is that the majority of the

magnetization cannot be recovered once it decays to its thermal equilibrium level. Therefore, the maximum imaging window for the 13C-pyruvate substrate and its products is about 1-2 min because of T1 decay. Furthermore, every RF excitation also uses up some of the hyperpolarized magnetization which limits our measurement times even more. Consequently, hyperpolarized MR acquisition necessitates very efficient and rapid k-space sampling.

2.4 References

1. A. C. Society, "Cancer Facts & Figures 2015. Atlanta: American Cancer Society," 2015.

2. Q. T. Ostrom, H. Gittleman, P. Farah, A. Ondracek, Y. Chen, Y. Wolinsky, N. E. Stroup, C. Kruchko, and J. S. Barnholtz-Sloan, "CBTRUS Statistical Report: Primary Brain and Central Nervous System Tumors Diagnosed in the United States in 2006-2010," *Neuro Oncology*, vol. 15, pp. ii1–ii56, Oct. 2013.

3. D. Vigneron, A. Bollen, M. McDermott, and L. Wald, "Three-dimensional magnetic resonance spectroscopic imaging of histologically confirmed brain tumors," *Magnetic Resonance Imaging*, 2001.

4. S. J. Nelson, T. R. McKnight, and R. G. Henry, *Characterization of untreated gliomas by magnetic resonance spectroscopic imaging.* Neuroimaging clinics of North America, 2002.

5. S. J. Nelson, "Multivoxel magnetic resonance spectroscopy of brain tumors.," *Molecular cancer therapeutics*, vol. 2, pp. 497–507, May 2003.

6. A. Pirzkall, X. Li, J. Oh, S. Chang, M. S. Berger, D. A. Larson, L. J. Verhey, W. P. Dillon, and S. J. Nelson, "3D MRSI for resected high-grade gliomas before RT: tumor extent according to metabolic activity in relation to MRI," *International Journal of Radiation Oncology*Biology*Physics*, vol. 59, pp. 126–137, May 2004.

7. X. Li, Y. Lu, A. Pirzkall, T. McKnight, and S. J. Nelson, "Analysis of the spatial characteristics of metabolic abnormalities in newly diagnosed glioma patients," *Journal of Magnetic Resonance Imaging*, vol. 16, pp. 229–237, Aug. 2002.

8. T. R. McKnight and M. H. von dem Bussche, "Histopathological validation of a three-dimensional magnetic resonance spectroscopy index as a predictor of tumor presence," *Journal of Neurosurgery*, 2002.

9. B. Wei, I. S. Khayal, J. M. Lupo, C. McGue, S. Vandenberg, K. R. Lamborn, S. M. Chang, S. Cha, and S. J. Nelson, "Multiparametric Characterization of Grade 2 Glioma Subtypes Using Magnetic Resonance Spectroscopic, Perfusion, and Diffusion Imaging," *Translational Oncology*, vol. 2, pp. 271–280, Dec. 2009.

10. E. Ozturk-Isik, A. Pirzkall, K. R. Lamborn, S. Cha, S. M. Chang, and S. J. Nelson, "Spatial Characteristics of Newly Diagnosed Grade 3 Glioma Assessed by Magnetic Resonance Metabolic and Diffusion Tensor Imaging," *Translational Oncology*, vol. 5, pp. 10–18, Feb. 2012.

11. X. Li, H. Jin, Y. Lu, J. Oh, S. Chang, and S. J. Nelson, "Identification of MRI and1H MRSI parameters that may predict survival for patients with malignant gliomas," *NMR in Biomedicine*, vol. 17, pp. 10–20, Mar. 2004.

12. J. Oh, R. G. Henry, A. Pirzkall, Y. Lu, X. Li, I. Catalaa, S. Chang, W. P. Dillon, and S. J. Nelson, "Survival analysis in patients with glioblastoma multiforme: Predictive value of choline-to-n-acetylaspartate index, apparent diffusion coefficient, and relative cerebral blood volume," *Journal of Magnetic Resonance Imaging*, vol. 19, no. 5, pp. 546–554, 2004.

13. T. R. McKnight, S. M. Noworolski, D. B. Vigneron, and S. J. Nelson, "An automated technique for the quantitative assessment of 3D-MRSI data from patients with glioma.," *Journal of Magnetic Resonance Imaging*, vol. 13, pp. 167–177, Dec. 2000.

14. M. Muruganandham, P. P. Clerkin, B. J. Smith, C. M. Anderson, A. Morris, A. A. Capizzano, V. Magnotta, S. M. McGuire, M. C. Smith, J. E. Bayouth, and J. M. Buatti, "3-Dimensional Magnetic Resonance Spectroscopic Imaging at 3 Tesla for Early Response Assessment of Glioblastoma Patients During External Beam Radiation Therapy," *Radiation Oncology Biology*, vol. 90, pp. 181–189, Sept. 2014.

15. S. J. Nelson, E. Graves, A. Pirzkall, X. Li, A. Antiniw Chan, D. B. Vigneron, and T. R. McKnight, "In vivo molecular imaging for planning radiation therapy of gliomas: An application of 1H MRSI," *Journal of Magnetic Resonance Imaging*, vol. 16, pp. 464–476, Sept. 2002.

16. N. A. Parra, A. A. Maudsley, R. K. Gupta, F. Ishkanian, K. Huang, G. R. Walker, K. Padgett, B. Roy, J. Panoff, A. Markoe, and R. Stoyanova, "Volumetric Spectroscopic Imaging of Glioblastoma Multiforme Radiation Treatment Volumes," *Radiation Oncology Biology*, vol. 90, pp. 376–384, Oct. 2014.

17. A. Deviers, S. Ken, T. Filleron, B. Rowland, A. Laruelo, I. Catalaa, V. Lubrano, P. Celsis, I. Berry, G. Mogicato, E. C.-J. Moyal, and A. Laprie, "Evaluation of the Lactate-to-N-Acetyl-aspartate Ratio Defined With Magnetic Resonance Spectroscopic Imaging Before Radiation Therapy as a New Predictive Marker of the Site of Relapse in Patients With Glioblastoma Multiforme," *Radiation Oncology Biology*, vol. 90, pp. 385–393, Oct. 2014.

18. I. Park, G. Tamai, M. C. Lee, C. F. Chuang, S. M. Chang, M. S. Berger, S. J. Nelson, and A. Pirzkall, "Patterns of Recurrence Analysis in Newly Diagnosed Glioblastoma Multiforme After Three-Dimensional Conformal Radiation Therapy With Respect

to Pre–Radiation Therapy Magnetic Resonance Spectroscopic Findings," *International Journal of Radiation Oncology*Biology*Physics*, vol. 69, pp. 381–389, Oct. 2007.

19. A. Laprie, I. Catalaa, E. Cassol, T. R. McKnight, D. Berchery, D. Marre, J.-M. Bachaud, I. Berry, and E. C.-J. Moyal, "Proton Magnetic Resonance Spectroscopic Imaging in Newly Diagnosed Glioblastoma: Predictive Value for the Site of Postradiotherapy Relapse in a Prospective Longitudinal Study," *International Journal of Radiation Oncology*Biology*Physics*, vol. 70, pp. 773–781, Mar. 2008.

20. S. J. Nelson, S. Huhn, and D. B. Vigneron, "Volume MRI and MRSI techniques for the quantitation of treatment response in brain tumors: presentation of a detailed case study," *Journal of Magnetic Resonance Imaging*, 1997.

21. S. J. Nelson, D. B. Vigneron, and W. P. Dillon, "Serial evaluation of patients with brain tumors using volume MRI and 3D 1H MRSI," *NMR in Biomedicine*, 1999.

22. L. L. Wald, S. J. Nelson, M. R. DAY, and S. E. Noworolski, "Serial proton magnetic resonance spectroscopy imaging of glioblastoma multiforme after brachytherapy," *Journal of Neurosurgery*, 1997.

23. S. J. Nelson, "Assessment of therapeutic response and treatment planning for brain tumors using metabolic and physiological MRI," *NMR in Biomedicine*, Apr. 2011.

24. T. R. Brown and B. M. Kincaid, "NMR chemical shift imaging in three dimensions," in *Proceedings of the National Academy of Sciences of the United States of America*, pp. 3523–3526, 1982.

25. A. A. Maudsley, S. K. Hilal, and W. H. Perman, *Spatially resolved high resolution spectroscopy by "four-dimensional" NMR*, vol. 51. Journal of Magnetic Resonance (1969), 1983.

26. D. L. Pavla, G. M. Lampman, G. S. Kriz, and J. A. Vyvyan, *Introduction to Spectroscopy*. Cengage Learning, 5th ed., Aug. 2015.

27. A. Haase, J. Frahm, and W. Hänicke, "1H NMR chemical shift selective (CHESS) imaging," *Physics in Medicine and Biology*, 1985.

28. C. Moonen and P. Van Zijl, "Highly effective water suppression for in vivo proton NMR spectroscopy (DRYSTEAM)," *Journal of Magnetic Resonance (1969)*, 1990.

29. F. W. Crawford, I. S. Khayal, C. McGue, S. Saraswathy, A. Pirzkall, S. Cha, K. R. Lamborn, S. M. Chang, M. S. Berger, and S. J. Nelson, "Relationship of pre-surgery metabolic and physiological MR imaging parameters to survival for patients with untreated GBM," *Journal of Neuro-Oncology*, vol. 91, pp. 337–351, Nov. 2008.

30. T. Tran, D. B. Vigneron, and N. Sailasuta, "Very selective suppression pulses for clinical MRSI studies of brain and prostate cancer," *Magnetic Resonance in Medicine*, pp. 1–11, Dec. 1999.

31. J. Frahm, K. D. Merboldt, and W. Hänicke, "Localized proton spectroscopy using stimulated echoes," *Journal of Magnetic Resonance (1969)*, 1987.

32. P. A. Bottomley, "Spatial localization in NMR spectroscopy in vivo," *Annals of the New York Academy of Sciences*, 1987.

33. S. Conolly, J. Pauly, and D. Nishimura, "Two-dimensional selective adiabatic pulses," *Magnetic Resonance in Medicine*, 1992.

34. D. Xu, A. P. Chen, C. Cunningham, J. A. Osorio, S. J. Nelson, and D. B. Vigneron, "Spectroscopic imaging of the brain with phased-array coils at 3.0 T," *Magnetic Resonance Imaging*, vol. 24, pp. 69–74, Jan. 2006.

35. I. Park, A. P. Chen, M. L. Zierhut, E. Ozturk-Isik, D. B. Vigneron, and S. J. Nelson, "Implementation of 3 T Lactate-Edited 3D 1H MR Spectroscopic Imaging with Flyback Echo-Planar Readout for Gliomas Patients," *Annals of Biomedical Engineering*, vol. 39, pp. 193–204, July 2010.

36. Y. Li, J. M. Lupo, R. Parvataneni, K. R. Lamborn, S. Cha, S. M. Chang, and S. J. Nelson, "Survival analysis in patients with newly diagnosed glioblastoma using pre- and postradiotherapy MR spectroscopic imaging," *Neuro Oncology*, vol. 15, pp. 607–617, Apr. 2013.

37. L. Yaan, I. Park, and S. J. Nelson, "Imaging Tumor Metabolism Using In Vivo Magnetic Resonance Spectroscopy," *The Cancer Journal*, vol. 21, no. 2, pp. 123–128, 2015.

Chapter 3

Technical Development of Multi-Channel RF Receive Coil & Numerical Phantom Simulation

3.1 Rationale

An array of multiple decoupled surface coil elements were originally proposed in the late 1980s as a method to increase NMR sensitivity and coverage (i.e. SNR and FOV) by extending the high-sensitivity detection area of small surface coil elements to larger areas (1). It wasn't till mid-1990s when most commercial scanners became equipped with four or more separate receiver channels providing the essential hardware for parallel imaging development to also reduce total scan times and thus increase patient comfort and reduce sensitivity to motion, or increased volumetric coverage and/or higher spatial resolutions depending on the available SNR. In the past two decades, with the success of parallel imaging methods, a new criterion has been added to the RF engineering list of requirements beyond the usual sensitivity, coverage, and patient comfort issues and that is the ability to accelerate the image encoding. It is important to note, these new coils are often very different from those produced in the past that were designed solely to maximize SNR.

The use of spatial information of different coil elements for parallel imaging has a strong influence on array design and MRI system architecture. For example, typical arrays for non-parallel imaging consist of anterior and posterior groups of elements which are organized in head-feet direction. Most of these arrays have no independent elements in left-right direction. This is due mainly to the fact that arrays with independent elements in the left-right direction need a significant larger number of RF channels but do not provide a major SNR improvement in the center region of the image. As a rule of thumb, the optimal SNR is achieved in a single-loop element at approximately one diameter depth from the coil (1), so if

one is imaging the abdominal area, then loops of approximately 20 cm diameter will perform well. Coils of this size can also be placed around the abdomen, thus, coil design is relatively simple. However, these simple measures for small number of receivers have been turned upside down by parallel imaging requirements. In parallel imaging applications, maximizing the SNR in the image center is only one of several design criteria. In addition to that, the elements of the array have to be organized along the phase-encoding direction in order to generate sufficient information for accelerated imaging. For a maximum degree of freedom, arrays for parallel imaging need to have elements in all three spatial directions, including left-right. This requirement leads to a significant larger number of array elements and RF channels for parallel imaging than for non-parallel imaging.

Both the quest for higher sensitivity and improved encoding acceleration drive the logic of expanding the array approach which is increasing the number of elements and reducing the size of the each receive coils to cover a fixed anatomical territory. Although exploring array larger than 32 channels risks hitting the upper limits identified by the studies on sensitivity and spatial encoding capabilities of coil arrays. Initially, the concept of the "ultimate" SNR that is achievable by an RF coil was introduced by Ocali and Atalar in1998 (2). In this study, an arbitrary coil sensitivity profile was generated from a complete set of basis functions satisfying Maxwell's equations and the maximum SNR at a given location in the sample was found by a linear combination. This work was expanded to include the "ultimate" SNR of an accelerated imaging by Sodickson and Pruessmann groups (3, 4) respectively. In these studies, the ultimate SNR was found by analyzing the performance of the complete basis set. The basis set itself was chosen to be either plane waves (2, 4) or spherical harmonics (3).

The first interesting conclusion of these analysis is that the sensitivity of MR detection is intrinsically limited. The significance of this finding for future array designs depends on how close current array designs are to this theoretical upper bound. Simulations of spherical coil distributions show that the ultimate possible SNR in the center of the head phantom is already closely approached at 3T when as few as 12 array elements are used (5). However, larger numbers of elements are required to approach the ultimate SNR in the periphery regions and there is substantial room for improvement. At a radial location equal to 80% of the coil radius, there is still a factor of 7 to go before the theoretical limit is achieved (5). Such important limitation must be extensively experimentally explored.

Furthermore, A comparison of a 96-channel and 32-channel helmet arrays showed that the central SNR was nearly identical and peripheral SNR increased in the higher channel coils (6). It is important to note that highly accelerated imaging techniques benefit from both the peripheral SNR gain and a reduced g-factor (discussed later), thus improving sensitivity in the center for accelerated acquisitions is essential.

Other technical difficulties associated with implementation of a larger number of smaller

coils are but not limited to the difficulty of inter-element decoupling, maintaining the high quality factor (Q) of the coil that measures sample noise-dominance, difficulty of placing higher counts of capacitors, difficulty to enclose very high-density coil arrays in compact housing, and the consideration of the housing design due to the different sample sizes and the necessity of maintaining close proximity to the body for small loops. Another obstacle is the reconstruction time versus number of channels specially for highly accelerated imaging data. High reduction factors result in a large numerical problem for the image reconstruction. For example, comparing a 3D volume with reduction factors of 3×3 acquired using 32-channel array to a 3D volume with reduction factor of 2 acquired using 8-channel array, the reconstruction time becomes many times slower. Efficient reconstruction will require improvements in computing, such as 64-bit architectures and massive parallel processing.

Coil design for parallel imaging is a very active area of research and development both in industry and academia. As stated above, while the technical issues of building arrays with large number of receive elements are challenging, both the theoretical simulations and the experimental prototypes suggest a huge potential for substantial benefits, especially for accelerated image encoding. In another word, large number of channels can have significant benefits in providing the overdetermination of the matrix inversion at the heart of parallel imaging (overdetermination means that the speed-up factor is smaller than the number of available coils, which improves the condition of the inverse problem, making the reconstruction more stable and less prone to g-factor noise), allowing higher speed up factors and making the coils more flexible in terms of imaging plane and field of view. Although these type of potentials are somewhat in their infancy, they will likely have their first and largest implications for "encoding-limited" imaging such as high-resolution 3D imaging, spectroscopic imaging and dynamic functional imaging.

Previous experimental studies with different number of array elements have supported the general findings of the simulation studies of coil elements, eventhough, the simulations make simplifying assumptions about body-noise dominance and element decoupling that are difficult to realize in practice. Therefore, the ability to optimize the geometry and number of elements for specific regions of interest with simulation prior to coil construction will be critical for optimizing reconstruction techniques specially for spectroscopic imaging.

This chapter describes the physical principles and develops a method to model the theoretical reception profile of an array of surface coils. These models are used in conjunction with information about the regions of interest to design and select coils for particular purpose. Additionally once the MR data are acquired with such coils, it can develop a correction algorithm that uses the theoretical reception profiles to remove the effect of the inhomogeneous reception profiles upon the acquired MR intensities.

This model is especially valuable for hyperpolarized C13 spectroscopic imaging, where external sensitivity references can be impractical. The majority of the initial pre-clinical experi-

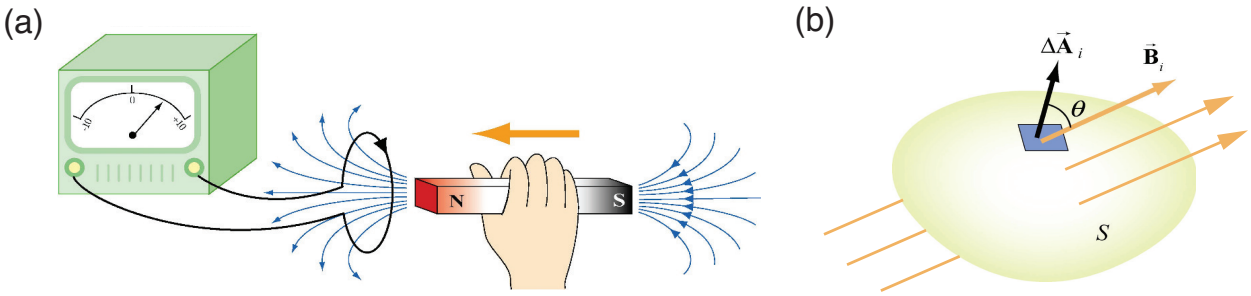

Figure 3.1: (a) Electromagnetic Induction. (b) Magnetic flux through a surface.

ments and the human prostate C13 studies used single channel RF coils. Having a model of the theoretical reception profile of the array coil are very beneficial for translation to larger animal model systems and to other human organs that requires increased coverage (field of view) and the relatively high sensitivity of multi-channel coils.

3.2 Physics Background

Faraday's law of Induction states that the changing magnetic flux ($\Phi_{\mathbf{B}}$) through a conducting loop induces an electromotive force (emf, $\mathcal{E}$) which causes an induced current. (Figure 3.1)

$$\mathcal{E} = -\frac{d\Phi_{\mathbf{B}}}{dt} = -\frac{d}{dt}\int_{area} \vec{\mathbf{B}} \cdot d\vec{\mathbf{A}} \tag{3.1}$$

where $\vec{\mathbf{B}}$ is the magnetic field vector and $\vec{\mathbf{A}}$ is the area vector ($\vec{\mathbf{A}} = A\hat{\mathbf{n}}$) where A is area of a surface and $\hat{\mathbf{n}}$ is its unit normal. According to Lenz's law the induced emf tends to oppose the change in the magnetic field, hence the minus sign the Equation 3.1

Maxwell's equations demonstrate the symmetry between electrical and magnetic fields:

$$\oint \vec{\mathbf{B}} \cdot d\vec{\ell} = \mu_0\epsilon_0 \frac{d\Phi_{\mathbf{E}}}{dt} = \mu_0\epsilon_0 \frac{d}{dt}\oint \vec{\mathbf{E}} \cdot d\vec{\mathbf{A}} \tag{3.2}$$

$$\oint \vec{\mathbf{E}} \cdot d\vec{\ell} = -\frac{d\Phi_{\mathbf{B}}}{dt} = -\frac{d}{dt}\oint \vec{\mathbf{B}} \cdot d\vec{\mathbf{A}} \tag{3.3}$$

The two physical constants in Maxwell's equations are μ_0 and ϵ_0 which are permittivity of free space related to the magnetic and electric susceptibilities of the material respectively. $\vec{\mathbf{E}}$ and $\vec{\mathbf{B}}$ are the electric and magentic field vectors respectively. $d\vec{\ell}$ is an infinitesimal vector element of the closed contour of a surface and $d\vec{\mathbf{A}}$ is an infinitesimal vector element of area of the surface. Both $d\vec{\ell}$ and $d\vec{\mathbf{A}}$ have a sign ambiguity and to get a correct sign the right-hand rule is used. Equation 3.2 states that the line integral of a magnetic field around an arbitrary

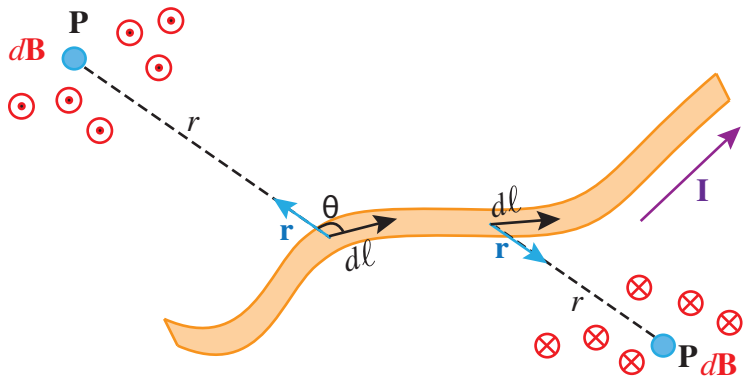

Figure 3.2: The magnetic field $d\mathbf{B}$ at point P due to current I through a length element $d\ell$ is given by the Biot-Savart Law. The direction of the field is in or out of the page depending on where point P is located based on the right-hand rule.

closed loop is equal to the flux of the charge carries through the surface bound by closed path $\boldsymbol{\ell}$, and Equation 3.3 illustrates the electric field that is associated with the changing magnetic field.

As described earlier, with NMR, nuclei precess about the magnetic field with a frequency given by $\boldsymbol{\omega} = \gamma\mathbf{B}$. since the magnetic moments of each nucleus precess, there is a net effect of a changing magnetic field in the tissue. Thus, the receiver coil is exposed to a changing magnetic field, which, as shown in Equation 3.3, induces an electric field in the coil. This induced electrical field is the NMR signal. The amount of current produced by this induced electrical field is dependent upon how far away the tissue magnetic moments are from the detector coil. As there is symmetry between the electrical and magnetic induced fields, the reception sensitivity profile can be more easily determined by calculating the magnetic field induced by a changing electrical field in the NMR detector coil. Biot-Savart law is an equation describing the magnetic field generated by an electric current. It relates the magnetic filed to the magnitude, direction, length and proximity of the electric current:

$$d\vec{\mathbf{B}} = \frac{\mu_0}{4\pi} \frac{I\, d\vec{\boldsymbol{\ell}} \times \hat{\mathbf{r}}}{r^2} \tag{3.4}$$

where small segment of the wire with length $d\ell$ carrying a current I. The direction of $d\vec{\boldsymbol{\ell}}$ is the direction of the current. $\hat{\mathbf{r}}$ is a unit vector pointing from the segment of wire to point P. This small segment will produce a small magnetic field $d\mathbf{B}$ at a point P whose magnitude and direction are given by Equation 3.4.

This formula can be used to calculate the theoretical reception profile of an MR receiver coil by representing the coil as a series of wire segments $d\ell$ and combining the resultant induced

magnetic fields $d\mathbf{B}$. This is detailed in the following section. This magnetic field calculation does not take into account all of the realities associated with scanning real samples. Inhomogeneities in the sample and the coil will change the resultant $\mathbf{B}$ field. Eddy currents may be induced in the sample that will also change the field (7). However, this simplified approach can produce a good approximation to the reception profile, yielding high quality coil corrections without the need for specific sample information.

Three dimensional maps of the reception profiles of various MR surface coils can be made based upon the Biot-Savart law and modeling each coil as a series of straight wire segments. These maps can be used to remove the reception profile effect upon surface coil images. How well this correction scheme works will indicate how close this theoretical model is to the actual experimental reception profiles of these coils. Unfortunately, acquisition noise cannot be completely eliminated (or corrected!), so the assessment of the model's accuracy cannot be absolute.

3.3 Biot-Savart Simulation for Modeling the Reception Profile of an Surface Coil

An important observation from Biot-Savart equation in regards to MRI detection is that the MR receiver does not pick up any signal from the z-axis which is the direction of the main static magnetic field. To understand this, one should be reminded that a changing magnetic field induces the signal in the coil. However, there are only two cases when there are changing magnetic fields along the z-axis.

The first is during the RF-excitation, when the magnetization rotates from being oriented with the main magnetic field to an orientation at least partially in the x-y plane. As the receiver is turned off (open-circuited) during excitation, it does not pick up any of this signal. The second case is during T_1 relaxation, when the magnetization realigns with the main magnetic field. This process takes on the order of several seconds, which is much, much slower than the changes found along the x-and y-axis, which take place in tens of nanoseconds. Thus, the signal in z direction is much smaller (several hundred million times smaller) and since the receiver is tunned to MHz range, this small, low frequency change in magnetic field along z direction is not received. Therefore, the z-axis component of the magnetic fields induced by coils should not be included in an estimate of the reception profile of the coils.

Theoretical sensitivity profiles must be calculated with coils orientated as they would be in the bore of the magnet. To model the magnetic field detected by a surface coil, the coil must be represented as a polygon of straight wire segments. Then with quasi-static assumption, the magnitude of the magnetic field in the x and y planes due to each of these wire segments

need to be calculated based on the Biot-Savart law (Equation 3.4) and all contributions need to be summed to obtain the total $\mathbf{B_1}$ field representation at given location. The constant values were ignored since the final result was normalized.

$$\Delta\mathbf{B_x} = \frac{\Delta\vec{\boldsymbol{\ell}} \times \hat{\mathbf{r}}_\mathbf{x}}{r_x^2} \tag{3.5}$$

$$\Delta\mathbf{B_y} = \frac{\Delta\vec{\boldsymbol{\ell}} \times \hat{\mathbf{r}}_\mathbf{y}}{r_y^2} \tag{3.6}$$

$$|\mathbf{B_{xy}}| = \sqrt{\Big(\sum_{wires} \Delta\mathbf{B_x}\Big)^2 + \Big(\sum_{wires} \Delta\mathbf{B_y}\Big)^2} \tag{3.7}$$

According to the quasi-static, B_1 field can only be calculated reliably based on the Biot-Savart law if the wavelength of the nuclei at the Lamar frequency is large compared to the size of the object being imaged.

$$\lambda = \frac{c}{f} = \frac{3 \times 10^8 \frac{m}{s}}{128 \times 10^6 Hz} = 2.3m \quad [^1\text{H - 3T}] \tag{3.8}$$

$$\lambda = \frac{c}{f} = \frac{3 \times 10^8 \frac{m}{s}}{32 \times 10^6 Hz} = 9.4m \quad [^{13}\text{C - 3T}] \tag{3.9}$$

However, this is not quite correct. The speed of light is reduced by $\sqrt{\epsilon}$ in the body and ϵ is about 81 in the body at these frequencies. That makes c about 9 times slower, so λ is about 9 times lower in vivo. However, in the case of brain imaging for ^{1}H and ^{13}C nuclei at 3T the quasi-static assumptions still holds.

As mentioned earlier, in MRI only the transverse magnetization produces significant signals, therefore, the complex reception function were calculated:

$$\mathbf{S}(\mathbf{r}) = \mathbf{B_x}(\mathbf{r}) + j\mathbf{B_y}(\mathbf{r}) \tag{3.10}$$

The $\mathbf{B_1}$ field calculation was implemented in the Matlab programming environment (The MathWorks, Natick, MA, USA) as been described using an analytic integration of the Biot-Savart equation. This MATLAB program modeled coils with rectangular shape as a series of wire segments. However, the program can be easily modified to model any regular polygonal shape as a series of wire segments by given a list of the start and end three dimensional coordinates for each of the series of wire segments. Unusual coil geometries could also be modeled manually by obtaining the start and end coordinates of the series of wires in three dimensional planes. In these simulations, the coil planes are assumed to be parallel to $\mathbf{B_0}$ field (z-direction). The MATLAB program calculated the magnitude of the $\mathbf{B_x}$, $\mathbf{B_y}$, and $\mathbf{B_z}$ components of the induced magnetic field, however, $\mathbf{B_x}$ and $\mathbf{B_y}$ components were the only ones contributed to the reception profile as described by Equation 3.10 and illustrated in Figure 3.3. Given the orientation of each coil element, length and width of each loop, this MATLAB tool placed the coil in the 3D space and computed the complex sensitivity map of each coil on a specified voxel grid in the field of view (FOV).

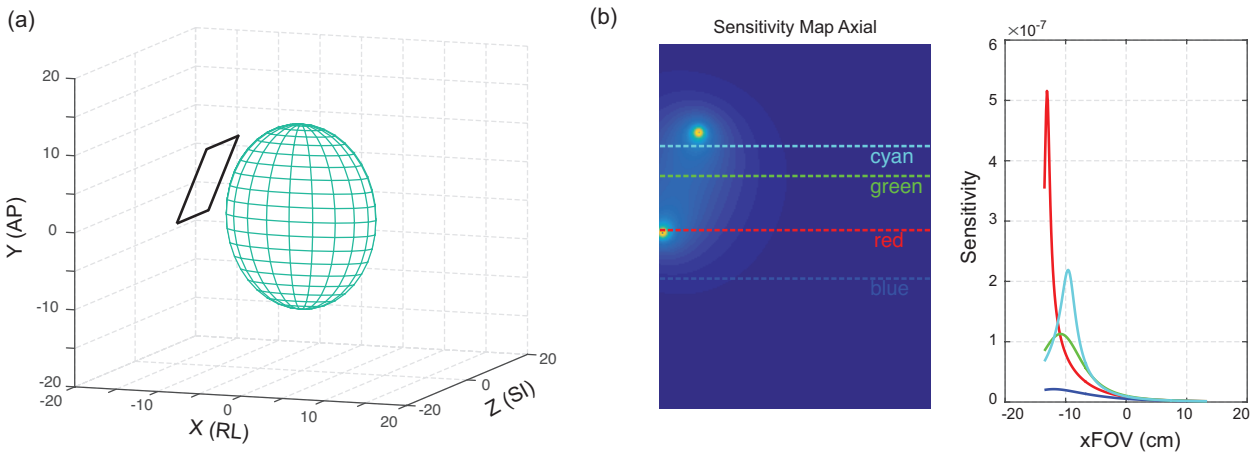

Figure 3.3: The simulated coil is a single 10.5 by 10.5 cm rectangular loop surface coil. For these initial simulations, an image FOV of 24cm by 18cm was considered to show approximately the depth of optimal in terms of SNR for these coils. (a) Simulated rectangular surface coil. (b) Simulated sensitivity map of the surface coil and cross-sections through it.

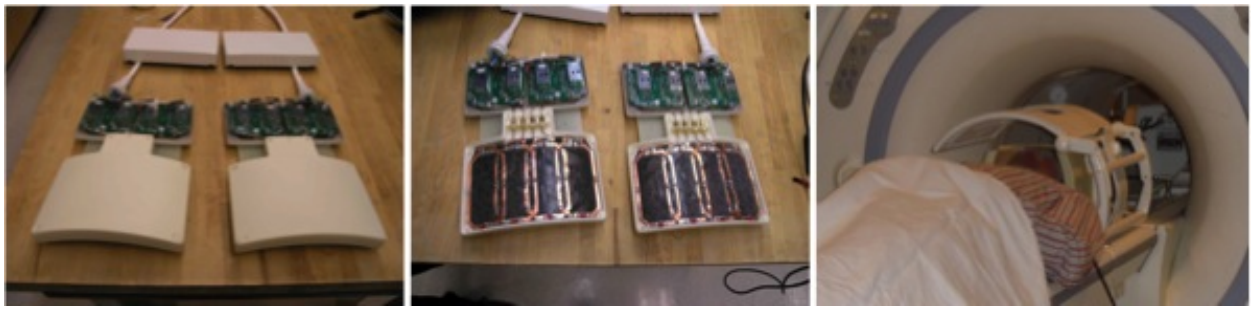

Figure 3.4: RF coils for human brain studies

3.4 Simulation and Verification of the Reception Profile for Head Coil Arrays

A ^{13}C bi-lateral 8-channel phased array receive coil was developed with a bore-insertable volumetric ^{13}C transmit coil with clamshell hinge for ease of patient loading (as shown in Figure 3.4) for the purpose of first-ever study of hyperbolized ^{13}C metabolic imaging in the clinical trials for patient with the brain cancer. These coils were designed and constructed by USA Instruments and Jim Tropp from GEs Applied Science Laboratory. In order to assess the performance of the designed coil for the application in hand and to compare its performance to other possible coil layouts or arrangements, we used our configurable head

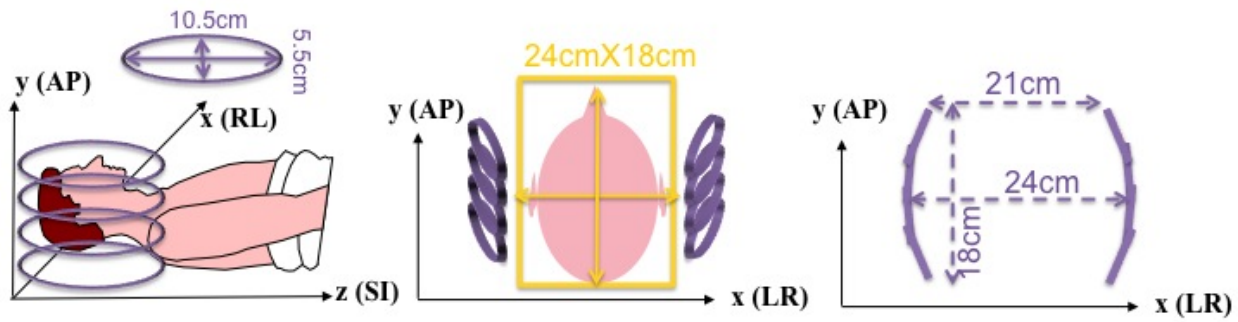

Figure 3.5: RF coils geometry and measurement for human brain studies

coil array toolbox in MATLAB to simulate variety of coil array shapes and sizes.

We modeled the 3D reception profile of this bi-lateral 8-channel phased array receive coil that can be placed on either side of the head. These sensitivity maps were theoretically calculated upon the Biot-Savart law and each coil was modeled as a series of straight wire segments. As illustrated in Figure 3.4 & 3.5, there are two paddles with curvature design, each paddle has 4 surface coils with major and minor axis of $10.5cm \times 5.5cm$ respectively. Adjacent surface coils are overlapped by $1.3cm$ to reduce mutual coupling between the elements and the length of one paddle is $18cm$ approximately as illustrated in Figure 3.5.

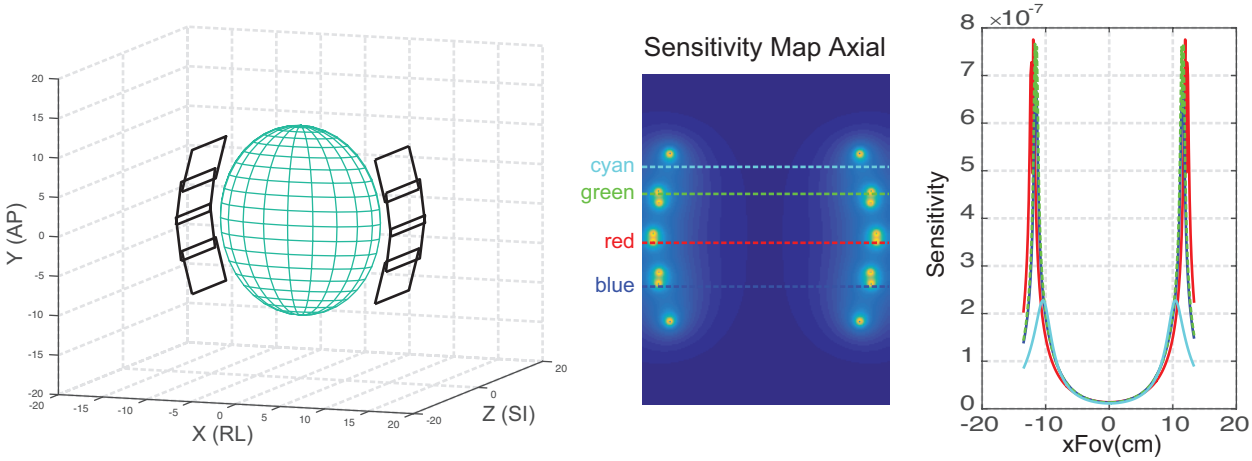

Figure 3.6: Biot-Savart simulation of the reception profile of the bi-lateral 8-channel phased array coil.

Figure 3.6 displays the geometry and the axial plane of the 3D reception profile of the bi-lateral 8-channel array-coil with 4 plotted cross-sections in right-left direction. The simulated FOV has the size of following dimensions: $36cm$ anterior-posterior (AP), $27cm$ right-left (RL), and $4cm$ superior-inferior (SI). The surface coils are placed (right-left) $12cm$ apart from the center of FOV with their appropriate angles. The highest field are about the coil

wires, and the central region bounded by the coil has generally higher field as well. While the reception profile appear to be highest closest to the paddle array, it drops as the distance from the coil increases (Figure 3.6). The maximum sensitivity near the coils (at $\approx 12cm$) was ≈ 36 times higher than the middle (at $\approx 0cm$). However, assuming the edge of a realistic phantom is placed at 8 or $9cm$, the sensitivity profile was ≈ 6 times higher than the middle (at $\approx 0cm$).

These maps can be used to remove the reception profile effect for more acurate coil combination. However, the key factor here is the incorporation of ^{13}C standards into the coil housing so that its spatial location can be defined on ^{1}H and ^{13}C images. This allows for signal calibration and for relating it to previously generated phantom or simulated profiles for use in parallel imaging reconstructions. In addition the need for coil sensitivity information is a major challenge in hyperpolarized ^{13}C imaging since external sensitivity references can be impractical due to low natural abundance of ^{13}C. Therefore, using numerical values for sensitivity is very beneficial. Furthermore any arbitrary multi-channel coil array can be designed and tested for advantages and dis-advantages for applications in hand before building the actual hardware.

How well this correction scheme works, or how liable the investigation of performance is depends on how close this theoretical model is to the actual experimental reception of these array coils. Unfortunately, acquisition noise can not be completely eliminated (or corrected) so the assessment of the model's accuracy can not be absolute but the question is can it be approximated well. To assess the accuracy of our model, a human head-shaped phantom containing ethylene glycol (HOCH2CH2OH, anhydrous, 99.8%, SigmaAldrich, St. Louis, Missouri, USA) was scanned using the clamshell transmitter with the paddle phased array coil configuration (Figure 3.7a). The phantom had the size of a human head with the following dimensions: $5cm \times 18cm \times 22cm$, in RL×AP×SI direction respectively. The distance between the centers of the two receive paddles was $17cm$. ^{13}C spectral data were acquired from a slice with a thickness of 1cm using a ^{13}C two-dimensional (2D) MR spectroscopic imaging sequence (TE/TR $3/3000ms$, $5kHz$ sweep width, 2048 spectral points). A 20×20 matrix size with the field of view of $20cm$ produced voxel sizes of 1cc. The geometry of the coil setup was also simulated. The spatially dependent sensitivity profiles of both results were normalized and displayed in Figure 3.7(a and b). A row and a column in the middle of the phantom and the simulation plane were plotted and overplayed against each other in Figure 3.7(e and f) illustrating the accuracy of the Biot-Savart simulation.

After verifying our model's accuracy, our MATLAB simulation toolbox was used to investigate how different size coils and arrangements would influence the sensitivity profile of the combined data since this particular coil design suffered from few shortcomings for the application in hand. To briefly reiterate, in designing coils for maximum SNR, the coil size is generally dictated by the size of the anatomical region of interest. As mentioned earlier, as a rule of thumb, the optimal SNR is achieved in a single loop element at approximately one

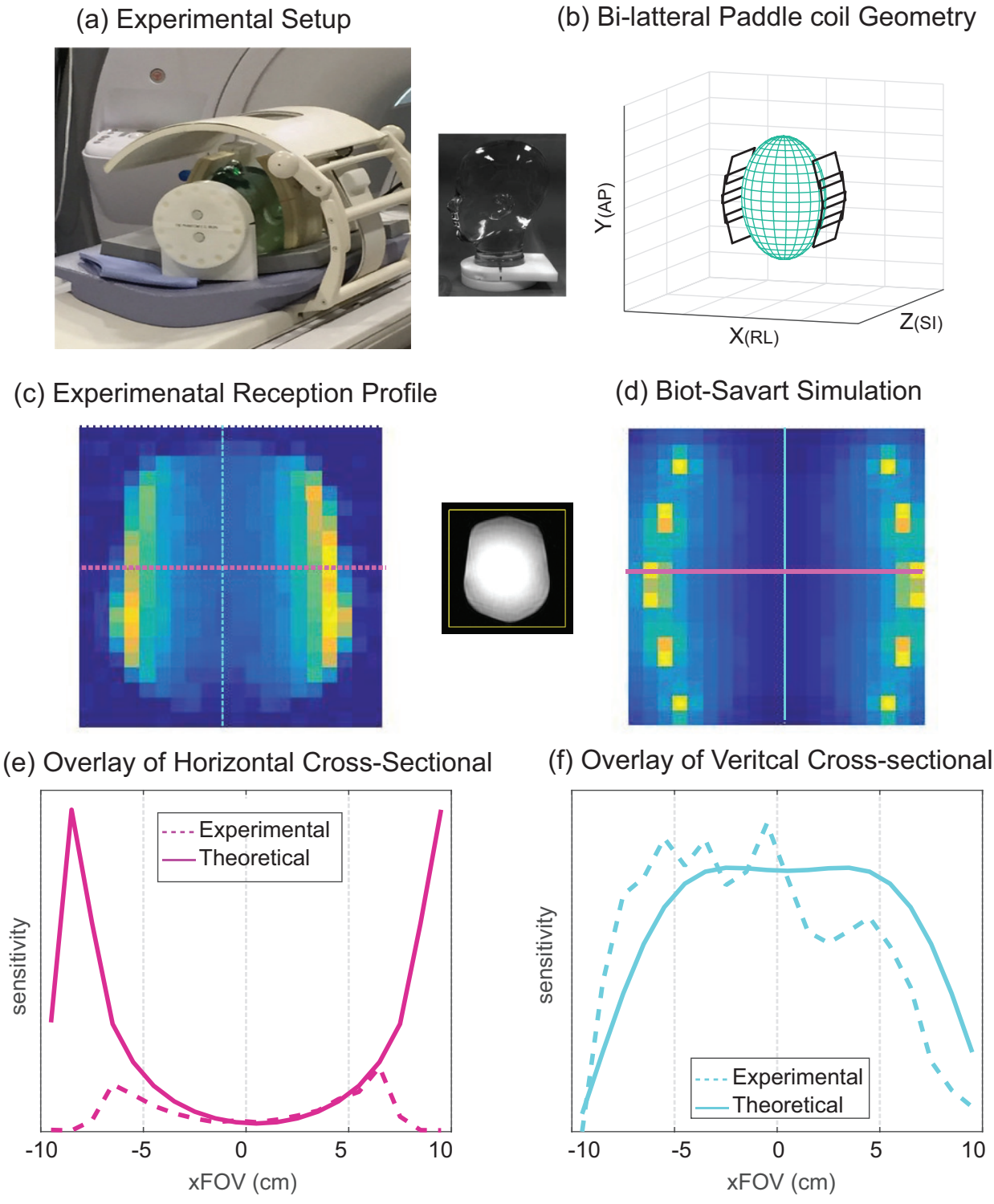

Figure 3.7: Comparison between experimental data and theoretical simulation

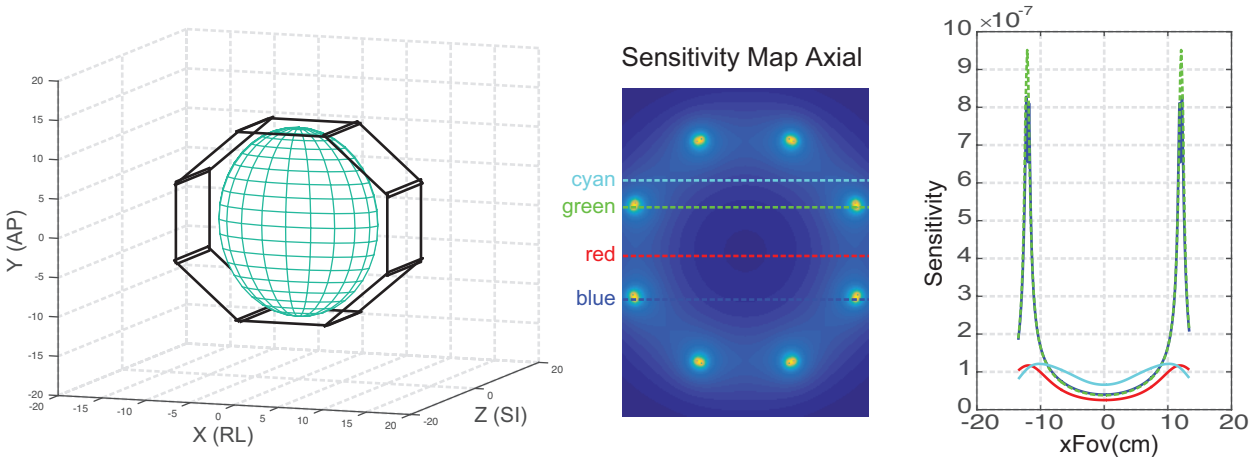

Figure 3.8: Biot-Savart simulation of the reception profile of the bi-lateral 8-channel phased array coil.

diameter depth from the coil. Thus in this particular design the optimal SNR is achieved at approximately $6cm$ depth from the coils which limits the size of the object. Furthermore, the current setup of this coil geometry forces the user to apply parallel imaging techniques only in AP direction, and possible (symmetric/flyback) EPSI related readout in RL direction for speedup factor which may not be optimal for applications in hands. Our region of interest and the optimal spatial coverage in our case is ($\approx 24cm \times 18cm \times 8cm$) respectively in ($AP \times RL \times SI$) direction. On the other hand, the performance of parallel imaging increases with the number of coil elements, particularly for 3/4/5D imaging where multiple dimensions are available for acceleration, at least up to the g-factor limits imposed by electro-dynamic constraints. Therefore, the approaches to coil design should differ depending on the reconstruction method being considered and the speed-up factor which depends on number of surface coils used and their geometries.

Figure 3.8 displays the axial plane of the 3D reception profile of the 8-channel volume array-coil with 4 cross-sections through the simulated coil profiles (right-left direction). The simulated FOV has the size with following dimensions: anterior-posterior (AP) $36cm$, right-left (RL) $27cm$, superior-inferior (SI) $4cm$. The surface coils are placed symmetrically around the head $12cm$ apart from the center of FOV with their appropriate angles. Each rectangular surface coil has major and minor axis of $10.5cm$ therefore the reception region is larger than the the bi-lateral 8-channel. The highest field are about the coil wires, and the central region bounded by the coil has generally higher field as well. While the reception profile appear to be highest closest to the coils, it drops as the distance from the coil increases (Figure 3.8). The maximum sensitivity near the coils (at $\approx 12cm$) was ≈ 5 times higher than the middle (at $\approx 0cm$). However, assuming the edge of a realistic phantom is placed at 8 or $9cm$, the sensitivity profile was ≈ 3 times higher than the middle (at $\approx 0cm$).

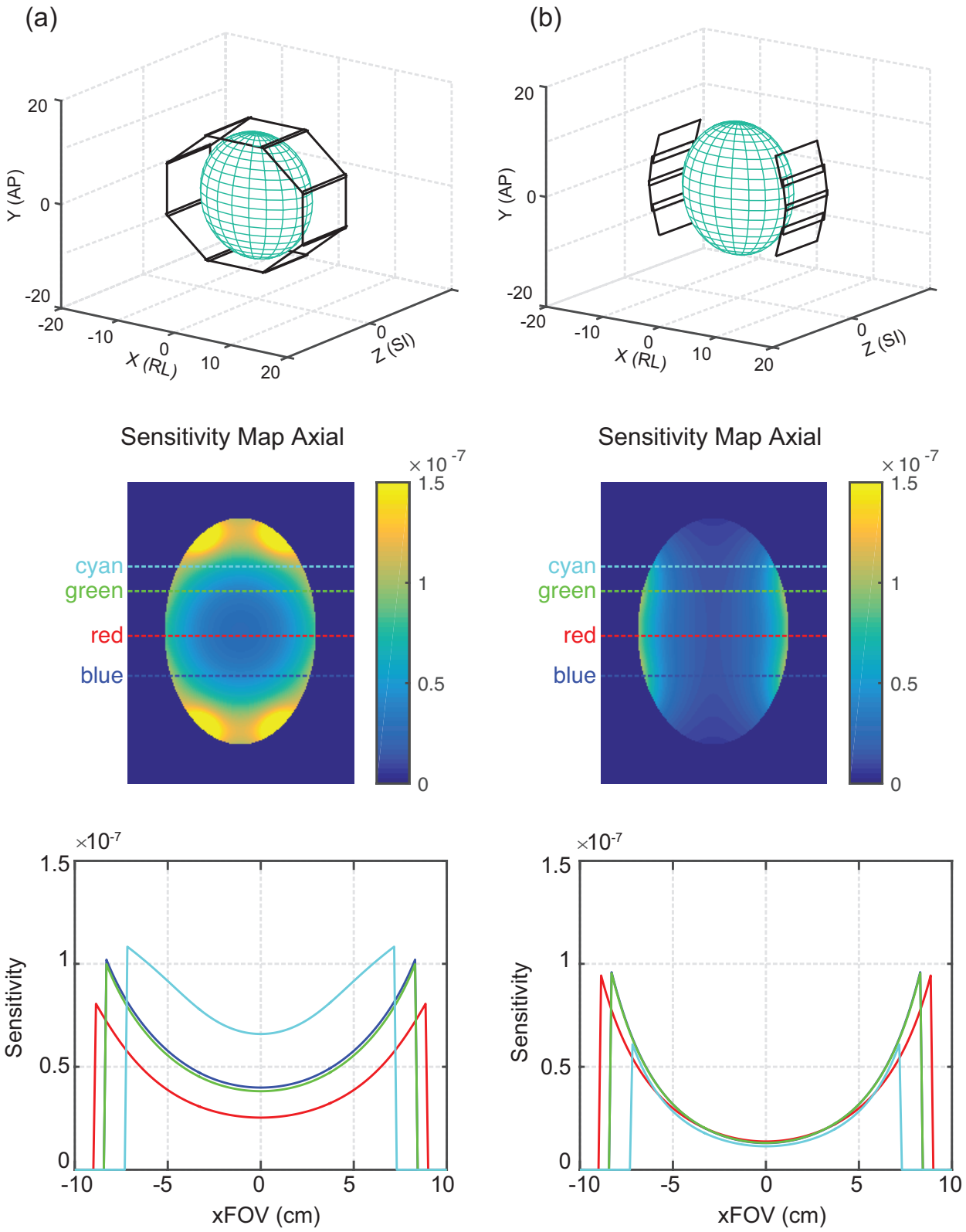

Figure 3.9: The comparison between the spatially dependent reception profiles of the two array coils

Figure 3.9 summarizes and compares these two coil setups side by side to high light the advantages and disadvantages of each design. The minor axis of the volume array coil is $10.5cm$ compare to $5.5cm$ for the paddle array coil. The cross-sections from the sensitivity maps clearly shows that larger coil elements arranged around the head in a circular fashion are likely to give better overall signal than the current paddles. In fact in comparison to the paddle array coil, the volume array coil setup produced 46% higher signal in the middle of the phantom (red cross-section at $0cm$). The volume array coil produced on average 83% higher signal in the middle of the phantom in the anterior and posterior region close to the receive coil surface (cyan and blue cross-section at $0cm$). Needless to say having coil elements in both right-left and anterior-posterior regions would allow the flexibility of acceleration in either one or two spatial directions which leads to higher acceleration factor. Although both volume array coil and paddle array coils displayed a distribution of signal across the phantom, the volume array coil rendered less signal drop across the phantom specially in anterior and posterior regions.

3.5 Two-Channel Circulary Polarized Microstrip Transmit and Receive Resonator for Traveling Wave Imaging

It is technically very challenging to build large-size RF coils to cover large FOV for human imaging at ultra-high magnetic field (such as 7T) due to high operation frequency (8, 9). Recently, traveling-wave technique has demonstrated its capability for large sample imaging using a relatively small patch antenna (compared to body coil) in a 7T scanner of which magnet bore is modeled as waveguide (10–13).

Typical means to excite and receive MR signals in traveling-wave MRI is a patch antenna. Antennas currently used for traveling wave MRI are typically complicated large patch antennas which are difficult to design and tune (11–13). We built and tested a simple new

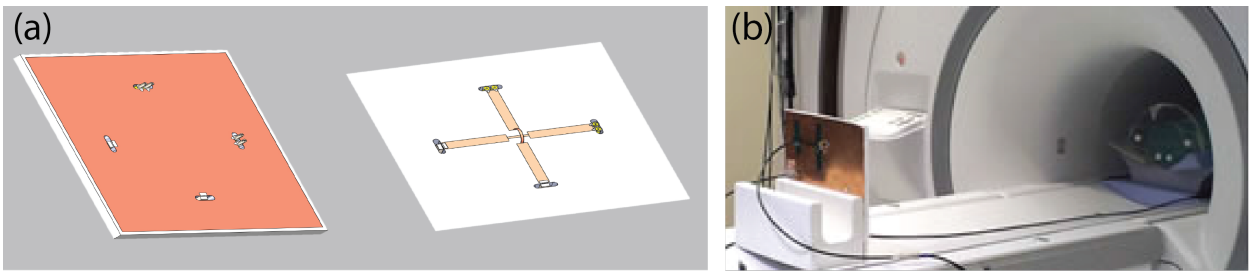

Figure 3.10: (a) A Front and back sides of the double-microstrip resonantor antenna on a teflon substrate. (b) Setup: $50cm$ antenna-phantom spacing in the scanner.

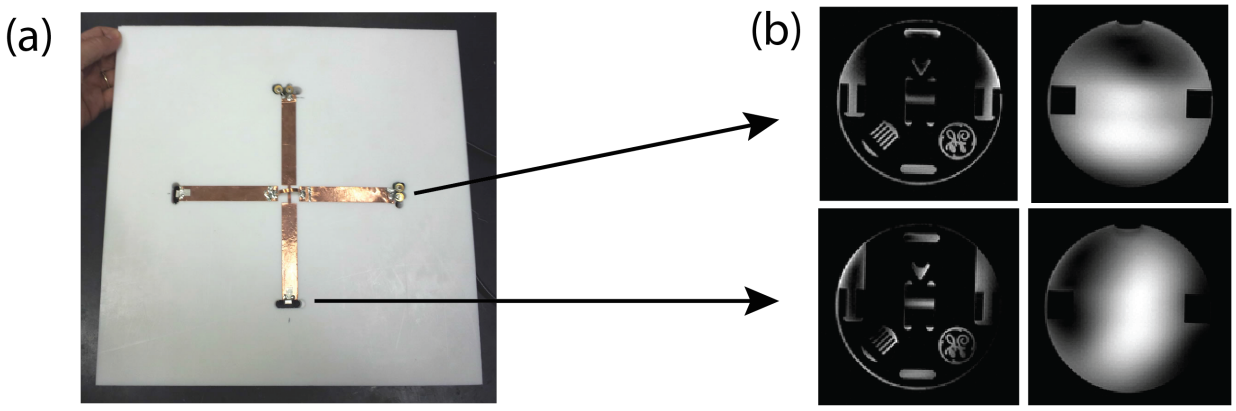

Figure 3.11: (a) A Front and back sides of the double-microstrip resonantor antenna on a teflon substrate. (b) 256 × 256 pixel images from 2D GRE sequence images (TR=250ms, TE=3.2 ms, 90° flip angle, 5mm thick slices, 31.25 kHz bandwidth, 3 averages). Top: slices from the microstrip oriented horizontally. Bottom: slices from the microstrip slices vertically.

design for a two-channel quadrature traveling wave antenna.

While a single-channel microstrip transmission line resonator is a very simple structure, a multi-channel design can run into complications due to coupling between channels. We found an elegant solution for a two-channel design: orient the strips orthogonally and use a 1cm copper loop to jumper one microstrip over the other at their centers. Figure 3.10(a) shows the final design implemented on a teflon plate with a copper-foil backside ground. Variable capacitors were mounted in holes at the ends of microstrips to facilitate tuning to 298 MHz and matching to 50 Ω, similar to that described in (9). During the tuning process, we verified that no mode-splitting was present, signaling good decoupling between the channels. The antenna was placed 50cm from a water phantom in a 7T scanner as shown in Figure 3.10(b) and images were acquired with a 2D GRE sequence as shown in Figure 3.11. I also studied the feasibility of using microstrip transmission line resonator array as signal excitation and reception for accelerated traveling wave in (14) which is outside the scope of this chapter.

3.6 Images and Spectra from Simulated Phantom that Represents a Brain Tumor

In order to develop an optimal strategy and flexible pipelines for robust reconstruction, coil combination and quantitative analysis of MRSI examinations, one needs to initially evaluate the influence of the key components of these procedures in both realistic simulation and empirical data from a phantom. Therefore, we have developed a MATLAB based simulation

tool for simulating configurable head-shape phantom representing a brain with different lesions and its corresponding metabolites for arbitrary resolution.

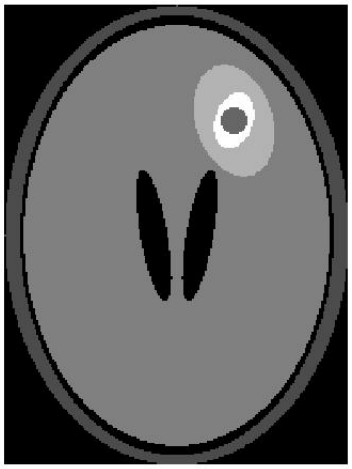

Figure 3.12: Simulated high resolution H-1 brain tumor phantom.

The signal measurement by MRSI is modified by the variation in excitation and reception profile of the RF coil even for a uniform phantom. In our simulation, it was assumed that the excitation was uniform but the reception was computed theoretically as described in section 3.4 and was represented by a 3D array of $S(\bar{r})$ with the same spatial resolution and dimension as the numerical phantom $P(\bar{r}, f)$. To model the complete picture, the pulse sequence acquisition was also represented by a 3D array of $V(\bar{r}) = v_x(r_x) \times v_y(r_y) \times v_z(r_z)$ which describes the selected volume, where $v_i(r_i)$ corresponds to the RF pulse profile in direction i for $i = x, y, z$. However, here the pulse profiles were simulated as ideal (rectangular with no chemical shift artifact). The measured MRSI signal corresponds to the element by element product of these three arrays:

$$P_{sv}(\bar{r}, f) = P(\bar{r}, f) \times S(\bar{r}) \times V(\bar{r}) \tag{3.11}$$

Modeling a realistic phantom can be achieved by simulating a sum of multiple simpler objects with different spatial distributions and spectral profiles in either domains because Fourier transforms are linear operations. Therefore, our numerical phantom $P(\bar{r}, f)$ was constructed as a sum of uniform objects $O_a(\bar{r})$ where a corresponds to the number of brain compartments and $\bar{r} = (r_x, r_y, r_z)$ represents 3D space, $r_i = 1, 2, \ldots, R_i$ for each dimension of $i = x, y, z$.

$$O_a(\bar{r}) \quad = \quad \begin{cases} C_a & \text{inside the object} \\ 0 & \text{outside the object} \end{cases} \tag{3.12}$$

Each object was assumed to have a free induction decay $d(t)$, where $t = 0, 1, 2, \ldots, N-1$ with spectrum given by the discrete time Fourier transform as:

$$D(f) = \frac{1}{\sqrt{N}} \sum_{t=0}^{N-1} d(t) \exp\Big(- \frac{2\pi j t f}{N}\Big) \tag{3.13}$$

The free induction decay of each object was represented as a sum of Lorentzian peaks:

$$d(t) = \sum_{m=1}^{M} I_m \exp\big(- L_m t\big) \exp\big(2\pi j f_m t\big) \tag{3.14}$$

with $m = 1, 2, \ldots, M$ where M corresponds to the number of metabolites with peak intensities of I_m, line-widths of L_m, and frequencies of f_m. Additionally baseline distortions can be represented by including a large peak such as residual water. Frequency and phase distortions can be simulated by applying shifts to the reconstructed data that were either constant or had a linear dependence on spatial location. Also complex Gaussian-distributed random noise can be added to provide peak SNRs ranging from 10:1 to 100:1.
To simplify the notation, first let's assume the numerical phantom was built with only one object. To simulate the k-space encoding for this object at frequency f, the matrix size of the object $O(\bar{r})$ was assumed to be significantly larger than the matrix size of the MRSI data. To take into account the coil reception profile S, and the phase encoding matrix V, the object $O_{sv}(\bar{r})$ was calculated as follows:

$$O_{sv}(\bar{r}) = O(\bar{r}) \times S(\bar{r}) \times V(\bar{r}) \tag{3.15}$$

The approximate k-space distribution ($O(\bar{k})$) of the object was then given by the 3D inverse discrete Fourier transform with respect to its spatial dimensions:

$$O_{sv}(\bar{k}) = \frac{1}{\sqrt{R_x R_y R_z}} \sum_{r_x=0}^{R_x-1} \sum_{r_y=0}^{R_y-1} \sum_{r_z=0}^{R_z-1} O_{sv}(\bar{r}) \exp\Big(- 2\pi j (\frac{r_x k_x}{R_x} + \frac{r_y k_y}{R_y} + \frac{r_z k_z}{R_z})\Big) \tag{3.16}$$

where $\bar{k} = (k_x, k_y, k_z)$ is k-space points. Then the simulated k-space array of spectra $O(\bar{k}, f)$ was constructed by the product of the k-space object $O_{sv}(\bar{k})$, and the spectrum for the object, $D(f)$.

$$O_{kspace}(\bar{k}, f) \;\; = \;\; O_{sv}(\bar{k}) \times D(f) \tag{3.17}$$

By performing an inverse Fourier transform of this product in the frequency dimension, the array of k-space FIDs that takes into account the spatial distribution of the object O, the coil reception profile S, and the phase encoding matrix V, was generated as follows:

$$O(\bar{k}, t) = \frac{1}{\sqrt{N}} \sum_{f=0}^{N-1} O(\bar{k}, f) \exp\Big(\frac{2\pi j t f}{N}\Big) \tag{3.18}$$

The numerical phantom $P_{sv}(\bar{r}, f)$ is computed from k-space object $O(\bar{k}, t)$ by applying a 1D time Fourier transform and a 3D spatial Fourier transform in appropriate dimensions. The objects used for our simulation were ellipses with dimensions similar to the brain of normal volunteers or patients. Our realistic H-1 MRSI phantom was simulated in MATLAB as a sum of elipses where each elipse was computed as described above with different spatial distributions and spectral profiles as summarized in Table 3.1.

Tissue	Shape and Size (cm)	NAA	Cho	Cr	Lip/Lac	H_2O
Normal Brain	elipse w/ radius (8×11)	1.5	0.9	1.0	0	10
CE Lesion	elipse w/ radius (1×1.5)	0	1.6	0	0	10
T_2 Lesion	elipse w/ radius (2×3)	0	2.4	1.0	0	10
Central Necrosis	elipse w/ radius (0.4× 0.7)	0	0	0	5	0
Ventricles	elipse w/ radius (0.7×3.5)	0	0	0	0	15
Subcutaneous fat	Annulus w/ thickness (1)	0	0	0	15	10

Table 3.1: H-1 MRSI Phantom Values

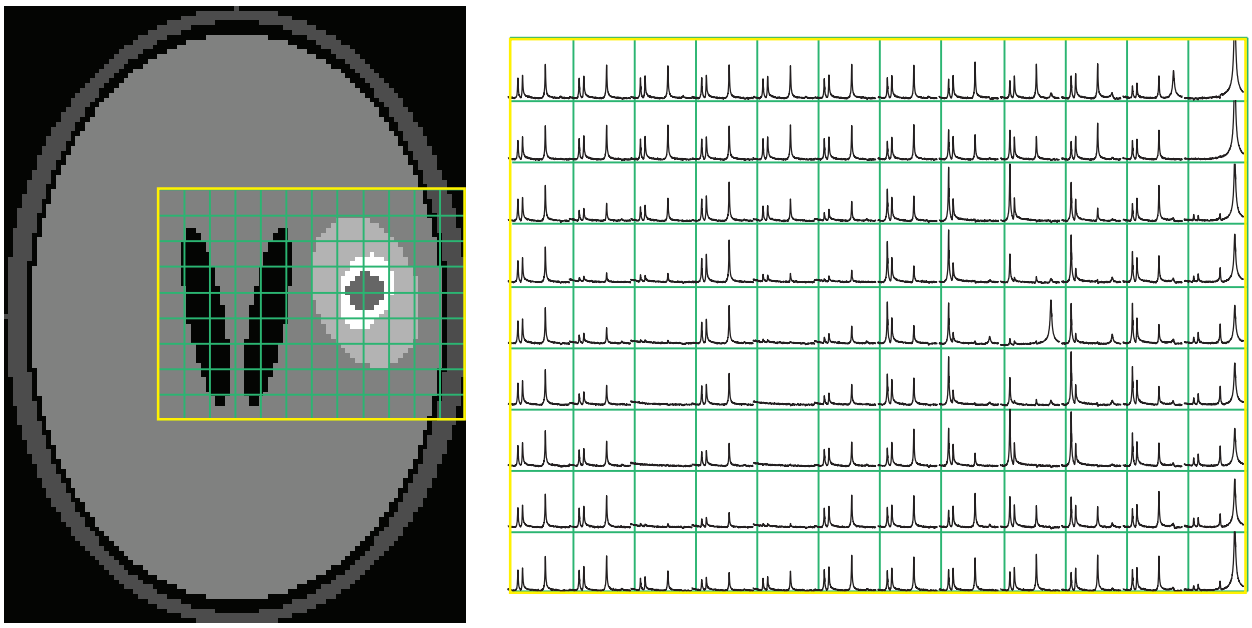

Figure 3.13: Simulated H-1 MRSI brain tumor phantom.

Furthermore, various size of ellipses represented subcutaneous fat, normal brain, ventricles, the contrast enhanced (CE) lesion, the T_2 lesion, and central necrosis. An example of an image including all these compartments is seen in Figure 3.14. High Resolution images were generated covering FOV of 24 cm (AP) by 18 cm (RL) with spatial resolution of 0.93 mm. Then for each pixel, a spectrum was generated by simulating a time domain FID resulting in several chemical species, located in 2.0 ppm (NAA), 3.2 ppm (cho), 3.0 ppm (cr), 1.3 ppm

(Lac/Lip), and 4.7 ppm (H_2O) covering 1 kHz bandwidth. Simulated images were reduced in resolution to a matrix size of 24×18 (spatial resolution of 1 cm) as illustrated in Figure 3.13.

This MATLAB tool was also used to create a C-13 numerical phantom with three different tissue types, Normal Tissue ($22cm \times 16cm$), Tumor Tissue ($4cm \times 4cm$) and the vasculature Tissue ($0.5cm \times 0.5cm$) and two different chemical species, one located on 173 ppm (Pryuvate) and one located in 185 ppm (Lactate) covering 581 Hz bandwidth.

Tissue	Shape and Size (cm)	Pyr	Lac
Normal Brain	elipse w/ radius (8×11)	4	0.5
Tumor	elipse w/ radius (2×2)	6	1.5
Vasculature	elipse w/ radius (0.25×0.25)	12	0.6

Table 3.2: C-13 MRSI Phantom Values

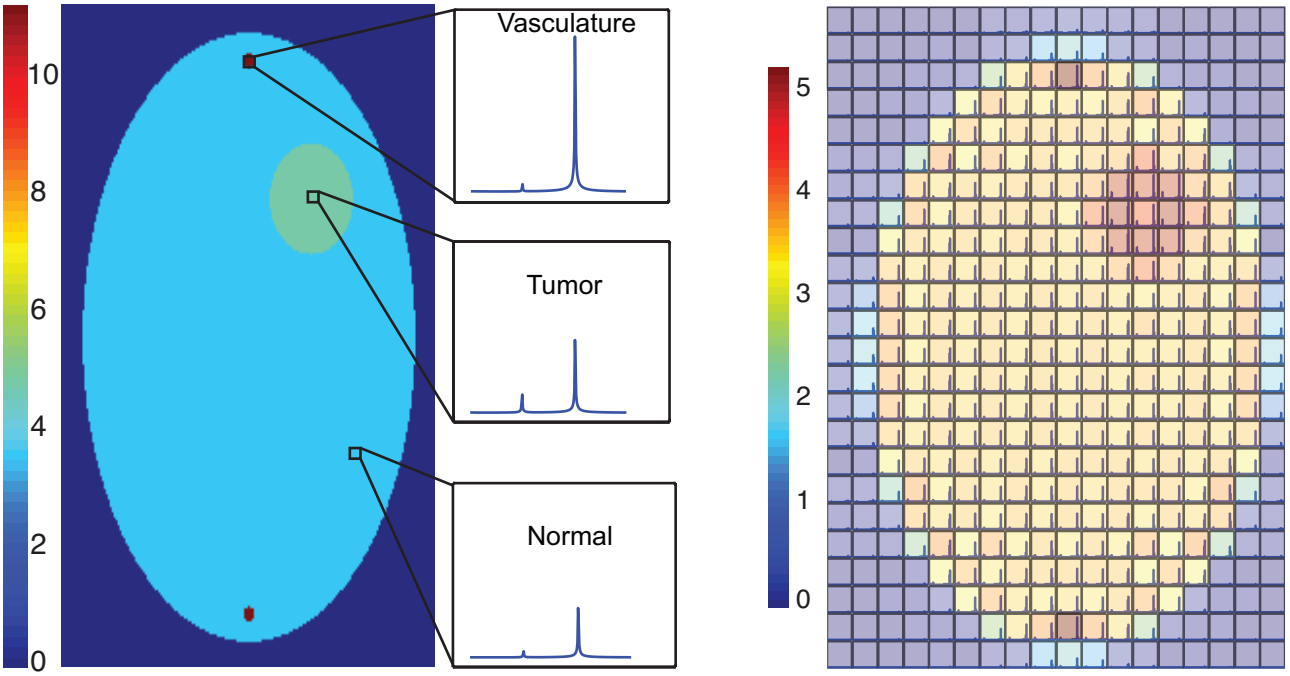

Figure 3.14: C-13 Numerical brain tumor phantom

3.7 Summary and Conclusion

This chapter discussed the requirements for the coil design for parallel imaging capability. It explained the original motivation that led to the introduction of array coils and how this concept was later extended to parallel imaging. Parallel imaging coil design is a very active area of research and development in both industry and academia. We developed a package for simulating the profiles of array coils with different sizes and shapes using the Biot-Savart Law. The accuracy of the simulation was verified empirically. The simulation tool has also been used to investigate how different size coils and arrangements would influence the sensitivity profile of the combined data and the reconstruction. The study showed that larger coil elements arranged around the head in a circular fashion are likely to give better overall signal with lower g-factor than paddle coils. The ability to optimize the geometry and number of elements for specific regions of interest prior to coil construction will be critical for studies being planned. The current version of the simulation tool was prototyped in MATLAB.

3.8 References

1. P. B. Roemer, W. A. Edelstein, C. E. Hayes, S. P. Souza, and O. M. Mueller, "The NMR phased array.," *Magnetic Resonance in Medicine*, vol. 16, pp. 192–225, Nov. 1990.

2. O. Ocali and E. Atalar, "Ultimate intrinsic signal-to-noise ratio in MRI," *Magnetic Resonance in Medicine*, vol. 39, pp. 462–473, Mar. 1998.

3. F. Wiesinger, P. Boesiger, and K. P. Pruessmann, "Electrodynamics and ultimate SNR in parallel MR imaging," *Magnetic Resonance in Medicine*, vol. 52, no. 2, pp. 376–390, 2004.

4. M. A. Ohliger, A. K. Grant, and D. K. Sodickson, "Ultimate intrinsic signal-to-noise ratio for parallel MRI: Electromagnetic field considerations," *Magnetic Resonance in Medicine*, vol. 50, pp. 1018–1030, Oct. 2003.

5. F. Wiesinger and N. De Zanche, "Approaching ultimate SNR with finite coil arrays," in *Proceedings of the 13rd Annual Meetin of ISMRM*, (Miami Beach), p. 672, 2005.

6. G. C. Wiggins, J. R. Polimeni, A. Potthast, M. Schmitt, V. Alagappan, and L. L. Wald, "96-Channel receive-only head coil for 3 Tesla: Design optimization and evaluation," *Magnetic Resonance in Medicine*, vol. 62, pp. 754–762, Sept. 2009.

7. S. M. Wright and L. L. Wald, "Theory and application of array coils in MR spectroscopy.," *NMR in Biomedicine*, vol. 10, pp. 394–410, Dec. 1997.

8. J. T. Vaughan, G. Adriany, C. J. Snyder, J. Tian, T. Thiel, L. Bolinger, H. Liu, L. DelaBarre, and K. Ugurbil, "Efficient high-frequency body coil for high-field MRI," *Magnetic Resonance in Medicine*, vol. 52, no. 4, pp. 851–859, 2004.

9. X. Zhang, K. Ugurbil, R. Sainati, and W. Chen, "An Inverted-Microstrip Resonator for Human Head Proton MR Imaging at 7 Tesla," *IEEE Transactions on Biomedical Engineering*, vol. 52, pp. 495–504, Mar. 2005.

10. D. O. Brunner, N. De Zanche, J. Fröhlich, J. Paška, and K. P. Pruessmann, "Travelling-wave nuclear magnetic resonance," *Nature*, vol. 457, pp. 994–998, Feb. 2009.

11. A. G. Webb, C. M. Collins, M. J. Versluis, H. E. Kan, and N. B. Smith, "MRI and localized proton spectroscopy in human leg muscle at 7 tesla using longitudinal traveling waves," *Magnetic Resonance in Medicine*, vol. 63, pp. 297–302, Feb. 2010.

12. Y. Pang, B. Yu, D. B. Vigneron, and X. Zhang, "Quadrature transmit array design using single-feed circularly polarized patch antenna for parallel transmission in MR imaging.," *Quantitative imaging in medicine and surgery*, vol. 4, pp. 11–18, Feb. 2014.

13. D. O. Brunner, J. Paška, J. Froehlich, and K. P. Pruessmann, "Traveling-wave RF shimming and parallel MRI," *Magnetic Resonance in Medicine*, vol. 66, pp. 290–300, Feb. 2011.

14. M. Vareth, A. Flynn, B. Wei, Y. Li, D. B. Vigneron, S. J. Nelson, and X. Zhang, "Accelerated Parallel Traveling Wave MR and Compressed Sensing Using a 2-Channel Transceiver Array," *Proceeding of the 21st Annual Scientific Meeting of the ISMRM*, pp. 1–1, Nov. 2013.

Chapter 4

Robust Coil Combination Technique for Clinical 2D/3D MRSI of 8- and 32-Channel Coils

4.1 Introduction

The power of in-vivo H-1 magnetic resonance spectroscopic imaging (MRSI) is to non-invasively obtain biologically relevant information for assessing underlying disease mechanisms and monitoring response to therapy. This is especially true for applications to patients with brain tumors, where parameters derived from 3D single-cycle and lactate-edited H-1 spectroscopic imaging have been shown to be relevant for defining target volumes for focal therapy (1–5) and predicting outcome (6–11). Constraints on scan time and signal-to-noise ratio (SNR) are primary factors in designing protocols for clinical applications. The use of echo planar spatial encoding and phased array coils can alleviate these limitations, but new challenges arise in combining data from different receive channels in an efficient manner. Meaning that the phase and the amplitude of signals from each channel will have different profiles that must be taken into account in order to produce a phase sensitive combination with the best possible SNR (Figure 4.1). Variations in coil geometry, wiring, and receiver delays can negatively affect the SNR of the combined data if not taken into account and differences in coil geometry and coil loading among subjects may necessitate the use of acquisition-specific corrections.

Several strategies have been proposed for producing phase sensitive coil combinations, with the majority focusing on signals from single voxel H-1 MR spectra (12–27). The general approach is to form a linear combination of spectra with complex-valued weights that provide constructive addition of the complex signals and give higher emphasis to coil elements with higher signal. The most common method used to estimate the phase and amplitude offsets

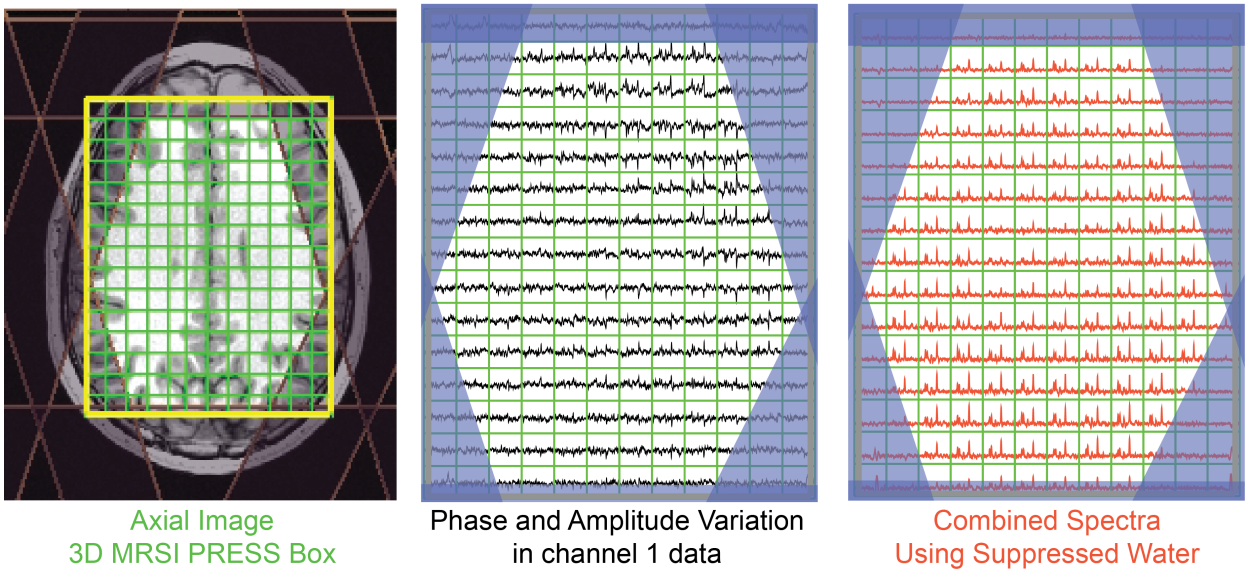

Figure 4.1: Phase and Amplitude Variation in MRSI Volunteer Data.

for individual coil elements for 2D and 3D H-1 spectroscopic imaging datasets has been the acquisition of a separate water reference scan (26–33). This provides spatially dependent weights with relatively high precision but longer overall acquisition times. Another possibility is to use reference peaks from residual water or from individual metabolites. For the voxel sizes used for in-vivo datasets, this is limited by the SNR of individual channels. Other methods such as first point phasing (FPphasing) and whitened singular value decomposition (WSVD) (15, 20, 21) are less dependent on individual peaks but may be more susceptible to spectral artifacts for multi-voxel acquisitions.

The purpose of this study was to compare coil combination strategies in order to find the most robust and accurate technique for evaluating 3D single-cycle and lactate-edited H-1 point-resolved spectroscopy (PRESS) localized, echo planar spectroscopic imaging (EPSI) data for clinically relevant acquisition schemes of approximately 10 minutes in length and to automate the reconstruction and processing pipeline. Methods of interest for this application were implemented and tested in phantoms and normal volunteers for commercially available 8- and 32-channel head coils. Simulations were applied to test the limitations on SNR for each approach. The robustness and practical application of the most relevant methodologies were evaluated by analyzing datasets obtained from a large population of patients with brain tumors.

4.2 Coil Combination Theory

The pre-processed spectrum $p_c(\bar{x}, f)$ for channel c is a function of voxel location x and frequency f as described by Equation 4.1

$$p_c(\bar{x}, f) = A_c(\bar{x})\ exp(-j\phi_c(\bar{x}))\ m_c(\bar{x}, f) + n_c(\bar{x}, f) \tag{4.1}$$

where $m_c(\bar{x}, f)$ is the spectrum from voxel x with between-channel phase offsets corrected and $n_c(\bar{x}, f)$ is complex-valued Gaussian distributed noise with zero mean and channel dependent variance (σ_c) i.e. $n_c \sim \mathcal{CN}(0, \sigma_c)$. $A_c(\bar{x})$ is the differential amplitude factor that represents the receive profile of channel c and $\phi_c(\bar{x})$ is the phase offset for each coil. These values change based on the position of the excited voxels with respect to the coil element (proximity), the geometry of the coil, dielectric property of the sample, and the amplifier gain of the channel.

In such system with c channels there are c measured spectra with associated signal $p_c(\bar{x}, f)$ and noise $n_c(\bar{x}, f)$. A variety of different approaches can be taken to combine the spectra from individual coil element depending on whether the ultimate goal is to correct for spatial variations in intensity of the spectra due to the profile of individual coil elements or to obtain the best possible SNR. Commonly, each individual spectrum is processed and weighted prior to combination to correct for individual coil sensitivities where $w_c(\bar{x})$ is the complex weighting factor compensating for differences in complex coil sensitivity. The combined spectrum can be presented as follows:

$$p(\bar{x}, f) \ = \ \sum_{c=1}^{C} \ w_c^H(\bar{x}) \ p_c(\bar{x}, f) \tag{4.2}$$

The above equation suggest w_c should be equal $A_c(\bar{x}) \exp(-j\phi_c(\bar{x}))$ in Equation 4.1 and the ideal choice for these factors should ensure that the signals are correctly aligned and that the coils more sensitive to the voxels are weighted more strongly, however, the challenge to determine these factors in practice remains unsolved.

The relationship in Equation 4.1 can also be equivalently presented in vector format:

$$\mathbf{P} = \mathbf{s}\ \mathbf{m} + \mathbf{N} \tag{4.3}$$

where $\mathbf{P}$ and $\mathbf{N}$ are $c \times k$ matrices of the spectrum and noise, respectively, with c being the total number of coil elements and k being the number of digitized MRS data points in the FIDs; $\mathbf{s}$ is the complex valued c-element column vector of coil sensitivities and $\mathbf{m}$ is a k-element row vector of the underlying signals.

For optimal combination one needs to determine three factors for each coil element:

1) Each coil element generally have different sensitivities due to hardware aspects such as cable length, connectors and preamplifier gain, as well as sequence parameters such as

receiver bandwidth. Direct combination of signals from different elements requires balancing these sensitivities, otherwise the coil with greater sensitivity will have greater impact in the combined signal which is not appropriate.

2) For commonly used MRSI techniques, the signal detected by all coils is generated by the same net magnetization, however, the coils that are in closer proximity to the excited volume, will detect higher signal amplitude ($A_c(\bar{x})$) compared to the ones further away.

3) The last term that must be determined is the phase compensation factor, $\phi_c(\bar{x})$. Since the different coils will be located in different positions surrounding the patient, then each coil axis will be at a different angle relative to the reference. Because of this, the relative perspective of each coil on the excitation volume will be different.

As a result, a simple addition of weighted signals from the coils would combine them destructively, causing signal cancelation. In short, the amplitude variations observed in both the time and frequency domain spectra are caused by individual differences in receive path sensitivity and differences in coil proximity to the voxel of the interest, while the phase differences are the result of differences in relative orientation of the coils to the net magnetization. Techniques are different in how they calculate these factors. Four most popular approaches for spectroscopy combination with multiple coils are explored here.

4.2.1 First Point Phasing Method (FPphasing)

FPphasing is the time domain combination method as described in (15) which incorporates phase information in the time domain, rather than manually correcting each spectrum in the frequency domain, and scaled each spectrum by its first point FID magnitude (i.e. by the mean value of spectrum) and then combined them by calculating the weighting factors for each time domain signal from the measured background noise of the corresponding coil.

$$p(t) = \sum_{c=1}^{C} w_c \, A_c \, \exp(-j(\delta\phi_c)) \; p_c(t) \tag{4.4}$$

$$w_c = \frac{\sigma_c}{\sqrt{(\sigma_1^2 + ... + \sigma_c^2)}} \tag{4.5}$$

where A_c is the magnitude of the first FID point and if a reference coil is chosen, then the phase of all other coils relative to the reference coil is simply $\delta\phi_c$.

In our experiments, the phase estimate for each voxel and coil were determined from the dataset itself, based upon the first point of each FID after the spatial Fourier transform. Amplitude weighting factors were estimated from the first point FID magnitude and the intensities in individual channels from the proton-density-weighted gradient-echo (GRE) im-

ages that were acquired using the manufacture-provided parallel imaging calibration sequence (ASSET).

4.2.2 Unsuppressed/Suppressed Water Referencing Method

In contrast to first point phasing method, where the first FID point in time domain is used, another approach is to look in frequency domain for points near largest peaks. Using a fixed reference point such as suppressed/unsuppressed water where the signal is assumed to be large, two different phase correction strategies are investigated. Either the spectral arrays from individual elements are corrected on a voxel by voxel basis before hand assuming spatially variant constant phase among channels or that a global phase offset is estimated for each coil assuming constant phase offset between channels.

For phasing, corrections were obtained by either (i) estimating a constant offset per channel from the phase of the reference peak by averaging data from the central eight voxels in the selected volume (RWcentral) or (ii) obtaining voxel-by-voxel maps of the phase of the reference peak in individual channels from same scan (NAAvoxel, RWvoxel) or reference scan (Wvoxel) (28). In the latter case, when voxels had reference peaks with SNR less than 5, the phase estimate was obtained by interpolating values from surrounding voxels. For amplitude weighting, the intensities were either obtained from (i) the height of the reference peak or (ii) using the image calibration scan intensities.

The automated phase correction algorithms used processes the spectra on a voxel by voxel basis to find phase corrections which impose symmetry upon a reference peak in the spectrum and minimize the negative baseline deviations on either side of the peak. After phase correction step, the individual coil data are combined using weighting functions from coil calibration images. Direct comparison of metabolite levels between different voxels must, however, take into account that there is still a spatial weighting on individual voxels caused by the non-uniformity of the combined coil reception profiles. These approaches approximate a matched filter.

4.2.3 Whitened Singular Value Decomposition Method (WSVD)

In contrast to previous methods where a largest signal or reference point or the mean of all the points are used to estimate the necessary phase and amplitude, the next logical step is to use all of the available data points which should minimize the influence of noise fluctuation or risk of degraded points. WSVD approach is shown to produce the optimal SNR in some cases (20, 21).

In this case the phase and amplitude estimations are intrinsic to the combination method. The algorithm decomposes the multi-channel data into a series of contributions of increasing

rank and chooses the best rank 1 decomposition in terms of a column vector that contains the complex coil sensitivities and a row vector containing the combined signals.

In Equation 4.6, the rows of $\mathbf{P}_{c\times k}$ are scalar multiples of signal vector $\mathbf{m}$ and therefore $\mathbf{P}$ is a rank 1 matrix and the SVD of $\mathbf{P}$ computes the maximum likelihood combined spectrum

$$\mathbf{P} = \mathbf{U} \times \mathbf{\Sigma} \times \mathbf{V^H} \tag{4.6}$$

where $\mathbf{U}_{c\times c}$ and $\mathbf{V}_{k\times k}$ are orthonormal singular vector matrices and $\mathbf{\Sigma}_{c\times k}$ is a diagonal matrix that contains the singular values in descending order. Based on low rank approximation theorem, the best estimate of m-rank $\mathbf{P_m}$ is given by zeroing out $r-m$ singular values of $\mathbf{P}$, that is

$$\mathbf{P_m} = \mathbf{U} \times \mathbf{\Sigma_m} \times \mathbf{V}^H$$

$$\mathbf{P_m} = \begin{bmatrix} u_{11} & u_{12} & \dots & u_{1c} \\ u_{21} & u_{22} & \dots & u_{2c} \\ \vdots & \vdots & \ddots & \vdots \\ u_{c1} & u_{c2} & \dots & u_{cc} \end{bmatrix} \times \begin{bmatrix} \sigma_{11} & 0 & \dots & 0 \\ 0 & 0 & \dots & 0 \\ \vdots & \vdots & \ddots & \vdots \\ 0 & 0 & \dots & 0 \end{bmatrix} \times \begin{bmatrix} v_{11} & v_{12} & \dots & v_{1k} \\ v_{21} & v_{22} & \dots & v_{2k} \\ \vdots & \vdots & \ddots & \vdots \\ v_{k1} & v_{k2} & \dots & v_{kk} \end{bmatrix}^H$$

and therefore an estimate of the signal vector $\mathbf{p}$ is from the principle columns of $\mathbf{V}$ and the weights associated with this combination method are contained in the principle columns of $\mathbf{U}$.

The first singular vectors of ($\mathbf{U}_{c,1}$and$\mathbf{V}_{k,1}$) corresponding to largest singular value $\mathbf{\Sigma}_{1,1}$ give the maximum likelihood coil sensitivities and combined spectrum respectively. From this, $\mathbf{w}$ can be calculated using Equations 4.7, 4.8

$$\mathbf{w} = \frac{\mathbf{u}_{c1}}{\lambda} \tag{4.7}$$

$$\mathbf{p} = \sigma_{11}\ \lambda\ \mathbf{v}_{k1}^H \tag{4.8}$$

where $\mathbf{w}$ is complex coil sensitivities where λ is an arbitrary amplitude/phase term for each voxel. The amplitude and phase are implicitly calculated from $\mathbf{w}$ for individual coils as described in Equations 4.9, 4.10.

$$\mathbf{w_c} = |\frac{\mathbf{U_{(c,1)}}}{\lambda}| \tag{4.9}$$

$$\phi_{\mathbf{c}} = \angle|\frac{\mathbf{U_{(c,1)}}}{\lambda}| \tag{4.10}$$

4.2.4 Generalized Least Squared Method (GLS)

In previous methods, either the transformed signals are individually or collectively phased and then weighted where the weighting factor for each channel was estimated from proton-density-weighted gradient-echo (GRE) images (i.e. estimated coil sensitivity images) or the

combined spectrum is computed from the transformed signals by singular value decomposition. The GLS method is optimal solution in the linear regression model when coil sensitivities are known or can be measured with sufficient accuracy (SENSE like techniques) and can be used here by setting the acceleration equal to 1.

However, GLS method incorporates a smoothness constrains on the coil sensitivities and therefore, one problem area that could cause the inversion errors would be the use of a very low resolution images as coil sensitivity maps, which are known to have anatomy-related contrast that diverges from the actual sensitivity values. By smoothing the coil sensitivity maps as suggested in previous works we believe these errors can be minimized.

Therefore, in this work, the coil sensitivity maps were initially calculated in two ways. The integral of the complex-valued unsurpressed water peak or NAA peak (22) was used to create the sensitivity map either by itself or using ESPIRiT algorithm (34) for each channel. Then the combined spectrum was computed according to SENSE reconstruction as follows:

$$\mathbf{m} = (\mathbf{s}^H \mathbf{\Psi^{-1}} \mathbf{s})^{-1} \mathbf{s}^H \mathbf{\Psi^{-1}} \mathbf{P} \tag{4.11}$$

where the receiver noise matrix $\mathbf{\Psi} = \mathbf{N}\mathbf{N}^H$. The phase and amplitude estimations are in the complex term $(\mathbf{s}^H \mathbf{\Psi^{-1}} \mathbf{s})^{-1} \mathbf{s}^H \mathbf{\Psi^{-1}}$.

ESPIRiT is a new technique to estimate sensitivity maps from auto-calibration signal (ACS) data (34). In the ideal case, this technique yields a single set of sensitivity maps, which can be used in SENSE. For data that is corrupted (by motion, chemical shift, aliasing, ghosting, etc), the SENSE model using a single set of smooth sensitivity maps is inconsistent and often yields additional artifacts. For corrupted data, ESPIRiT often yields multiple sets of maps in an attempt to fit the data into a subspace. Coil sensitivities can be estimated in the image domain as eigenvector maps from a point-wise eigen decomposition of a related operator. In case of corruption, additional eigenvalues appear which correspond to signal components not consistent with a single set of maps. In our experiments the generated ESPIRiT coil sensitivity maps and complex integral coil sensitivity maps produced the same results and no improvement was evident (Figure 4.2).

If the sensitivity maps are real valued, with assumption of no noise in the system, the Equation 6.1 simplifies to

$$\begin{aligned} \mathbf{m} &= (\mathbf{s}^H \mathbf{I^{-1}} \mathbf{s})^{-1} \mathbf{s}^H \mathbf{I^{-1}} \mathbf{P} \\ \mathbf{m} &= \frac{1}{\mathbf{s}^H \mathbf{s}} \mathbf{s}^H \mathbf{P} \\ \mathbf{m} &= \frac{\mathbf{s}^H}{|\mathbf{s}|^2} \mathbf{P} \end{aligned} \tag{4.12}$$

which is the weighted sum as discussed earlier.

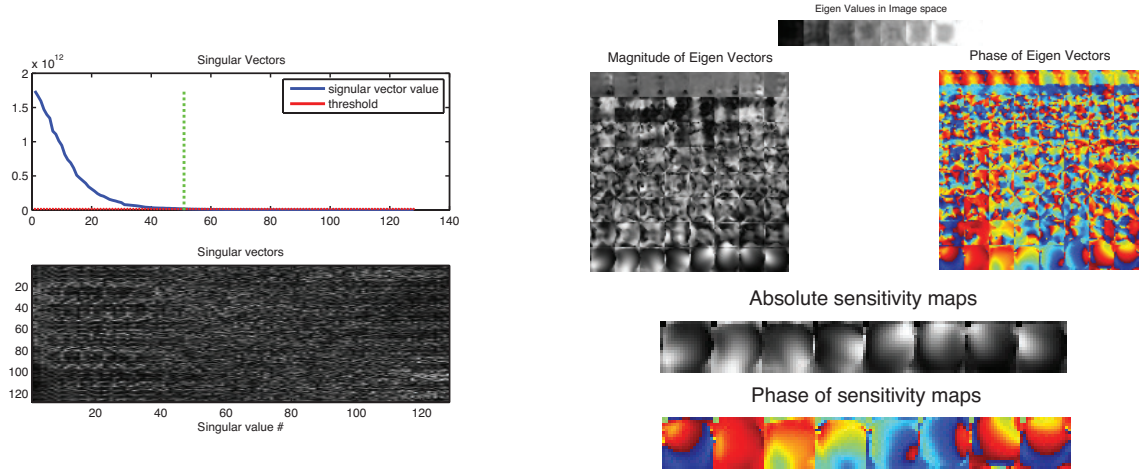

Figure 4.2: Singular value decomposition (SVD) of the integrated water peak matrix is shown. The zoomed view of the V matrix of the SVD and a plot of the singular values show that the calibration matrix (that is created form the integrated water peaks) has a null space. Explicit sensitivity maps using eigenvalue decomposition are shown. The last set of eigenvectors corresponding to eigenvalue of 1 looks like sensitivity maps,

4.3 Materials and Methods

4.3.1 Experiments

Single-cycle and lactate-edited 3D H-1 PRESS localized EPSI data were acquired from a commercially available MR spectroscopy phantom, 6 healthy volunteers and 55 patients with glioma (30 males, 25 females, 25-71 years old). Volunteers and patients provided informed consent as approved by the Institutional Review Board at our institution. Data were obtained using a 3T scanner (GE Medical Systems, Milwaukee, WI) with body coil transmit and commercially available 8-channel (MRI Devices, Gainesville, FL) or 32-channel (Nova Medical, Wilmington, MA) phased array receive coils.

4.3.1.1 Phantom Data

The MR spectroscopy head phantom comprised 3 mM choline, 10 mM creatine, 12.5 mM NAA, 12.5 mM glutamate, 7.5 mM myo-Inositol and 5 mM lactate. Calibration and 3D volumetric T_1-weighted images were also obtained. The 3D EPSI data were obtained as described previously with 2-D phase encoding and a flyback echo planar readout in the superior-inferior direction that provided 712 dwell points and 988 Hz bandwidth. The PRESS selected volume was prescribed as $120 \times 120 \times 60$ mm^3, but utilized over-PRESS factors of 1.5 in all three spatial dimensions (TR/TE = 1500/144 ms, FOV = = $18 \times 18 \times 16$ cm^3, nominal

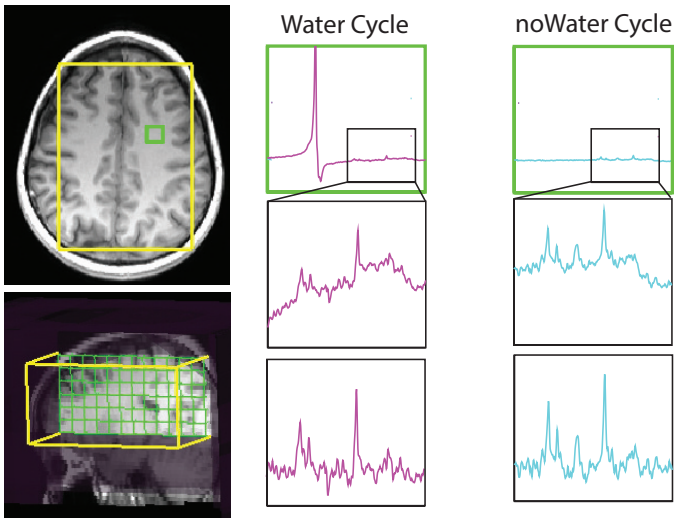

Figure 4.3: Lactate-edited 3D PRESS localized EPSI data set from a volunteer

voxel size = 1 cm^3). Very spatially selective (VSS) pulses were applied to remove signal from the voxels on the edge of the over-PRESS region and hence eliminate chemical shift artifacts (35). The acquisition included an unsuppressed water scan, a single-cycle scan with CHESS water suppression and a two-cycle lactated-edited scan with BASING and CHESS water suppression (36). For the latter, the cycle using the editing pulse had low residual water and the cycle without the editing pulse had much larger residual water.

4.3.1.2 Volunteer Studies

Three healthy volunteers received 2 MR exams on different days within a period of 2 weeks using the 8-channel coil. The 3D EPSI acquisitions were automatically prescribed (37) and acquired using the PRESS sequence described above (38, 39). Three other healthy volunteers received 2 sets of MR exams, the first with the 8-channel and the second with the 32-channel head coil. Each dataset included 3D PRESS localized EPSI acquisitions that were automatically prescribed from similar regions based on an atlas definition (40) single-cycle with CHESS, single-cycle without CHESS, and lactate-edited with CHESS (36). These 3 acquisitions were prescribed with excited volumes of $150 \times 180 \times 60$ and over-PRESS factors of 1.2, 1.2, and 1.5, respectively, with both octagonal and automatically generated saturation bands (38).

4.3.1.3 Patient Studies

A total of 105 MR exams were acquired from 55 patients with brain tumors. The scan protocol included low-resolution calibration images for estimating coil element profiles, T_2-weighted FLAIR images, pre- and post-contrast T_1-weighted images, 3D lactate-edited PRESS

localized H-1 EPSI data with TE = 144 ms, TR = 1104-1500 ms, spectral array = 16×16×16 or 18 × 18 × 16 and effective spatial resolution = 1.014/1.013 cc (T_{acq} = 4.7-8.1 min). The selected volume (prior to applying over-PRESS factors of 1.2, 1.2 and 1.5) varied from 192 to 1512 cm^3.

4.3.1.4 Simulations

The performance of the combination algorithms was tested with the phantom data by simulating spectra with different SNRs. The noise level was estimated from the average standard deviation of 75 points at the end of the FID (σ). Complex-valued Gaussian-distributed white noise was added to the raw data to generate noise levels of $\lambda\sigma$, where $\lambda = 1, 1.2, 1.4, \ldots 8, 10, \ldots, 16$. For volunteer data, the impact of the magnitude of the residual water on the reliability of coil combination was assessed using weighted sums of the lactate-edited data. The residual water was added with weight levels of 0, 5, 10, 15, ..., 100. The magnitude of the residual water peak relative to NAA (H_2O/NAA) in these experiments ranged from 0 to 18-fold.

4.3.2 Data Processing

Processing of individual channel MRSI data

Steps used to process the data are represented in Figure 4.4. These included reconstruction of individual channel spectral arrays, coil combination, and post-processing to perform baseline subtraction, removal of residual phase variations in the metabolite peaks, and quantification of peak intensities. The reconstruction and peak quantification used software previously developed in our laboratory (41). The input to the coil combination algorithms comprised spatial arrays of spectra, with 1 array per channel for unsuppressed water or single-cycle data, and 2 arrays per channel for lactate-edited data. To examine the effect of poor lipid suppression, four patients with the poorest performance in WSVD were selected to examine the impact of pre-processing to remove the undesirable lipid signal using non-iterative time-domain fitting with the Lanczos-based version of HSVD to filter out signals from 1.8 to -1.0 ppm (42).

4.3.2.1 Evaluation of phase variations among channels between coils

The phase in voxels from each channel includes contributions due to field inhomogeneity, applied gradients, sequence encoding, and coil receiver phase offset (ϕ_c). It was assumed that phases from datasets with unsuppressed water represented ground truth. These corrections were used to generate phase maps for both 8- and 32-channel coil arrays. By subtracting the average phase (θ_c) from the central voxels for each element, the remaining net phase difference (Ψ_c) should depend only on the geometry of the coil and will highlight the spatial phase variations between individual coils (Equation 4.13).

$$\psi_c(\bar{x}) = (\phi_c(\bar{x}) - \theta_c) \tag{4.13}$$

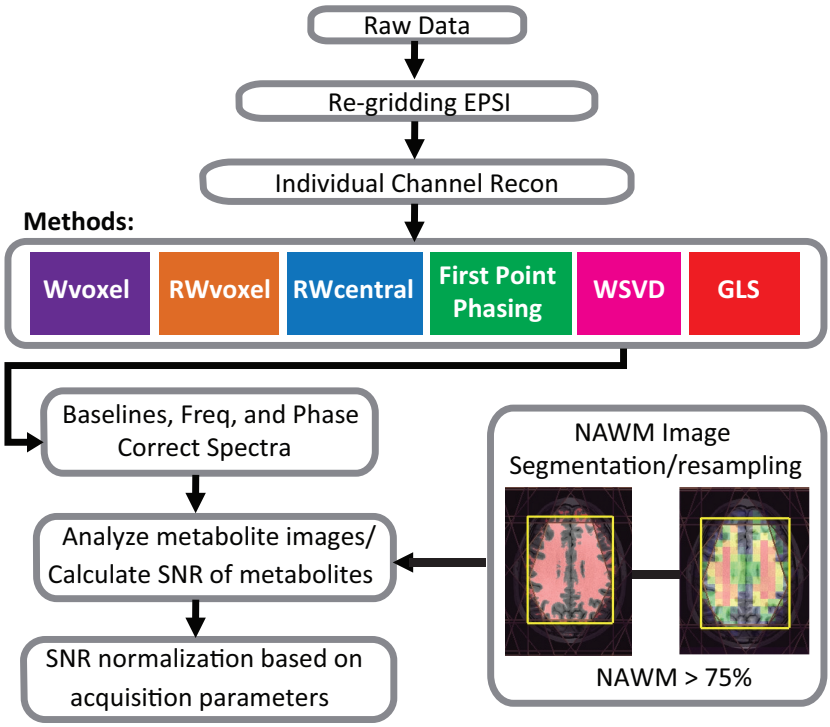

Figure 4.4: 3D MRSI Processing Diagram. The flowchart describes the pre and post-processing routines for our spectroscopy data.

The between-channel variation in phase maps was assessed by taking the standard deviation of phase values as follows

$$\psi(\bar{x}) = SD[\psi_c(\bar{x})] \tag{4.14}$$

4.3.2.2 Coil Combination

To obtain a combined spectrum with optimal SNR the phase offsets $\phi_c(\bar{x})$ in Equation 4.1 must first be removed and the individual channel spectra weighted to account for differences in the amplitude factors $A_c(\bar{x})$ in Equation 4.1.

$$p(\bar{x}, f) = \sum_{c=1}^{C} \frac{|w_c|}{\sqrt{\sum_{i=1}^{C}(|w_i|^2)}} \times exp(j\hat{\phi}(\bar{x})) \times p_c(\bar{x}, f) \tag{4.15}$$

The data from individual channels were combined based on Equation 4.15 using a phase estimate of $(\hat{\phi}(\bar{x}))$ and a weighting function that divides by the square root of the sum of squares of the amplitudes of the individual coil weights. This is preferred for initial analysis and viewing of the data because it maintains similar noise levels in each spectrum. Direct comparison of metabolite levels between voxels must also take into account the spatial

Table 4.1: Summary of the coil combination methods that were evaluated.

Method	**Abbrevation**	**Phase Estimation**	**Amplitude Weights**
Unsuppressed water peak from separate dataset	Wvoxel	voxel by voxel	reference peak hight or calibration images
Residual water peak from same dataset	RWvoxel	voxel by voxel	reference peak height or calibration images
Residual water peak from same dataset	RWcentral	constant offset	reference peak height or calibration images
Generalized least squares using residual water peak	GLS_{RW}	direct estimation from peak region	
NAA peak from same dataset	NAAvoxel	voxel by voxel	reference peak height or calibration images
NAA peak from same dataset	NAAcentral	constant offset	reference peak height or calibration images
Generalized least squares using NAA peak	GLS_{NAA}	direct estimation from peak region	
First point FID phasing	FPphasing	voxel by voxel	first FID point height or calibration images
Whitened singular valued decomposition	WSVD	direct estimation from spectra	

weighting of signals in individual voxels that is caused by the non-uniformity of the combined coil reception profiles.

The combination methods evaluated in this chapter are summarized in Table 4.1. The first seven strategies are characterized by using a reference peak for estimation of the relevant parameters. For Wvoxel, the water peak from a separate dataset that was acquired without water suppression was used to provide the phase reference and the amplitude weighting factors were obtained either from the height of the reference water peak or from intensities in proton-density-weighted gradient-echo (GRE) calibration images acquired using the manufacture-provided parallel imaging calibration sequence (ASSET CAL). The related methods (RWvoxel and NAAvoxel) used similar strategies but obtained estimates for combining the data using either the residual water or NAA peaks from the same acquisition as the reference. For voxels with reference peaks having SNR less than 4, the phase estimate was obtained by interpolating values from the surrounding voxels. The RWcentral and NAAcentral methods used similar amplitude weighting but assumed that there was a constant phase offset between channels and estimated its value from the reference peaks in the central voxels of the spectral array.

The GLS algorithms used the complex integral of the spectra over the reference peak (residual water or NAA) to measure coil sensitivity maps for individual channels. The combined spectrum was then calculated according to sensitivity encoding (SENSE) reconstruction described by Equation 6.1 (22).

The other two methods (FPphasing and WSVD) apply corrections to each voxel independently but differ in that they make use of information from the entire frequency range. The simplest of these, which is used by several scanner manufacturers, is the FPhasing strategy. As its name suggests, it applies a correction based on the phase from the first point of the free induction decay (FID) from each voxel. If one considers the properties of the discrete Fourier transform, it can be readily appreciated that this is equivalent to averaging the signals from the real and imaginary parts of the spectrum and then using them to provide the phase estimate at that voxel location.

For the WSVD method, the phase and amplitude estimations are intrinsic to the calculation itself. The first step is to whiten the noise contribution using an additional noise prescan as described in (20). For cases in which the noise acquisition was not available, the covariance matrix was estimated from a region of the spectra between -0.4 and -1.0 ppm that contained 75 noise samples.

4.3.2.3 Post-processing

The spectral arrays were processed as described previously (41). For the lactate-edited data this included summing the two cycles of data to produce a 3D spectral array containing choline, creatine, NAA, and lipid, and subtracting them to provide a 3D array containing only lactate. Quantification of peak intensities for individual spectra included additional frequency, phase, and baseline correction on a voxel-by-voxel basis. This was necessary because, although the spectra from different channels had been correctly phased, the phases of the metabolite peaks in the combined spectra were not always identical. Maps of metabolite peak intensity were determined from the phase-sensitive, baseline-subtracted data. In each case, a region of 75 spectral points without metabolite signals was selected to estimate the standard deviation (SD) of the noise for each voxel in the selected volume and then averaged to obtain a single normalization factor for each subject.

For the patient and volunteer data, final SNRs were normalized according to Equation 4.16 in order to account for differences in acquisition and repetition times using the relaxation constant (43) for individual metabolites and an estimate of the effective spatial resolution by accounting for the point spread function of the acquisition matrix (44).

$$\mathrm{nSNR} = \frac{\mathrm{SNR}_{measured}}{res\sqrt{T_{acq} \times N_{acq}}(1 - exp(\frac{-\mathrm{TR}}{T_1}))} \tag{4.16}$$

Metabolites peaks were considered detectable if the they had a raw SNR value greater than

5. Lipid peaks were considered detectable if they had a peak height greater than 25% of the mean NAWM NAA peak. Voxels in the volunteers and patients that contained a detectable lipid peak were considered to have lipid contamination.

4.3.2.4 Image processing

The spectral data from volunteers and patients were referenced to the 3D anatomic T_1-weighted images, assuming that there was no movement of the subjects between the image and spectra acquisitions. FLAIR images were aligned to the corresponding 3D T_1-weighted images using FSL's linear registration tool (FLIRT (45)). Segmentation of the brain was performed automatically using a program that is based on a Markov random field model (46). The segmented white matter (WM) mask was then used to identify spectral voxels that had at least 75% normal-appearing white matter (NAWM) to use for comparative analysis of metabolite levels for volunteer and patient data. Metrics used for comparison were the average SNR of NAA and the coefficient of variance (CV) of the SNR of NAA. For volunteer and phantom experiments where an additional, non-water suppressed MRSI dataset was obtained, the phase estimates that it provided (Wvoxel) were used to assess the performance of the other methods.

4.4 Results

4.4.1 Noise Analysis

Noise Correlations Among channels: Because of some the combination methods presented in this study account for the noise correlation between the channels, it is beneficial to investigate noise correlation levels for considered datasets. The noise covariance matrices were estimated by calculating the covariate matrix of the noise data acquired with RF excitation disabled. The noise correlation matrices of both 8- and 32-channel coils for a phantom and a volunteer are shown in Figure 4.5 and demonstrate low noise correlation between the coil elements with mean value of off-diagonal correlation coefficients being 0.22 for 8-channel and 0.11 for 32-channel.

Noise Behavior After Combination: Colored-noise inherently exists in any kind of coil-weighted summation. One thing to be aware of is that for the WSVD and the GLS methods, the noise is not uniformly distributed across FOV and therefore the SNR calculation and comparison may be questionable. SNR was calculated in the same manner for all the techniques, however, as indicated throughout this chapter, an additional measure (coefficient of variance) was considered solely for that reason, however the outcome was similar. Figure 4.6 shows the spatial distribution of estimated SD of the noise for each combination technique (slice by slice) for one volunteer for both 8- and 32-channel coils. As expected it is not uniform and the maps vary for each technique; It is true that SNR is not the most optimal

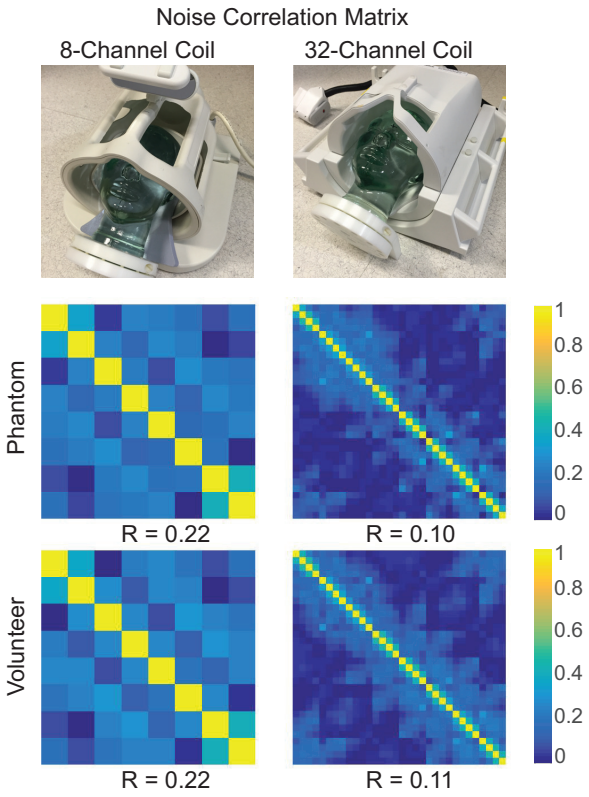

Figure 4.5: The noise correlation matrix for phantom and volunteer data with 8- and 32-channel detection.

measure in these cases due to the behavior of the noise, but it is robust, easy to calculate and used in almost all previous studies in coil combination.

4.4.2 Analysis of Phantom Data

One Voxel with overlayed spectra from the two cycles of lactate-edited data is shown in Figure 4.7(a). The average SNR of the residual water and NAA peak in the combined spectra from the lactate-edited cycle that had high residual water were 5500 and 70 respectively, and from the lactate-edited cycle with low residual water were 44 and 75, respectively. Note the differences in phase between the metabolites and residual water peaks, as well as the elevated baseline caused by the tail of the residual water peak that remains prior to post-processing. The residual water signal is only used in the phase correction step, meaning even if it is significantly altered by CHESS water suppression module compared to the metabolites, as long as it is altered the same way for every coil element, after phase correction we will be adding voxels from every coil element constructively (which is the main goal: achieving the same "relative" phase across channels). Note that after constructive addition, we removed the baseline and phased the metabolites of the combined data again. (These steps are

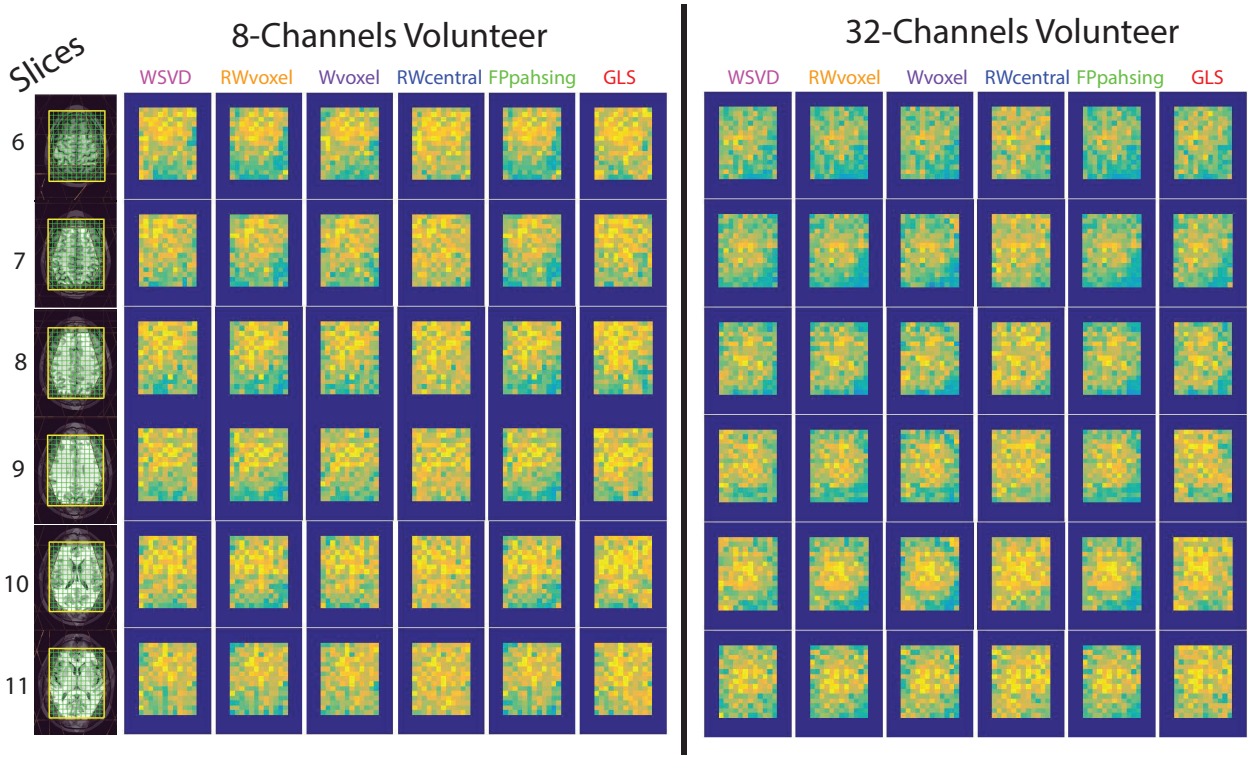

Figure 4.6: Spatial distribution of estimated standard deviation of the noise for each combination technique (slice by slice) for both 8- and 32-channel coils.

shown in the flow chart in Figure 4.4). In Figure 4.9 we showed that the amplitude maps of unsuppressed water and residual water were very similar to one another, ultimately, the calibration images which are more representative of the coil sensitivity map were used as weighting factors for our combination.

Spectra from the center four voxels for the combined lactate-edited 8-channel head coil data with simulated noise levels are shown in Figure 4.7(b) where the phase offsets and amplitude factors were estimated using the Wvoxel method. These simulated spectra were used to test the algorithms performance and patient data lies somewhere between 5σ and 7σ noise level.

Table 4.2 summarizes the raw SNR performance and the percent signal increase relative to the gold standard (Wvoxel method) in a phantom for all the algorithms for both 8- and 32-channel coils. A comparison of these head array coils showed 25% increase in SNR across all techniques for larger array elements. This SNR improvement reaches 40% for volunteer data sets (as shown in Table 4.3). This is because the head phantom is smaller than average human head and while the central SNR is nearly identical, the peripheral SNR increases in the higher channel coils (47) which accounts for the 15% difference.

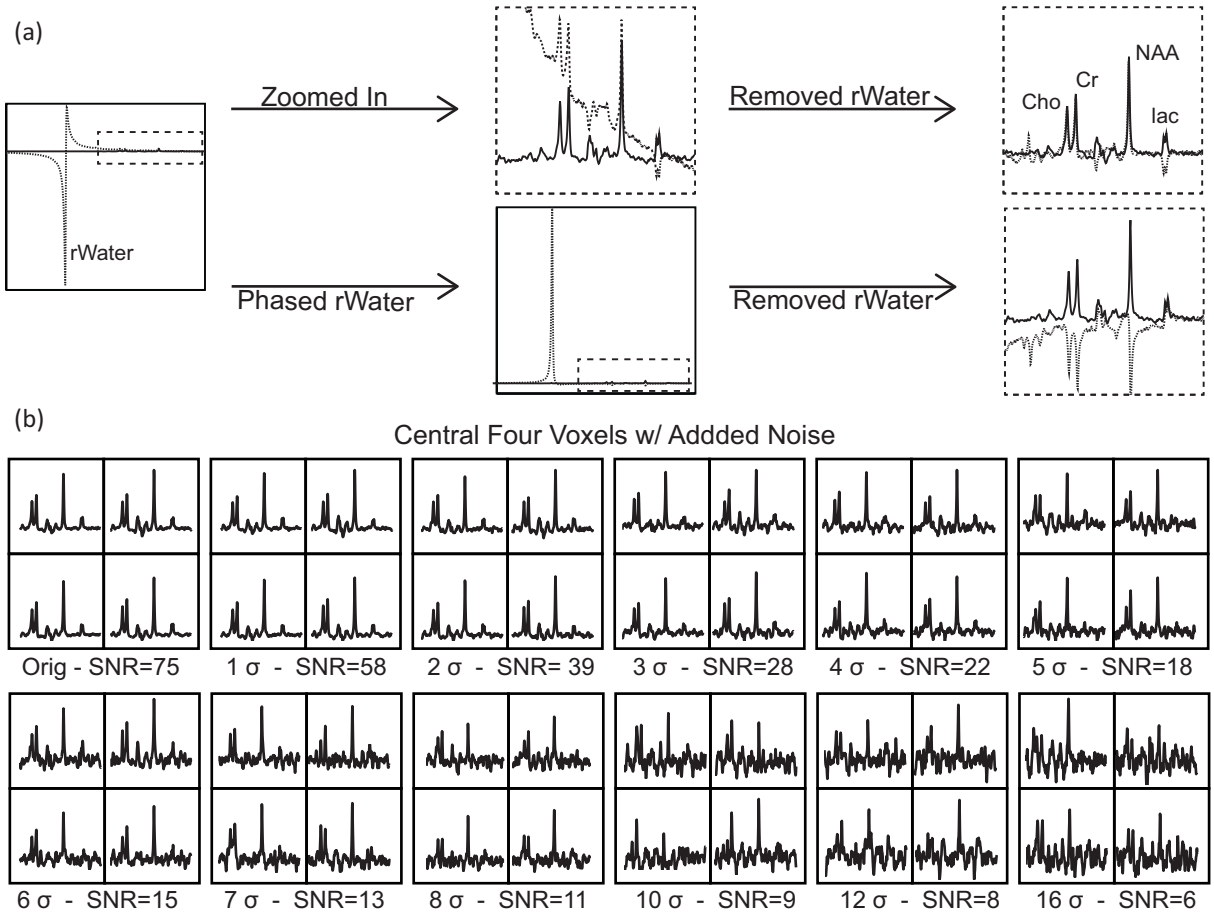

Figure 4.7: Phantom Data. (a) Comparison of one voxel of lactate-edited 3D MRSI sequence. The spectra in the cycle with large residual water (rWater) is presented in dashed line and the spectra in the cycle with very little residual water is presented in solid line. (b) The central four voxels of the combined spectra is shown with additional simulated noise levels.

8-channel: When using the cycle with residual water to estimate parameters for combination, the performance of the relevant techniques was similar for all except the RWcentral method, which was 14% worse than the Wvoxel method (NAA SNR for Wvoxel = 69.39, for RWvoxel = 69.76, for GLS_{RW} = 67.18, for FPphasing = 69.63, for WSVD = 70.06 and for RWcentral = 60.23). For the cycle with very little residual water, NAA was used as the reference peak. In this case, the performance of NAAvoxel, FPphasing and WSVD was similar to Wvoxel (NAA SNR = 74.98, 74.40, 74.95 compared with 74.6), but worse for GLS_{NAA} (NAA SNR = 69.48, 7.3% lower) and NAAcentral (NAA SNR = 63.60, 15.2% lower).

32-channel: The estimates of NAA SNR were higher for data obtained using this coil but the trends for the coil combination algorithms were the same as for the 8-channel coil. For

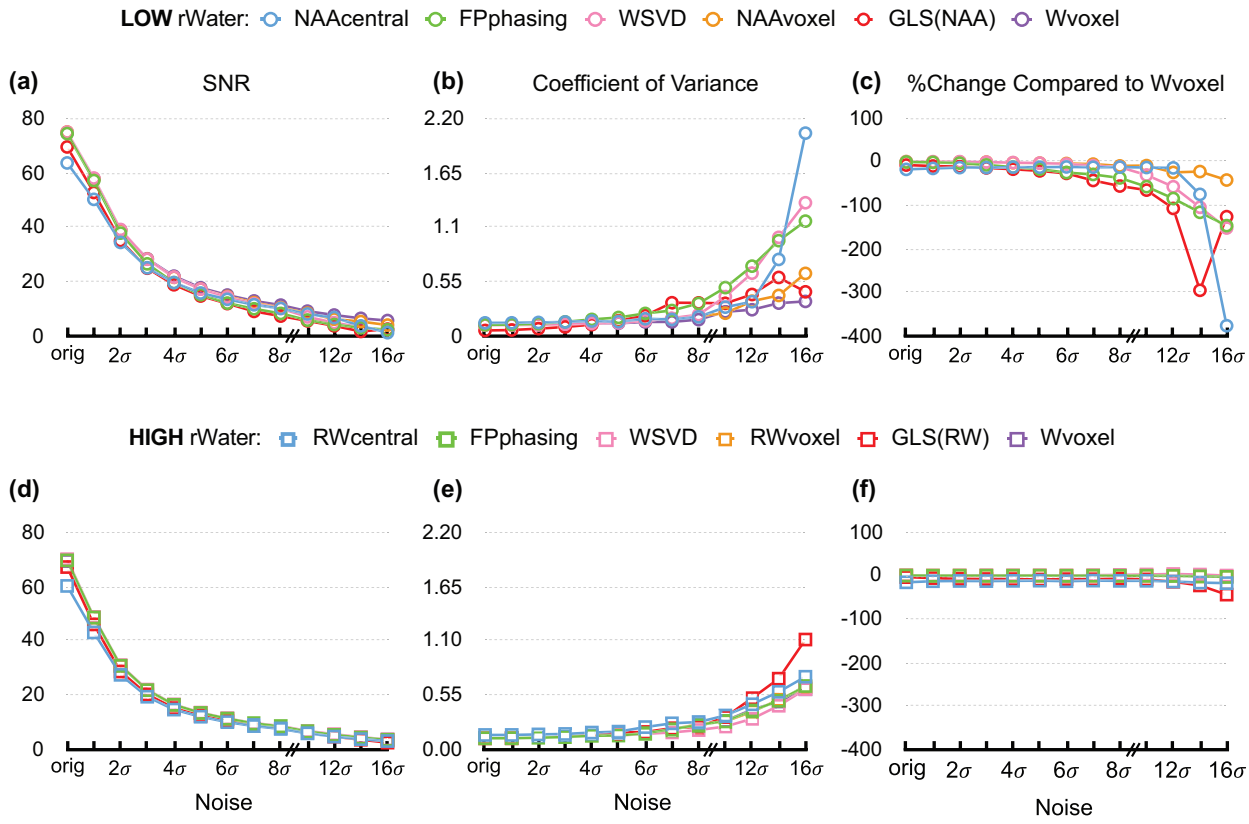

Figure 4.8: Summary of coil combination performance as a function of SNR in phantom. (a,b,c) plots present the results from the cycle with minimal residual water. (d,e,f) plots present the results from the cycle with large residual water. Three measures are compared: (c,d) SNR, (b,e) coefficient of variance, (c,f) percent increased of all techniques compared to the gold standard which is Wvoxel.

the cycle with residual water the NAA SNR for Wvoxel, RWvoxel, GLS_{RW}, FPphasing and WSVD were (86.80, 86.6, 83.79, 86.2, and 87.47) but for RWcentral was 70.89 (19% lower than Wvoxel). For the cycle with very little residual water, the NAA SNR for Wvoxel, NAA voxel, FPphasing, WSVD were 93.55, 94.25, 92.82 and 94.25 respectively, for GLS_{NAA} the SNR was 78.68 (16.5% less than Wvoxel) and for NAAcentral was 75.76 (19.6% less than Wvoxel).

Figure 4.8 summarizes how these algorithms behaved for synthetic data generated from the phantom results in the 8-channel dataset by adding higher noise levels. Three measures are provided: the average combined SNR the coefficient of variance (CV), and the percent signal increase (PI) relative to the gold standard (Wvoxel method). When the additional random noise was added, the performance remained strong for the cycle with high residual water but rapidly degraded for the cycle where NAA was used as a reference peak Figure 4.8(a,d).

Table 4.2: Raw SNR and Percent Change compared to Wvoxel Values for All Techniques for NAA in a Phantom

8-Chennel					
Cycle w/ rWater			Cycle w/o rWater		
Methods	SNR	%	Methods	SNR	%
Wvoxel	69.4	-	Wvoxel	74.6	—
RWvoxel	69.7	< 1%	NAAvoxel	75.0	< 1%
GLS_{RW}	67.2	-3%	GLS_{NAA}	70.0	-6%
FPphasing	69.6	< 1%	FPphasing	74.4	< 1%
WSVD	70.1	< 1%	WSVD	75.0	< 1%
RWcentral	60.2	-13%	NAAcentral	63.6	-15%
32-Chennel					
Wvoxel	86.8	-	Wvoxel	93.6	—
RWvoxel	86.6	+2%	NAAvoxel	94.3	< 1%
GLS_{RW}	83.8	-4%	GLS_{NAA}	78.7	-16%
FPphasing	86.2	< 1%	FPphasing	92.8	< 1%
WSVD	87.5	< 1%	WSVD	94.3	< 1%
RWcentral	70.9	-19%	NAAcentral	75.8	-19%
	+25%			+ 25%	

The performance of the Wvoxel method was unchanged because it uses the data from a reference scan to compute values for phase and amplitude. All of the other methods became unstable as the SNR decreased, especially when a strong reference peak did not exist. It is important to note that these data-driven methods failed at different SNR values, although it is difficult to determine which algorithm performed the best in the absence of a strong water peak. For the cycle with large residual water, the WSVD marginally outperformed the other techniques in terms of having high SNR, low CV, and the largest PI. At lower SNRs, the RWvoxel and FPphasing combination methods were comparable to WSVD in SNR, CV, and PI (e.g. at 12σ, SNR = 5.5, 5.5, and 5.7, respectively; CV = 0.38, 0.39, and 0.31; PI = 0.2, -0.3, and 3.8), while the GLS_{RW} method performed poorly (SNR = 4.8, CV = 0.52, PI = -13.9 at 12σ) and the RWcentral method performed the worst across all SNRs (e.g. at 12σ SNR = 4.9, CV = 0.46, PI = -13.4).

4.4.3 Amplitude Factors and Phase Offsets for Volunteer Data

Combined amplitude factor maps for calibration images, non-suppressed water, residual water and NAA peaks for 8-channel and 32-channel data are shown in Figure 4.9(a,b). The differences observed are not only due to variations in SNR in the reference peaks, but to the

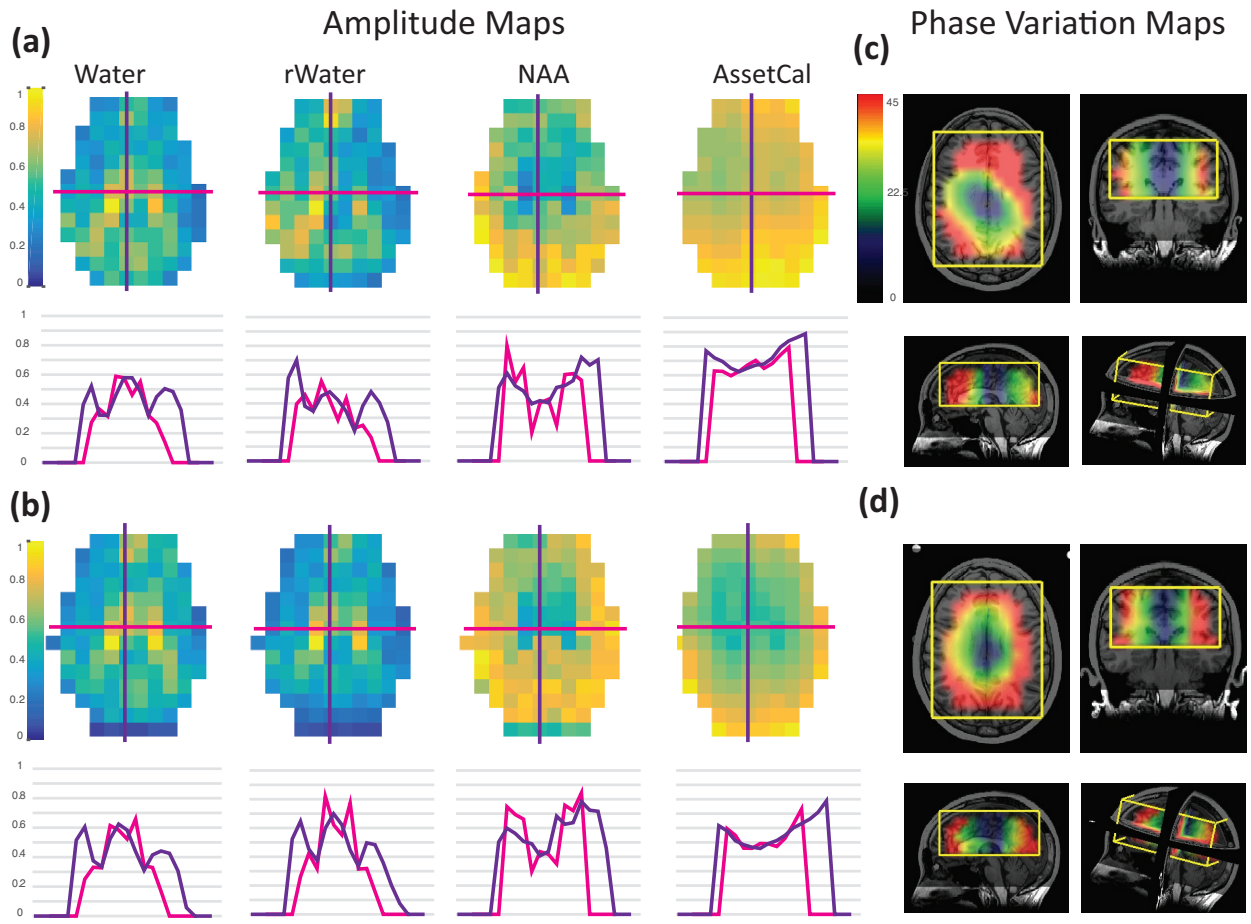

Figure 4.9: Amplitude factors and phase offsets for volunteer data. (a,b) Amplitude maps with cross sectional plots for a volunteer with 8 and 32 channel coil respectively. (c,d) Phase variation maps in axial, coronal, sagittal, and 3D view for the same volunteer.

longer T_2 of water in cerebrospinal fluid (CSF) and the distribution of NAA. Intensities in the central voxels relative to the outer voxels were 1.08, 0.92, 0.81, and 0.90 for the four maps (Water, residual-water (rWater), NAA, and ASSET CAL) for the 8-channel coil compared to 1.13, 1.24, 0.82, and 0.81 for the 32-channel coil. Clearly the SNR of the NAA reference peak was too low to be reliable in weighting data from different channels and one of the other weighting methods would need to be used.

The impact of the different coil geometries on the spatial variation of the phase offset is represented in the phase offset deviation maps calculated from the non-suppressed water acquisition shown in Figure 4.9(c,d). In the center of the selected volume the offsets were relatively constant, but the between-channel deviation increased for voxels closer to the coils up to an average of $94° - 89°$ degrees, and was larger for the 32- versus the 8-channel coil.

The net phase difference for each channel was calculated by relating the phase of each voxel to an arbitrarily designated reference channel. The mean offsets varied substantially between acquisitions, by 10° to 40° degrees for the 8-channel coil and 5° to 30° degrees for the 32-channel coil, and followed no clear pattern. The presence of such large variations implies that phase offset values could not be pre-calculated and stored for reconstructing other datasets.

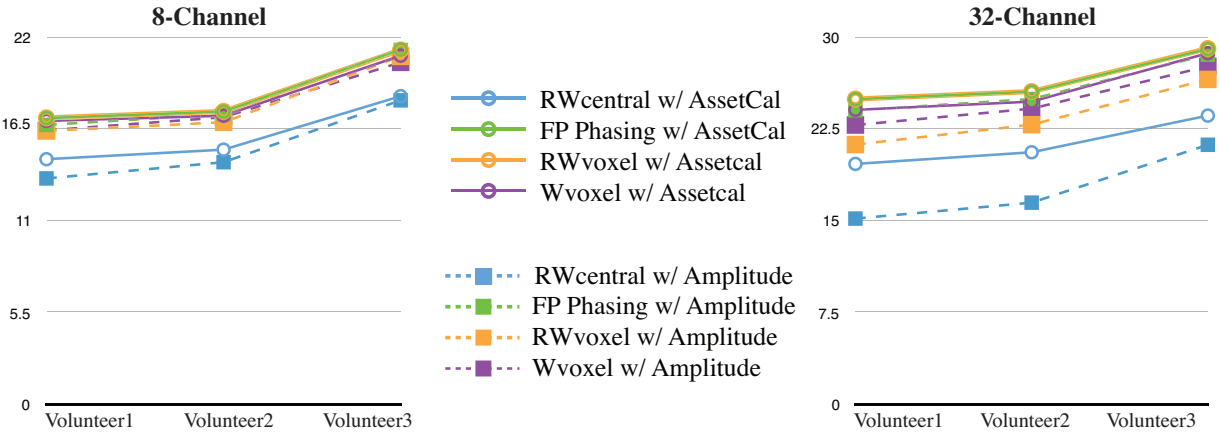

Figure 4.10: Coil Combination Techniques with Different Weighing Factors.

4.4.4 Comparison of Combination Methods for Volunteer Data

As mentioned earlier, weighting by the reference peak intensity/first FID intensity is an option and we have performed the analysis on our volunteer data using both that option and the calibration image intensities. We found that using the calibration image intensities gave either similar or better results than the reference peak intensities (see Figure 4.10). In addition, as Figure 4.9 suggests, the calibration (ASSETCAL) images are more representative of the true coil sensitivity map. Since these are typically generated for the imaging component of the examination, they are available for use in the spectral reconstruction. We therefore used this weighting method in the analysis of the robustness of the algorithms for the patient data.

The differences between methods for the 3 volunteers and for the 8- versus 32-channel coil spectral arrays with large residual water are represented in Figure 4.11. The RWvoxel combination gave 18% and 25% higher NAA SNR for these coils compared to the RWcentral method, with the 32-channel coil having 40% and 33% increases in NAA SNR over the 8-channel coil for the RWvoxel and RWcentral methods, respectively. The performance of the other methods showed similar trends between these two extremes. For the data that was acquired using lactate-edited MRSI, we evaluated the combination methods for the two

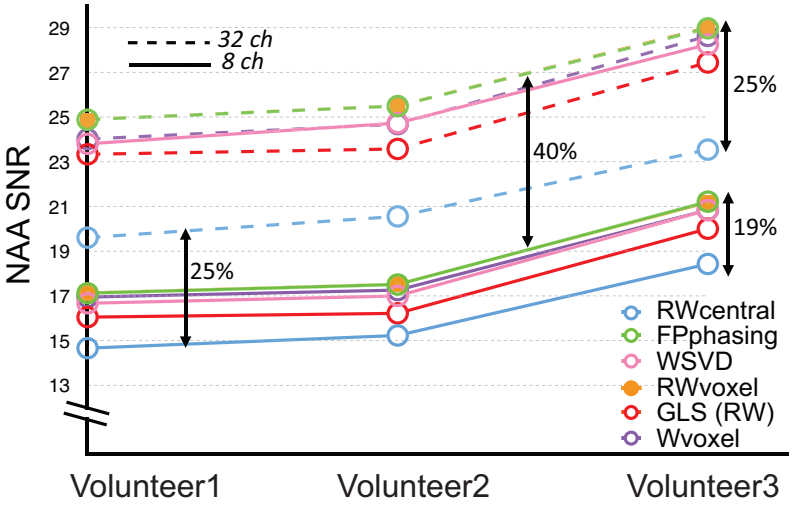

Figure 4.11: The SNR performance of all the techniques among three volunteers with both 8- and 32- channel coils.

cycles individually by choosing residual water as a reference when the cycle had high residual water, and choosing NAA as a reference when the editing cycle had a very low residual water peak.

Table 4.3 shows mean raw SNR and mean nSNR (±SD) of NAA from NAWM in addition to the percent signal increase relative to the gold standard (Wvoxel method) in 3 volunteers for all the algorithms for both 8- and 32-channel coils. In addition mean percentage of voxels containing aliased lipid and mean percentage of detectable voxels were computed (not shown in the Table). Analysis of spectral quality showed that between 98% to 100% of all voxels outside the ventricles had detectable NAA peak (SNR $>$ 5) for all techniques except GLS_{NAA} which the value was 88%. For the 8-channel coil, for the cycles with high residual water, the mean±SD percentage of voxels with lipid peaks greater than 25% of the mean NAA signal from NAWM for Wvoxel, RWcentral, RWvoxel, GLS_{RW}, FPphasing, and WSVD methods were 4.2%±2.6, 4.6%±3.4, 4.0%±2.6, 4.7%±2.2, 4.0%±2.6, and 4.2%±3.1 respectively. For the cycles with low residual water, for the Wvoxel, NAAcentral, NAAvoxel, GLS_{NAA}, FPphasing, and WSVD methods the values were 3.4%±3.8, 3.7%±2.3, 3.9%±3.4, 8.5%±3.0, 4.6%±3.8, and 3.9%±3.4 respectively. It is important to note that for both cycles, no voxels had lipid peaks equal or greater than mean NAA SNR in NAWM.

For the cycles with high residual water, the RWvoxel and FPphasing had the maximum values and RWcentral was the only method with significantly lower performance. For the 8-channel coil, the average NAA SNR in NAWM for the 3 volunteers for Wvoxel, RWcentral, RWvoxel, GLS_{RW}, FPphasing, and WSVD methods were 17.2, 15.0, 17.5, 16.0, 17.5, and 16.9 respectively, whereas for the 32-channel coil the values were 24.1, 19.8, 24.5, 22.6, 24.4, and 23.9. The performance of each technique relative to the Wvoxel method was -12%, +2%, -7%, +2%, and -1% respectively for the 8-channel coil and -18%, +2%, -6%, +2%, and -1% respectively for the 32-channel coil.

Table 4.3: Mean Raw SNR, Normalized SNR (nSNR : $cm^{-3}min^{-1/2}$) and Percent Change compared to Wvoxel Values for All Techniques for NAA in 3 Volunteers*

8-Chennel							
Cycle w/ rWater				Cycle w/o rWater			
Methods	SNR	%	nSNR	Methods	SNR	%	nSNR
Wvoxel	17.2±1.9	-	9.9±1.1	Wvoxel	18.1±1.3	—	10.4±0.8
RWvoxel	17.5±1.9	+2%	10.1±1.1	NAAvoxel	17.7±1.6	-2%	10.5±0.9
GLS_{RW}	16.0±1.7	-7%	9.3±1.0	GLS_{NAA}	9.2±1.2	-49%	5.3±0.7
FPphasing	17.5±1.9	+2%	10.1±1.1	FPphasing	17.±1.1	-2%	10.2±0.6
WSVD	16.9±1.9	-1%	9.8 ±1.1	WSVD	17.3±1.5	-5%	9.9±0.9
RWcentral	15.0±1.9	-13%	8.7±1.1	NAAcentral	15.9±1.4	-12%	9.2±0.8
32-Chennel							
Wvoxel	24.1±2	-	13.9±1.2	Wvoxel	25.3±2	—	14.6±1.2
RWvoxel	24.5±2	+2%	14.1±1.3	NAAvoxel	24.8±2	-2%	14.3±1.4
GLS_{RW}	22.6±3	-6%	13.0±1.5	GLS_{NAA}	14.2±4	-44%	8.2±2.6
FPphasing	24.4±2	+2%	14.1±1.3	FPphasing	23.1±1	-8%	13.3±0.6
WSVD	23.9±2	-1%	13.8±1.3	WSVD	24.4±2	-3%	14.1±1.0
RWcentral	19.8±1	-18%	11.4±0.9	NAAcentral	20.6±2	-19%	11.9±1.1
+40%				+ 40%			

*Standard deviation between the 3 volunteers is shown as mean±SD.

For the cycles with low residual water, the maximal SNR value was obtained from the Wvxoel combination. The NAAcentral and GLS_{NAA} methods both performed poorly. For the 8-channel coil, the average NAA SNR in NAWM for the 3 volunteers for the Wvoxel, NAAcentral, NAAvoxel, GLS_{NAA}, FPphasing, and WSVD methods were 18.1, 15.9, 17.7, 9.2, 17.7, and 17.3 respectively, whereas for the 32-channel coil the values were 25.3, 20.6, 24.8, 14.2, 23.1, and 24.4. The performance of each technique relative to the Wvoxel method was -12%, -2%, -49%, -2%, -5% and -19%, -2%, -44%, -8%,-3% respectively for the 8- and 32-channel coils.

4.4.5 Impact of the Magnitude of Residual Water

Given that the lactate-edited data had one cycle with large residual water and one cycle with very little water, it was possible to simulate single-cycle datasets with intermediate residual water peaks by adding different combinations of the cycles together. Figure 4.12 shows the impact of the amount of residual water left in the dataset on the NAA SNR for the RWvoxel, RWcentral, GLS_{RW}, FPphasing, and WSVD methods. This result indicates that modifying the sequence acquisition parameters to leave residual water at least 10-15

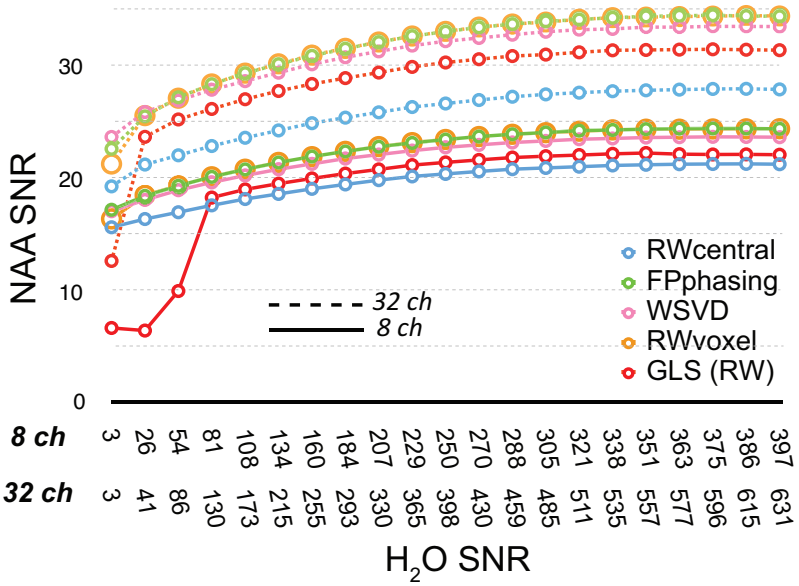

Figure 4.12: The performance of all the techniques in terms of SNR for one volunteers with different levels of residual water (simulated) for both receive coils.

times higher than NAA would obviate the need for a reference scan for both head coils and stabilize the performance of the techniques.

4.4.6 Application to Patients with Brain Tumors

The challenge for clinical applications is to have a robust method for distinguishing variations in metabolite levels in different regions of the brain within a modest acquisition time. Figure 4.13 summarizes the performance of the methods described above for voxels from NAWM for 105 lactate-edited datasets from 55 patients with brain tumors.

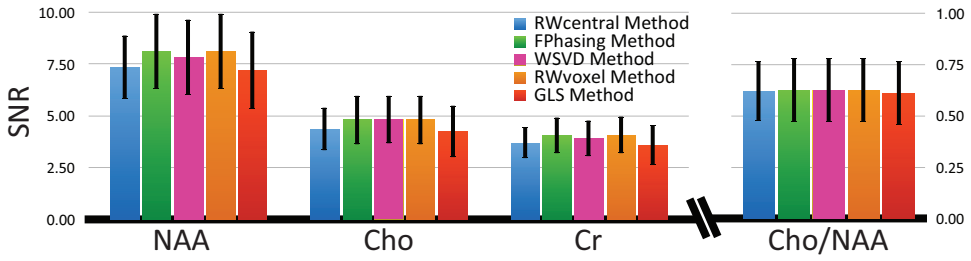

Figure 4.13: The average nSNR of 3 main metabolites and their ratios in NAWM from 55 patients (105 exams) with brain tumor are shown in different color bars representing each technique.

For the reference methods, the combination parameters were estimated from the cycle with the larger residual water. Overall, the performance was similar to that in normal volunteers, even though a wide range of selected volumes, patient ages, and disease states were included. The improvement in SNR for RWvoxel was more noticeable for volumes larger than 720 *cc*,

with a 4% increase at 200 *cc*, 10% increase at 700 *cc*, and 14% increase at 1500 *cc* for the RWvoxel method relative to the RWcentral method. The WSVD method gave a more modest improvement in SNR for larger selected volumes. It is important to note that the results being reported are from within the NAWM, which lies more in the central region than periphery of the brain. Figure 4.15 shows an example of 16 voxels of lactate-edited data from a region of T_2-hyperintensity for the various combination techniques in a patient with a brain tumor. Differences in the pattern of metabolite levels are clearly visible in the area of T_2-hyperintensity and contrast enhancement. Although the choline is significantly increased relative to creatine and NAA in these voxels, all methods that used the residual water for coil combination produced similar average metabolite ratios.

An added complication for applying methods that use the whole spectrum rather than reference peaks to estimate phase corrections for patient data is the increased likelihood of lipid artifacts, due to either prior surgery or the lesion being in a location that is difficult to cover using PRESS volume selection. Figure 4.14 demonstrates the influence of lipid contamination on the quality of the WSVD algorithm when there is low residual water. While the method performed well in some voxels, regions near the lesion have lipid contamination that caused the coil weightings and phases to be inconsistent and led to low intensity spectra in regions of tumor. The combined spectra in Figure 4.14 that were obtained using WSVD had good SNR for voxels a and b, but voxels c and d lacked any signal (magenta spectra). This is due to large lipid signals in channels 1 and 8 of the uncombined spectra that impact the overall estimation. After lipid removal, the performance of the WSVD algorithm was improved in voxels c and d, but degraded for voxel b (black spectra). An examination of the individual channel data showed that the HSVD lipid removal algorithm (42) did not perform well in voxel b for channels 1 and 8 so that these voxels ended up with higher lipid levels than in the original data. For voxels c and d, where the lipid was successfully removed, the combined spectra improved.

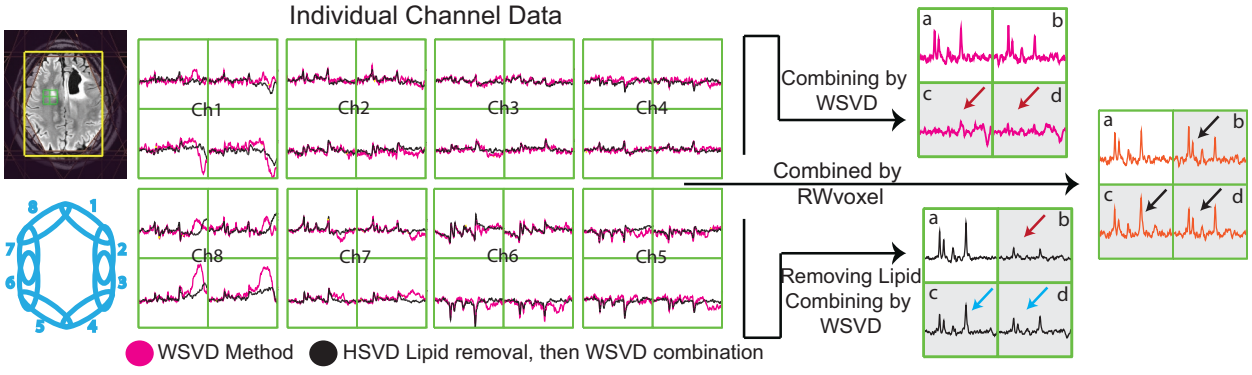

Figure 4.14: Impact of the lipid contamination on WSVD combination with imperfect solution.

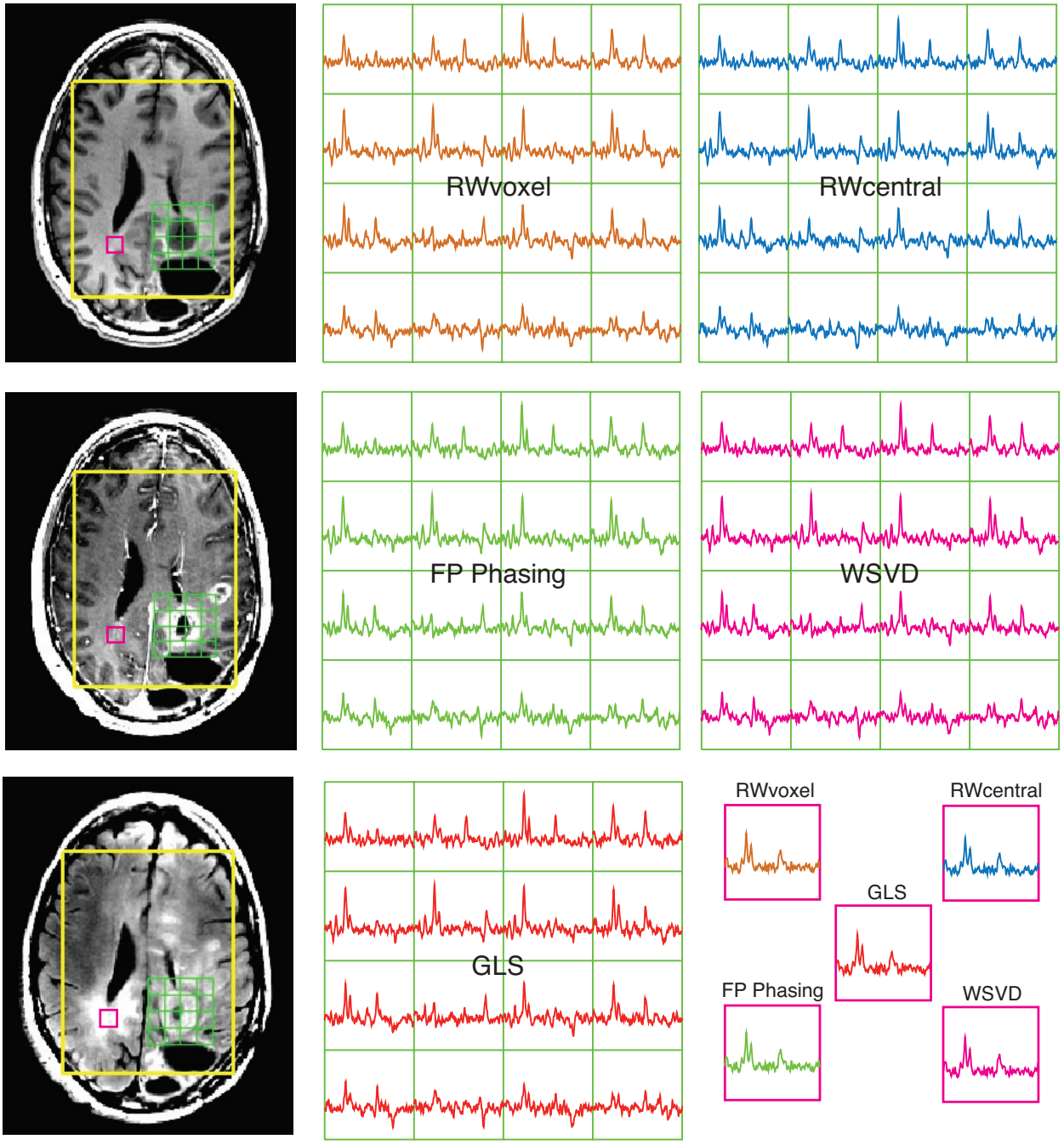

Figure 4.15: Combined spectra from all presented techniques. Pre and post-gadoliniumT1-weighted, fluid-attenuated inversion recovery (FLAIR) and partial MRSI data from a patient with grade IV is shown. The combined spectra from each technique for 16 voxels around the tumor region are displaced in corresponding colors with additional one voxel from contra lateral region. In the presence of sufficient residual water, all methods produced consistent metabolite levels and ratios.

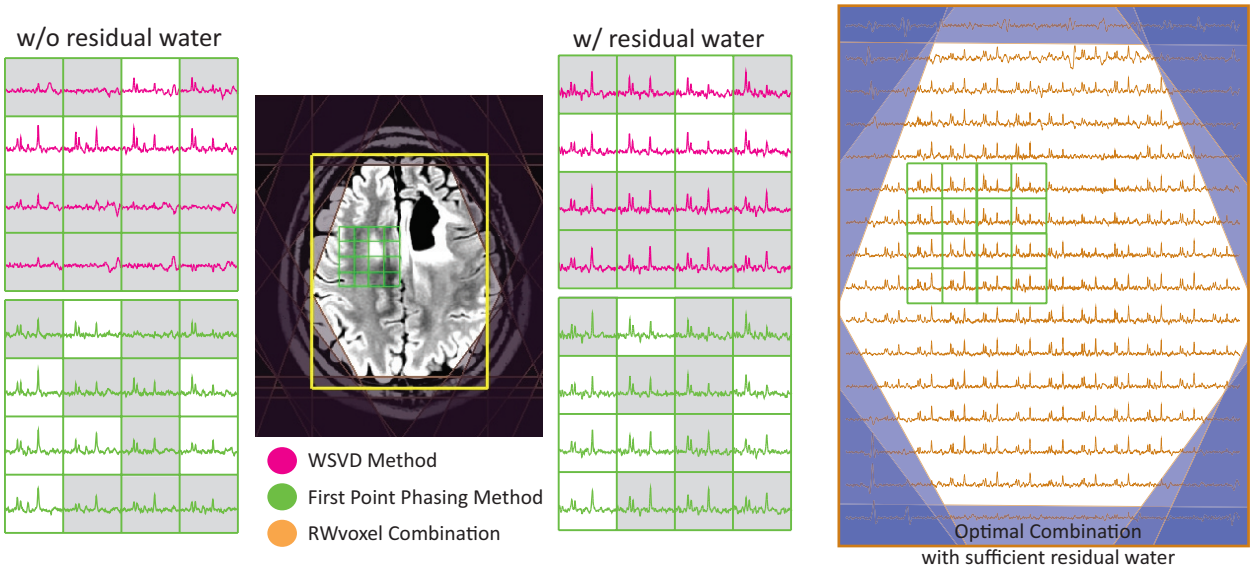

Figure 4.16: Outcome of the WSVD and FPphasing on patients with large lipid contamination with practical solution.

A better solution is to add sufficient residual water to recover some of the missing signals in these voxels and make both WSVD and FPphasing less sensitive to lipid artifacts as shown in Figure 4.16. Several spectra from some of the most interesting regions near the lesions are shown for WSVD and FPphasing algorithms with and without sufficient residual water. The presence of a large lipid signal results in a lack of metabolite signals in the combined spectra in voxels where there was an absence of a large reference peak such as residual water or NAA. This was improved when sufficient residual water was added (voxels with the most improvement are shaded gray for direct comparison).

Tabel 4.4 shows mean normalized SNR of NAA from NAWM in 51 patients (105 scans) for all techniques possible along with percentage of voxels containing aliased lipid. Voxels were considered to either have normal amount of aliased lipid if the lipid SNR was greater than 25% of the mean SNR of NAA in NAWM or extreme amount of aliased lipid if the lipid SNR was equal or greater than the mean SNR of NAA in NAWM. The latter case influences the result of WSVD and FPphasing combination significantly and causes them to fail in many voxels. The patient that is used as an example in Figure 4.14 and 4.16 to illustrate the visual differences among the methods only had extreme lipid contamination in 2% of its voxels. 30% of the patient data sets had extreme lipid contamination in 1% to 87% of their voxels. Within that cohort, for cycles with low residual water the mean±SD percentage of voxels with lipid peaks equal or greater than mean NAA SNR in NAWM for WSVD and FPphasing methods were 15.1%±20.2, and 8.3%±9.7 respectively with detectable voxels of 78.2%±20.5 and 80.3%±13.00 respectively. However, If the combination parameters were estimated from the cycles with high residual water (RWvoxel method), the lipid contamina-

Table 4.4: Mean Normalized SNR (nSNR : $cm^{-3}min^{-1/2}$) Values for All Combination Techniques for NAA in Patients*

Cycle w/ rWater				Cycle w/o rWater			
Methods	nSNR	% voxels (Lip>25%NAA)	% voxels (Lip≥NAA)	Methods	nSNR	% voxels (Lip>25%NAA)	% voxels (Lip≥NAA)
RWvoxel	8.0±1.5	25.4±19.9	1.4±3.7	NAAvoxel	—	—	—
GLS_{RW}	7.8±1.5	26.1±20.4	1.2±3.5	GLS_{NAA}	—	—	—
FPphasing	8.0±1.5	25.4±20.0	1.4±3.9	FPphasing	8.2±1.7	31.3±21.8	2.4±6.3
WSVD	7.7±1.4	25.5±19.4	1.5±3.9	WSVD	8.0±1.8	33.5±23.8	4.3±2.7
RWcentral	7.3±1.3	26.1±19.2	1.1±3.2	NAAcentral	—	—	—
				RWvoxel†	8.6±1.6	28.8±20.9	1.0±2.8

*N=105 exams, 51 Patients.

*Standard deviation between scans are shown as mean±SD.

† Combination parameters estimated from the other cycle.

tion decreased to average of 3.6%±4.2 with higher detection of 88%±10. For the cycles with high residual water the mean±SD percentage of voxels with lipid peaks equal or greater than mean NAA SNR in NAWM for WSVD, FPphasing and RWvoxel methods were 6.3%±5.3, 5.5%±5.9 and 5.8%±5.3 respectively with detectable voxels of 83.4%±11.3, 85.6%±9.6 and 85.6%±9.4 respectively. This is because aliased lipid signals didn't contribute as much to the combination parameters since there was a large reference peak present.

4.5 Discussion

The study presented here addresses the performance of different coil combination methods for 3D single-cycle and lactate-edited multi-channel H-1 PRESS localized EPSI studies from large regions of the brain. Critical requirements are that these methods are robust across various locations, can be used for a wide variety of selected volumes, and can cope with voxels with relatively low SNR. While it is clear that a separate non-water suppressed scan can be used to estimate amplitude factors and phase offsets for individual channels and apply them to the data of interest (Wvoxel), there are many circumstances where limitations on acquisition time make it preferable to do the combination without obtaining an additional scan. Several strategies for achieving this were evaluated, including those that use residual water and NAA peaks as a reference (RWcentral, RWvoxel, GLS_{RW}, NAAvoxel, NAA central, GLS_{NAA} (22), FPphasing (15), and WSVD algorithms (20, 21).

In a previous study, Rodgers et al (20) showed that using WSVD, FPphasing, and Wvoxel all gave good results for analysis of single voxel spectroscopy data obtained from a normal

volunteer using a 3T scanner with 12 receiver elements, but that WSVD gave the best overall performance. In a subsequent study, An et al (22) demonstrated that, for data obtained with a 7T scanner and 32-channel RF coil, the WSVD method was more sensitive than the GLS method to baseline errors that originate from water or lipid signals coming from outside the voxels of interest. This resulted in the GLS method outperforming the WSVD method with respect to the coefficient of variance. It is important to note that in this latter paper, NAA rather than unsuppressed or residual water was used as the reference peak. The results obtained from our analysis of multi-voxel MRSI data from a phantom, which had no lipid contamination and different simulated noise levels, were consistent with these data.

In another recent study, Abdoli et al (32) used a volumetric spin-echo EPSI acquisition with an interleaved water-reference data (TR = $1.71s$, TE = $70ms$ and $T_{acq} = 26min$) to evaluate amplitude weighting and combination strategies for data from normal volunteers. They reported that using the signal, signal-to-noise, and signal-to-noise squared weighting from the water reference scan performed similarly and gave better results than the SVD, WSVD, and GLS combination methods. For the normal volunteers considered in our study we found that using calibration image intensities to estimate amplitude weighting factors gave similar or better results than the non-suppressed water (Wvoxel) or large residual water (RWvoxel) reference peak intensities and the intensities from the FPphasing algorithm. The SNRs obtained from our large patient cohort verified the initial finding that the RWvoxel methods consistently had maximum metabolite SNR.

For the in-vivo analysis of 3D MRSI that included tumor voxels with very little to no NAA and some lipid contamination for voxels within the selected volume, a residual water peak of 10-15 times higher than the NAA in NAWM was found to give robust estimates of phase and amplitude parameters. Note that an overpress factor of 1.5 was used for these data to avoid chemical shift artifacts and spatial variations in the residual water peak on the edge of the selected volume. This meant that there was a residual water peak in almost every voxel of the 3D array for the cycle without the editing pulse. We also showed that, with sufficient residual water, the RWvoxel combination method was the most robust and accurate method, with low computational complexity. The response of these methods to baseline/signal artifacts was variable, but the overall performance became similar if the largest peak in the spectrum was the residual water.

For in-vivo data, the techniques that incorporated spatially varying phase offsets outperformed the RWcentral and NAAcentral methods, which assumed a constant offset between channels. Voxel-by-voxel phase correction was especially important for coils with higher numbers of elements and for larger excitation volumes. Among the voxel-by-voxel correction techniques, the RWvoxel and FPphasing methods performed better than the WSVD and GLS_{RW} methods. This behavior was consistent among all volunteer exams, but different from that obtained in the phantom study, mainly due to baseline errors and lipid contamination. In the absence of a strong residual water peak, the WSVD and FPphasing methods

suffered due to the presence of large lipid signals from outside the voxel of interest, but the distinction between these two algorithms is that FPphasing uses information from an average of all the points to estimate phases and weights while WSVD uses each of the data points individually.

The impact of the different coil geometries on the spatial variation of phase offset was studied using deviation maps that were calculated from the non-suppressed water acquisition. In the center of the selected volume these offsets were relatively constant, but the between-channel deviation increased for voxels nearer to the coils up to an average of 94° - 89° and was larger for the 32- versus the 8-channel coil. The accuracy of the combination methods depends on the quality of the phase and amplitude maps that are estimated either implicitly or explicitly. One way to compare the methods is to look at the consistency of the phases and weights in different datasets compared to the unsuppressed water reference scan. We showed empirically that adding sufficiently high levels of residual water will make these maps very similar to those calculated from the unsuppressed water scan reference. To test the sensitivity of the maps to differences in coil loading, we compared results from three volunteer scans and showed that the amplitude varied by factors of 2 to 10 while the phase varied from 5° to 40°. This suggests that between subject variations in coil loading is significant and extrapolating from phantom or other previously acquired data may be unreliable.

The spectroscopic data used in this study were acquired with 8 and 32 channel RF coils at 3T with PRESS localization using an overpress factor of 1.2 for single-cycle or 1.5 for lactate editing data, with CHESS pulses for water suppression, and VSS pulses for suppression of unwanted signals outside the region of interest. Even with these conservative strategies, it was observed that there were unsuppressed residual lipid resonances in some of the voxels from the 3D array. In some cases this was due to the point spread function (PSF) of the phase encoding method and in other cases to artifacts or physical motion. Lipid contamination from signals outside the prescribed voxel resulted in suboptimal combination for the WSVD and FPphasing methods. When processing in-vivo data, it may therefore be better to employ a combination technique that suppresses such artifacts, even if it sacrifices some SNR in the combined spectra.

Previous studies have also proposed a number of methods for reducing or removing unwanted lipid by post-processing approaches such as time domain fitting (48), data extrapolation (49), or using the sensitivity information of the 8-channel phased array coil and SENSE to unalias the lipid resonances (50). In this study, we applied non-iterative time-domain fitting with the Lanczos-based version of the HSVD method to reduce the outer volume lipid signals (42). The results obtained demonstrated that this provided improved results in some voxels but in others made the situation worse. Our analysis suggested that the WSVD algorithm cannot robustly combine channels when the unwanted lipid signal is at a level comparable in magnitude to the true metabolite signals. In a recent paper by Rodgers et al (21), it was suggested that this could be avoided by either reducing the acquisition bandwidth so the

contaminating signals are not recorded, or by zeroing the signal for the range of chemical shifts around the contaminated signal before applying the WSVD combination method. This is not a practical solution for brain tumors, as the presence of high lipid can provide evidence for apoptosis or necrosis and it is important to be able to detect these peaks for voxels within the tumor. However, modifying the acquisition parameters to leave sufficient residual water seems to be a more effective solution.

4.6 Summary and Conclusion

The most common methods proposed for coil combination have been applied to multi-voxel single-cycle and lactate-edited PRESS localized EPSI data from the brain obtained with two different head coils (8- and 32-channel). Results obtained in volunteers and from a large cohort of patients with brain tumors indicate that the method which employed large residual water peaks to estimate voxel-by-voxel phase offsets for each channel, is able to outperform more sophisticated algorithms. This is based on our analysis of SNR and coefficient of variance of NAA in normal-appearing white matter. Although WSVD was shown to be a viable technique for analyzing spectra with small selected volumes and limited lipid contamination, it was not a robust choice for evaluating multi-voxel spectra from larger regions of the brain. While the GLS method was less sensitive to these issues and performed well in terms of the coefficient of variance, it provided a lower average SNR.

4.7 References

1. I. Park, G. Tamai, M. C. Lee, C. F. Chuang, S. M. Chang, M. S. Berger, S. J. Nelson, and A. Pirzkall, "Patterns of Recurrence Analysis in Newly Diagnosed Glioblastoma Multiforme After Three-Dimensional Conformal Radiation Therapy With Respect to Pre–Radiation Therapy Magnetic Resonance Spectroscopic Findings," *International Journal of Radiation Oncology*Biology*Physics*, vol. 69, pp. 381–389, Oct. 2007.

2. A. Laprie, I. Catalaa, E. Cassol, T. R. McKnight, D. Berchery, D. Marre, J.-M. Bachaud, I. Berry, and E. C.-J. Moyal, "Proton Magnetic Resonance Spectroscopic Imaging in Newly Diagnosed Glioblastoma: Predictive Value for the Site of Postradiotherapy Relapse in a Prospective Longitudinal Study," *International Journal of Radiation Oncology*Biology*Physics*, vol. 70, pp. 773–781, Mar. 2008.

3. B. Wei, I. S. Khayal, J. M. Lupo, C. McGue, S. Vandenberg, K. R. Lamborn, S. M. Chang, S. Cha, and S. J. Nelson, "Multiparametric Characterization of Grade 2 Glioma Subtypes Using Magnetic Resonance Spectroscopic, Perfusion, and Diffusion Imaging," *Translational Oncology*, vol. 2, pp. 271–280, Dec. 2009.

4. S. J. Nelson, "Assessment of therapeutic response and treatment planning for brain tumors using metabolic and physiological MRI," *NMR in Biomedicine*, Apr. 2011.

5. E. Ozturk-Isik, A. Pirzkall, K. R. Lamborn, S. Cha, S. M. Chang, and S. J. Nelson, "Spatial Characteristics of Newly Diagnosed Grade 3 Glioma Assessed by Magnetic Resonance Metabolic and Diffusion Tensor Imaging," *Translational Oncology*, vol. 5, pp. 10–18, Feb. 2012.

6. S. J. Nelson, "Multivoxel magnetic resonance spectroscopy of brain tumors.," *Molecular cancer therapeutics*, vol. 2, pp. 497–507, May 2003.

7. X. Li, H. Jin, Y. Lu, J. Oh, S. Chang, and S. J. Nelson, "Identification of MRI and1H MRSI parameters that may predict survival for patients with malignant gliomas," *NMR in Biomedicine*, vol. 17, pp. 10–20, Mar. 2004.

8. J. Oh, R. G. Henry, A. Pirzkall, Y. Lu, X. Li, I. Catalaa, S. Chang, W. P. Dillon, and S. J. Nelson, "Survival analysis in patients with glioblastoma multiforme: Predictive value of choline-to-n-acetylaspartate index, apparent diffusion coefficient, and relative cerebral blood volume," *Journal of Magnetic Resonance Imaging*, vol. 19, no. 5, pp. 546–554, 2004.

9. T. R. McKnight, S. M. Noworolski, D. B. Vigneron, and S. J. Nelson, "An automated technique for the quantitative assessment of 3D-MRSI data from patients with glioma.," *Journal of Magnetic Resonance Imaging*, vol. 13, pp. 167–177, Dec. 2000.

10. M. Muruganandham, P. P. Clerkin, B. J. Smith, C. M. Anderson, A. Morris, A. A. Capizzano, V. Magnotta, S. M. McGuire, M. C. Smith, J. E. Bayouth, and J. M. Buatti, "3-Dimensional Magnetic Resonance Spectroscopic Imaging at 3 Tesla for Early Response Assessment of Glioblastoma Patients During External Beam Radiation Therapy," *Radiation Oncology Biology*, vol. 90, pp. 181–189, Sept. 2014.

11. Y. Li, J. M. Lupo, R. Parvataneni, K. R. Lamborn, S. Cha, S. M. Chang, and S. J. Nelson, "Survival analysis in patients with newly diagnosed glioblastoma using pre- and postradiotherapy MR spectroscopic imaging," *Neuro Oncology*, vol. 15, pp. 607–617, Apr. 2013.

12. S. M. Wright and L. L. Wald, "Theory and application of array coils in MR spectroscopy.," *NMR in Biomedicine*, vol. 10, pp. 394–410, Dec. 1997.

13. L. L. Wald, S. E. Moyher, M. R. DAY, S. J. Nelson, and D. B. Vigneron, "Proton Spectroscopic Imaging of the Human Brain Using Phased-Array Detectors," *Magnetic Resonance in Medicine*, vol. 34, pp. 440–445, Sept. 1995.

14. T. Schaffter, P. Bornert, C. Leussler, I. C. Carlsen, and D. Leibfritz, "Fast H-1 spectroscopic imaging using a multi-element head-coil array," *Magnetic Resonance in Medicine*, vol. 40, pp. 185–193, Aug. 1998.

15. M. A. Brown, "Time-domain combination of MR spectroscopy data acquired using phased-array coils," *Magnetic Resonance in Medicine*, vol. 52, pp. 1207–1213, Nov. 2004.

16. J. P. Debbins, J. P. Felmlee, and S. J. Riederer, "Phase alignment of multiple surface coil data for reduced bandwidth and reconstruction requirements.," *Magnetic Resonance in Medicine*, vol. 38, pp. 1003–1011, Dec. 1997.

17. N. Sandgren, P. Stoica, F. J. Frigo, and Y. Selén, "Spectral analysis of multichannel MRS data," *Journal of Magnetic Resonance*, vol. 175, pp. 79–91, July 2005.

18. M. Bydder, G. Hamilton, T. Yokoo, and C. B. Sirlin, "Optimal phased-array combination for spectroscopy," *Magnetic Resonance Imaging*, vol. 26, pp. 847–850, July 2008.

19. N. Martini, M. F. Santarelli, G. Giovannetti, M. Milanesi, D. De Marchi, V. Positano, and L. Landini, "Noise correlations and SNR in phased-array MRS," *NMR in Biomedicine*, vol. 23, pp. 66–73, Jan. 2010.

20. C. T. Rodgers and M. D. Robson, "Receive array magnetic resonance spectroscopy: Whitened singular value decomposition (WSVD) gives optimal Bayesian solution," *Magnetic Resonance in Medicine*, vol. 63, pp. 881–891, May 2010.

21. C. T. Rodgers and M. D. Robson, "Coil combination for receive array spectroscopy: Are data-driven methods superior to methods using computed field maps?," *Magnetic Resonance in Medicine*, Mar. 2015.

22. L. An, J. Willem van der Veen, S. Li, D. M. Thomasson, and J. Shen, "Combination of multichannel single-voxel MRS signals using generalized least squares," *Journal of Magnetic Resonance Imaging*, vol. 37, pp. 1445–1450, Nov. 2012.

23. E. L. Hall, M. C. Stephenson, D. Price, and P. G. Morris, "Methodology for improved detection of low concentration metabolites in MRS: Optimised combination of signals from multi-element coil arrays," *NeuroImage*, vol. 86, pp. 35–42, Feb. 2014.

24. O. Natt, V. Bezkorovaynyy, T. Michaelis, and J. Frahm, "Use of phased array coils for a determination of absolute metabolite concentrations," *Magnetic Resonance in Medicine*, vol. 53, no. 1, pp. 3–8, 2004.

25. S. A. Wijtenburg and J. Knight-Scott, "Reconstructing very short TE phase rotation spectral data collected with multichannel phased-array coils at 3 T," *Magnetic Resonance Imaging*, vol. 29, pp. 937–942, Sept. 2011.

26. N. I. Avdievich, J. W. Pan, J. M. Baehring, D. D. Spencer, and H. P. Hetherington, "Short echo spectroscopic imaging of the human brain at 7T using transceiver arrays," *Magnetic Resonance in Medicine*, vol. 62, pp. 17–25, July 2009.

27. Z. Dong, "Proton MRS and MRSI of the brain without water suppression," *Progress in Nuclear Magnetic Resonance Spectroscopy*, vol. 86-87, pp. 65–79, Apr. 2015.

28. A. A. Maudsley, C. Domenig, V. Govind, A. Darkazanli, C. Studholme, K. Arheart, and C. Bloomer, "Mapping of brain metabolite distributions by volumetric proton MR spectroscopic imaging (MRSI)," *Magnetic Resonance in Medicine*, vol. 61, pp. 548–559, Mar. 2009.

29. C. Gasparovic, T. Song, D. Devier, H. J. Bockholt, A. Caprihan, P. G. Mullins, S. Posse, R. E. Jung, and L. A. Morrison, "Use of tissue water as a concentration reference for proton spectroscopic imaging," *Magnetic Resonance in Medicine*, vol. 55, no. 6, pp. 1219–1226, 2006.

30. Z. Dong and B. Peterson, "The rapid and automatic combination of proton MRSI data using multi-channel coils without water suppression.," *Magnetic Resonance Imaging*, vol. 25, pp. 1148–1154, Oct. 2007.

31. N. Maril and R. E. Lenkinski, "An automated algorithm for combining multivoxel MRS data acquired with phased-array coils," *Journal of Magnetic Resonance Imaging*, vol. 21, no. 3, pp. 317–322, 2005.

32. A. Abdoli and A. A. Maudsley, "Phased-array combination for MR spectroscopic imaging using a water reference," *Magnetic Resonance in Medicine*, Sept. 2015.

33. L. Fang, M. Wu, H. Ke, A. Kumar, and S. Yang, "Adaptively optimized combination (AOC) of magnetic resonance spectroscopy data from phased array coils," *Magnetic Resonance in Medicine*, July 2015.

34. M. Uecker, P. Lai, M. J. Murphy, P. Virtue, M. Elad, J. M. Pauly, S. S. Vasanawala, and M. Lustig, "ESPIRiT-an eigenvalue approach to autocalibrating parallel MRI: Where SENSE meets GRAPPA," *Magnetic Resonance in Medicine*, vol. 71, pp. 990–1001, May 2013.

35. L. Yaan, J. A. Osorio, E. Ozturk-Isik, A. P. Chen, D. Xu, J. C. Crane, S. Cha, S. Chang, M. S. Berger, D. B. Vigneron, and S. J. Nelson, "Considerations in applying 3D PRESS H-1 brain MRSI with an eight-channel phased-array coil at 3 T," *Magnetic Resonance Imaging*, vol. 24, pp. 1295–1302, Dec. 2006.

36. I. Park, A. P. Chen, M. L. Zierhut, E. Ozturk-Isik, D. B. Vigneron, and S. J. Nelson, "Implementation of 3 T Lactate-Edited 3D 1H MR Spectroscopic Imaging with Flyback Echo-Planar Readout for Gliomas Patients," *Annals of Biomedical Engineering*, vol. 39, pp. 193–204, July 2010.

37. E. Ozhinsky, *Automated Acquisition of Brain MRSI Data*. PhD thesis, University of California San Francisco, 2012.

38. E. Ozhinsky, D. B. Vigneron, S. M. Chang, and S. J. Nelson, "Automated prescription of oblique brain 3D magnetic resonance spectroscopic imaging," *Magnetic Resonance in Medicine*, vol. 69, pp. 920–930, June 2012.

39. E. Ozhinsky, D. B. Vigneron, and S. J. Nelson, "Improved spatial coverage for brain 3D PRESS MRSI by automatic placement of outer-volume suppression saturation bands," *Journal of Magnetic Resonance Imaging*, vol. 33, pp. 792–802, Mar. 2011.

40. Bian, W, L. Yaan, J. C. Crane, and S. J. Nelson, "Towards Robust Reproducibility Study for MRSI via Fully Automated Reproducible Imaging Positioning ," *Proc 23rd Scientific Meetin & Exhibition (ISMRM)*, p. 1, 2015.

41. S. J. Nelson, "Analysis of volume MRI and MR spectroscopic imaging data for the evaluation of patients with brain tumors," *Magnetic Resonance in Medicine*, vol. 46, no. 2, pp. 228–239, 2001.

42. W. W. F. Pijnappel, A. van den Boogaart, R. DeBeer, and D. Van Ormondt, "SVD-based quantification of magnetic resonance signals," *Journal of Magnetic Resonance*, vol. 97, pp. 122–134, Jan. 1992.

43. L. Yaan, R. Srinivasan, H. Ratiney, Y. Lu, S. M. Chang, and S. J. Nelson, "Comparison of T1 and T2 metabolite relaxation times in glioma and normal brain at 3T," *Journal of Magnetic Resonance Imaging*, vol. 28, pp. 342–350, Aug. 2008.

44. M. L. Zierhut, E. Ozturk-Isik, A. P. Chen, I. Park, D. B. Vigneron, and S. J. Nelson, "1H spectroscopic imaging of human brain at 3 Tesla: Comparison of fast three-dimensional magnetic resonance spectroscopic imaging techniques," *Journal of Magnetic Resonance Imaging*, vol. 30, pp. 473–480, Sept. 2009.

45. M. Jenkinson, P. Bannister, M. Brady, and S. Smith, "Improved Optimization for the Robust and Accurate Linear Registration and Motion Correction of Brain Images," *NeuroImage*, vol. 17, pp. 825–841, Oct. 2002.

46. Y. Zhang, M. Brady, and S. Smith, "Segmentation of brain MR images through a hidden Markov random field model and the expectation-maximization algorithm.," *IEEE transactions on medical imaging*, vol. 20, pp. 45–57, Jan. 2001.

47. G. C. Wiggins, J. R. Polimeni, A. Potthast, M. Schmitt, V. Alagappan, and L. L. Wald, "96-Channel receive-only head coil for 3 Tesla: Design optimization and evaluation," *Magnetic Resonance in Medicine*, vol. 62, pp. 754–762, Sept. 2009.

48. R. DeBeer, F. Michels, D. Van Ormondt, B. Van Tongeren, P. Luyten, and H. Van Vroonhoven, "Reduced Lipid Contamination in in-Vivo H-1 Mrsi Using Time-Domain Fitting and Neural-Network Classification," *Magnetic Resonance Imaging*, vol. 11, no. 7, pp. 1019–1026, 1993.

49. N. Schuff, M. W. Weiner, and A. A. Maudsley, "Removal of lipid artifacts in 1H spectroscopic imaging by data extrapolation," *Magnetic Resonance in Medicine*, 1996.

50. E. Ozturk-Isik, J. C. Crane, S. Cha, S. M. Chang, M. S. Berger, and S. J. Nelson, "Unaliasing lipid contamination for MR spectroscopic imaging of gliomas at 3T using sensitivity encoding (SENSE)," *Magnetic Resonance in Medicine*, vol. 55, no. 5, pp. 1164–1169, 2006.

Chapter 5

Development of Compressed Sensing for MRSI Applications

5.1 Introduction

While MRI is a popular noninvasive medical imaging method due to its capability in providing excellent soft tissues contrast in human body and has its advantages over other medical imaging modalities, it suffers from much longer acquisition times compared to other modalities, such as CT imaging. To reconstruct an image, conventional MRI requires the entire spatial Fourier domain of the image to be sampled according to Nyquist criteria. Rapid sampling in Fourier domain is further limited by MR physical constraints (e.g. gradient strength and slew rate) and human physiological conditions (e.g. avoiding nerve stimulation). There is an increasing interest in speeding up the MRI sampling process to make it more comfortable for patients, compensate for their minor movements, increase end throughput.

Since the data collection has its fundamental limits, many researchers have focused on developing methods to reduce the amount of acquired data without degrading the image quality. These reduced sampling methods are based on the fact that MRI data is redundant, so that the underlying information should be able to be extracted from fewer measurements than traditionally considered necessary by Nyquist rate. The source of these redundancies can be divided to two main categories: (I) the use of multiple receive channels (II) the compressibility of images. One of the most significant clinical impacts of reduced sampling methods has been accomplished by parallel imaging with multiple receiver channels which will be discussed in detail in the next chapter. This can be seen intuitively in Figure 5.1 because combining the signals from the different coils in the array to mimic the modulations (spatial harmonics) that would normally be produced by a phase encoding gradient would provide fewer acquisitions per scan. Another source of redundancy that has been gaining significant attention is the sparsity and compressibility of various MR signals. This effort has been

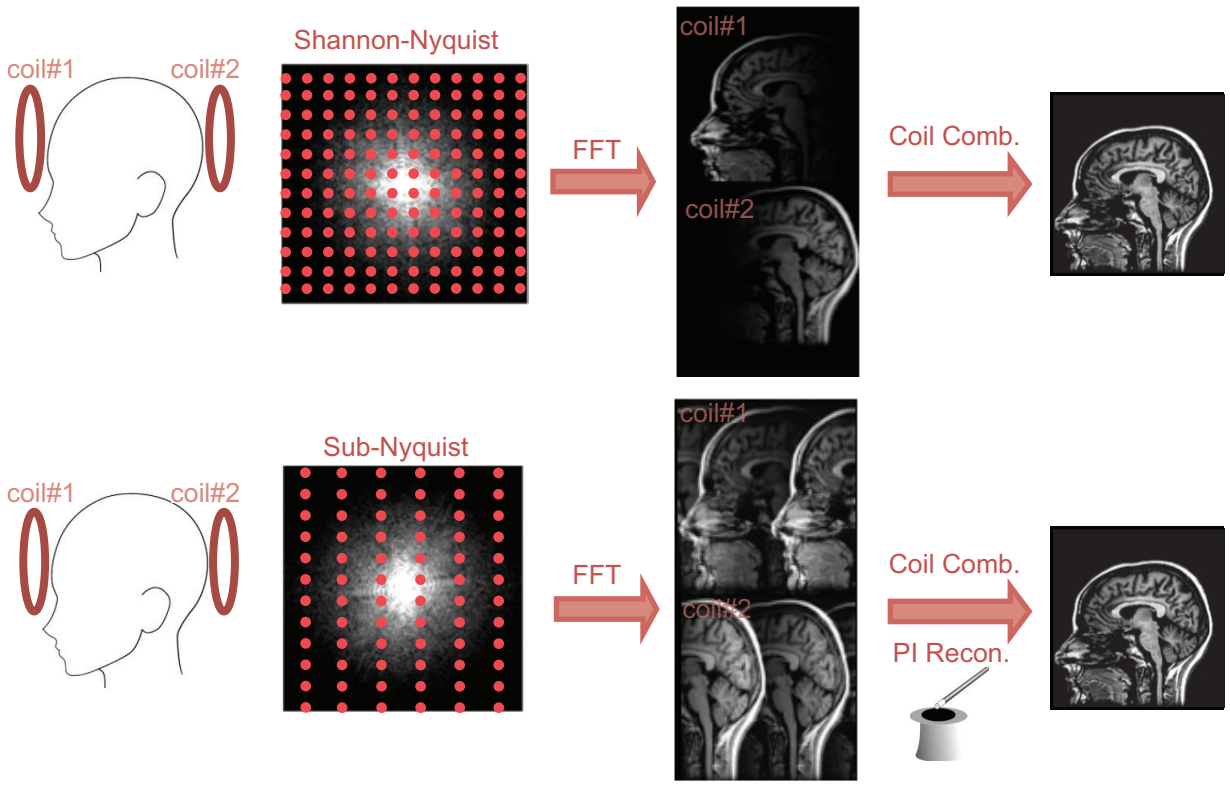

Figure 5.1: Redundancy I: multiple receive channel. Spatial differences in coil sensitivity can reduce the number of gradient encoding steps.

motivated by the fact that images often have a sparse representation in some domain (such as finite difference, wavelet), where the number of coefficients needed to describe the image accurately is significantly less than the number of pixels in the image. This observation is based on the theory of compressed sensing, a general theory for sampling of sparse signal (1–3), but is particularly applicable to MRI. The sparsity is exploited by constraining the reconstruction to have a sparse representation and be consistent with the measured k-space data (Figure 5.2).

Compressed sensing (CS) is a non-traditional signal processing method, which allow us to recover undersampled signal even though the sampling violates the Nyquist criteria. This appealing characteristic makes it a new rapidly growing research topic in MR imaging. It is potentially a technology that provides a new way of thinking about how to acquire and code signals in the most efficient manner. Traditionally, data acquisition typically works by collecting massive amount of data only to be discarded at the compression stage in order to facilitate storage and transmission. One can think of this process as acquiring a high resolution pixel array, computing the complete set of transform coefficients, encoding the largest coefficients and discarding all the others. This is a very wasteful process. What CS

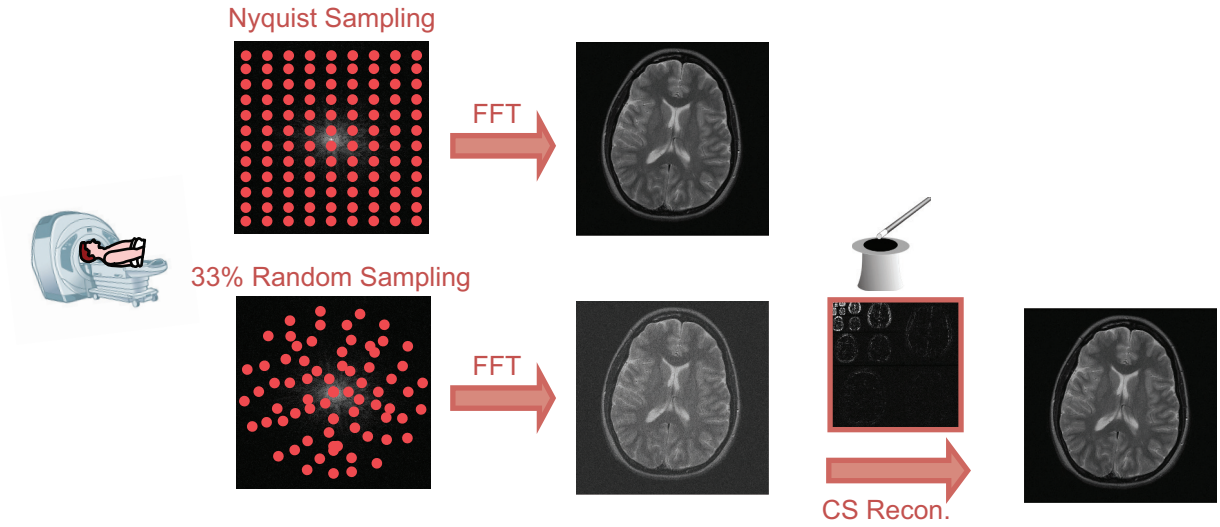

Figure 5.2: Redundancy II: most images are compressible. Images can be described in significantly less number of coefficients in some domain.

does instead, is directly acquire the important information about the object of interest from the beginning. In other words, CS protocols essentially translate analog data into an already compressed digital form so that one can decompress the measured data later.

Once undersampled data are obtained, a concomitant issue is how to reconstruct the signal. Signal reconstruction or recovery is a long existing topic in signal processing, and a number of algorithms have been developed. However, there is no doubt that some modifications must be done to tailor these algorithms to CS data. Signal reconstruction in CS can be converted to a problem of signal denoising once certain undersampling scheme is satisfied. Although optimal undersampling is a key step in CS signal reconstruction, in this chapter, the following discussion will focus more on the reconstruction algorithms that are well suited to be applied for MR image reconstruction.

In this chapter, the theories and shortcomings behind compressed sensing techniques are thoroughly reviewed in the context of MRI applications and are then extended to MRSI applications. The chapter is organized in the following manner: first the theory of CS is introduced with emphasis on the key steps that guarantee the success of CS; followed by an simple 1D example that is provided to illuminate how those ideas in the theory can be applied in practice; finally, three different non-linear reconstruction techniques for CS-MRI are considered: Non-Linear Conjugate Gradient **(NL-CG)**, Stagewise Orthogonal Matching Pursuit **(StOMP)** and Projection Over Convex Sets **(POCS)**. These algorithms are studied, implemented, and applied to a Shepp-Logan phantom and a 2D MRI brain image. The efficiency of these algorithms was compared and are shown in terms of image

reconstruction quality and computation time. The best performed technique is then applied to an MRSI application: "multi-channel spectroscopic imaging reconstruction using water-referencing with compressed sensing"

5.2 Theory of Compressed Sensing

Underlying the most well-known image compression methods such as JPEG, JPEG2000 are the Discrete Wavelet Transform (DWT) and Discrete Cosine Transform (DCT). In practice these methods are used to compress the data soon after capturing (sensing) the image. The transforms are useful because they convert the image content into a vector of sparse coefficients, and the standard strategy is, with some tolerable error, to encode only the most significant coefficients and store them for later decoding. The images are fully reconstructable and with compression they take less space for storage or transmission.

The question that has sparked a lot of research interests in recent years however is, since the data can be compressed after sensing (e.g., by DCT or DWT), is it possible to just acquire less measurements to begin with? According to Candes (1) and Donoho (2), if the underlying image exhibits transform sparsity, and if k-space undersampling results in incoherent artifacts in that transform domain, the image can be recovered from randomly undersampled frequency domain data, provided an appropriate nonlinear reconstruction scheme is used.

When k-space is undersampled, the Nyquist criterion is violated and aliasing artifacts are introduced. As indicated in (4), many schemes have been proposed to deal with the reduced sample data and they all fall into three main categories:

1. Methods generating artifacts that are incoherent at the expense of reduced SNR
2. Methods exploiting redundancy in temporal, spatial or both domains
3. Methods exploiting redundancy in k-space such as parallel imaging

In this chapter the approaches in 1 and 2 are combined. Sparsity in MR images are exploited in a pixel, wavelet or any other possible transform domain. The important condition is that the underlying object that is being recovered needs to have a sparse representation in a known and fixed mathematical transform domain. In Shannon theory the signals are bandlimited and the limited non-zero coefficients are grouped together. In compressed sensing theory the spread of these limited number of non-zero coefficients applies to a more general case (1). In short, to successfully apply Compress Sensing (CS) in MRI, there are three key requirements:

1. **Transform Sparsity:** The image domain or one of its transform has to be sparse.
2. **Incoherence of Undersampling Artifacts:** The aliasing artifacts in a linear reconnstruction of udersampled data must be incoherent (noise-like) in the sparse domain.

3. **Recovery by Solving a Non-Linear Convex Optimization:** The reconstruction methods should enforces both sparsity and data consistency.

Natural images can often be compressed with little or no loss of information which has been demonstrated countlessly by images on the web everyday . As shown in (5), MR images can also be represented using only subset of the largest coefficients by applying a sparsifying transform. This indicate that first requirement is met. The MR acquisition can be designed to achieve incoherent undersampling by carefully designing the gradient waveforms that allow for incoherent measurement of k-space and so the second requirement is also met. There are several efficient and practical schemes proposed for non-linear reconstruction of undersampled data which could fulfill the last requirement. To develop an intuition and deeper understanding of the importance of these three requirements, a very simple 1D example will be considered.

5.3 Intuitive Examples of 1D/2D Signals

This 1D example illustrates the correlation between the compressed sensing and denoising. The main idea in compressive sampling is that the number of samples needed to capture a signal depends primarily on its structural content, rather than its bandwidth. As a concrete example, suppose that $f(n)$ is a discrete signal of length 128 which is composed of 5 complex sinusoids of whose frequencies, phases, and amplitudes are unknown.

The DFT of $f(n)$ has 5 nonzero components as shown in Figure 5.3(a). If there are no restriction on the frequencies in $f(n)$ then any of the 128 components of DFT can be nonzero. According to Shannon/Nyquist criteria to recover this signal via linear *sinc* interpolation, all 128 samples are needed in the time domain.

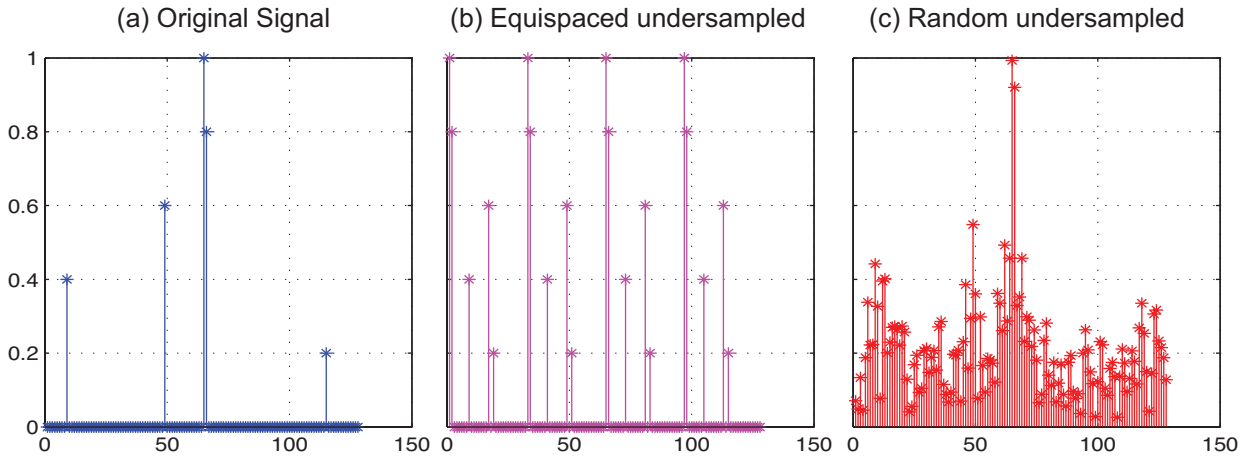

Figure 5.3: An intuitive example of the importance of incoherence undersampling

Now let's assume two sets of 32 samples exist. One set is obtained by equispaced undersampling of f and the other set is obtained by random undersampling. Then the zero-filled inverse Fourier Transform of each set. With equispaced undersampling, this reconstruction generates a superposition of shifted signals resulting in unreversible aliasing distortion. This reconstruction is the ℓ_2 norm solution and recovery is impossible since it is equally likely for each of the replica to be the solution, shown in Figure 5.3(b).

With random undersampling, the zero-filled Fourier reconstruction presents incoherent aliasing that behave like additive random noise. Random undersampling causes energy leakage from each individual nonzero value of the original signal and this energy appears in other reconstructed coefficients. In this example the largest component in the original sparse signal stands above the level of interference and maybe recoverable by appropriate iterative thresholding which suggest a nonlinear reconstruction scheme. So, there is hope for recovering the signal. That is why incoherent undersampling and nonlinear reconstruction are important in compressed sensing. In other words, by random undersampling, the ill-conditioned problem has been turned into a sparse signal denoising problem. Hence, the "noise" is not really noise but incoherent aliasing that is contributed by the signal itself, shown in Figure 5.3(c).

By knowing that the signal of interest is sparse, a different approach can be taken to this problem. Given the 32 observed samples, the set of all 128-length signals with samples matching our observations is an affine subspace of dimension 96 $(128 - 32)$. From the candidate signals in this set, the one whose DFT has minimum ℓ_1 norm is chosen, that is, the sum of the magnitudes of the Fourier transform is the smallest. In doing the original signal is recovered. Figure 5.4(a) shows the original signal and Figure 5.4(b) shows the Fourier transform of randomly undersampled data. Figure 5.4(c,d) illustrates the reconstructed signals that have gone under 300 iterations with two different threshold values.

In general, if there are K sinusoids in the signal, it is possible to recover the signal using ℓ_1 minimization from (on the order of) $K \log n$ samples (1). The framework is easily extended to multidimensional measurements. Suppose that instead of taking m samples in the time domain, the signal is projected onto a randomly chosen m-dimensional subspace. Then if f is K sparse in a known orthobasis, and m is on the order of $K \log n$, f can be recovered without error by solving an ℓ_1 minimization problem.

Before diving into 2D applications and addressing their non-linear reconstruction algorithms in detail, Figure 5.3 summarizes the three essential ingredients for successful compressed sensing approach for MRI applications. Finding the optimal domains where the images are spares are important (Ingredient I). Creating an incoherent aliasing artifact in the image by random sampling is essential (Ingredient II), however, another important aspect of random sampling of 2D signals is matching the power spectrum of the image. Meaning, if the energy is concentrated in lower spatial frequencies (in the case of MR k-space), more samples should be allocated there.

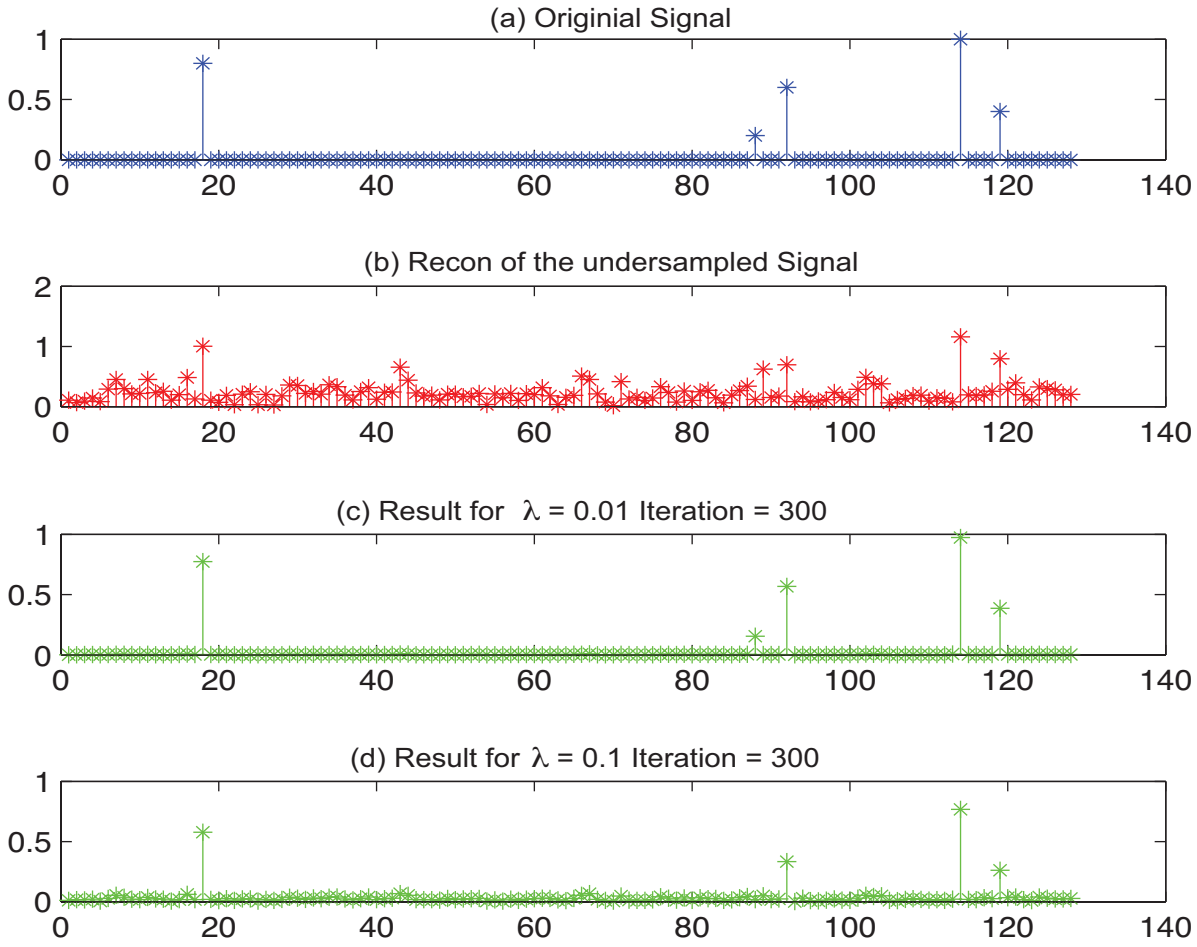

Figure 5.4: An intuitive reconstruction of a sparse signal from random undersampling

To illustrate this point, the zero-field Fourier reconstruction of two randomly undersampled k-space data with same number of samples were compared: one being randomly undersampled from uniform probability distribution function (pdf) (Figure 5.3) and the other from variable density pdf (Figure 5.3). The difference image of each case that are shown in Figure 5.3 and Figure 5.3, suggest the aliasing artifacts is only "white noise" like when the appropriate pdf is chosen for random sampling based on the underlying data. Non-linear reconstructions (Ingredient III) are studied in detail in the following chapter.

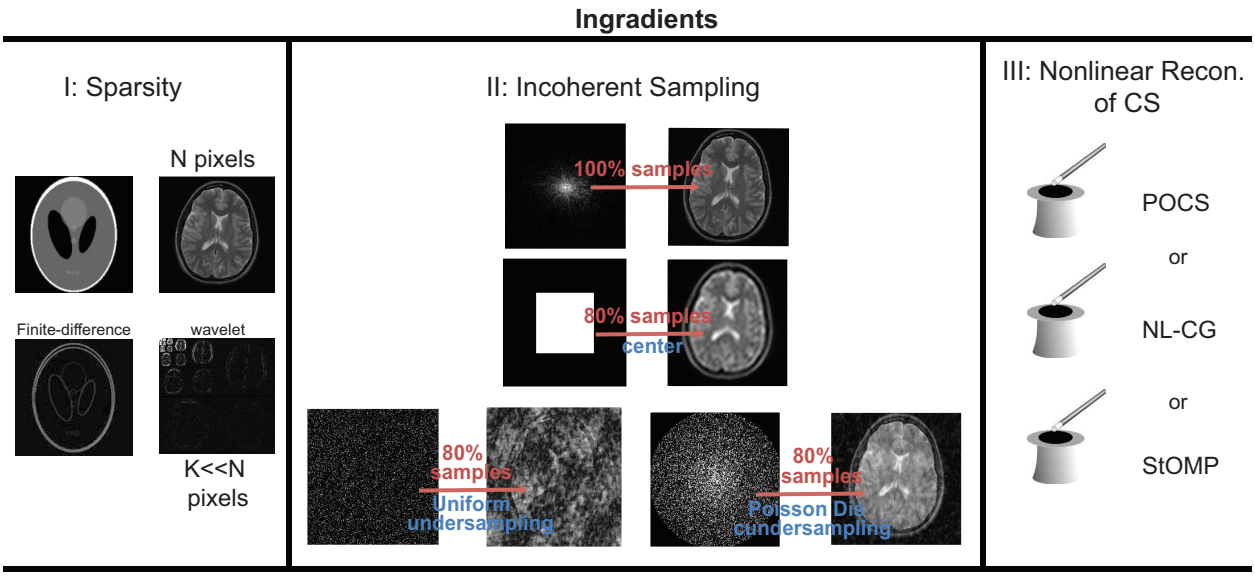

Figure 5.5: Three essential ingredients of successful compressed sensing for MRI images.

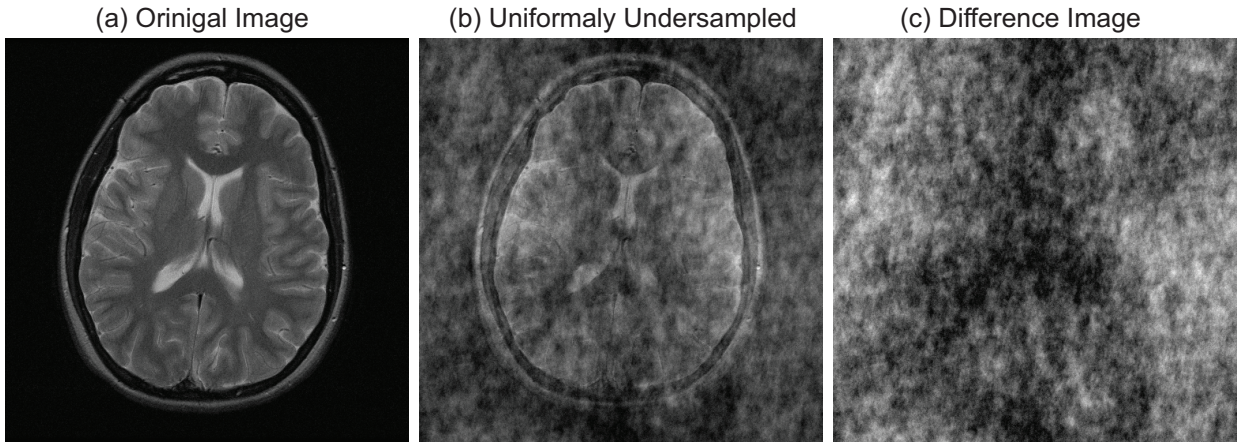

Figure 5.6: Randomly undersampled k-space by uniform pdf

5.4 Compressed Sensing Reconstruction Methods for MRI Images

An underdetermined system of linear equations ($y = \Psi x$) has more unknowns than equations and generally has an infinite number of solutions. In order to choose a unique solution to such a system, one must impose extra constraints or conditions. In the compressed sensing framework, as shown in Figure 5.8, one adds the constraint of sparsity, allowing only solutions which have a small number of nonzero coefficients. Not all underdetermined systems of

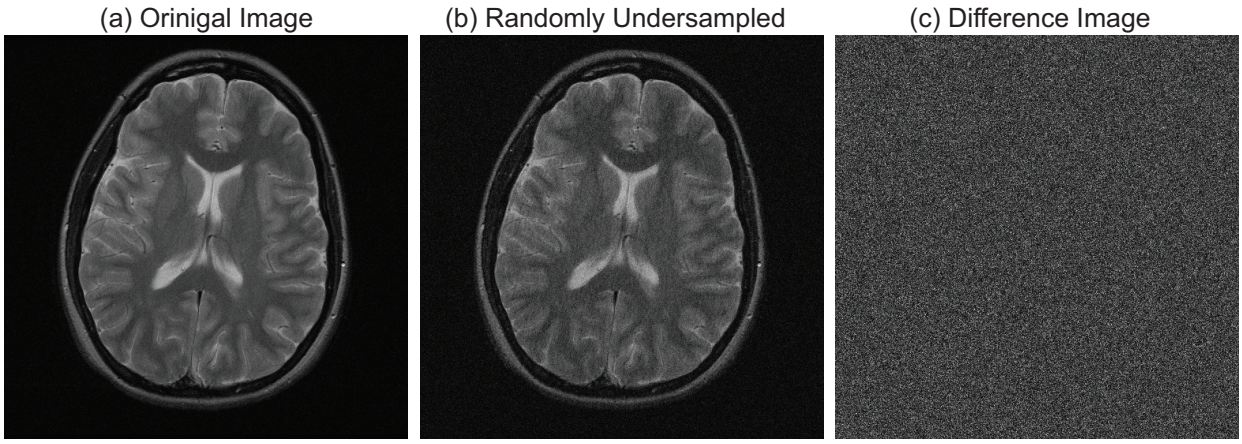

Figure 5.7: Randomly undersampled k-space by gaussian pdf

linear equations have a sparse solution. However, if there is a unique sparse solution to the underdetermined system, then the compressed sensing framework allows the recovery of that solution.

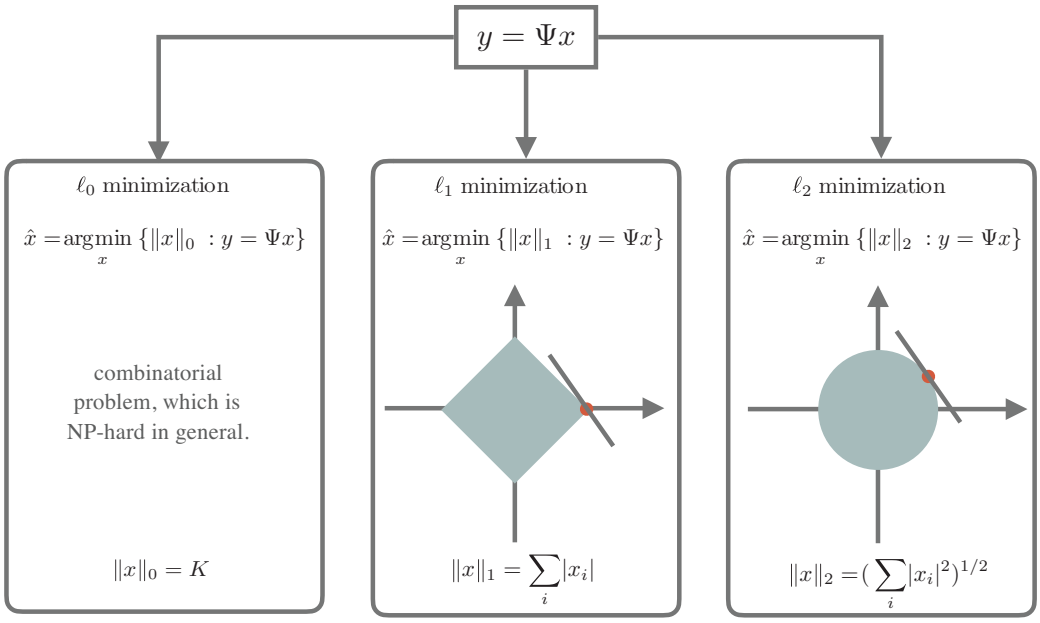

Figure 5.8: Unique sparse solution (ℓ_0,ℓ_1,ℓ_2 minimization) to underdetermined system of $y = \Psi x$

Let's assume x is a vector $[n \times 1]$ with K non-zero coefficients, Ψ is a matrix $[m \times n]$, and y is vector $[m \times 1]$. As an engineer, we may try to use least-squares i.e., to find the minimum ℓ_2 norm solution since ℓ_2 minimization has a closed form solution, provides minimum energy,

and the algorithm is very fast. Unfortunately, in doing one is looking for the intersection of a sphere and a plane, which will most likely not be on a coordinate axis where sparse solutions lie.

The next approach is to minimize cardinality by ℓ_0 minimization which is number of non-zero coefficients. So, if we look for the minimum ℓ_0 solution, we will find the original signal but unfortunately, looking for such a solution is a combinatorial problem, which is NP-hard in general. However, for most large underdetermined equations we can obtain the same answer as the minimum ℓ_0 norm, for a trade off of acquiring ($m = K\log(n)$) measurements rather than ($m >= K$) measurements and minimizing ℓ_1 norm (6).

Looking for the minimum ℓ_1 solution is a convex optimization problem, which can be solved numerically very efficiently. Intuitively, using ℓ_1, we are looking for the intersection of a plane and a polyhedron. we can think of the polyhedron as being "peaky", so this time the intersection will most likely lie on an axis.

Many schemes can be found which implement different algorithms performing the ℓ_1 minimization. For example, one reconstruction can be obtained by solving the following constrained optimization problem:

$$\begin{aligned} \underset{x}{\text{minimize}} \quad & \|\Psi x\|_1 \\ \text{subject to} \quad & \|\mathcal{F}_U x - y\|_2 < \epsilon \end{aligned} \tag{5.1}$$

Where x is complex vector representing the reconstructed image, Ψ is the linear operator that transforms from pixel domain into sparse domain, $\mathcal{F}_U$ is undersampled Fourier Transform, y is the measured k-space from MRI scanner and ϵ is the noise level. Obviously minimizing the ℓ_1 norm of $\|\Psi x\|_1$ develop sparse solution and the constraint $\|\mathcal{F}_U x - y\|_2 < \epsilon$ enforces consistency.

In the following sections, a brief intuitive description will be given of three different iterative algorithms that solve the underdetermined system $y = \Psi x$ with a sparsity constraint and they will be applied to the MRI applications. There are:

1. Non-Linear Conjugate Gradient in (4): Converting the constrained convex optimization to a unconstrained one and solving it using non-linear conjugate gradient descent with back-tracing line search.
2. Stagewise Orthogonal Matching Pursuit in (6): It uses matched filter and hard thresholding to selects all predictors that have high correlation with original data at each stage, adds to current model and fits by least squares.
3. Projection Over Convex Sets: includes two projections for each iteration: the first projection applies a threshold to the input data, the second projection inserts the original observed measurement into the solution and essentially ensures that any solution

proposed exactly fits the observed data or equivalently only the missing measurements are predicted.

5.4.1 Non-Linear Conjugate Gradient (NL-CG)

Converting the constrained convex optimization problem in Equation (5.1) to unconstrained optimization problem gives the following objective function to be minimized:

$$\underset{x}{\text{argmin}} \quad \|\mathcal{F}_U x - y\|_2^2 + \lambda \|\Psi x\|_1 \tag{5.2}$$

where $\mathcal{F}_U$ is the undersampled Fourier operator associated with the measurements, y is k-space measurements, λ is a regularization parameter that determines the trade-off between the data fidelity and the sparsity, Ψ is sparsifying transform operator (e.g. Wavelet transform operator), and x is the reconstructed image. Since the objective function is convex, optimization using gradient method is a natural choice. The diagram of the algorithm is summarized in Figure 5.9.

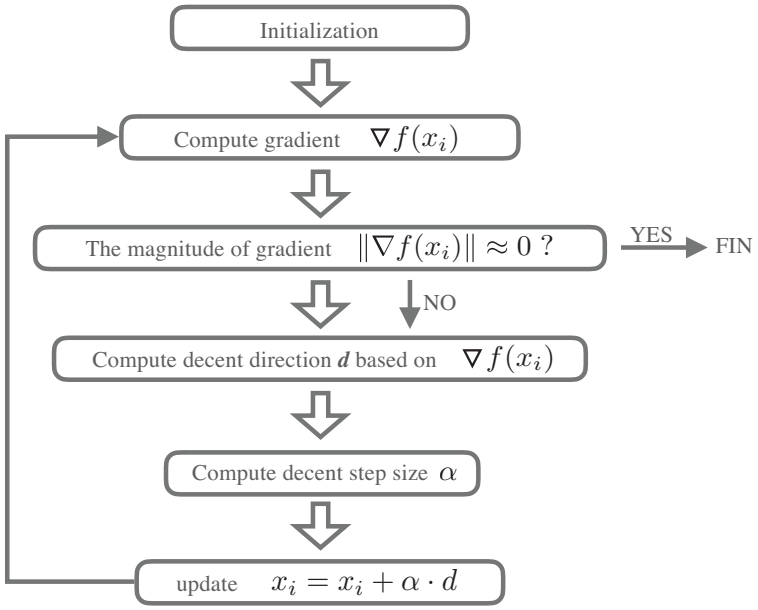

Figure 5.9: The diagram of Non-Linear Conjugate Gradient (NL-CG) algorithm

Different gradient methods have different strategies to find out decent direction and step size. Usually, using a conjugate gradient method to find the descent direction makes the iteration converge faster than the steepest descent method. The convergence can usually be guaranteed when no backtracking line search method is used to find the step size. The conjugate gradient requires computation of the gradient of the object function. A problem with this is that ℓ_1 norm is not differentiable at origin (x=0). One way to overcome this is to

approximate the ℓ_1 norm with a smooth function, e.g. $|x| \approx \sqrt{x'x + \mu}$ and $\mu \in [10^{-15}, 10^{-6}]$. Another method to circumvent the problem is to use sub-gradient method, which needs not to choose smooth function but is known for slower convergence. The regularization parameter, λ, can be determined empirically. For example, different λ can be tried to solve the optimization problem, and then choose the one that gives the best result. Alternatively, it can be determined automatically using generalized cross validation.

In practice, when Ψ is chosen to be wavelet operator and wavelet based CS reconstruction is performed, small high frequency artifacts may appear in the reconstruction. To attenuate these artifacts, a small Total Variation (TV) penalty is added and the objective function becomes:

$$\underset{x}{\text{argmin}} \quad \|\mathcal{F}_U x - y\|_2^2 + \lambda\|\Psi x\|_1 + \lambda TV(x)$$

By adding TV term into objective function, it seeks to represent the image sparsely both in wavelet domain and finite-differences domain, where λ determines the trade-off of sparsity between two domains.

5.4.2 Stagewise Orthogonal Matching Pursuit (StOMP)

While ℓ_1 minimization, which finds the solution having minimal ℓ_1 norm, enjoys some particularly striking theoretical properties, such as rigorous proofs of exact reconstruction under seemingly quite general circumstances, ℓ_1 minimization is much too slow for large-scale applications. StOMP is a method for approximate sparse solution of underdetermined systems, which is claimed to be significantly faster that general ℓ_1 norm based minimization. Considering MR image reconstruction usually involves large scale matrix computation, it seems worthwhile to adapt this algorithm to compressed sensing MR image reconstruction.

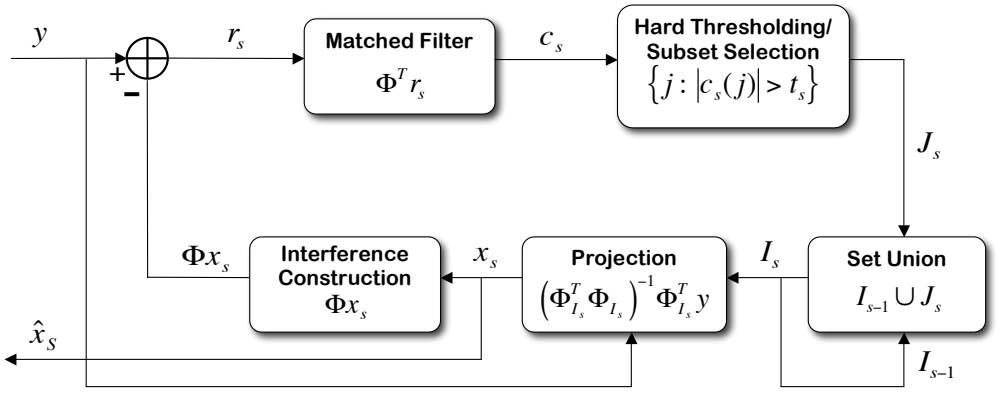

Figure 5.10: StOMP Schematic [*Courtesy of (6)*]

StOMP aims to achieve an approximation to the solution of $y = \Phi x_0$ where Φ is random matrix and x_0 is the sparse signal and y is the measurement. StOMP diagram is shown in

Figure 5.10.

The algorithm starts with initial solution of $x_0 = 0$ and initial residual $r_0 = y$ and iterates in S stages to obtain the final $\hat{x}$ which is equal x_S. Each stage applies matched filtering to the current residual ($\Phi^T r_s$), obtaining a vector of residual correlations (c_s) which only has few non-zero element. The procedure next performs hard thresholding to find those non-zero elements and put them in a set $J_s = \{j : |c_s(j)| > t_s\}$ where t_s is a threshold parameter. Given I_s is the index value of those nonzero element, we merge the subset of newly selected coordinates with the previous one ($I_s = I_{s-1} \cup -J_s$). Then the vector y is projected on the columns of Φ that are chosen using index set I. This is our new approximation: $x_s = (\Phi_{I_s}^T \Phi_{I_s})^{-1} \Phi_{I_s}^T y$ and the updated residual is $r_s = y - \Phi x_s$.

The statistical modeling of this problem goes as follows. One is given data $y = \Phi x$, Φ is random matrix with independent columns that are predictors and x is a vector of coefficients that is sparse. It is believed that most potential predictors are irrelevant, and only a few predictors should be used, but it is unknown which ones are most likely to be. Equivalently, most of the coefficients in x are zero, but the positions of the nonzeros are unknown. The StOMP method selects all predictors that are having a significant correlation with the original signal at each stage and adds it to the current model, which is then fits by least squares.

5.4.3 Projection Over Convex Sets (POCS)

Explaining the POCS method requires a trip to the abstract function space. In the infinite function space, every point represents a solution function for an arbitrary inversion problem. This figure shows two function sub-spaces. Each set represents all solution functions with a common characteristic. For example, set A contain all solutions that are positive, and set B contain all solutions that are real for any arbitrary problem. Initial solution is picked and is iteratively projected onto sets A and B until the solution converges to one answer in set C.

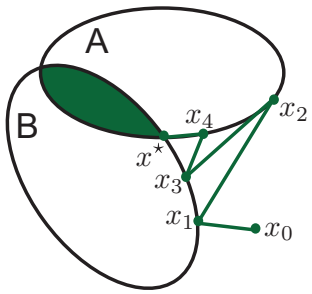

Figure 5.11: POCS algorithm solves by projection for $\{x \in \mathbb{R}^n \; s.t. \; x \in A \cap B\}$

Schematic Representation of the POCS algorithm is shown in Figure 5.18. The proposed POCS algorithm includes two projections for each iteration. The first projection applies a threshold to input data. The second projection inserts the original observed measurement into the solution. This projection essentially ensures that any solution proposed exactly fits the observed data or equivalently only the missing measurements are predicted.

This diagram represents the iterative process as follows: a 2D inverse Fourier transform is applied to the undersampled k-space that is obtained from the MRI scanner. Then a 2D discrete wavelet transform (DWT) is applied to the resulted image for sparsity transformation.

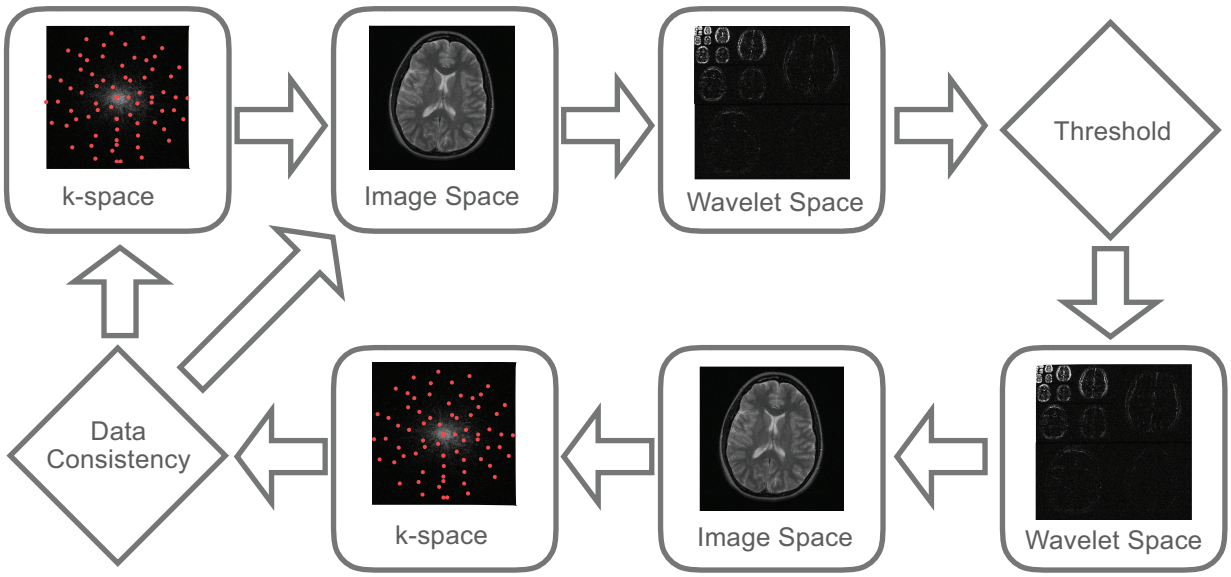

Figure 5.12: POCS Schematic

The algorithm applies the threshold to the resulting wavelet coefficients. An inverse DWT is then applied to bring the data back to the image domain and then a DFT is applied to bring back the data to the k-space domain before the original, observed data are placed into the solution. This procedure is applied for a number of iterations before the output is taken.

5.5 Results and Discussion for CS-MRI Images

In order to get an exposure to how CS reconstruction algorithm works, three algorithms were examined and their performance compared in term of relative error and processing time for MR image reconstruction.

Projection Over Convex Set is simply a 2D extension of the method mentioned earlier in 1D example. The POCS algorithm is very flexible. Additional constraints can be applied to the reconstruction by implementing suitable projections in the algorithms. We have observed that the way the threshold is chosen or even varied with iteration affects the convergence and the results of the reconstruction. Non-linear Conjugated Gradient method was proposed in (4), which is one of the very first paper that applies CS theory specifically to MR imaging. NL-CG is used to solve an unconstraint optimization problem iteratively based on gradient method. Stagewise Orthogonal Matching Pursuit is an algorithm to finding sparse solution for large scale system. The StOMP method selects all predictors that are having a significant correlation with the original signal at each stage and adds it to the current model, which is then fits by least squares.

Demo scrips provided in SparseMRI-v0.2 were used to show the NL-CG result. The code provided in SparseLab200 qas modified to apply the StOMP algorithm to MRI data. The POCS method was implemented in MATLAB.

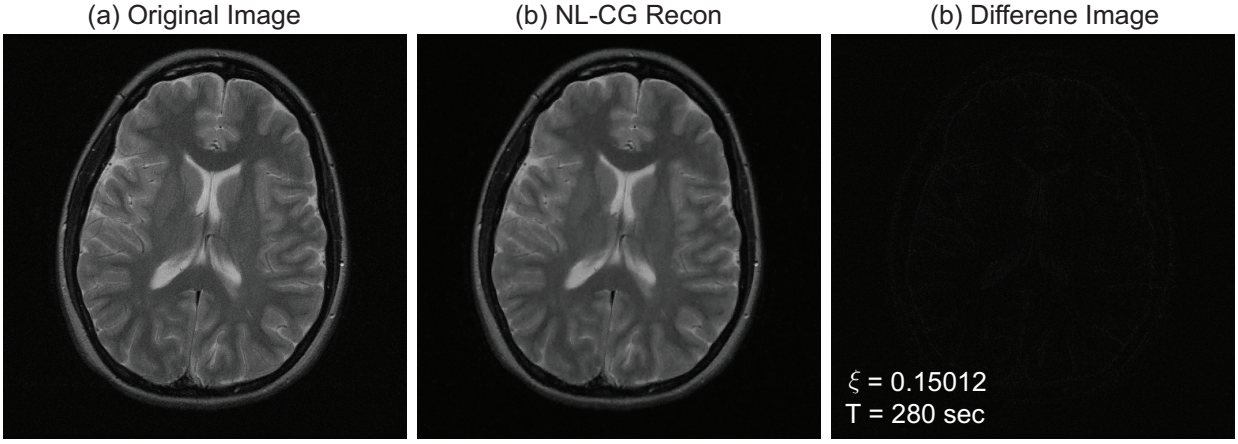

Figure 5.13: NL-CG algorithm with Error = 0.150152 and Time = 280 seconds.

In implementating the POCS algorithm, different values of λ, the threshold, and the number of iterations were considered. The algorithm iterated about 20 times which took about 30 seconds each. The results are shown in Figure 5.15. As illustrated, lower λ resulted in sharper reconstructed image with more high-frequency noise, whereas, the higher threshold resulted in blurrier image but less high-frequency noise. Table 5.1 summarizes the POCS results with different λ's and associated relative errors. The relative error was calculated as following:

$$\xi = \frac{\|I - \hat{I}\|_{frobenius}}{\|I\|_{frobenius}}$$

When $\lambda = 0.1$ we obtained the best image based on visual quality and ξ error.

Algorithms	Threshold (λ)	Relative Error (ξ)
POCS	0.006	0.26129
	0.06	0.21813
	0.1	0.18839
	0.3	0.22743

Table 5.1: λ's choices and associated relative error

Figure 5.13 shows the result from the NL-CG algorithm. Figure 5.13(a) shows the original image, Figure 5.13(b) shows NL-CG reconstruction, and Figure 5.13(c) shows the difference

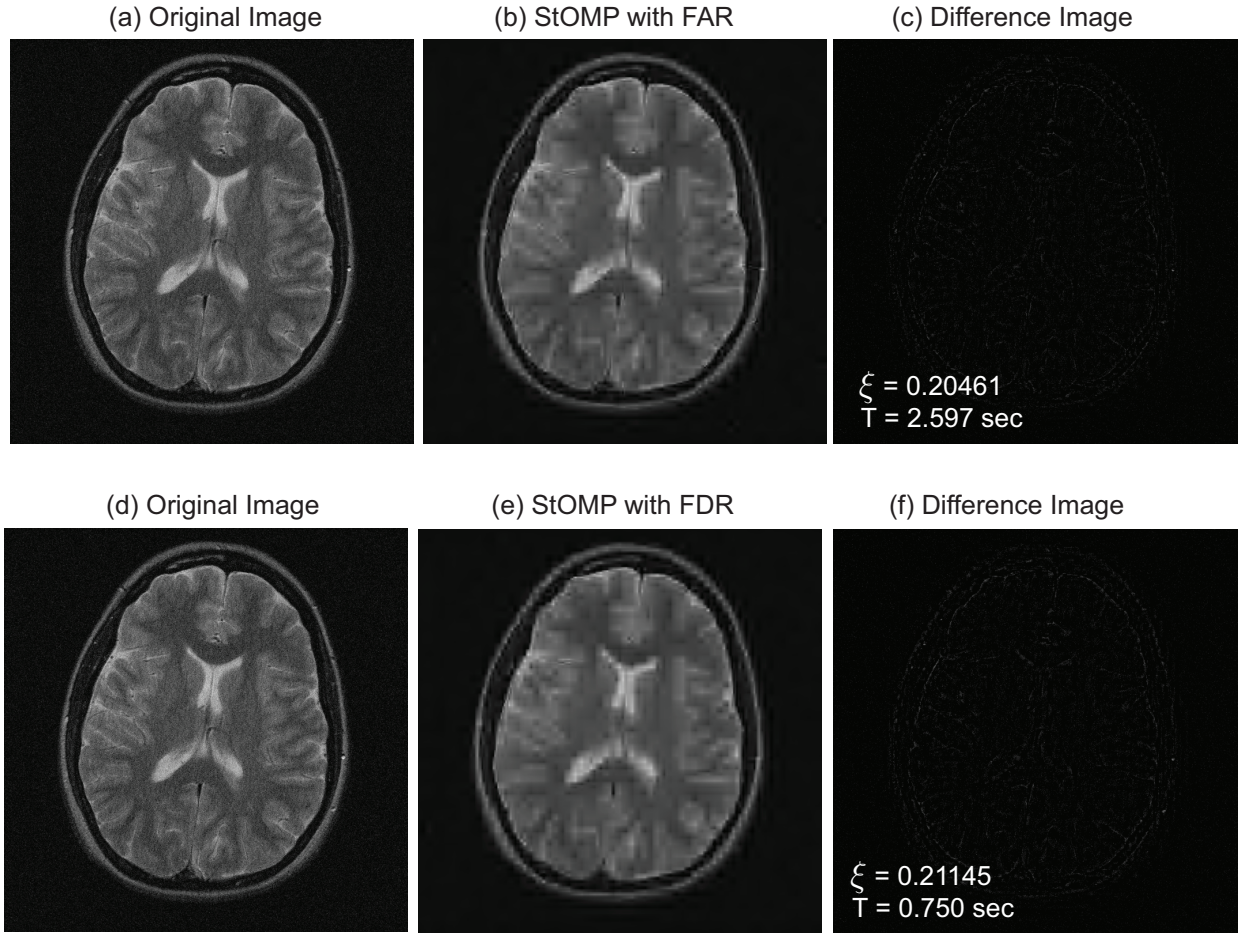

Figure 5.14: StOMP algorithm with FDR and FAR threshold.

image. The algorithm iterated about 5 times which took about 280 seconds with relative error of $\xi = 0.150152$.

The results from the StOMP algorithm is shown in Figure 5.14. FAR threshholding with $\xi = 0.20461$ gives a better image than FDR threshholding with $\xi = 0.21145$. However, the total computation time of FAR thresholding was over 3 times longer than the total computation time of FDR threshholding.

The computation times and relative errors from all three algorithms are listed in Table 6.4. NL-CG generated the best results in terms of both relative error and visual quality, while StOMP provided the fastest reconstruction as the algorithm expected to be. POCS, on the other hand, provided the simplest algorithm, but required choosing the value of lambda whose value plays a critical role in image reconstruction quality subjectively. This drawback

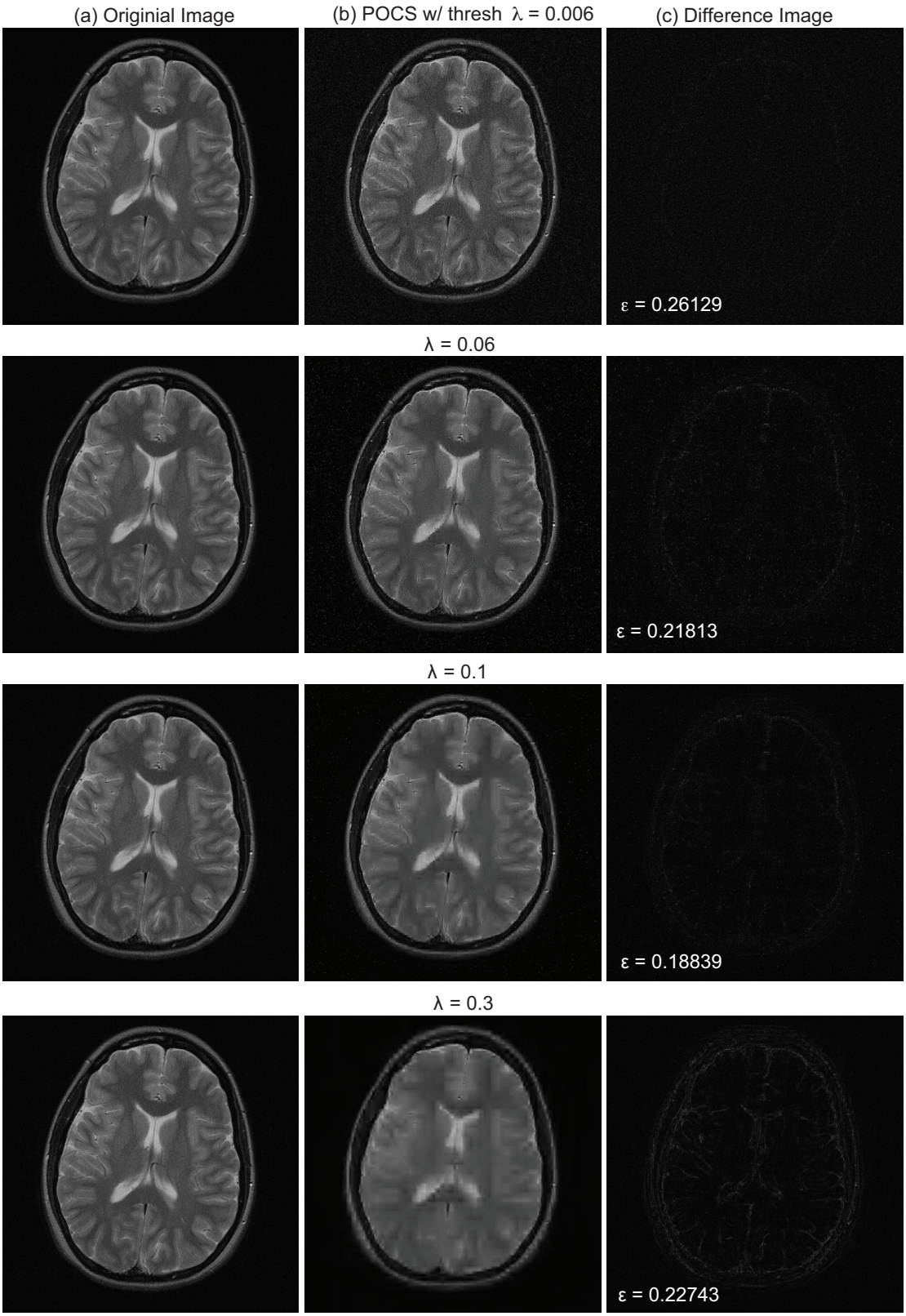

Figure 5.15: POCS algorithm with several different threshold, 30 seconds

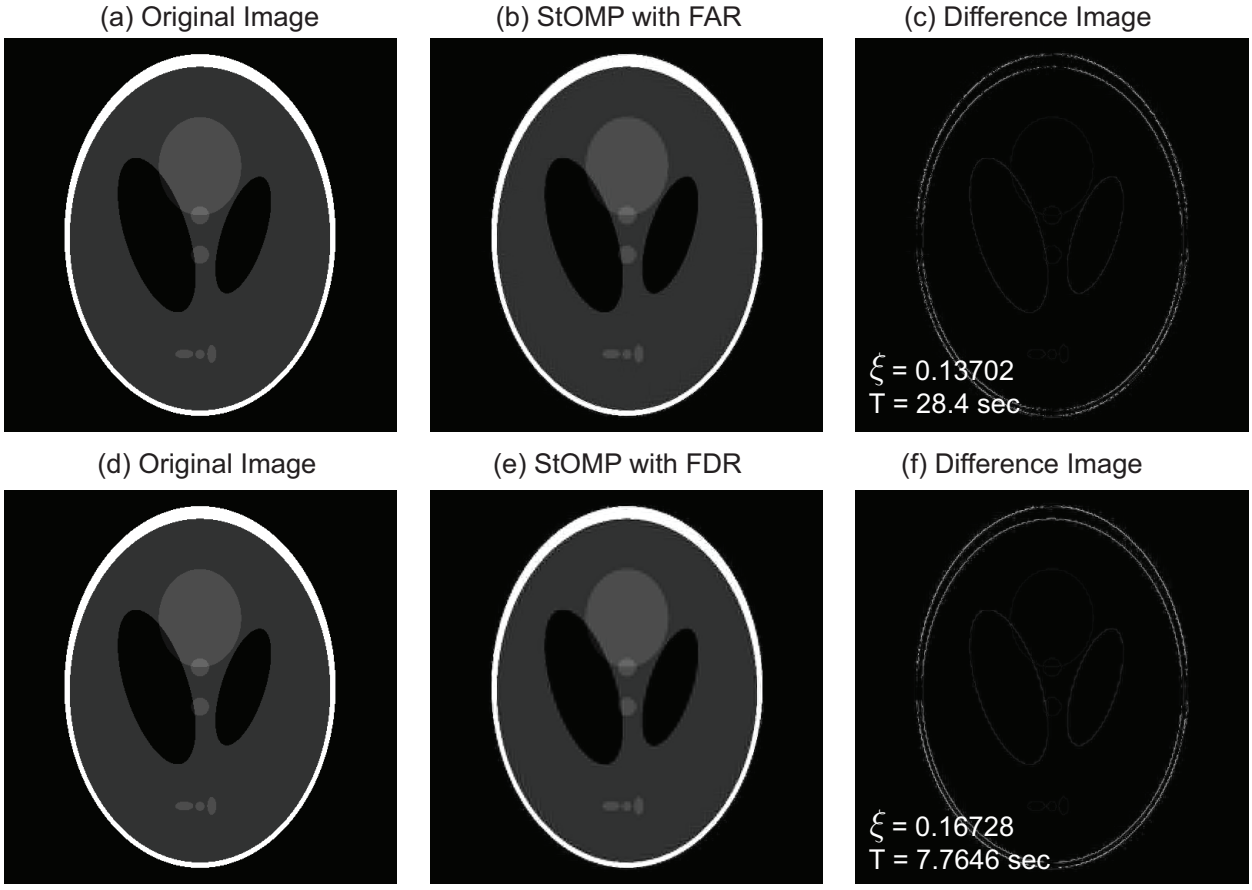

Figure 5.16: StOMP algorithm with FDR and FAR threshold.

may prevent its practical use in clinical setting. StOMP had the worse performance with the fastest computation time, we think this is due to the fact that StOMP doesn't deal with complex data sets since the reconstruction of the phantom was almost perfect as shown in Figure 5.5.

The interesting observation is that there may be oscillating high frequency artifacts showing up somewhere around skull in both StOMP images and POCS algorithms, and this may verify the reason behind using Total Variation (TV) in conjunction with wavelet transform in NL-CG. By adding TV in StOMP, it is presumed that one can further reduce the relative error. A comparison of the difference-image of all the algorithms showed that some of them exhibit "structured" traces. Presumably the algorithms that result in non-structured "difference image" have a higher quality reconstruction even though their calculated relative error may not necessary reflect that conclusion. This means one should not rely purely on the relative error as it may not give the best outcome.

It should be noted that the comparison of computed time made here may not represent the true difference among the algorithms, because none of the MATLAB codes used to compare these algorithms have been optimized. In addition, it is hard to analytically justify the quality of medical images, even though one may look better than the other one from the SNR, CSNR, or any other error measure perspective. At the end of the day, radiologist are the ones who will judge the quality and accuracy of these reconstructed images.

Algorithms	Relative Error	Time (sec)
POCS ($\lambda = 0.1$)	0.18839	30
StOMP (w/ FAR)	0.20461	2.597
StOMP (w/ FDR)	0.21145	0.751
NL-CG	0.15015	280

Table 5.2: Summary of computation times and relative errors of all the algorithms

5.6 Multi-Channel MRSI Reconstruction Using Water-Referencing with Compressed Sensing

As discussed in great details in Chapter 4, although the use of multi-channel receiver coils can increase the SNR of MRSI data, obtaining the optimal SNR from the raw data requires robust phase correction to achieve the constructive combination of signal from different receiver coils. The simplest strategy was to assume that there is a constant phase offset between the spectra in different channels and use the residual water from voxels in the central region of the selected volume to estimate these offsets prior to coil combination (7, 8) (RWcentral). While this is robust for data with moderate SNR, voxels on the outer edge of the selected volume may not be optimally phased as shown in Figure 5.17.

We have demonstrated in (9) that the best strategy is the one which incorporates the assumption of spatially varying phase offset by calculating the phase between the spectra in different channels using the residual water on voxel-by-voxel bases (RWvoxel). Another potentially robust approach is to obtain a second dataset with unsuppressed water and use that to estimate phase and frequency corrections (9, 10) (Wvoxel). Acquiring a separate dataset with no water suppression is time consuming, but the high signal to noise of the water resonance allows for an accurate estimate of frequency and phase parameters for all voxels in the selected region. In a more recent study, Abdoli et al (11) obtained a water reference data with minimal impact on scan time using volumetric spin-echo EPSI acquisition that includes an interleave water-reference data (TR = $1.71s$, TE = $70ms$ and T_{acq} = $26min$) at 3T Siemens scanner. In our cohort, the limitations on clinical scan-time for PRESS localized (a.k.a double spin-echo) Lactate-edited sequence precluded the implementation of interleaved acquisition of a water-reference on its own. A more effective solution

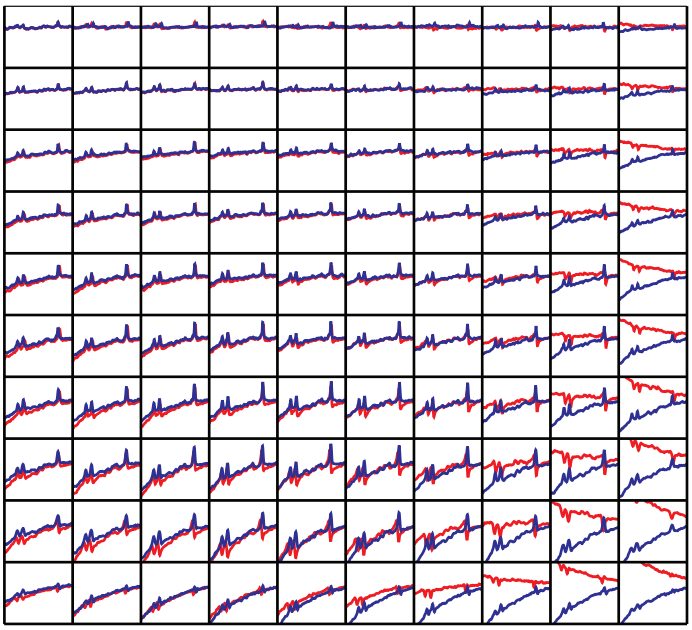

Figure 5.17: Phantom MRSI acquisition of one coil is presented with and without water-referencing. The blue spectra shows the water referenced spectra and the improvement in phase is apparent.

will be to apply compressed sensing technique that is based on random undersampling and a nonlinear reconstruction technique to acquire the water reference data in order to obtain the optimal speed and spatial coverage. These techniques can also be applied to the first-cycle of the lactated-edited data for the recovery of residual water peaks.

According to compressed sensing theory, if the underlying data exhibits transform sparsity, and if k-space undersampling results in incoherent artifacts in that transform domain, then the data can be recovered from randomly undersampled k-space data, provided an appropriate nonlinear scheme is used. Compressed sensing works well when underlying signals exhibit sparsity and have adequate SNR, but may fail if any of those conditions are not met (4). Being only interested in recovering a single peak which is water in the spectrum, makes the frequency domain an ideal and efficient domain to exploit the sparsity. Additionally, the natural abundance of hydrogen typically provides high SNR water spectra making this an excellent application for compressed sensing.

One of the key design challenge in implementing compressed sensing for specific MRSI applications is the development of pulse sequences and acquisition schemes that incorporate "incoherent" sampling, which is achieved by pseudo random undersampling (4). An initial flexible design incorporating pseudo random undersampling in two spatial dimensions and one temporal dimension (k_x, k_y, k_f) into a spectroscopic imaging sequence to achieve accelerations is discussed in details in the next section. This random undersampling pulse sequence design that our laboratory has used extensively for 3D-MRSI with flyback readout was simulated in MATLAB from the fully acquired k-space data for our initial investigation.

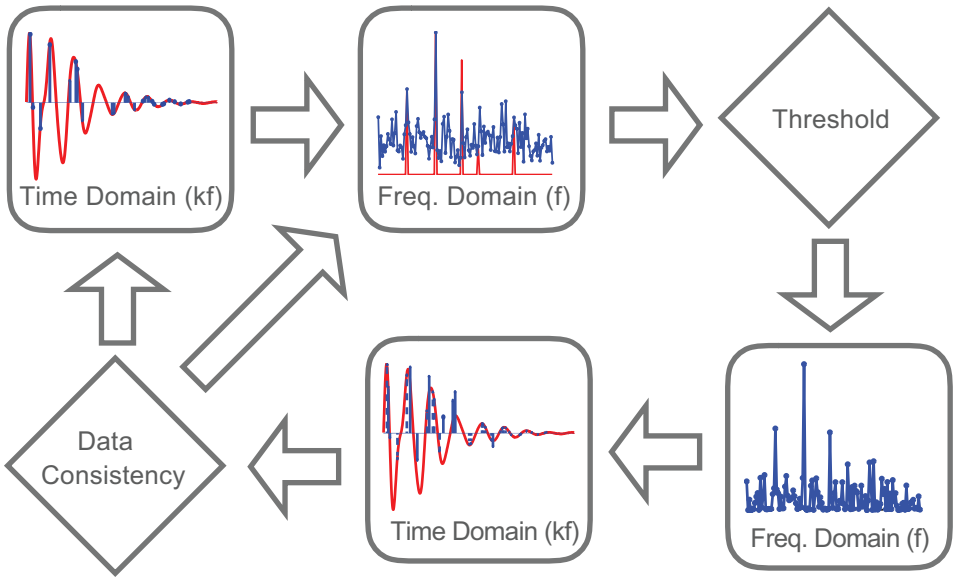

Figure 5.18: This diagram represents the iterative process as follows: a 1D inverse Fourier transform is applied to the undersampled k-space that is obtained from the MRI scanner. The DFT (Discrete Fourier Transform) is also used as sparsity transformation. The spectra domain is sparse since we are only looking for one peak in our case. Then the algorithm applies the threshold to the resulted spectrum. An inverse DFT is then applied to bring the data back to the k-space domain before the original, observed data are placed into the solution. This procedure is applied for a number of iterations before the output is taken.

Based on the results from the previous sections, the compressed sensing reconstruction technique that was chosen to be implemented into this MRSI application to improve the quality of the reconstructed data while reducing the computational complexity was POCS that uses an efficient 2-stage nonlinear iterative algorithm. As illustrated in Figure 5.18, the proposed POCS algorithm includes two projections for each iteration. The first projection applies a threshold to input data. The second projection inserts the original observed measurement into the solution. This projection essentially ensures that any solution proposed exactly fits the observed data or equivalently only the missing measurements are predicted. To the best of our knowledge, this was the first time that POCS was implemented for undersampled MRSI reconstruction.

Anatomic MR images and MRSI data were acquired from a commercially available MRS phantom and from human subjects using a GE 3T scanner (GE, Medical Systems, Milwaukee, WI) with 8 channel phased-array head coil using PRESS pulse sequence. The parameters for the data acquisitions were TR/TE = $1110/144ms$, with a FOV of $16 \times 16 \times 16$ using flyback echo-planner encoding in the SI direction. The MRSI data were first reconstructed using

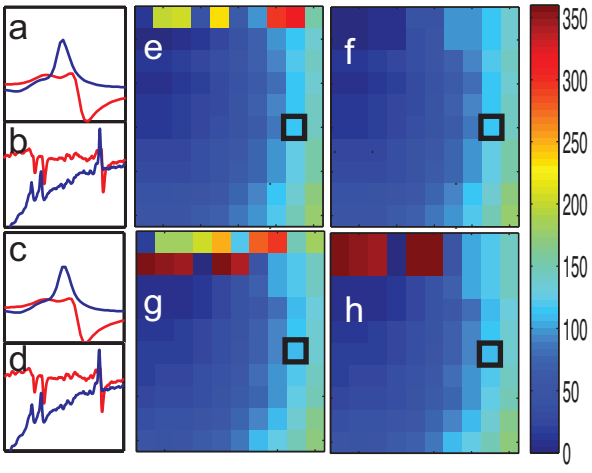

Figure 5.19: Conventional Acquisition: (a) and (b) show the unsuppressed water peak and metabolite peaks respectively phased with water-referencing (in red) and without (in blue). (e) and (f) show the initial and final phase-map from water-referencing respectively. Rapid Acquisition: (c) and (d) show the unsuppressed water peak and metabolite peaks respectively phased with water-referencing (in red) and without (in blue). (g) and (h) show the initial and final phase-map from water-referencing respectively. The comparison suggests the phase information is preserved by compressed sensing.

either conventional Fourier transforms or a custom designed compressed sensing algorithm. The steps to process undersampled H-1 3D-MRSI data have been described previously.

The major steps were as follows: 1) the readout data were reordered to pick out the data from flat portions of the flyback readout and organize all the data into a 4D (k_f, k_x, k_y, k_z) array 2) the missing k-space data in each undersampled (k_f, k_x, k_y) set were filled in with the iterative nonlinear ℓ_1 algorithm and 3) standard processing was performed, including apodization, linear phase correction for the flyback's tilted k-space trajectory, and a 4D Fourier transform. The additional component beyond conventional processing needed to account for the missing data fromundersampling. The optimal phase for each voxel in each channel was then determined using the unsuppressed water peak by imposing symmetry upon the reference peak in the spectrum. For the voxels with a water peak having a SNR of less than predefined threshold, nearest neighbor estimation was used to interpolate the phase values to yield a piece-wise constant interplant. The estimated phase and frequency corrections were then applied to the data set acquired with water suppression and the channels were combined.

Figure 5.19 illustrates the initial and improved phase estimation map for conventional vs rapid compressed sensing acquisition. The compressed sensing with POCS reconstruction does preserve the water phase information. Simulations showed that our algorithm would reduce the acquisition time by a factor of 5 (from 5 min to 1 min) for 3D data with a matrix size of 16x16x16. Unlike the method described by Hu et al (12) which uses NL-CG, the sparsity is forced in the spectral domain vs. wavelet domain, which reduces the complexity and computation time tremendously. With 50 iterations the reconstruction took about 1.6 minutes. Applying the estimated frequency and phase correction to each voxel of each

channel prior to coil combination results in constructive interference producing uniformly high SNR of metabolite peaks in the final data (Figure 5.20). As demonstrated in the previous section, the amplitude of the reconstructed water peak is not preserved, however, the fact that the amplitude of separately acquired calibration images were used for the coil combination weighting rather than the water peaks from separately acquired data was a further advantage that is directly scalable for many different coil configurations.

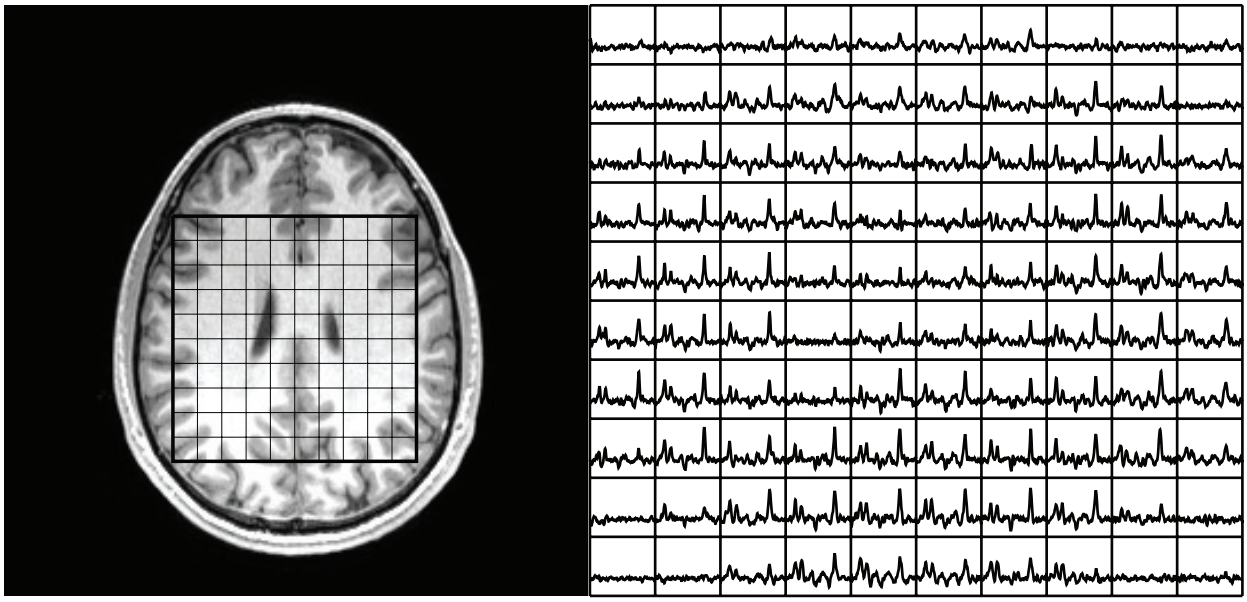

Figure 5.20: (a) T1 weighted image from a healthy volunteer superimposed with PRESS box. The grid shows the voxel locations corresponding to the spectra on the right. (b) water-referenced spectra of the volunteer (after coil combination)

5.7 Schemes for CS-MRSI Pulse Sequence Design and k-space Trajectories

To implement compressed sensing for MRSI, the main design challenge was to incorporate pseudo-random undersampling into a practical pulse sequence. The starting point was a PRESS localized sequence with phase encoding in x and y direction and a flyback echo-planar spectroscopic imaging (EPSI) readout in z and frequency dimensions (13).

The design inputs are spectral bandwidth, spatial resolution, spatial coverage (FOV), and gradient performance parameters (slew rate and amplitude). In the flyback readout, the time between flyback lobes controlled spectral bandwidth, and the number of lobes in conjunction with spectral bandwidth determined the spectral resolution possible. The GE 3T clinical MRI system equipped with $0.4(\frac{mT}{cm})$ and $1.50(\frac{mT}{m \quad ms})$.

Design Inputs	
spectral bandwidth	988Hz
spatial/spectral resolution	$1cm/1.4$Hz
spatial coverage	$20 \times 24 \times 16 \ \ (RL \times AP \times SI) \ \ cm^3$
gradient amplitude	$0.4 \ (\frac{mT}{cm})$
gradient slew rate	$1.5 \ (\frac{mT}{m/ms})$

To take advantage of the sparsity in frequency domain as was done in the simulations, a method was needed to undersample three k-space dimensions, including the time dimension (k_x, k_y, k_f) but excluding the fully sampled k_z EPSI readout dimension. To accomplish this, the design trick of placing gradient blips during the rewind portions of the flyback readout was employed to randomly hop around in k-space as described in (14). Figure 5.21 shows the schematic of the complete pulse sequence with double spin-echo refocusing pulses (PRESS), flyback readout, and x and y gradient blips.

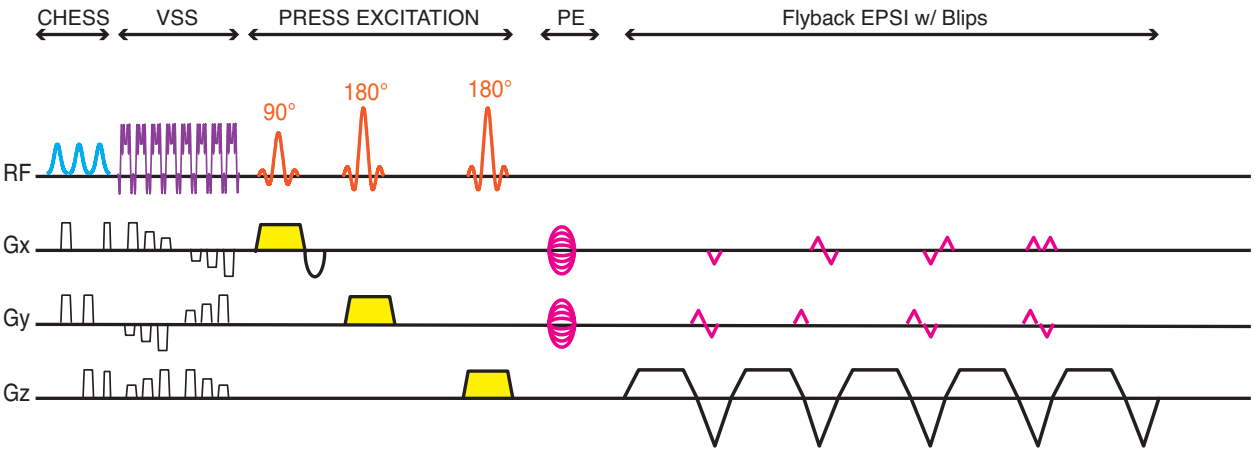

Figure 5.21: Schematic of Compressed Sensing 3D-MRSI pulse sequence. Phase encode localization occurred in x/y with flyback readout in z/f. The key design trick was placing x/y gradient blips during the rewind portions of the flyback readout. The blip areas were integer multiples of phase encode steps, allowing for hopping around and random undersampling of (k_x, k_y, k_f) space using blips. The blips segmented out the acquisition over several lines in k-space during one TR.

In this project, the compressed sensing methodology was substantially enhanced to incorporate a very flexible k-space trajectories for 3D spectroscopic imaging in both acquisition and reconstruction pipelines, which then was investigated through simulations, phantom testing, and in-vivo experiments. Development of these flexible features and ensuring their seamless interoperability is very important for future research in this area.

Current Data Acquisition Methodology: The software development toolkit is provided to institutions that have research agreements with the vendor. Over the years UCSF researchers have implemented many features to the branches of the product pulse sequences of GE scanners. Some of these features have been incorporated by the vendor into the product sequence and are now available on clinical scanners. GE Pulse sequences are developed in a custom programming language (EPIC) that is preprocessed into C code. The preprocessor generates two sets of source files: one for the Linux-based console computer and the other one for the embedded computers, responsible for pulse generation, data acquisition and real time control over the sequence being executed. This toolkit also handles the conversion and transfer of variables and data structures between these systems. Other executable and object files can be installed on the MRI scanner, running in a "Research" mode.

Current Data Reconstructions and Visualizations: The evaluation of MRSI data is made more complex than typical MRI data because files are typically encoded with vendor-specific file formats and there is a lack of standardized tools for reconstruction, processing, and visualization. SIVIC is a flexible open-source software framework and application that enables a complete scanner to workstation workflow for evaluation and interpretation of MRSI data. SIVIC is routinely used at UCSF to support the acquisition and analysis of clinical H-1 MRSI datasets. It supports conversion of vendor-specific formats into the DICOM MR spectroscopy (MRS) standard, provides modular and extensible reconstruction and analysis pipelines, and provides tools to support the unique visualization requirements associated with such data (15).

Traditionally, obtaining data with undersampled and/or non-linear k-space trajectories requires the development of customized softwares both in acquisition and reconstruction process per each trajectory design. My initial attempts at simplifying this whole process for future developments applied MATLAB routines to define a subset of rectilinear points in k-t space and output them as a file of weights that could be fed into the sequence in order to specify which points were acquired. The pulse sequence code for H-1/C-13 MRSI data acquisition were modified to make sense of these files and execute accordingly. The file was then linked to the raw data and used to define the reconstruction modules to be applied.

Figure 5.22 shows examples of random sampling in both k-space and time axes that generated in MATLAB and is converted to a readable text file for data acquisition and reconstruction. The strategy being proposed here is essentially dividing the k-space into arbitrary blocks which are distinguished by their associated number. For example, the blocks that are identified by number "1" are fully sampled and generally belong to the central region of the k-space with no gradient blips; the other blocks each have specific set of gradient blips in both x and y directions that moves the reading of k_f data up or down to a particular location in k_x and k_y as desired. Therefore, the corresponding trajectory descriptor file format has three main sections. The first line is a "comment line" and it is ignored by the pulse sequence code, however can be used as an identifier in the reconstruction pipeline. The second line

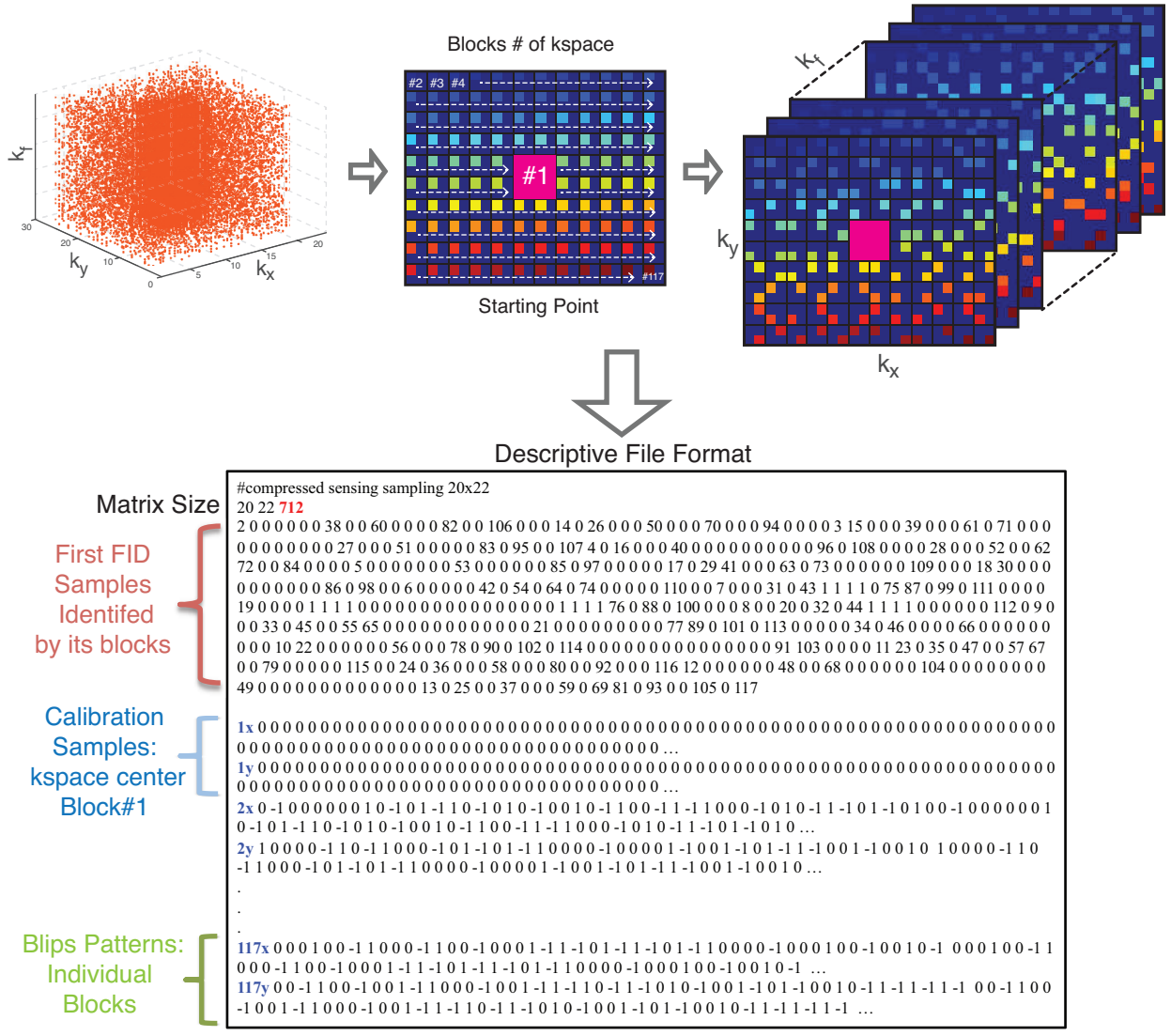

Figure 5.22: Preliminary MATLAB version of the rectilinear time/k-space sub-sampling file formats. Random undersampling pattern in (k_f, k_x, k_y)

has three parameters indicating the MRSI matrix size (N_x, N_y, N_f): the first two values are the number of phase encodings in x and y direction, the third value is the number of flyback lobes and an identifier for whether the random sampling is only spatially or both spatially and temporally. The next section provides information for each k-space location $(k_{ix}, \Delta k_{iy})$ whether to not acquire data (0's) or acquire data ($\neq$0) where then the pulse sequence code will search for (block#x and block#y) identifiers in the following sections of the file to play the corresponding gradient blips based on the weights that presented to achieve the desired sampling patten for that particular block.

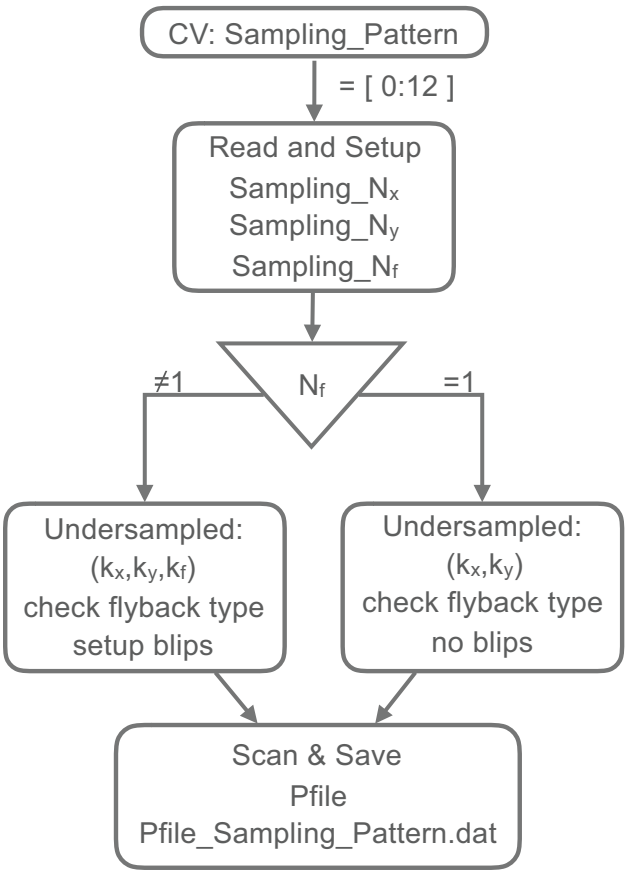

Figure 5.23: Flowchart of the Epic Implementation.

A user control variable,"sampling_pattern" ,toggled by the operator on the scanner prescription screen, controls loading of this externally defined k-space trajectory file and its parameters into the pulse sequence code. Figure 5.23 shows the diagram of the Epic code logic. These parameters were saved by the prescription software as an ASCII text file with a name of "Pfile_sampling_pattern.dat" in a special directory on the scanner's hard disk and were loaded by the pulse sequence before the start of the acquisition.

The headers in the raw data files that are currently output by MR scanners contain a relatively small number of parameters for describing the data acquisition procedures. Reconstructing data obtained using these new modified sequences that are developed with undersampled and/or non-rectilinear k-space trajectories requires the development of customized software to re-order, re-grid or otherwise pre-process the data so that it can be reconstructed and processed with standardized modules in SIVIC. This was addressed in MATLAB by creating data mappers to read the "Pfile_sampling_pattern.dat" to apply hard-coded parameters to re-order and zero-fill that data into a full, rectilinear k-space grid.

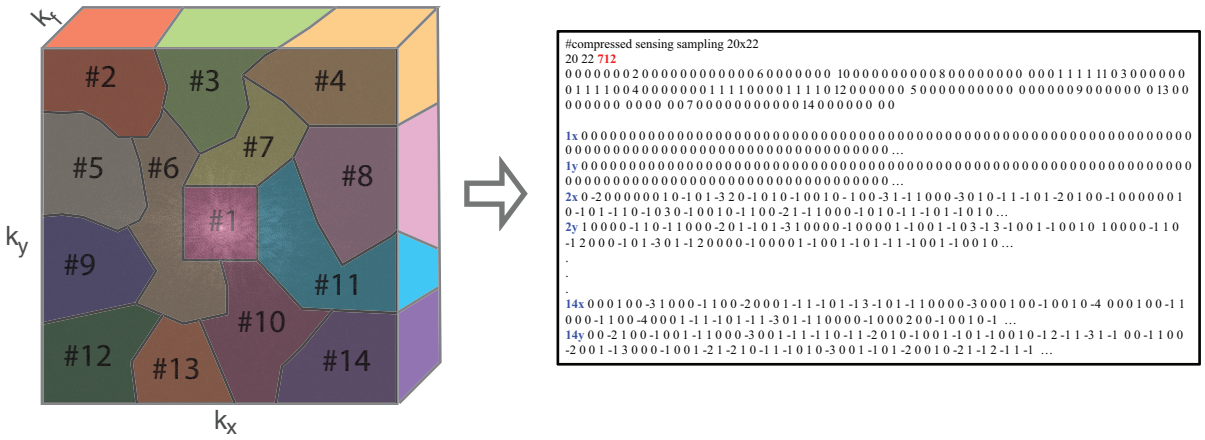

Figure 5.24: Flexible arbitrary random k-space sampling strategy.

Expanding this concept to the larger range of k-space trajectories are very intuitive as shown in Figure 5.24. In these cases the blips areas are allowed to be qual the area of two or more phase encode steps, providing larger (k_x, k_y) blocks to increased acceleration or randomization (given the limitation of the gradient of MRI scanner).

5.8 Summary and Conclusion

In this study the focus was given to the performance of non-linear reconstruction techniques for CS-MRI. Three different algorithms were studied, and their efficiency was compared in terms of image reconstruction quality and computation time. Based on the results provided in this chapter, the compressed sensing reconstruction technique that was chosen to be implemented into the MRSI application was POCS that uses an efficient 2-stage nonlinear iterative algorithm. CS-MRI is still in its infancy and many crucial issues remain unsettled, such as optimizing sampling trajectories and developing improved sparse transforms that are incoherent to the sampling operator. Without taking these factors into consideration, reconstruction algorithm design would be suboptimal.

In this work, a method for applying POCS compressed sensing to MRSI was presented to obtain a water-reference dataset for a purpose of correcting phase and frequency, and coherently combining multichannel 1H MRSI data from the brain with a 5-fold reduction in acquisition time. This is an encouraging step forward in automating and optimizing the analysis of such spectra so that they can be used routinely in a clinical setting. In addition, the random undersampling of the compressed sensing was incorporated in the MRSI pulse sequence and should be generally applicable for other MRSI studies as well. Future work will include evaluation of the performance of this technique in whole-brain MRSI data sets for which phase correction is more of a challenge, investigating the benefits in terms of efficiency

and quality in combining the compressed sensing and parallel imaging techniques to achieve higher accelerated 3D dataset.

5.9 References

1. E. J. Candes, J. Romberg, and T. Tao, "Robust uncertainty principles: Exact signal reconstruction from highly incomplete frequency information," *IEEE Transactions on Information Theory*, vol. 52, pp. 489–509, Feb. 2006.

2. D. L. Donoho, "Compressed sensing," *IEEE Transactions on Information Theory*, vol. 52, pp. 1289–1306, 2006.

3. Y. Tsaig and D. L. Donoho, "Extensions of compressed sensing," *Signal Processing*, vol. 86, pp. 549–571, Mar. 2006.

4. M. Lustig, D. Donoho, and J. M. Pauly, "Sparse MRI: The application of compressed sensing for rapid MR imaging," *Magnetic Resonance in Medicine*, vol. 58, no. 6, pp. 1182–1195, 2007.

5. M. Lustig, D. L. Donoho, J. M. Santos, and J. M. Pauly, "Compressed Sensing MRI," *IEEE Signal Processing Magazine*, vol. 25, pp. 72–82, Aug. 2008.

6. D. L. Donoho, Y. Tsaig, I. Drori, and J.-L. Starck, "Sparse Solution of Underdetermined Systems of Linear Equations by Stagewise Orthogonal Matching Pursuit," *IEEE Transactions on Information Theory*, vol. 58, pp. 1094–1121, Aug. 2006.

7. S. J. Nelson, "Multivoxel magnetic resonance spectroscopy of brain tumors.," *Molecular cancer therapeutics*, vol. 2, pp. 497–507, May 2003.

8. S. J. Nelson, "Magnetic resonance spectroscopic imaging," *Engineering in Medicine and Biology Magazine, IEEE*, vol. 23, no. 5, pp. 30–39, 2004.

9. M. Vareth, L. Yaan, J. M. Lupo, and S. Nelson, "Comparison of Several Coil Combination Techniques in Multi-Channel 3D MRSI for Brain Tumor Patients ," *Proceeding of the 23rd Annual Scientific Meeting of the ISMRM*, Dec. 2015.

10. D. Spielman, P. Webb, and A. Macovski, "Water referencing for spectroscopic imaging," *Magnetic Resonance in Medicine*, 1989.

11. A. Abdoli and A. A. Maudsley, "Phased-array combination for MR spectroscopic imaging using a water reference," *Magnetic Resonance in Medicine*, Sept. 2015.

12. S. Hu, M. Lustig, A. Balakrishnan, and D. B. Vigneron, "3D compressed sensing for highly accelerated hyperpolarized 13C MRSI with in vivo applications to transgenic mouse models of cancer," *Magnetic Resonance in Medicine*, 2010.

13. M. L. Zierhut, E. Ozturk-Isik, A. P. Chen, I. Park, D. B. Vigneron, and S. J. Nelson, "1H spectroscopic imaging of human brain at 3 Tesla: Comparison of fast three-dimensional magnetic resonance spectroscopic imaging techniques," *Journal of Magnetic Resonance Imaging*, vol. 30, pp. 473–480, Sept. 2009.

14. S. Hu, M. Lustig, A. Chen, J. Crane, A. Kerr, and D. B. Vigneron, "Compressed sensing for resolution enhancement of hyperpolarized 13C flyback 3D-MRSI," *Journal of Magnetic Resonance Imaging*, 2008.

15. J. C. Crane, M. P. Olson, and S. J. Nelson, "SIVIC: Open-Source, Standards-Based Software for DICOM MR Spectroscopy Workflows," *International Journal of Biomedical Imaging*, vol. 2013, no. 2, pp. 1–12, 2013.

Chapter 6

Development of Parallel Imaging for MRSI Applications

6.1 Introduction

Multiple receiver coils have been used since the beginning of MRI, mostly for the benefit of increased signal-to-noise ratio (SNR). In the late 1980s and early 1990s, several groups proposed to use the multiple receivers for scan acceleration (1–7) however the first practical technique didn't develop till late 1990s. The phrase "parallel imaging" refers to the simultaneous, or parallel, acquisition of data from multiple coils in order to reduce the necessary number of phase-encoding steps and hence to reduce the MRI acquisition time.

In 1987, the first k-space parallel imaging method was introduced by Carlson (then at University of California, San Francisco). He realized very early on that one could accelerate image acquisition using a combination of both phase-encoding gradients and RF coils to reconstruct an image (1–3). His method successfully reconstructed phantom data as early as 1989 and in vivo reconstructions were acquired using his method as early as 1993. In 1989, the first image-domain parallel imaging reconstruction was proposed by Kelton, Magin and Wright (4) from the University of Illinois. While any of these early methods could have started the parallel imaging revolution, they did not catch on due to important limitations such as lack of scanners with multi-channel capability, suboptimal system electronics and inefficient sequences.

It was not till late 1990s, when the idea of parallel imaging found wide acceptance in all areas of MRI because the scanner technology was starting to change by providing multi-channel array coils, better imaging sequences and improved electronics. The method that initiated the modern parallel imaging era was SMASH (8), which was introduced by Sodickson and Manning in 1997. It was the first technique to be successfully implemented in vivo and

worked with a broad range of coil arrays. Later, Pruessmann et al. proposed the SENSE (9) with an SNR-optimized reconstruction and a coil sensitivity mapping methodology that ensured the robustness of its process.

Over the past two decades, many different parallel imaging reconstruction methods have been developed. They are summarized in Table 6.1. These differ by the way the sensitivity information is estimated and used in reconstruction. Based on historical precedents, most researchers divide the techniques into three groups: those that operate in the image space, those that operate in k-space and those that operate partially in both spaces (hybrid). Image-domain methods like SMASH(8), SENSE (9), PARS (10) and kSPA (11) explicitly require the coil sensitivities to be known and operate in image domain. k-space methods like AUTO-SMASH (12), PILS (13), GRAPPA (14), and SPRiT (15) implicitly use the sensitivity information for reconstruction and operate in k-space. Hybrid approaches like SPACE-RIP (16), GEM (17), and the generalized SMASH (18) combine features of both image and k-space reconstruction for improving robustness. In practice, it is very difficult to measure the coil sensitivities with high accuracy. Errors in the sensitivity are often amplified and even small errors can result in visible artifacts in the image. It is worth noting, the auto-calibration methods avoid some of those difficulties that are associated with explicit estimation of the sensitivities.

Table 6.1: Properties of some parallel imaging reconstruction methods.

Methods	Reconstructed Image	Sensitivity	Reconstruction
SMASH	single	explict	indirect, “restricted” coil sensitivities
SENSE	single	explict	direct, iterative non-cartesain
AUTO-SMASH	single	implicit	direct, cartesian
SPACE-RIP	single	explict	direct, 1D non-cartesian
kSPA	single	expilict	direct, non-cartesian
PILS	coil-by-coil	implicit	“restricted” coil arrangment
GRAPPA	coil-by-coil	implicit	indirect, cartesian
PARS	coil-by-coil	explicit	direct, non-cartesian
SPIRiT	coil-by-coil	implicit	iterative cartesian and non-cartesian
SAKE	coil-by-coil	n/a	iterative

Another way to categorize the methods is whether the technique arrives at its solution directly or indirectly. Most image-domain methods and some k-space methods reconstruct the image by directly inverting the reconstruction problem such as SENSE, which effectively

unfolds the aliased image. To name a few more, SPACE-RIP, PILS, generalized SENSE (19), GEM, and generalized SMASH all directly invert the reconstruction problem. The other category of methods includes those that use a small amount of acquired data to reconstruct the data that were skipped in the acquisition, such SMASH, in which one line of acquired k-space is used to regenerate several lines in the reconstructed k-space. AUTO-SMASH and GRAPPA are in this category and the key feature of these indirect methods is that no assumption is made about the source data used in the reconstruction. Parameters can be derived to provide the minimum error reconstruction from nearly any configuration of source lines to any set of missing lines and this provides a large degree of freedom in the reconstruction. In general, all of the above parallel imaging methods result in similar reconstructed images if accurate coil sensitivity information can be obtained. One area of practical importance where these two classes of methods perform differently is how they deal with aliasing in the full-FOV of the reconstructed image. It has been reported and widely observed that SENSE reconstruction fails whenever the reconstructed FOV is smaller than the object being imaged (20, 21). This can be a hindrance in practice, since the operator must ensure that the chosen FOV is always larger than the object. On the other hand, GRAPPA has been used to reconstruct images with aliasing in the reconstructed FOV, as in conventional imaging, without any modification of the reconstruction code (14, 21).

A further key difference between these techniques is presented in the reconstruction target. SMASH, SENSE, SPACE-RIP, kSPA and AUTO-SMASH attempt to directly reconstruct a single combined image. Coil-by-coil methods, PILS, PARS, GRAPPA and SPIRiT directly reconstruct the individual coil images leaving the choice of combination to the user. Roemer et al.'s (22) observed that the optimal SNR in a reconstructed image from multiple coils is achieved by combining the signals on a pixel-by-pixel basis, weighting each coil by the sensitivity of the coil at that location in space. In this way pixels close to a single coil element obtain the vast majority of their information (and noise) from only that coil, and pixels located between elements have shared information. Of course, what Roemer et al. also observed was that in general the spatial sensitivity of the coils is unknown, and varies throughout space. Although, they observed that for most SNRs, the sum-of-squares combination approximated the sensitivity-combined result to within approximately 10%, in practice, coil-by-coil methods tend to be more robust to inaccuracies in the sensitivity estimation, often exhibit fewer visible artifacts, (23) and are better suited for MRSI applications.

In this chapter, the theories and shortcomings behind Parallel Imaging (PI) techniques alone and in combination with compressed sensing (PI&CS) are reviewed in MRI and then extended to some MRSI applications. More specifically, SENSE, GRAPPA, SPRiT, and ℓ_1-SPIRit algorithms are briefly introduced, the auto-calibration options are implemented, and applied to a 2D MRI brain image of a 8-channel array coil to compare the efficiency of these algorithms in terms of image reconstruction quality and computation time. Furthermore, the obstacles of applying these techniques to MRSI applications are presented along with ways to overcome some of the complications associated with MRSI application.

6.2 Theory of Parallel Imaging for MRI images

The basic idea of parallel imaging is as simple as employing several independent receiver coil elements and acquire data in parallel to reduce the number of phase-encoding steps which leads to faster MRI acquisition time. The acceleration factors are achieved by skipping every second, third, or forth k-space line depending on the desired acceleration rate. Undersampling in k-space reduces the FOV and leads to aliasing in the image domain as illustrated in Figure 6.1 (fully sampled vs undersampled by a factor of 2).

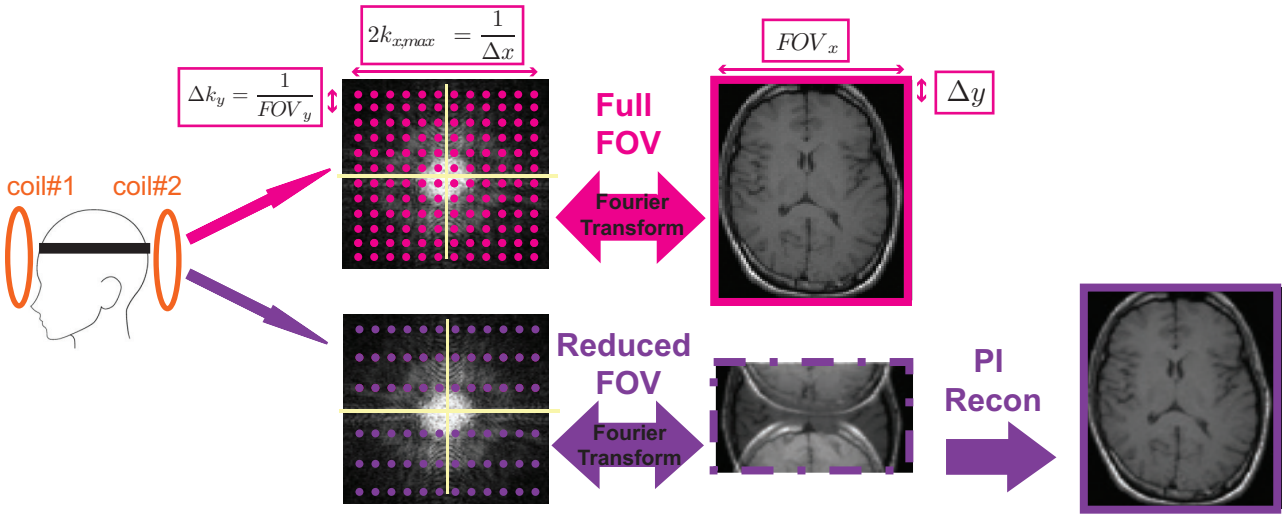

Figure 6.1: Data in k-space are usually collected on a Cartesian Grid. The Fourier Transform is used to convert the k-space data to an image of size $(N_x \times N_y)$ pixels. The extent of k-space covered (k_{xmax} and $k_{y,max}$) is inversely proportional to the image resolution (Δx and Δy). The spacing between adjacent samples in k-space (Δk_x and Δk_y is inversely proportional to the filed-of-view (FOV_x and FOV_y). A high resolution image covering the full FOV requires collection of data in closely-spaced lines that span a large region of k-space. Increasing Δk_y, while holding $k_{y,max}$ constant maintains the image resolution but decreases the FOV, resulting in spatial aliasing in the corresponding image.

Recalling the relationship between k-space and the image domain, the FOV (as determined by the spacing of the phase-encoding lines) should be at least as large as the size of the object. This requirement on the FOV (and the k-space sampling interval) is known as the Nyquist criterion. If this criterion is satisfied in both k_x and k_y directions, an image can be reconstructed from the k-space data without spatial aliasing. However, if fewer phase-encoding lines are collected (ex. k_y direction is undersampled as shown), this undersampling results in reduction of the FOV and aliasing in the phase encoding direction of the image. The following algorithms will unfold these aliased images in different ways:

6.2.1 SENSE

SENSE is a general image-domain parallel imaging method which has been successfully implemented by many groups and is available on most modern clinical scanners. In contrast to other previous image-domain reconstruction methods that are mentioned, SENSE includes a practical coil mapping procedure as well as an SNR-optimized reconstruction. The advantage of the SENSE approach is that it is very general. It can be used with arbitrary sampling trajectories, and other priors on the image can be easily incorporated. It is the optimal solution when the coil sensitivities are exact. However, it is often very difficult to accurately and robustly measure the sensitivities, and even small errors can lead to visible artifacts in the image.

SENSE poses parallel imaging reconstruction as an inverse problem in image space. Provided that the coil sensitivities are known or can be measured with sufficient accuracy, the problem can be formulated as a set of linear equations. Let m be the underlying magnetization image, s_c be the sensitivity of the c^{th} coil and let $\mathcal{F}_{\mathcal{P}}$ be a partial Fourier operator corresponding to the k-space undersampling scheme. For simpler mathematical representation, matrix $\mathcal{E}$ can be defined as an encoding matrix that incorporates the coil sensitivities s_c and the partial Fourier operators $\mathcal{F}_{\mathcal{P}}$ in vector format as following:

$$q_c = \mathcal{F}_{\mathcal{P}}\ s_c\ m \Longrightarrow \mathbf{q} = \mathcal{E}\ \mathbf{m} \tag{6.1}$$

The system in Equation 6.1 is then solved by least-squares either directly (9) or iteratively (19). It is important to note that SENSE reconstruction can be achieved by unfolding the aliased pixels, but only strictly enforces the elimination of aliasing in the voxel centers. It is therefore labeled as a weak reconstruction and residual aliasing may occur when coil sensitivities vary considerably over the extent of the voxel and it's significant side lobes. This is not a concern for high resolution imaging where coil sensitivities vary smoothly at the scale of common voxel sizes but it is a big problem for MRSI due to the low-resolution nature of spectroscopy. Two techniques can reduce these artifacts (1) extrapolating the coil sensitivity beyond the subject border and (2) applying a cosine filter in k-space.

6.2.2 GRAPPA

In contrast to the SENSE method, which works entirely in the image domain, there are many methods which work entirely in k-space. Currently, the only k-space method available on clinical scanners is GRAPPA-like. The intuition behind the k-space based approach is that the image weighting applied to the image by multiple array coils is equivalent to k-space blurring so that the k-space becomes locally correlated as depicted in Figure 6.2 and each potential missing k-space point can be estimated from its neighboring points. GRAPPA poses the parallel imaging reconstruction as a synthesis problem in k-space and it is a self-calibrating coil-by-coil method that attempts to reconstruct the individual coil images directly.

In traditional GRAPPA (14), a non-acquired k-space point ($p_c(\bar{r})$) in the c^{th} coil, at position $\bar{r}$, is synthesized by a linear combination of acquired neighboring k-space data from all C coils as depicted in Figure 6.3(b). Let $\mathcal{P}_{c\bar{r}}$ be a vector of all points on a Cartesian grid in the neighborhood of $p_c(\bar{r})$ in the c^{th} coil, and let $\mathcal{P}^a_{c\bar{r}}$ be a subset of $\mathcal{P}_{c\bar{r}}$ that chooses only those points acquired. The retrieval of the missing point $p_c(\bar{r})$ is given by:

$$p_c(\bar{r}) = \sum_{j=1}^{C} \langle \mathcal{W}^a_{jc}, \mathcal{P}^a_{j\bar{r}} \rangle \tag{6.2}$$

where $\mathcal{W}^a_{jc}$ is the vector set of weights for the acquired neighboring points obtained by calibration. The c^{th} coil corresponds to coil that has the missing point and j^{th} coil corresponds to all the other coils. Thus the full k-space grid is reconstructed by solving Equation 6.2 for each missing point in all coils and all positions.

The GRAPPA calibration kernel, $\mathcal{W}^a_{jc}$, used in Equation 6.2, are obtained by calibrating a fully acquired central k-space region as depicted in Figure 6.3(c). The calibration finds the set of weights that is the most consistent with the calibration data in the least-squares sense. Mathematically this process transfers to solving the following equation:

$$\underset{\mathcal{W}^a_{ji}}{\operatorname{argmin}} \sum_{\bar{x} \in \text{CalibRegion}} \left\| \sum_j \langle \mathcal{W}^a_{ji}, \mathcal{P}^a_{j\bar{x}} \rangle - p_i(\bar{x}) \right\|^2 \tag{6.3}$$

This equation is often solved as Tikhonov regularized least-squares, which has an analytic

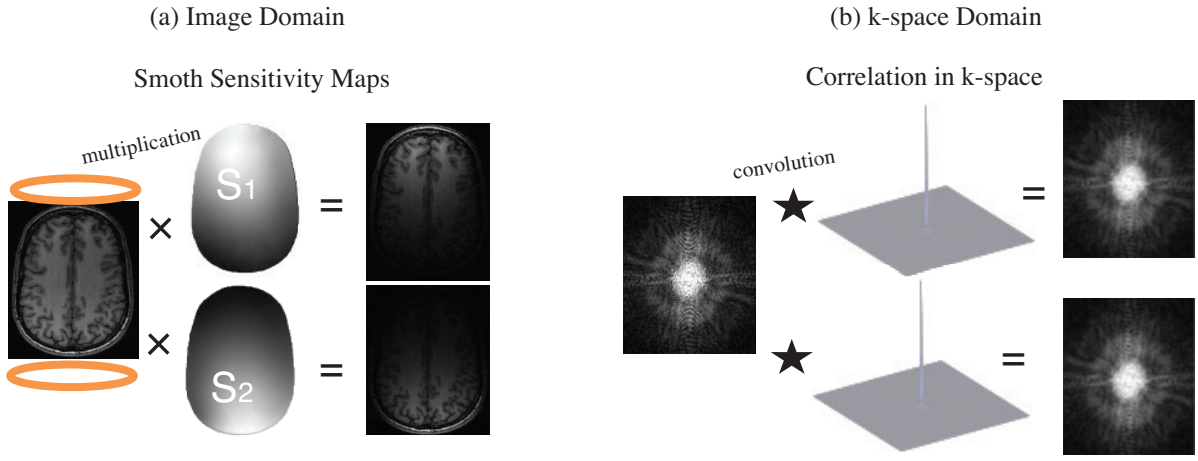

Figure 6.2: Intuition behind auto-calibration approach: image weighting is equivalent to k-space blurring. Coil sensitivities are smooth, therefore the blurring kernel is compact and therefore the k-space becomes locally correlated.

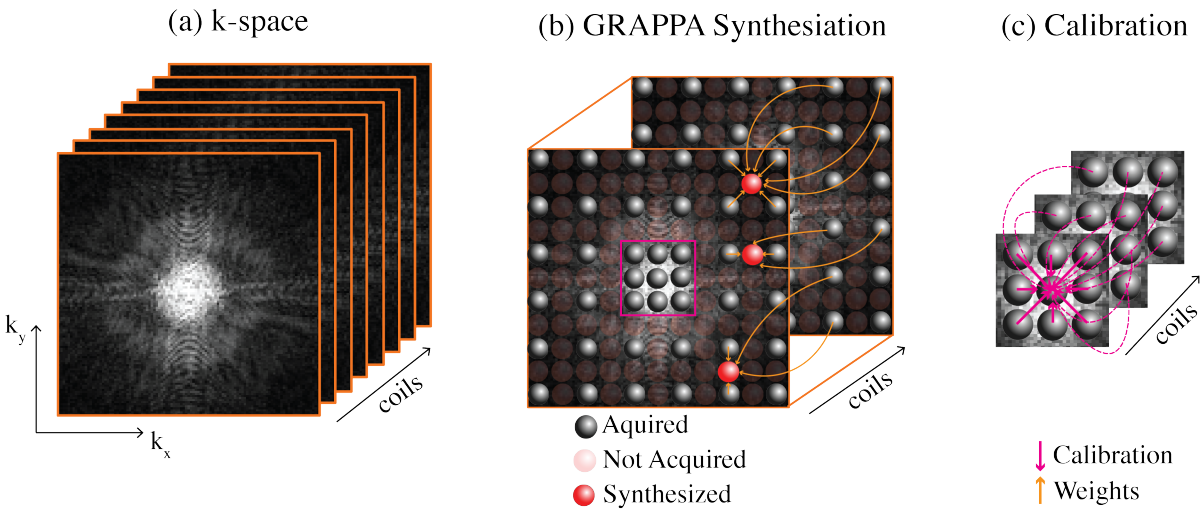

Figure 6.3: Traditional 2D GRAPPA: Missing k-space data are synthesized from neighboring acquired data. The synthesized kernel depends on the specific sampling pattern in the neighborhood of the missing point. The reconstruction of a point is independent of the missing points.

solution. The main assumption here is that if the calibration consistency holds within the calibration area (central k-space), it also should hold in other parts of k-space.

In traditional GRAPPA ,different sets of weights must be obtained for each sampling pattern. The 2D GRAPPA reconstruction depicted in Figure 6.3(b), portrays three equations to solve three missing data points. Each of the equations uses a different set of calibration weights. The neighborhood size is a matrix of three by three k-space pixels.

6.2.3 SPIRiT

SPIRiT is similar to GRAPPA in that it uses auto-calibration lines from the densely sampled center of k-space to find linear weights to synthesize missing k-space but it differs in the way it enforces data consistency. SPRiT describes the reconstruction as an inverse problem governed by the data consistency constraints that are split into two parts: (1) consistency with the calibration, and (2) consistency with the data acquisition. These constraints are formulated as sets of linear equations and the desired reconstruction is the solution that satisfies these equations according to a suitable error measure criteria.

(1) The calibration consistency equation for any k-space data point is given by,

$$p_c(\bar{r}) = \sum_{j=1}^{C} \langle \mathcal{W}_{jc}, \mathcal{P}_{j\bar{r}} \rangle \overset{vector}{\Longrightarrow} \mathbf{p} = W\mathbf{p} \tag{6.4}$$

where $\mathcal{W}_{jc}$ is set of weights obtained by calibration, similar to Equation 6.2 and W is a matrix containing the weights in the appropriate locations. The important difference from the traditional GRAPPA kernels, $\mathcal{W}^a_{jc}$, and SPIRiT kernels, $\mathcal{W}_{jc}$, is that SPIRiT kernel is a full kernel where all the k-space points are included whether they are acquired or not. While traditional GRAPPA enforces calibration consistency only between synthesized points and the neighboring acquired points, SPIRiT enforces calibration consistency between every point on the grid, $p_c(\bar{r})$, and its entire neighborhood across all coils, $\mathcal{P}_{c\bar{r}}$ which in exchange requires an additional data consistency constraint to be enforced for the algorithm to converge. More simply put, Equation 6.2 defines a large set of "decoupled" linear equations that can be solved separately however, Equation 6.4 defines a large set of "coupled" linear equations which need to be solved iteratively. Thus, during each iteration an additional constraint needs to be enforced by keeping the acquired data the same through out the N iterations.

(2) The data acquisition consistency equation for any k-space data point is given by,

$$q_c(\bar{r}) = \sum_{j=1}^{C} \langle \mathcal{V}_{jc}, \mathcal{P}_{j\bar{r}} \rangle \overset{vector}{\Longrightarrow} \mathbf{q} = V\mathbf{p} \tag{6.5}$$

where $\mathcal{V}_{jc}$ is an operator that selects only acquired k-space locations and V is a matrix that selects an arbitrary sampling pattern in Cartesian coordinates and an interpolation matrix in non-Cartisian ones. In other words, the reconstruction must also be consistent with the acquired data $\mathbf{q}$ and it is satisfied with this operation.

Considering Figure 6.4 which has a similar sampling setup as the 2D GRAPPA problem in Figure 6.3. In the figure, two equations are portrayed. It shows that the synthesis of a missing central point depends on both acquired and missing points in its neighborhood and that the equations are coupled.

Calibration is computed once prior to image reconstruction. Due to noise and calibration errors the linear equations in Equation 6.4 and 6.5 can only be solved approximately. Therefore, the k-space reconstruction is a solution to an optimization problem given by:

$$\begin{aligned} \underset{p}{\text{minimize}} \quad & \|(W - I)\mathbf{p}\|^2 \\ \text{subject to} \quad & \|D\mathbf{p} - \mathbf{q}\|^2 < \epsilon \end{aligned} \tag{6.6}$$

The parameter ϵ is introduced as a way to control the consistency by trading off the data acquisition consistency with calibration consistency. A useful reformulation of Equation 6.6

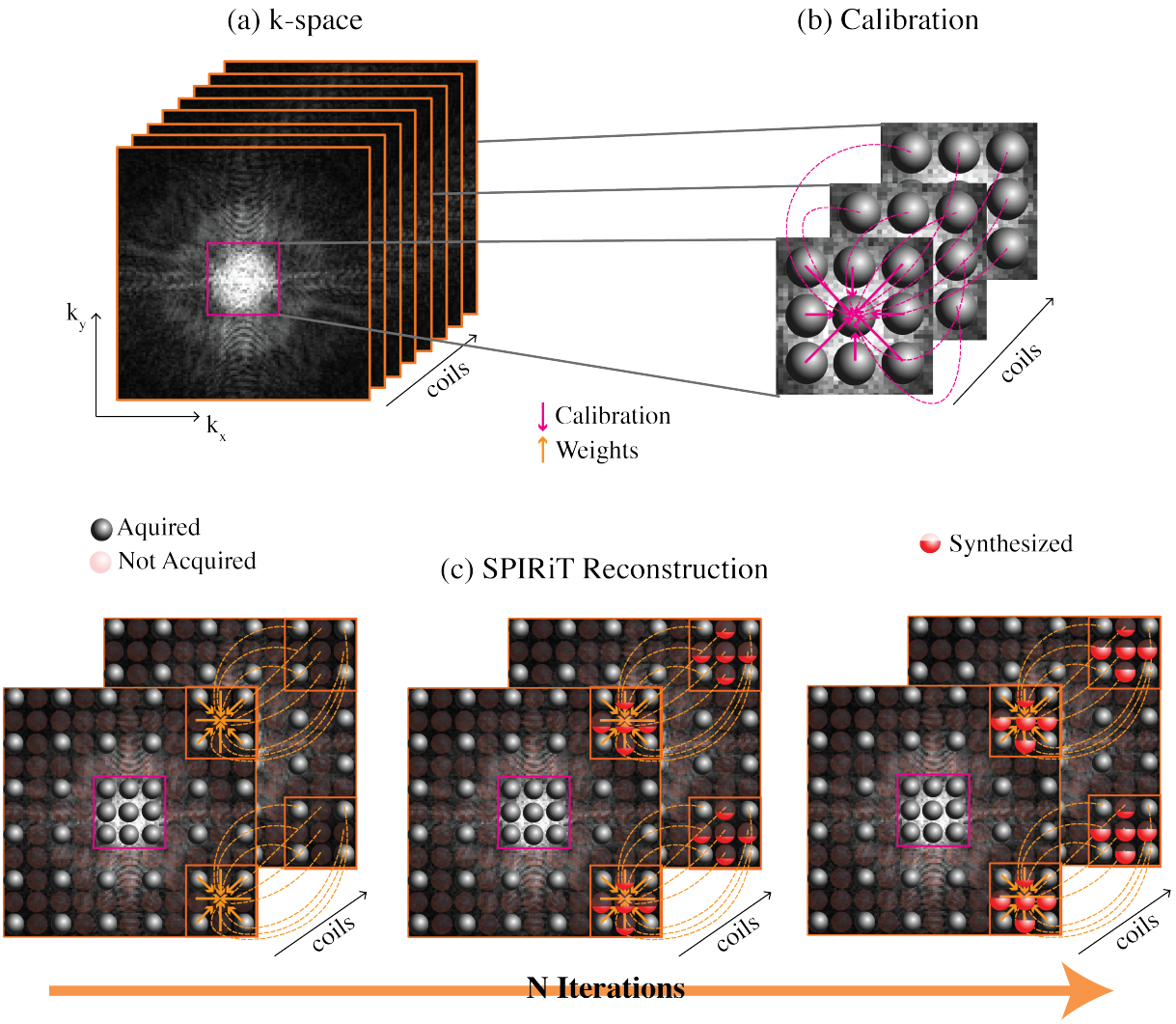

Figure 6.4: 2D SPIRiT: Missing k-space data are estimated iteratively from the entire neighboring points acquired or not acquired. The reconstruction of missing point depends on the reconstruction of other missing points. The SPIRiT kernel is independent of any specific sampling pattern.

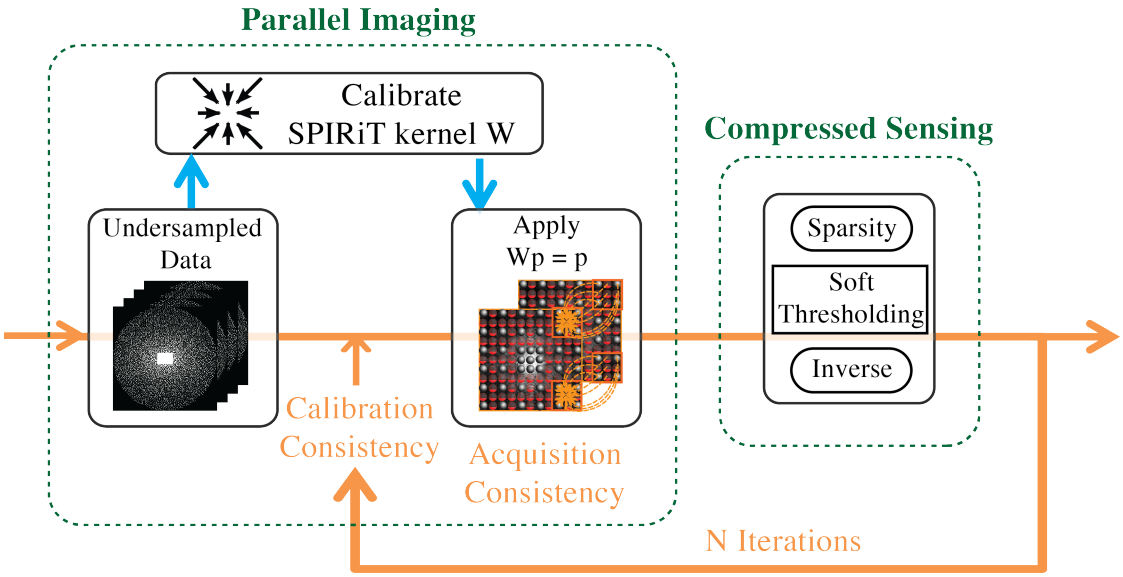

Figure 6.5: ℓ_1-SPIRiT Diagram for MRI images.

is the unconstrained Largangian which can be solved by methods such as the conjugate gradient (CG) algorithm or projection over convex sets (POCS) and is given by:

$$\underset{p}{\operatorname{argmin}} \|(V\mathbf{p} - \mathbf{q})\|^2 + \lambda(\epsilon) \|(W - I)\mathbf{p}\|^2 \tag{6.7}$$

where the parameter λ can be chosen experimentally. The POCS algorithm does not solve the constrained minimization exactly, but instead minimizes the related Lagrangian objective function. The POCS algorithm converges to a fixed-point that satisfies the above constraints, often within 50-100 iterations.

6.2.4 ℓ_1-SPIRiT

The ℓ_1-SPIRiT is an extension of the original SPIRiT that in addition to enforcing consistency constraints with calibration and acquired data, enforces joint-sparsity of the coil images in the Wavelet domain as illustrated in a diagram in a Figure 6.5. The reconstruction problem solves a constrained non-linear optimization over the image matrix. The non-linearity of this optimization necessitates an iterative reconstruction.

ℓ_1-SPIRiT is an approach for accelerated acquisition by combining compressed sensing with an auto-calibration parallel imaging technique. In this case, the sampling pattern needs to be optimized to provide the incoherence that is required for compressed sensing yet be compatible for parallel imaging as depicted in Figure 6.6. Uniform undersampling makes coherent aliasing which harms CS reconstruction. Random undersampling is either bunched

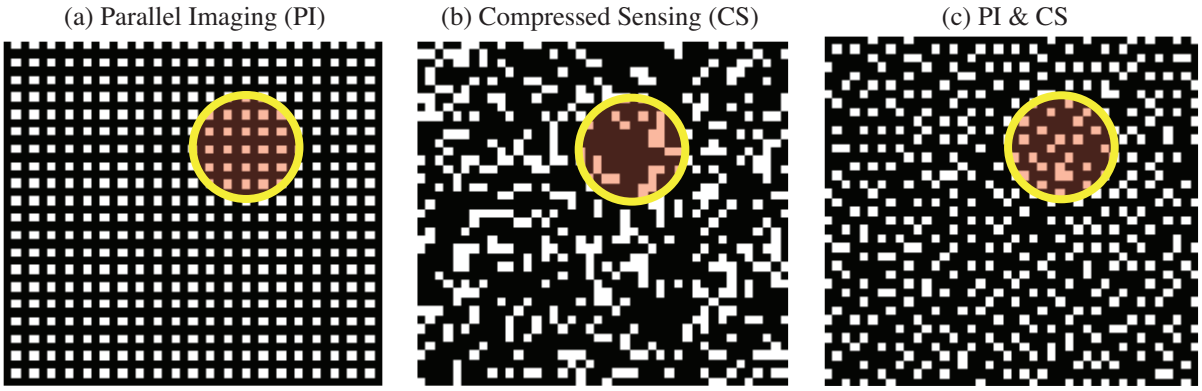

Figure 6.6: (a) Uniform undersampling (Not incoherent) harms compressed sensing reconstruction. (b) Random undersampling (bunched or too many "holes") harms parallel imaging reconstruction. (c) Locally uniform and globally random undersampling (Poisson-Disc Sampling).

together or has too many "holes" which harms PI reconstruction because coil information is local in k-space and uniform local acceleration has a good noise properties. Therefore for ℓ_1-SPIRiT one needs a locally uniform and incoherent sampling pattern such as Poisson-Disc Distribution.

It is important to note that ℓ_1-SPIRiT is computationally more intensive than SPIRiT. There are four operations which dominate runtime: SPIRiT auto-calibration, Fourier transforms during the k-space consistency projection, Wavelet transforms during the joint soft-thresholding, and the image-domain implementation of SPIRiT interpolation. Note that PI calibration must be performed only once per reconstruction, and is not part of the iterative loop. The resulting runtimes demonstrate that computational expense is a substantial obstacle to clinical deployment of ℓ_1-SPIRiT.

Although the underlying mechanism of SENSE, GRAPPA, SPIRiT, and ℓ_1-SPIRiT are reasonobly simple, there are many factors to consider in developing the most optimal and appropriate reconstruction techniques for particular MRI applications. These can be divided into three broad main categories: (1) hardware, (2) software, (3) theory and algorithms.

Hardware requirements and components:

- **Multiple Receiver Coils** must be positioned so that each coil has a different sensitivity over the FOV, especially in the direction that the acceleration is applied. One major consideration is the choice of the optimal relationship among the arrangement of coil elements, coil positioning, and desired orientation of the imaging plane, since these factors directly influence the g-factor of the acquisition. For array coils to produce max-

imum SNR they must be "independent", i.e. there is no crosstalk between coils. The maximum acceleration factor (R) is then limited by the number of independent coil elements. However, there is still a gap between the theoretical speed-ups that should be achieved and those that actually are. Coil design is a rapidly evolving area with parallel imaging criteria and approaches can differ depending on the reconstruction method being considered (more details in Chapter 3).

- **SNR:** The reduced SNR of PI-MRI is an intrinsic disadvantage common to all accelerated techniques that acquire a reduced data set in order to shorten the scan time. The classic SNR equation for parallel imaging that was proposed by Pruessmann is $\mathrm{SNR}_R = \frac{\mathrm{SNR}_O}{g\sqrt{R}}$. The baseline SNR is proportional to the square root of the total time spent for data acquisition $\mathrm{SNR}_O = \Delta x \times \Delta y \times \Delta z \times \sqrt{T_{acq}} \times \mathbf{B_0}$. Accelerating by a factor of 2 produces 50% loss in SNR. Therefore PI is only suited for applications with high SNR. The SNR losses become even more significant if PI is applied to increase the spatial resolution. Keeping the acquisition time constant but increasing $1 \times 1 \times 1 mm^3$ spatial resolution to $0.5 \times 0.5 \times 0.5\ mm^3$ reduces the voxel volume by eight-fold.

- **Noise or g-factor:** The noise distribution in parallel imaging is described by a spatially varying geometry noise called g-factor (g). The g-factor is related to coil geometry, image orientation, the FOV, the speed-up factor (R), and the k-space sampling pattern. The g-factor noise originates in the aliased input data, not in the sensitivity measurement of the coils; however, the sensitivity data amplifies this noise, in other words, the g-factor term arises as a result of the coil sensitivities being too similar. The ideal g-factor is 1. Parallel imaging is fundamentally limited by the g-factor. There are numerous strategies available to reduce its impact, much of which involves improved coil design.

- **Sequence development for undersampling** Reducing the sampling density and increasing the number of coil elements can be combined with almost all types of MR pulse sequences. The only precondition with respect to the pulse-sequence design is that the phase-encoding sampling density in k-space can be varied, and this is true for virtually all pulse sequences that acquire at least two-dimensional k-space data. Therefore, the implementation of parallel imaging in conventional pulse sequences is relatively uncomplicated. Parallel imaging can be combined with conventional Cartesian k-space trajectories as well as with non-Cartesian sampling strategies such as radial or spiral trajectories; however, the complexity of the image reconstruction differs substantially depending on the k-space sampling strategy. In Cartesian k-space sampling, reducing the sampling density simply corresponds to choosing a smaller field of view. Only if the acquisition of coil-sensitivity profiles is to be integrated into the sequence, additional considerations are required to avoid inefficient sequence designs. In the case of MRSI, more complex pulse-sequence modifications are required (more details in Chapter 5).

Software requirements and components:

- **Computation Intensities** In PI, the hardware delivers one dataset per channel, and the role of the software computation is to reconstruct a clinically useful image. A big challenge for massively accelerated image acquisition is therefore the increase in time and hardware capability for post-processing. The more independent receiver coils employed, the higher the allowance the reduction rates and the lower the g-factors achieved at the expense of computation intensities. Some PI techniques pose feasibility limits in terms of invertibility and storage, even on state-of-the-art workstations. A speed up factor of 2 with an 8-channel array coil and Cartesian sampling are computationally an entirely different issue from speed up factor of 5, with 32-channel coils, and non-Cartesian or arbitrary sampling.

- **Parallel computing** Although the required operation does not necessarily need thousands of lines of code, the factors that slow down the reconstruction are related to the number of channels, number of iteration, and the use of very large matrices. For this reason using parallel computing is very beneficial and necessary. Real-time parallel MRI is feasible, though challenging, because fast parallel imaging reconstruction requires powerful computers and optimized reconstruction algorithms.

Theory and algorithm optimizations:

- **Assumptions and Conditions** Underlying requirements and assumptions of each parallel imaging method vary quite a bit, and since these directly relate to the potential image artifacts seen in images reconstructed with any particular parallel imaging method, one needs to pay particular attention to them. For example, this class of methods works very well in situations where there is enough time to acquire coil sensitivity images of moderate resolution without patient motion, e.g., in brain exams; however, these methods can be sensitive to patient motion, particularly in breath-hold exams, and can produce serious errors whenever aliasing is present in the coil sensitivity maps, since the assumption of smoothness used in the polynomial fit is violated.

- **Optimization of reconstruction parameters** In order to optimize the reconstruction, one needs to be able to manipulate the parameters which affect it. That means finding and defining these parameters for each application. For example, the reconstruction equations are often badly conditioned, which means that if they are solved using a straightforward method, the errors due to noise get amplified. Two procedures that can be implemented in software to handle this are preconditioning and regularization which need to be defined empirically. Regularization allows for a practical trade-off between noise minimization, effective voxel size, and unaliasing.

- **Iterative methods** Sometimes approximate iterative methods enable fast reconstructions where they would have not been possible otherwise. However, they may be numerically unstable and slow (compared to the direct methods) with the stopping criteria and convergence of the techniques being important factors.

6.3 From GRAPPA to SPIRiT to ℓ_1-SPIRiT Implementation for MRI images: Lessons Learned

The auto-calibration methods discussed earlier in this chapter are summarized in Table 6.2. Although the mathematical foundation of the various reconstruction methods is similar, they involve different assumptions and approximations. Consequently, each method performs differently under given conditions (e.g. array geometry, k-space sampling schemes and underlying applications). Methods also vary in terms of numerical stability and computational complexity.

To develop and deploy parallel imaging techniques for a specific application, it is desirable to qualitatively and quantitatively characterize and analyze the different techniques. Therefore, GRAPPA, POCS SPIRiT and POCS ℓ_1-SPIRiT were implemented in MATLAB to provide data simulation, image reconstruction, and performance analysis for a 2D brain images. The current version of the algorithms works with rectilinear k-space data that could be undersampled along any phase encoding direction with an arbitrary pattern.

The SPIRiT-like algorithms can easily cope with arbitrary sampling patterns and have advantages in reconstructions for highly nonuniform sampling patterns since the calibration step for SPIRiT is very simple and happens once. In GRAPPA, reconstruction from such sampling schemes requires numerous calibration calculations. The difference in computation times are very noticeable in a 2D brain MRI images and are presented in Table 6.3.

Three undersampling patterns were used with two of them being designed by choosing samples according to Poisson-Disc sampling density and the other one uniformly undersampled as shown in Figure 6.7 . The fully sampled area of 24×24 samples was left in the center of k-space for calibration.

The undersampled data sets were reconstructed using GRAPPA, POCS SPIRiT and POCS ℓ_1-SPIRiT, followed by a square root of sum of squares combination of the 8 coils images. Comparing Figure 6.8 and Figure 6.9 illustrates that upgrading from uniform random sampling to Poisson-Disc random sampling gives better quality images. Also with Poisson-Disc random sampling, the POCS ℓ_1-SPIRiT outperforms the POCS SPIRiT and GRAPPA. At higher acceleration, where each data measurement counts, the difference in the reconstruction becomes even more significant.

In all our experiments, the SPIRiT and ℓ_1-SPIRiT reconstruction had better noise performance than GRAPPA, specially when the acceleration is pushed to the limit (example: Figure 6.10) . This is because SPIRiT-like algorithms use the acquired data more efficiently. Since, SPIRiT is an iterative process, the operation is repeated in every iterations so the "information" travels in kspace. The acquired data in one location of k-space affects the

Table 6.2: Summary of the formulation, conditions and assumptions for compressed sensing techniques as well as parallel imaging techniques for GRAPPA, SPIRiT, and ℓ_1SPIRiT.

Algorithms	**Formula**	**Conditions**
CS	$\underset{p}{\text{minimize}} \quad \|\Psi p\|_1$ subject to $\quad \|\mathcal{F}_s p - q\|_2 < \epsilon$	Objective enforces sparsity. Constraint enforces data consistency.
GRAPPA	$p_c(\bar{r}) = \sum_{j=1}^{C} \langle \mathcal{W}^a_{jc}, \mathcal{P}^a_{j\bar{r}} \rangle$	Enforcing calibration consistency: between synthesized points and the acquired neighbor points.
SPIRiT	(1) $p_c(\bar{r}) = \sum_{j=1}^{C} \langle \mathcal{W}_{jc}, \mathcal{P}_{j\bar{r}} \rangle \implies \mathbf{p} = W\mathbf{p}$ (2) $q_c(\bar{r}) = \sum_{j=1}^{C} \langle \mathcal{V}_{jc}, \mathcal{P}_{j\bar{r}} \rangle \implies \mathbf{q} = V\mathbf{p}$ $\underset{p}{\text{minimize}} \quad \|(W-I)\mathbf{p}\|^2$ subject to $\quad \|D\mathbf{p} - \mathbf{q}\|^2 < \epsilon$	Enforcing consistency w/ (1) Calibration: between every point and its entire neighborhood. (2) Data acquired: replaces the estimated points to acquired points Objective enforces consistency with calibration. Constraint enforces consistency with data acquisition.
ℓ_1**SPRiT**	$\underset{p}{\text{minimize}} \quad$ **Joint** $\ell_1(\Psi p)$ subject to $\quad W\mathbf{p} = \mathbf{p}$ $\mathbf{p}\|_{acq} = \mathbf{q}$	Enforcing consistency w/ (1) Calibration (2) Data acquired (3) Joint-sparsity of the coil images.

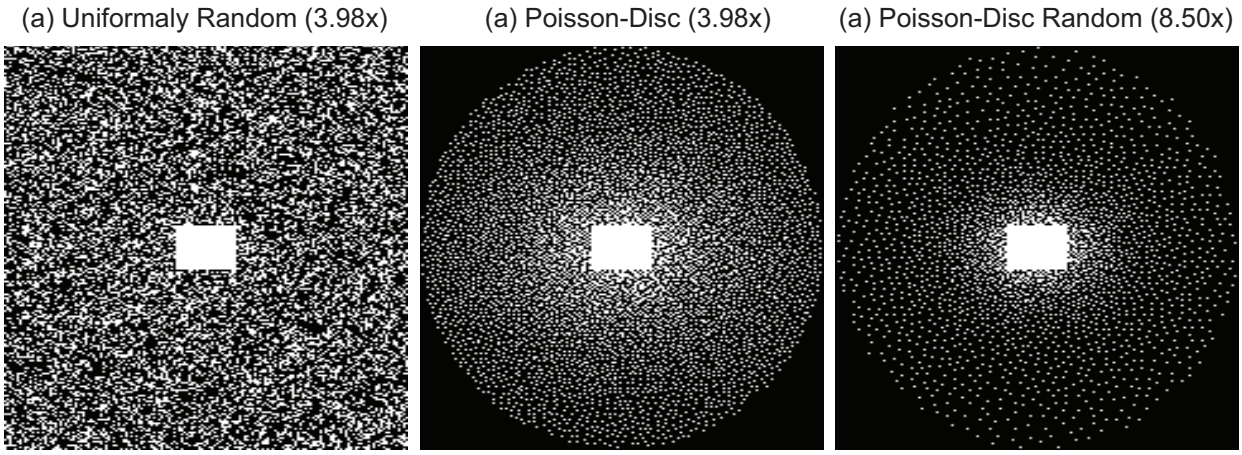

Figure 6.7: Random Undersampling Patterns of kspace used in our experiments

reconstruction of k-space locations far beyond the kernel radius and this is very similar to averaging the effect of noise.

The calculation of SNR in the reconstructed image in parallel imaging is potentially complex. Autocalibrating parallel imaging methods, such as GRAPPA and other variable density k-space sampling techniques, maintain full sampling at the center of k-space in order to obtain calibration information to use for unwrapping the aliased data, which adds tremendous complexity to the SNR analysis of these images. The central part of k-space provides most of the contrast information (background) in an image and carries most of the image power (signal intensity) which affects SNR. Higher spatial frequencies (details) that carry important edge information are undersampled and the noise distribution will be non-uniform across the image. Therefore, the SNR calculation requires multiple measures. In our comparison, the results are presented in terms of relative difference error and computation time. The relative error was calculated as follows:

$$\xi = \frac{\|I - \hat{I}\|_{frobenius}}{\|I\|_{frobenius}}$$

The results for 3.98x acceleration is summarized in Table 6.3, where the longest computation time and the largest error belongs to GRAPPA. Although POCS SPIRiT has similar relative error to POCS ℓ_1-SPIRiT with much lower computational time and complexity, ℓ_1-SPIRiT provides the benefit of compressed sensing. It is important to note that the computation time for the iterative algorithms varies based on their number of iterations and convergence. The Figure 6.10 shows that introducing an additional ℓ_1 constraint to the basic SPIRiT algorithm allows accelerations beyond the level that parallel imaging alone would tolerate.

The POCS algorithm is efficient, converges rapidly, and performs a minimal number of

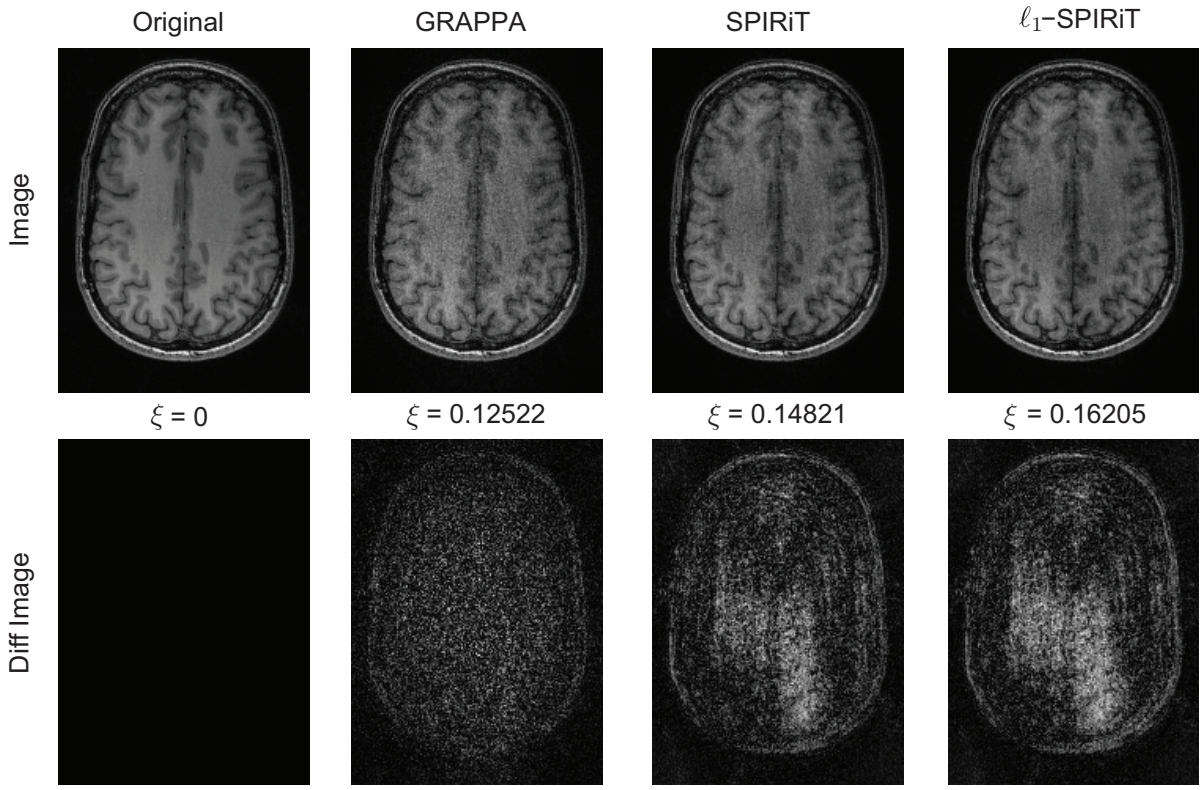

Figure 6.8: Actual acceleration of 3.980 (2x in each direction), Uniformly Undersampled

Algorithms	Relative Error	Time (sec)
GRAPPA	0.1318	193.7
POCS-SPIRiT	0.0945	39.08
POCS-ℓ_1-SPIRiT	0.0930	119.8

Table 6.3: Summary of computation times and relative errors for actual acceleration of 3.98

operations per iterations. However, a massively parallel and well-optimized software implementation is still needed to achieve clinically feasible runtimes. As it is discussed in (24) the computational complexity of SPIRiT-like calibration alone is of the order of C^4, where C is the number of channels. This is prohibitively expensive for large coil arrays. The term $\mathcal{O}(C^2\ v)$, where v is number of voxels per channel, is representation of SPIRiT-like interpolation and is asymptotically the bottleneck for the POCS algorithm.

Despite the fact that SPIRiT and ℓ_1-SPIRiT are iterative and computationally intensive

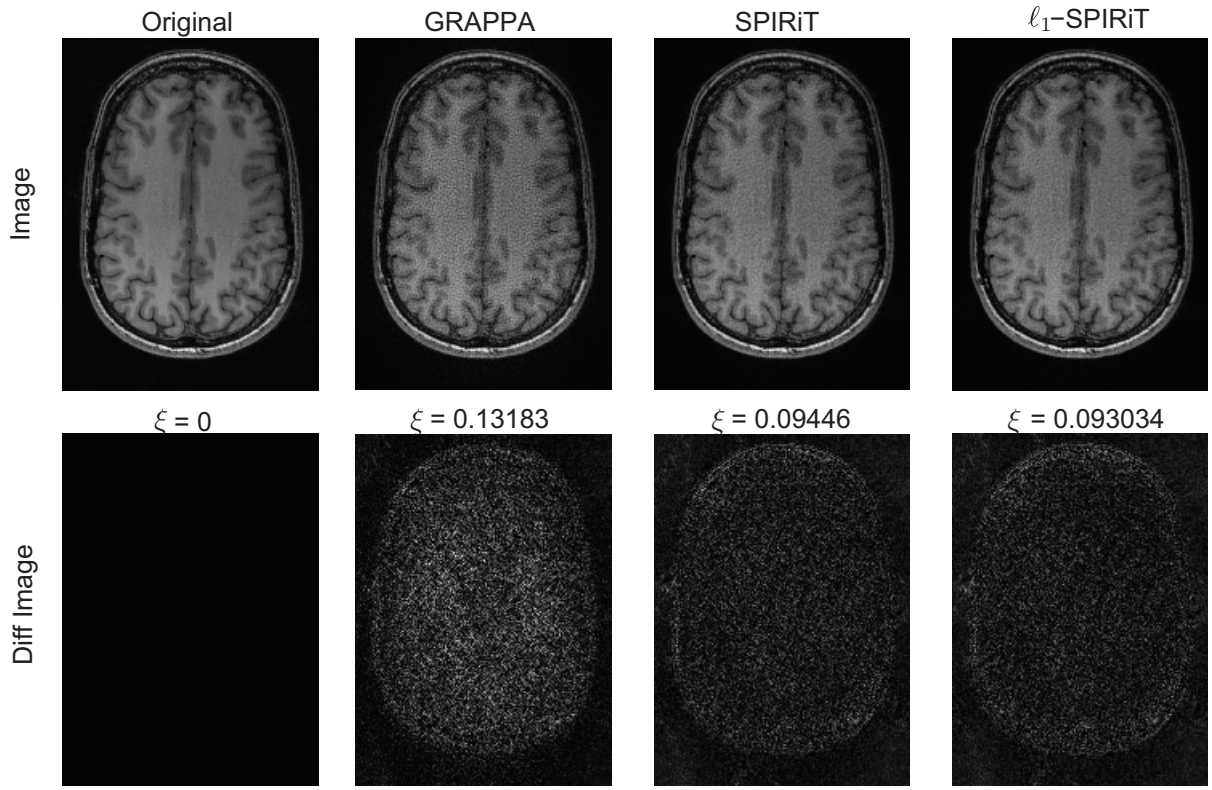

Figure 6.9: Actual acceleration of 3.98 (2x in each direction), Poisson-Disc Undersmapled

algorithms, with more parameters to define/tweak for particular application, they provide more flexibility and acceleration that can be tailored towards a particular application. Therefore, these promising results provided motivation to extend these implementations to MRSI applications.

6.4 Barriers to Adopting Parallel Imaging & Compressed Sensing techniques for MRSI (H-1 and C-13) Applications

Although MRSI uses the similar phase encoding techniques that are used in MRI, MRSI faces additional challenges to embrace PI and CS techniqes. For H-MRSI, the signals are produced by metabolites within the tissue being imaged. The molecular concentrations of these metabolites are at least 10,000 times lower than water, which produces a relatively low SNR. To provide sufficient sensitivity for quantification, H-MRSI must be acquired with much larger voxel sizes (in order of cm^3 rather than mm^3). Although phased array coils

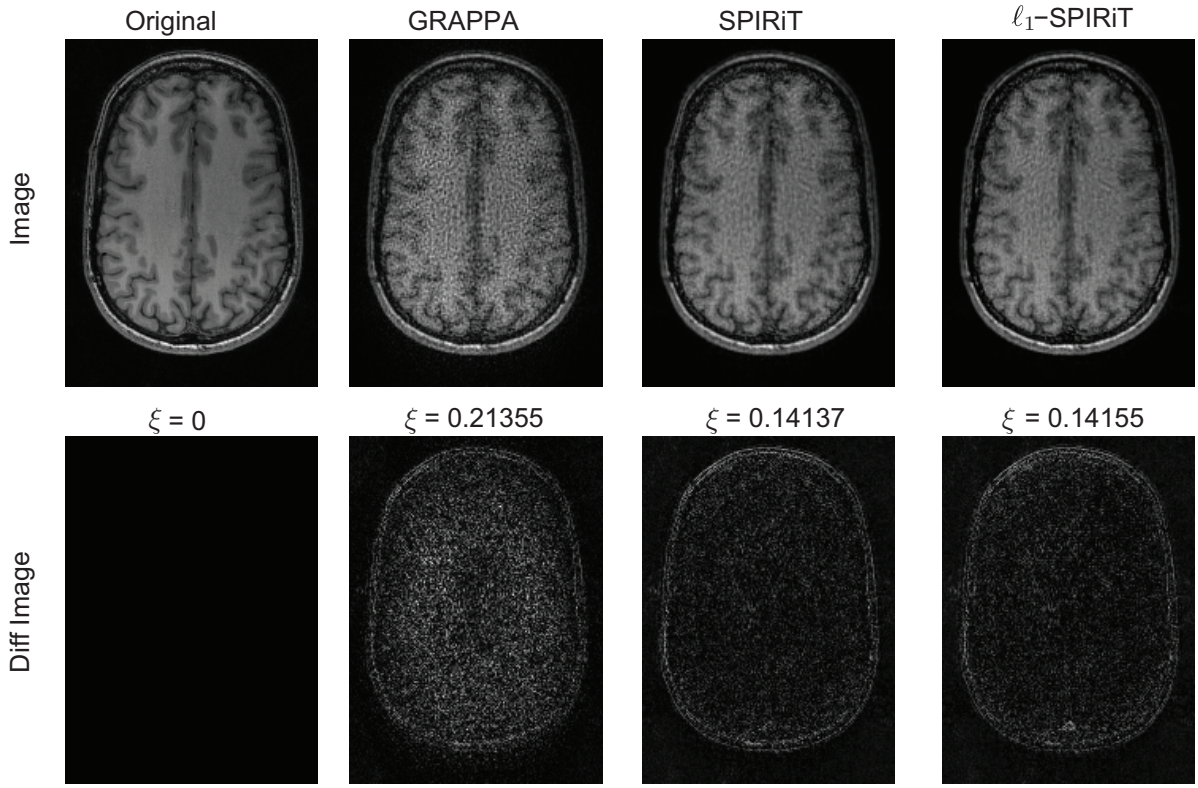

Figure 6.10: Actual acceleration of 8.496920 (3x in each direction)

allow for smaller voxel volumes or shorter acquisition time, the maximum acquisition time or voxel volume reduction is ultimately limited by the metabolite's low concentration.

Consequently, the low spatial resolution of MRSI makes consideration of the spatial point spread function (PSF) more important. For MRI applications, a pixel can be approximated by a Dirac function, but in MRSI acquisitions, the PSF or "shape of a pixel" is represented by a sinc-like function only remotely resembling a Dirac function. A pixel in the aliased dataset is therefore not only a sum of corresponding unaliased signals, but contains contributions from many other spatial positions. Therefore, for successful reconstruction of accelerated MRSI data, the design of optimal sampling patterns becomes more critical by controlling the aliased artifacts in the image domain.

MRSI is also highly sensitive to macroscopic magnetic field inhomogeneity within a voxel and across the volume of the interest. This introduces regionally varying spectral line broadening. In H-MRSI there may also be artifacts related to water and lipid signals caused by field inhomogeneity and the PSF. This can severely harm the PI reconstruction.

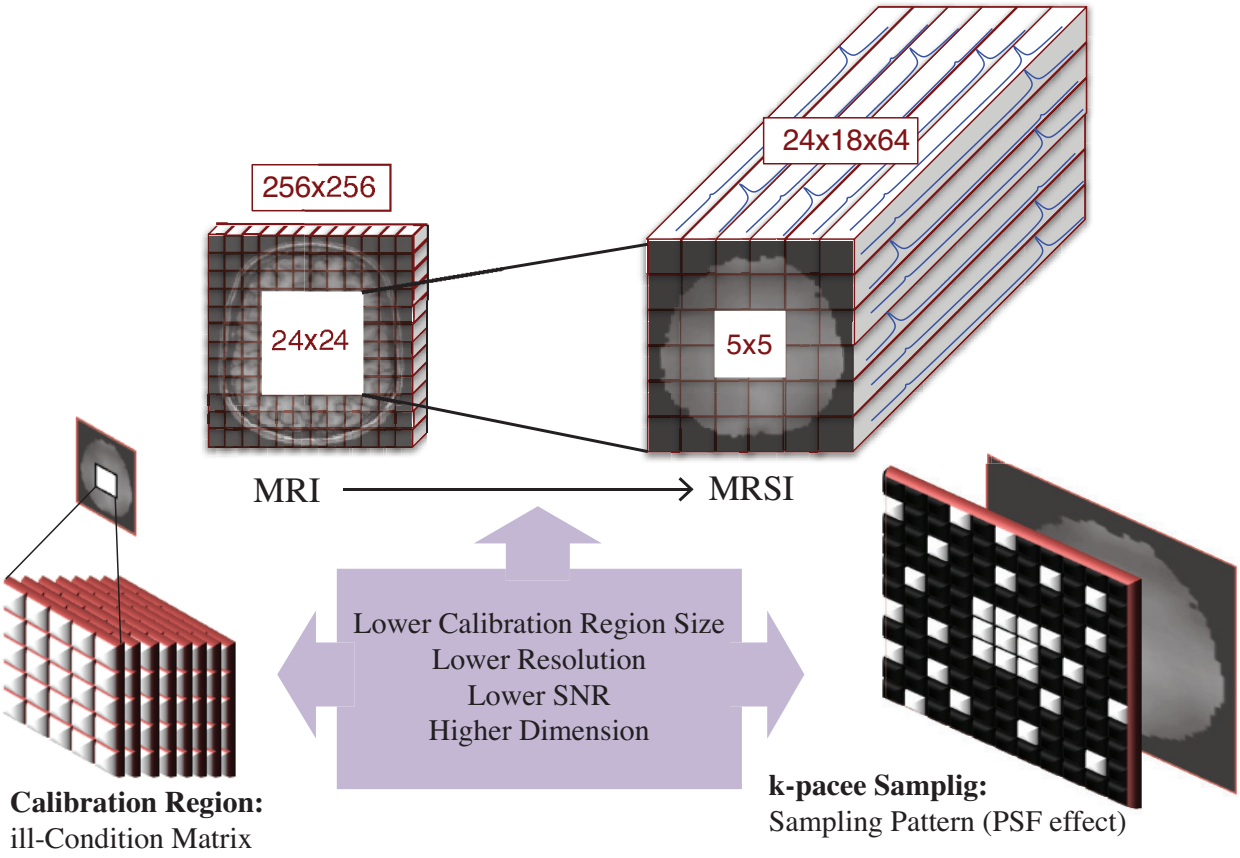

Figure 6.11: Additional parallel imaging obstacles of MRSI vs MRI.

Self-calibrating parallel imaging techniques are attractive for MRSI because coil sensitivity information is estimated from the data itself, but the dense sampling of the center of k-space required for accurate reconstruction is disadvantageous for MRSI, where the typical 16×16 phase encodes allows for at most a 5×5 calibration region. It is important to note that in MRI application the calibration regions are usually on the order of 27×27. Acceleration in PI-MRSI is also limited by noise amplification due to reduced number of phase encodes (g-factor – similar to MRI), instability in the inverse reconstruction (due to not enough independent measurements), condition numbers and "converge-ability" of iterative reconstruction methods.

Acceleration of H-MRSI is highly desirable to increase coverage volume, reduce motion sensitivity and decrease scan time, if SNR permits. Several approaches are available to reduce the SNR penalty and thus increase the acceleration capability, such as use of a ultra high-field scanner (e.g. 7T), coil arrays with large number of elements (e.g. 32- or 64-channel), and regularization of the inverse reconstruction techniques; each of which comes with additional

costs. At ultra high-fields, MRSI benefits from increased SNR, as well as the possibility to quantify more metabolites as a result of better separation of neighboring resonances. In this case the gain can be translated to either higher spatial resolution or faster scanning. However, there are several technical limitations with higher field, such as stricter specific absorption rate (SAR) constraints, SNR loss as a result of shorter T_2 relaxation times, spatially varying flip angles caused by $\mathbf{B_1}$ inhomogeneities, less reliable lipid/water suppression, increased chemical shift artifacts and larger $\mathbf{B_0}$ inhomogeneities. While array coils with higher number of elements and 3D geometry result in higher SNRs and higher acceleration factors (at-least up to the g-factor limit), they also add to the computation complexity (time and storage).

Acceleration of hyperpolarized C13-MRSI is desirable due to the amount of time available before the signal decays. Hyperpolarized technology uses Dynamic Nuclear Polarization (DNP) to enable a direct monitoring of C13 metabolites in-vivo at relatively a high SNR compared with natural abundance C13 (25, 26). The major technical challenge for in-vivo applications of hyperpolarized C13 MR is the subminute lifetime of the hyperpolarized signal (due to T_1 decay). Since the polarization is from an exogenous source, each excitation pulse destroys a portion of the available signal, which also limits our measurement times. Consequently, hyperpolarized C13-MRSI acquisition necessitates very efficient and rapid k-space sub-sampling and reconstruction. The high SNR and sparse spectrum of C13-MRSI along with the necessity of fast acquisition makes this a perfect application for utilizing parallel imaging and compressed sensing techniques. we anticipate that we will need to combine all the strategies in order to achieve the desired temporal resolution, spatial resolution and increased volumetric coverage within the required time window.

Parallel imaging was initially applied to 2D spectroscopic imaging employing SENSE method (27). However, phase cancellations reduced metabolite signal and introduced artifacts. In MRSI, to avoid phase cancellation, coherent phase alignment between the data from the individual coils in a phased array is required. However, spectral phase alignment is difficult to integrate into the SENSE algorithm because in SENSE, aliased images are constructed from each coil element prior to image unfolding and combination. Therefore, phase alignment of the spectra is confounded by contamination from aliased voxels at this stage. In contrast, GRAPPA which allows reconstruction of unfolded images for each coil element, provides greater flexibility for spectral phase alignment. Furthermore, the need for coil sensitivity information could be a major challenge to reconstruct optimally. In Hyperploarized 13C-MRSI imaging, external sensitivity references can be impractical due to low natural abundance of 13C. Therefore, self-calibrating parallel MR techniques are more attractive because necessary coil sensitivity information is acquired as part of the acquisition. Thus we investigated GRAPPA-based methods and their feasibilities in our studies. GRAPPA is one of the self-calibrating techniques, and SPIRiT algorithm is just a generalized GRAPPA, however, it has the ability to enforce an additional ℓ_1 constraint to take advantage of compressed sensing as well. ℓ_1-SPRiT allows the compressed sensing method to be used to accelerate beyond what

parallel imaging alone would support.

6.5 From GRAPPA to SPIRiT to ℓ_1-SPIRiT Implementation for MRSI data: Lessons Learned

The purpose of next few studies were to develop and validate a strategy for combining echo planar k-space sampling with self-calibrating parallel imaging and compressed sensing techniques to rapidly acquire and reconstruct metabolic imaging data from the brain. Due to our promising preliminary results in MRI applications, we initially started with SPIRiT-like reconstructions.

In the first two projects, we introduced a new approach for the reconstruction of accelerated 3D-EPSI-MRSI data using our "modified-SPIRiT" and "modified-ℓ_1SPIRiT" algorithms for two separate MRSI applications (7T 32-channel H1-MRSI and 3T 8-channel C13-MRSI) and to the best of our knowledge these are the first MRSI studies based on these iterative algorithms. In this approach the whole spectrum is used to offset the small calibration region for robust estimation of SPIRiT calibration kernels, and voxel-by-voxel spectral phase alignment between metabolites from individual coil elements is performed in the frequency domain. The performance of these techniques were compared to the fully encoded 3D-EPSI.

The data from 3D-MRSI acquisition has 3 spatial frequency dimensions and a time dimension for free induction decay (k_x, k_y, k_z, k_f). After an inverse Fourier transform in the z-direction ("slice" direction), the spectral data can be processed by two-dimensional SPIRiT-based reconstruction for each slice separately. Figure 6.12 shows a flow chart for the 2D-SPIRiT-based reconstruction. The SPIRiT kernel is calibrated from autocalibrations lines from all the coils and all the time points k_f of the FID using least-squares. The consistency equation for any k-space data point is given by,

$$p_c(\bar{r}, f) = \sum_{j=1}^{C} \langle \mathcal{W}_{jcf}, \mathcal{P}_{j\bar{r}f} \rangle \overset{vector}{\Longrightarrow} \mathbf{p} = W\mathbf{p} \tag{6.8}$$

The calibration matrix W has lower spatial-frequency but additional frequency information compared to its MRI counterpart. This matrix is very ill-conditioned and the implementation of Tikhonov regularization and/or truncated-SVD technique should further improve the conditioning of the this matrix. In each iteration SPIRiT kernel is applied to all the k-space points to enforce consistency with calibration. In the case of ℓ_1-SPIRiT, sparsity is enforced next in the transform domain (frequency: the spectrum is sparse) by soft-thresholding (chosen experimentally as discussed in Chapter 5) which is equivalent to minimizing the ℓ_1-norm. However, this step is skipped for SPIRiT. Then acquired k-space data points will replace their estimated values to enforce data consistency and the algorithm moves to the next iteration until the stopping criteria is reached.

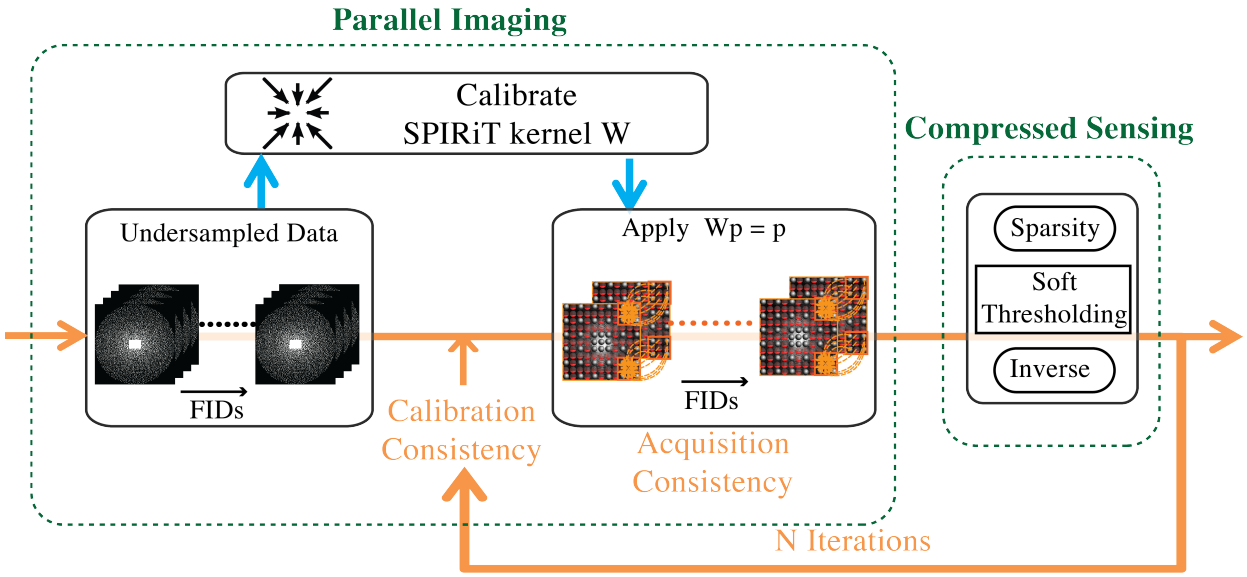

Figure 6.12: Modified SPRiT and ℓ_1-SPIRiT Diagram for MRSI.

It turned out that accuracy of reconstruction in k-space strongly depended on the selection of the k-space subset, and/or reconstruction kernel specially for MRSI. In general there is an insufficient understanding of how to automatically control these parameters and their associated errors. Obviously, the optimal k-space subset depends on coil sensitivities, coil placement, and the object itself. Increasing the subset size from a single sample to a few samples distributed in the phase encoding direction and enlarging it to two-dimensional configurations significantly improved image quality. However, increasing the size of subsets degrades the benefits of implementing parallel imaging acquisition in k-space. Moreover, there is no guarantee that simply enlarging k-space subsets will provide acceptable image quality.

6.5.1 SPIRiT, ℓ_1SPIRiT, and CS for Metabolic Imaging Using Hyperpolarized C-13 MRSI at 3T

The subject was a 9-year old female cynomolgus monkey (body weight=4.3 kg) who was imaged on multiple occasions to verify the experimental setup being developed for human brain studies (Figure 6.13). A clamshell volumetric C13 transmit coil and bi-lateral 8-channel phased array receive coil were used on a GE 3T scanner (GE, Medical Systems, Milwaukee, WI).

Acquisition: Prior to each C13 imaging experiment, T_1-weighted anatomical images were obtained in the axial and sagittal planes using an inversion recovery spoiled gradient echo (IRSPGR) sequence (echo time/repetition time/inversion time = 2.5/8.4/400 ms, 25 cm

FOV, 256×256 matrix, 3 mm slice thickness, and 5 NEX) from the body coil. The hyperpolarized [1-13C]-pyruvate was produced using a prototype SpinLab (General Electric, Niskayuna, New York, USA). Fully sampled 2D dynamic datasets with a symmetric EPSI in RL direction providing an in-plane resolution of $1cm$ were acquired (TE/TR=4.6/130ms) from a 20 mm slice through the brain at a time resolution of $3s$ following an injection of 5.9 mL [1-13C]-pyruvate (250 mM) through the saphenous vein.

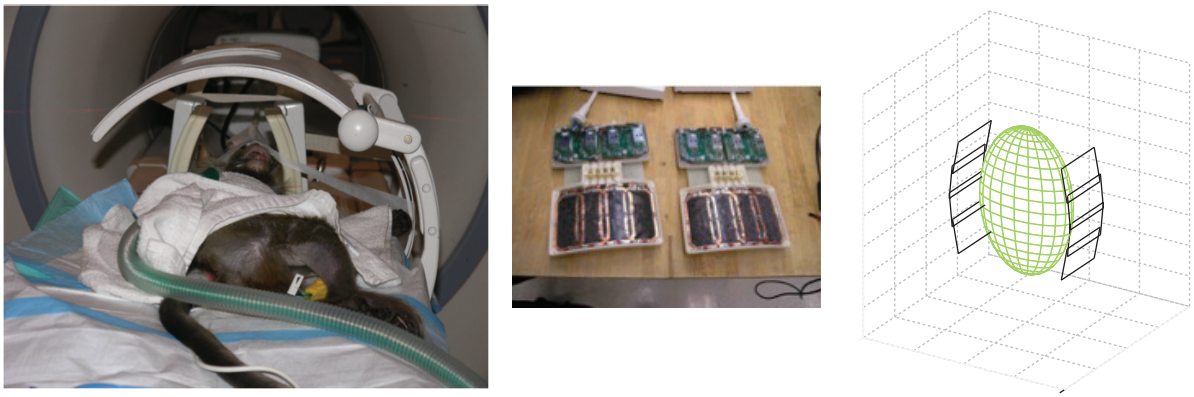

Figure 6.13: bi-lateral 8 channel 13C receive coil and its simulation. Setup for C13 primate.

Reconstruction: Poisson-Disc undersampling patterns with acceleration factors of 2, 4 and 6.7 (corresponding to undersampling of 50%, 75% and 85%) were simulated from the fully-sampled individual channel data and were reconstructed using SPIRiT, CS (Chapter 5) and ℓ_1-SPIRiT algorithms with POCS implementation. This is an effective implementation that requires very simple operations: convolutions, Fourier, and Sparsity transforms and soft-thresholding. For each pattern, to understand the effect of k-space subset size, calibration regions of size $[4 \times 4]$,$[5 \times 5]$ and $[6 \times 6]$ were used with kernel size of $[3 \times 3]$.

An example of using a numerical phantom with calibration size of $[6 \times 6]$ with kernel size of $[3 \times 3]$ and undersampling of 75% is presented in Figure 6.14. The reconstructed Pyruvate and Lactate maps for fully sampled data, zero-filled, POCS SPIRiT, POCS CS and POCS ℓ_1-SPIRiT show promising outcomes for feasibility. SPIRiT performs a better reconstruction for Lactate (lower peak) and CS performs a better reconstruction for Pyruvate (higher peak) and ℓ_1-SPIRiT combines the advantages of both techniques. This observation supports the intuition that POCS CS algorithm is sensitive to low SNR of the metabolites and to a certain degree, it is controlled by the adjustable empirical thresholding. However, lowering the threshold too much will add a lot of noisy-peaks to the data.

Figure 6.15 shows the reconstructed Pyruvate and Pyruvate-Hydrate maps of the non-human primate for the fully sampled, zero-filled, POCS SPIRiT, POCS CS, and POCS ℓ_1-SPIRiT

reconstructions ([abcde],[fghij]) of the hyperpolarized C13 data using a calibration size of 4, kernel size of 3 and 50% undersampling. In the same figure, two voxels with overlaid spectra for the different techniques are also presented. The maps are well estimated in all cases but CS is more successful in recovering the Pyruvate peak, whereas SPRiT is more successful in recovering the Pyruvate Hydyrate. The combination of SPIRiT and CS (hence ℓ_1-SPIRiT) produced the better result.

The metabolite (Pyruvate and Pyruvate-Hydrate) intensities from accelerated data were plotted against those form fully sampled k-space data in Figure 6.16. Linear regressions show similar correlations between the techniques. Correlation between SPIRiT and gold standard is presented with correlation coefficients of $R^2_{pyr} = 0.99$ and $R^2_{pyrhyd} = 0.98$. The correlation coefficients calculated from the pairs of CS and the gold standard are $R^2_{pyr} = 0.99$ and $R^2_{pyrhyd} = 0.97$. The correlation of coefficients from ℓ_1-SPIRiT and the gold standard are $R^2_{pyr} = 0.99$ and $R^2_{pyrhyd} = 0.97$. The raw mean Ratio of Pyruvate and Pyruvate-Hydrate calculated from the full, SPIRiT, CS, and ℓ_1-SPIRiT spectra in brain is also summarized in Table 6.4.

Algorithms	Pyr/PyrHyd
Full	0.3 ± 0.03
SPIRiT	0.3 ± 0.04
CS	0.2 ± 0.03
ℓ_1SPIRiT	0.3 ± 0.03

Table 6.4: Mean ratio of Pyr/PyrHyd for all the accelerated reconstructions.

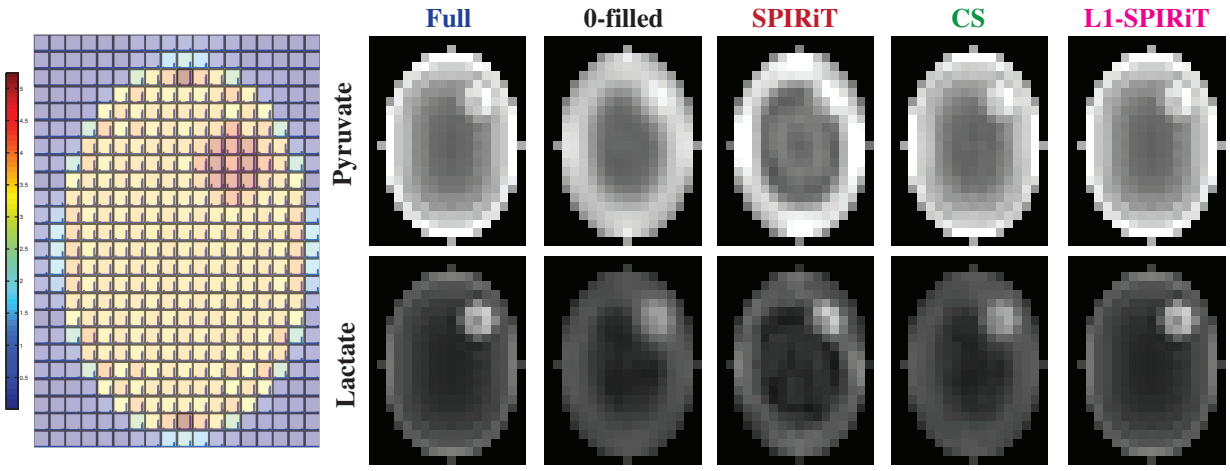

Figure 6.14: A numerical phantom representing brain with lesions with corresponding metabolites maps from the simulated reconstruction methods.

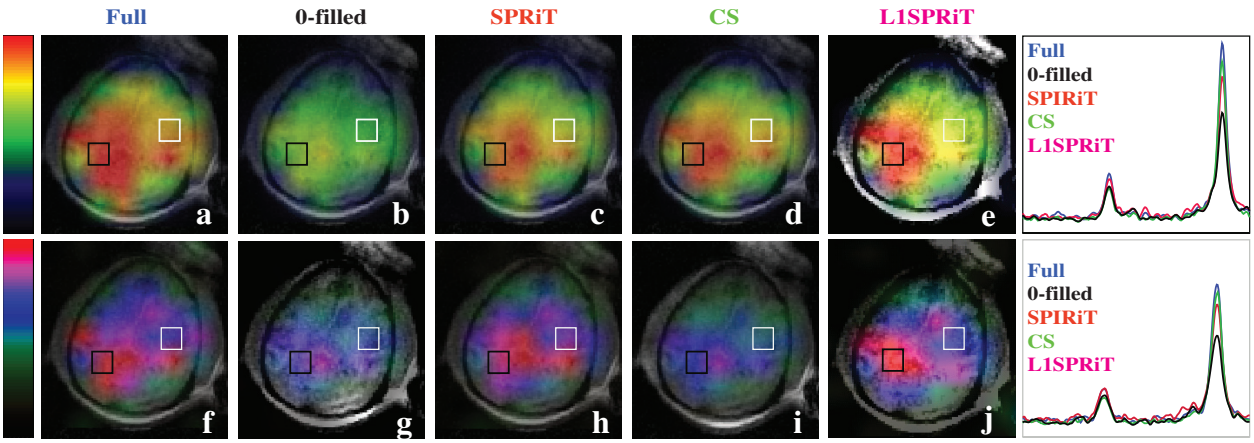

Figure 6.15: 2D-localized Hyperpolarized C13 spectroscopic data from a non-human primate brain acquired using the clamshell phased array coils. Pyruvate (a-e) and Pyruvate-Hydrate (f-j) maps are from fully-sampled (a,f), zero-filled (b,g), SPIRiT (e, h), CS (d,i) and ℓ_1-SPIRiT (e,j). The corresponding C13 spectra for all the techniques are overlaid on the right.

A novel approach was described in "modified-SPIRiT" and "modified ℓ_1-SPIRiT" that was based on the original MRI-SPIRiT algorithm to show the feasibility of these approximate iterative techniques for 2D-MRSI data. We have shown that utilizing the whole spectrum from each coil in calibration stage is essential for correct spectral reconstruction and yields similar image quality and metabolite intensities compared to results from the full k-space data. Note that the high signals from Pyruvate and Pyruvate-Hydrate that were observed in both the brain and the surrounding tissues of the non-primate human with no baselines, along with the limited number of peaks both worked in favor of the chosen algorithms and their implementation. Therefore, the soft-thresholding parameter of the POCS implementation was easily and manually adjusted from high penalty to low penalty for a particular example which often lead to much faster convergence of the iterations. In future work, this parameter should automatically and continuously be modified during the iteration for the best performance.

There are several details that are worth mentioning: (a) using the whole spectrum for calibration adds to the reconstruction complexity by increasing runtime and storage requirement. Although in most MRI cases both W and V operations and their adjoints (calibration stage) can be calculated very quickly, MRSI suffers from the additional complexity due to the overall condition of the matrices and the number of spectral points. (b) Another limitation of this study is the the additional hurdle of imposing an appropriate stopping criteria to insure convergence in MRSI applications. This criteria is not well understood for spectroscopy applications and the convergence properties are less favorable. In short, dealing with low

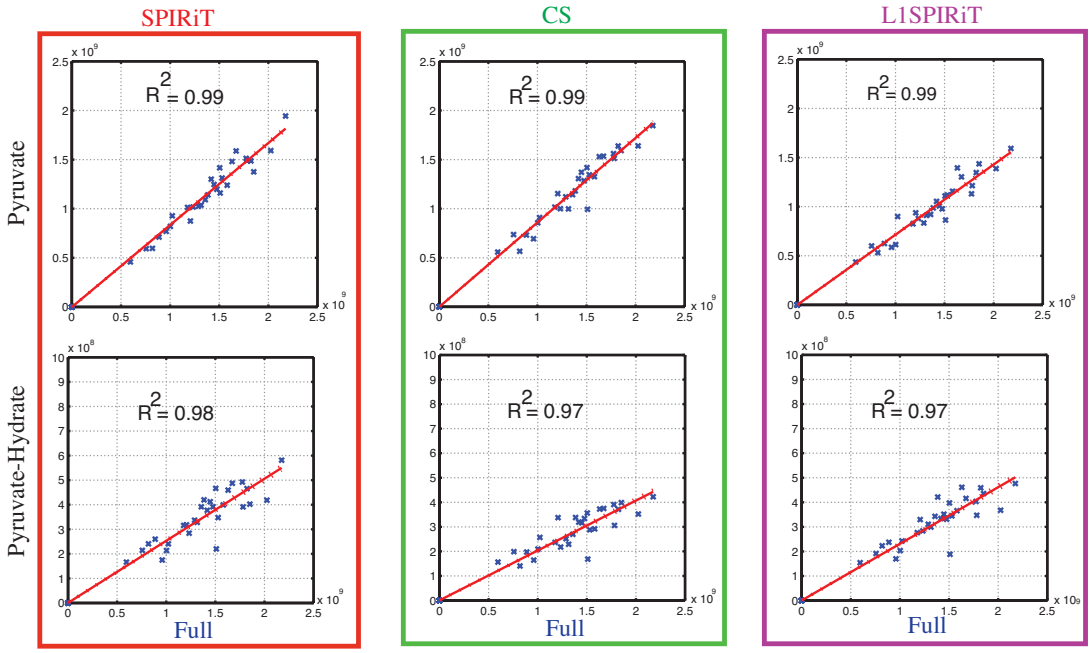

Figure 6.16: The linear fit of the Pyruvate and Pyruvate-Hydrate intensities calculated from a non-human primate's SPIRit, CS, $\ell - 1$-SPIRiT versus full spectra. Linear regressions indicate a strong correlation between SPIRiT, CS, ℓ_1-SPIRiT and the gold standard (fully-sampled).

resolution data such as spectroscopy highlights the need for optimizing the calibration area and kernel size necessary for robust reconstruction.

6.5.2 2D-SPIRiT and traditional-GRAPPA for accelerated H1-MRSI of the brain at 7T

The purpose of this project was to acquire a 3D H1-MRSI acquisition with matrix size of $18 \times 22 \times 16$ and $1cc$ resolution in about 5-7 minutes which requires a robust reconstruction of 3-5x acceleration factor.

We further developed our previous"modified-SPIRiT" and "modified ℓ_1-SPIRiT" algorithms in MATLAB to accommodate the MRSI data from the 32-channel array coil at 7T. Since the readout direction (slice direction) was fully sampled, we were able to compute the inverse Fourier transform and work on the separable 2D reconstruction problem. This approach reduced the complexity, simplified the implementation, and made it easier to parallelize the process internally within a slice. We have successfully improved the reconstruction runtime using multi-core CPUs as parallel execution platform for SPIRiT, however failed to achieve the same result for ℓ_1-SPIRiT on our machines due to its higher computational

intensity. Combination of large matrices ($18 \times 22 \times 16 \times 712 \times 32$, ($k_x$,$k_y$, k_z,k_f,C)), high acceleration factors and many iterations create very large numerical problem that requires a lot of memory and processing power beyond MATLAB's capability. Therefore, in this study we only evaluated the SPIRiT reconstruction strategy using various sampling patterns and calibration regions to achieve the most accurate and robust accelerated MRSI data at 7T.

Subjects: An MRS phantom and 6 healthy adult volunteers were involved in the study. Written informed consent from the volunteers was obtained in accordance with the guidelines of the local ethics regulations.

Acquisition: Anatomic MR images and MRSI data were acquired using a 32-channel receive array with volume coil transmit on a GE 7 Tesla scanner. 2D H-1 MRSI was localized with CHESS water suppression, 8 VSS outer volume suppression, and spin echo slice selection, using a TE/TR= $90/2000ms$ and spectra array= 18×22. A $\mathbf{B_1}$-map was acquired to calculate the optimal transmit power for H-1 MRSI. Fully-sampled, water-suppressed (WS) and nonwater-suppressed (NWS) data were acquired in 13 *min* and used as either a gold standard or to determine the optimal calibration region for a 60% undersampling scheme, respectively. The % undersampling was then increased to 63, 71, 76, and 80%, corresponding to acquisition times of $\approx$ 5, 4, 3 and 2 *min*, acceleration factors of 2.7x, 3.5x, 4.2x, and 5x using the four variable density sampling patterns shown.

Pulse Sequence: Capability of arbitrary sampling patterns was incorporated in spectroscopic imaging on the GE scanner to allow undersampling along any of the phase encoding directions. These variable density k-space sampling patterns were also combined with an interleaved flyback echo-planar trajectory that can be applied in the SI or AP direction. Also, to undersample in time domain, modification of the flyback echo planar readout with desirable blips based on specific sampling patterns was incorporated allowing undersampling in three directions (k_x, k_y, k_f). Sampling patterns were generated in MATLAB and played out on the scanner as explained in Chapter 5.

Reconstruction: The cartesian MRSI k-space samples were converted from the individual channels' raw data into MATLAB. SPIRiT acceleration for higher factors were simulated. The encoding matrix was constructed explicitly based on the assumed Cartesian k-space sampling pattern. The reconstruction matrix was calculated as explained previously with the additional option of using the entire fully sampled NWS data as its calibration region.

To evaluate the accuracy of each reduced k-space and calibration scheme, the fully sampled data was reconstructed as a gold standard and regression plots of all brain voxels were used to compare metabolite peak heights and ratios among the different calibration regions and between each undersampling scheme and full k-space data. The correlation coefficient R^2 value from each linear regression was then used as a measure of accuracy.

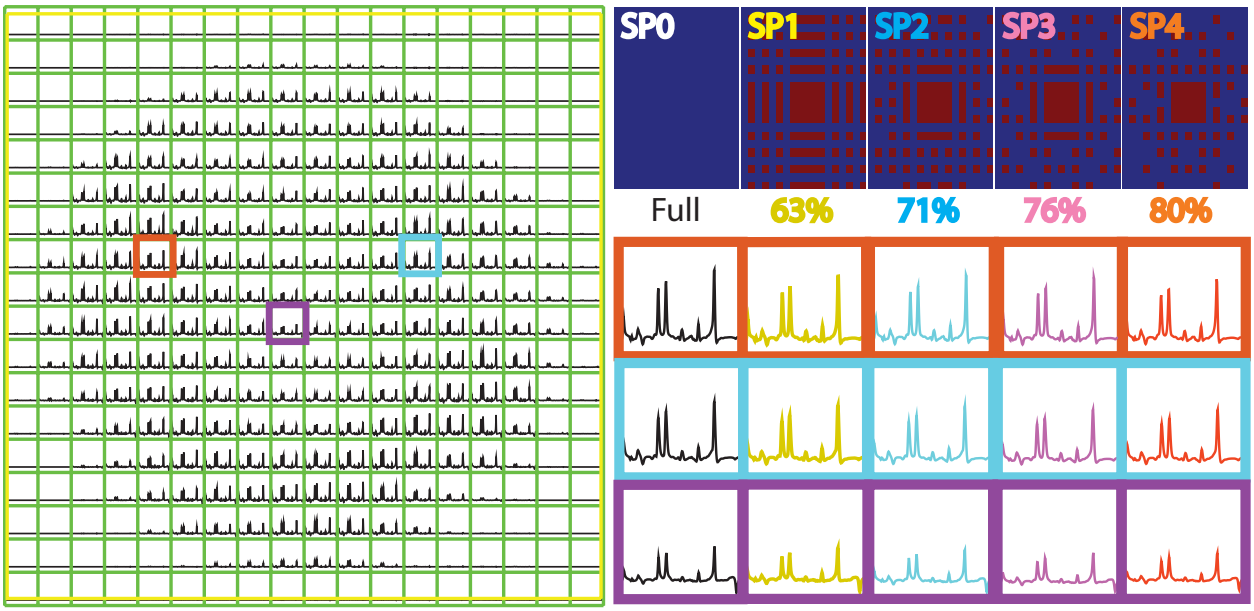

Figure 6.17: Phantom: Fully sampled spectra with enlargement of three voxels of 32-channel data with varying degrees of simulated acceleration and SPIRiT reconstruction are presented.

The full FOV reconstruction of fully-sampled spectra in a phantom is shown in Figure 6.17. The three enlarged voxels from various locations in a phantom show the SPIRiT reconstruction using 5×5 calibration region (from its central k-space) for the 4 sampling patterns. The variable density pattern with more structure near the center and pseudo-random patterns outside performed best, tolerating a higher acceleration even in areas of lower SNR (Figure 6.17, bottom row purple voxels).

Although in the phantom, the difference between R^2 values obtained from SPIRiT using fully-sampled NWS and 5×5 calibration region compared to the original data were not significantly different (0.99 for peak heights and 0.90 for ratios for both calibrations), the choice of calibration region impacted the performance of SPIRiT in the volunteer data, as shown in Figure 6.18, where the SPIRiT reconstruction with 18×22 NWS acquisition serving as the auto-calibrating signal (in blue) more closely reflects the fully sampled spectra (in white) than the center 5×5 calibration region (in pink). The overestimation of the metabolite intensities of the smaller calibration region is clearly seen in the enlarged voxels. Additionally, significantly higher R^2 values were observed for all metabolic peak heights and ratios using the fully-sampled 18×22 NWS compared to the 5×5 calibration region. Utilizing the fully-sampled NWS calibration subsequently allowed for accelerations of up to 80% undersampling without compromising reconstruction quality as shown by the R^2 values in Figure 6.19.

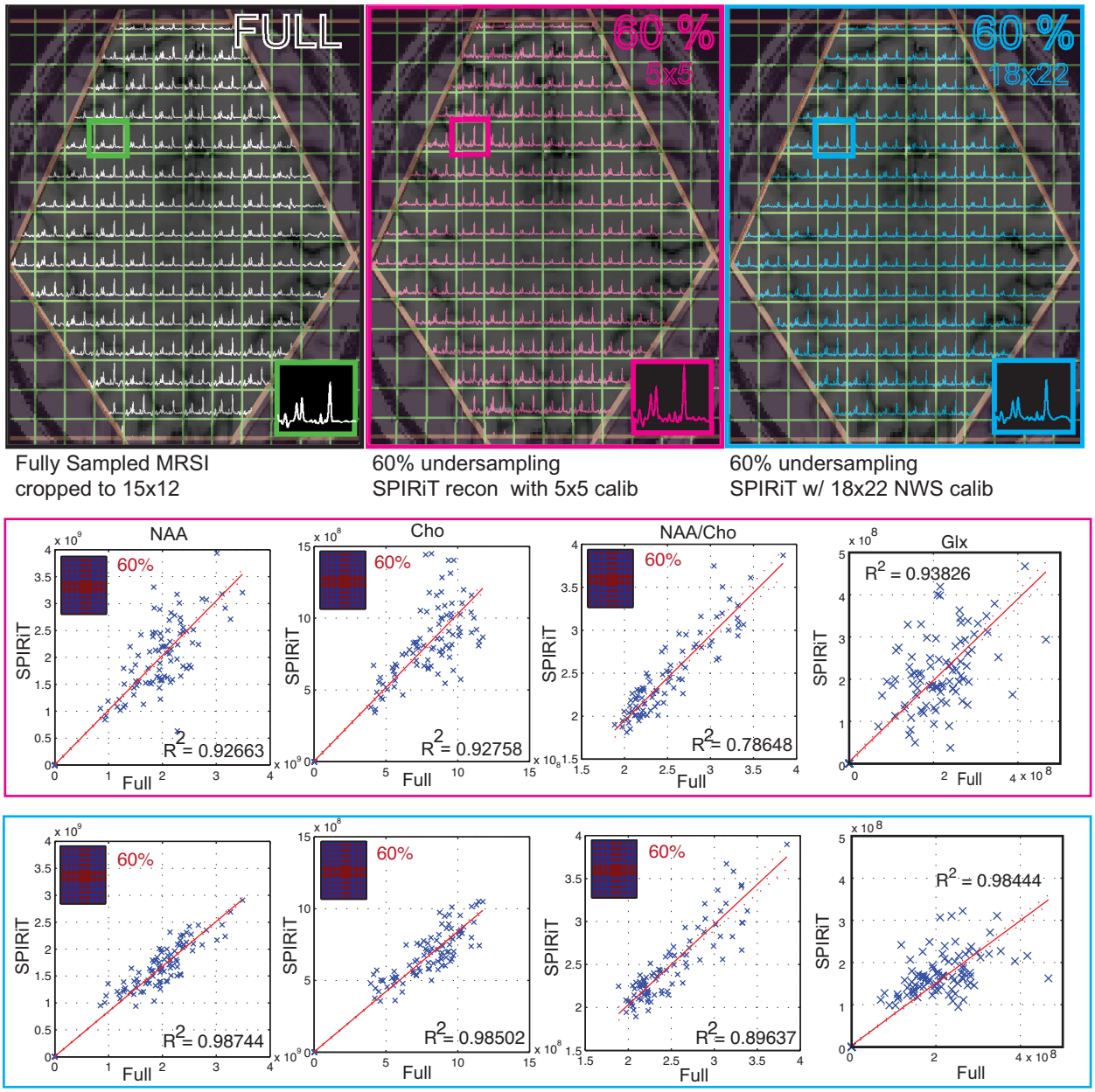

Figure 6.18: Volunteer: Example of an MRSI obtained from 32-channel array coil for 1 sampling pattern and a choice of two different calibration regions. Full FOV of fully sampled spectra (in white), SPIRiT 2.5x acceleration with 5×5 calibration region (in pink), and SPIRiT 2.5x acceleration with 18×22 calibration region (in blue) are presented. Voxel metabolite intensities and ratios of the whole brain from SPIRiT with 5×5 calibration region (top) and SPIRiT with 18×22 calibration region (bottom) are plotted against those obtained with full k-space.

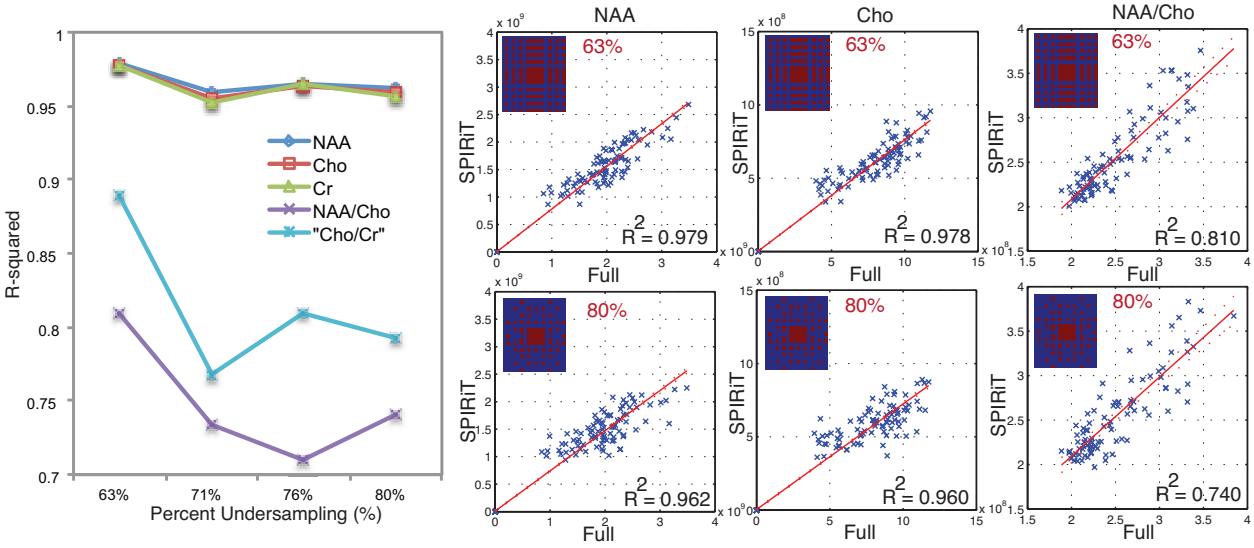

Figure 6.19: Correlation coefficient results from a volunteer for the 4 distinct sampling patterns using the 18×22 NWS calibration region.

The impact of different calibration regions is visible in Figure 6.18. The result clearly demonstrates that the reconstruction accuracy is much higher with a tighter linear regression fit for reconstructed data from 60% undersampling (2.5x acceleration factor) using 18×22 reference NWS calibration. This is because as the number of k-space fits increases, the calibrated kernel more accurately represents actual frequency shifts rather than noise, improving the reconstruction. The impact of various sampling patterns and acceleration factors are revealed in Figure 6.19. Using the less ill-conditioned calibration region allowed for farther acceleration even up to 80% undersampling (acceleration factor of 5x) while maintaining a comparable result.

This work advocates that MRSI at 7T can be accelerated by 5-fold to provide high quality spectra in under 3 min if a NWS dataset is also acquired. It has become evident that achieving a high acceleration factor with SPIRiT is highly dependent on the calibration region, especially with small matrix size acquisitions like MRSI. We were able to improve the conditioning and quality of the calibration using a fully-sampled NWS acquisition which is often acquired and is useful for automatic phase and frequency alignment to increase SNR (28) and for enhancing spectral quality (29), however the overall scan time is not reduced as desired. Implementation of Tikhonov regularization and truncated-SVD of the calibration region should improve the conditioning to potentially reduce the size of the calibration region. Another alternative is to explore a faster way to acquire a fully-sampled calibration region using a PD image of the MRSI region, which will allow for greater flexibility when a NWS acquisition is not feasible. These calibration improvements will allow for ultra-fast whole

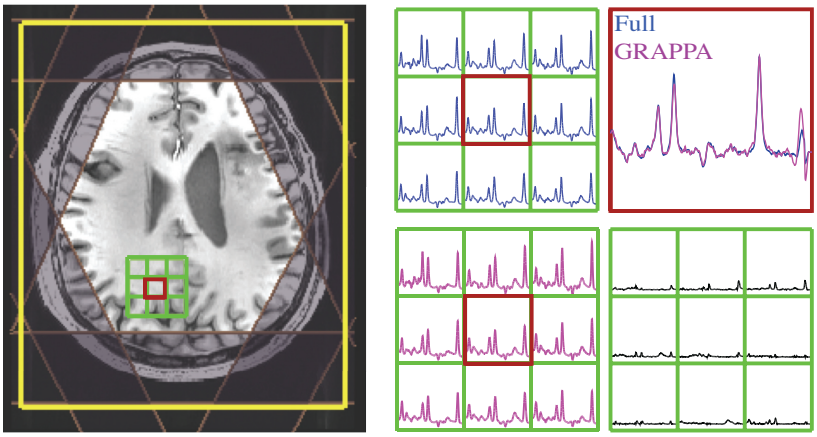

Figure 6.20: H-1 MRSI patinet A data at 7T. Fully sampled spectra is presented in blue and grappa recon is presented in pink, the difference is shown in black.

brain MRSI acceleration suitable for routine patient studies at 7T.

Since iterative methods have certain challenges in regards to their runtime, stopping criteria and convergence conditions, we used the traditional GRAPPA as explained in (30, 31) for several data sets. 5 patients with brain tumors were studied using a 32-channel receive-only array with a volume transmit head coil on a GE 7 Tesla scanner (GE Healthcare, Waukesha, WI). 3D H-1 MRSI was localized with CHESS water suppression, 8 VSS outer volume suppression, spin echo slice selection TE/TR= $30/2000ms$, spectra array= $18\times22\times8$ with an interleaved flyback echo-planar trajectory with spatial resolution of 1 cm. The total acquisition time is about 10 minutes. The 32 channels of data were combined, processed as described previously and then quantified using LCModel. Undersampling by a factor of 2 was simulated by eliminating the appropriate k-space components and the data were reconstructed with traditional GRAPPA.

Figure 6.20 shows the GRAPPA for 3D H1-MRSI obtained from the brain using an 32-channel head coil. The array on the top (in blue) was fully sampled with an acquisition time of 10 min and the one on the bottom (in pink) uses traditional GRAPPA with an R=2 factor with an acquisition time of 5 min. The enlarged voxel shows the overlay spectra of fully sampled data and GRAPPA. Figure 6.21 summarizes the results for all 5 patients in a table format. No significant difference (P>0.05) was found in (GPC+PC)/NAA between fully sampled spectra and spectra with the GRAPPA reconstruction; and the number of voxels with quantifiable Glu was similar between the two methods. These results are very promising and when implemented experimentally would reduce the acquisition time to 5 minutes, which is ideal for patient studies.

Although ℓ_1-SPIRiT appeared to operate well for 8-channel C13-MRSI data, it became completely infeasible (in the current implementation) for 32-channel H-MRSI data at 7T. Even for SPIRiT alone (without enforcing sparsity), to reduce the burden of post-processing to a manageable scale, we only acquired a 2D-MRSI data which had to further be parallelized

ID	(GPC+PC)/NAA						Number of voxels with Glu CRLB<=20	
	T2		NAWM		GM			
	Full	GRAPPA	Full	GRAPPA	Full	GRAPPA	Full	GRAPPA
A	0.23 ± 0.10	0.21 ± 0.06	0.14 ± 0.03	0.14 ± 0.03	0.09 ± 0.03	0.09 ± 0.03	137	129
B	0.26 ± 0.14	0.24 ± 0.12	0.16 ± 0.04	0.16 ± 0.04	0.16 ± 0.04	0.15 ± 0.04	84	74
C	0.13 ± 0.02	0.10 ± 0	0.13 ± 0.06	0.14 ± 0.07	0.14 ± 0.06	0.15 ± 0.07	133	92
D	0.38 ± 0.15	0.36 ± 0.13	0.16 ± 0.03	0.15 ± 0.03	0.10 ± 0.03	0.09 ± 0.03	72	60
E	0.18 ± 0.07	0.18 ± 0.08	0.17 ± 0.01	0.17 ± 0.02	0.11 ± 0.01	0.11 ± 0.02	95	89

Figure 6.21: The ratio of $\frac{(GPC+PC)}{NAA}$ from T_2, NAWM and GM regions of 5 patients for fully sampled data and 2x GRAPPA reconstruction.

using multi-core CPUs. As an iterative reconstruction, the computational complexity of SPIRiT can be more intensive than direct reconstruction. The Cartesian POCS algorithm requires in each iteration an operation similar to a single GRAPPA reconstruction. The algorithm often requires about 15-20 iterations to converge; however with a larger number of iterations, while the algorithm may converge initially, the residual of the objective function may diverge at the end. Although the solution becomes more accurate with each iteration, the noise in the reconstruction is increased and at some point (7-10 iterations), it might be worthwhile to terminate the reconstruction as the POCS iterations start fitting the noise creating large artifacts in the data probably due to the low SNR of MRSI data. While the results demonstrated were promising in general, there were clearly trade-offs in terms of artifacts, stability and reconstruction time. Furthermore, sampling patterns, calibration region size, kernel size, stopping criteria, tolerable error measure (objective function and its residual), and conversion criteria were too many parameters to optimize over for large MRSI matrices with large number of individual coils while dealing with long processing time.

The SPIRiT approach has an advantage of using highly nonuniform sampling patterns while the traditional-GRAPPA has much accurate, faster, and stabler reconstruction. It seems that modifying and reformulating the traditional-GRAPPA to handle arbitrary sampling patterns will increase its flexibility while avoiding optimizing numerous parameters all at once.

6.5.3 Arbitrary Variable Density (AVD)-GRAPPA with EPSI of short-echo whole brain 3D-MRSI

The purpose of this project was to achieve short-echo 3D whole-brain MRSI with higher spatial resolution of $0.56cc$ in $< 10min$ with adequate SNR at 3T if possible. This work investigates the impact of the sampling patterns, calibration regions, and kernel sizes of AVD-GRAPPA on the reconstructed MRSI data with the feasibility of using AVD-GRAPPA for future routine clinical exams.

A number of studies have investigated the use of GRAPPA for H1-MRSI and were presented by Banerjee et al (30, 31), Zhu et al (32), Rueckert et al (33), and Sabati et al al (34). Zhu et al (32) proposed an approach, called "spectral phase correction in GRAPPA" (SPC-GRAPPA). The SPC-GRAPPA was modified to apply the GRAPPA reconstruction algorithm developed by Griswold et al (13) to undersampled metabolites and interleaved water reference k-space data at each time point of the FID, following voxel-by-voxel spectral phase alignment prior to coil combination. Sabati et al (34) implemented a modified GRAPPA reconstruction algorithm based on the method of Zhu et al (32) utilizing the whole spectrum from the interleaved water reference. Rather than obtaining the GRAPPA reconstructing kernel weights from a single time point of the FID signals and then using the same weights for the GRAPPA reconstruction of other time points, the weights were determined at each time point of FID for a GRAPPA reconstruction of that same time point, since this was shown to improve performance in (33).

2D AVD-GRAPPA enabled EPSI: The key feature of this reconstruction scheme is supporting arbitrary cartesian sampling patterns with an option of using a high-resolution external sensitivity information for calibration (GRAPPA meets SENSE meets random sampling). The reconstruction was implemented in MATLAB and it operates by looking at a point and calibrating according to its neighborhood to synthesize the missing point. The AVD-GRAPPA incorporates the spectrum domain in a way of either obtaining the kernel weights from a single time-point of the FID and then using the same weights for all the other time-points, or the weights can be determined at each time-point of FID for the same time-point. This reconstruction also incorporates the option of using an external calibration for training its data set. The GRAPPA kernel weights that are calculated from the previous options are then used so that the missing k-space data points are synthesized as a linear combination of the acquired data. The Tikhonov's regularization was implemented to condition the calibration matrix in all of the options. The individual reconstructed channel data was pre-processed, phased-aligned then combined as previously described in Chapter 4.

Subjects: An MRS phantom and 3 healthy adult volunteers were involved in the study. Written informed consent was obtained from all the volunteers prior to the examination.

Data Acquisition: Anatomic MR images and MRSI data were acquired on using a 32-channel receive array on a GE 3T scanner. A high resolution spin echo (SE) imaging sequence with matched spectroscopy parameters (TR/TE=35/1300ms) was acquired (≈1min) to be used as an external calibration. 3D H-1 MRSI was localized with CHESS water suppression, 10 VSS outer volume suppression, and spin echo slice selection, TE/TR=35/1300ms, spectra array=$28 \times 32 \times 16$ using flyback echo-planner trajectory in the SI direction and spatial resolution of $0.56cc$. Fully-sampled MRSI data were acquired (≈20min) and used as a gold standard and then retrospectively under-sampled by factor of 2, 3, and 4 corresponding to acquisition times of $\approx$ 10, 7, and 5 min using the five variable density sampling patterns shown in Figure 6.22.

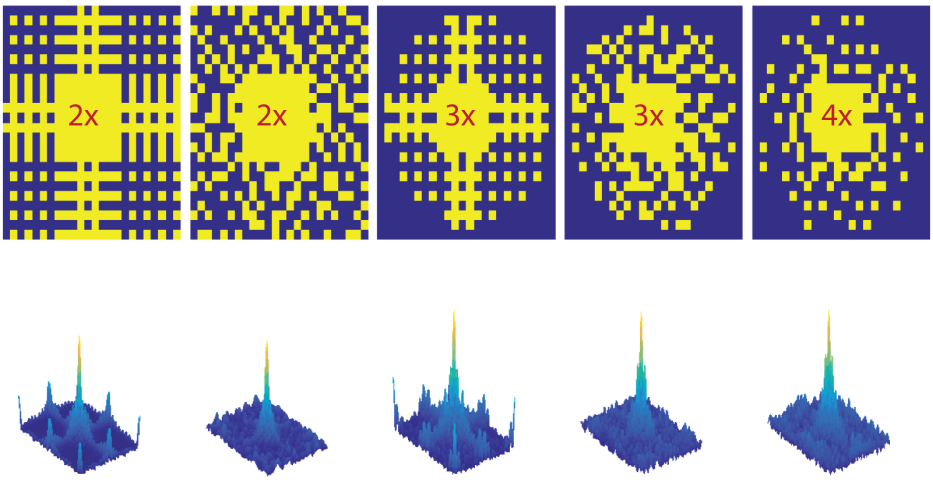

Figure 6.22: Sampling patterns (structured and random) with acceleration factors of 2x ,3x, and 4x with their corresponding Point Spread Function (PSF) are illustrated. All the sampling patterns are computed with variable density and the random ones are based on Poisson distribution ensuring certain number of points within a given region with the largest incoherence. For uniform k-space sampling, the PSF is a *sinc* function, however, the PSF of non-uniform sampling patterns are not simple *sinc* and are more complex resulting on different type of errors in reconstruction.

Data Analyses: The reconstructed combined spectra were fitted with LCModel. The basis set was simulated using jMRUI package. Metabolite levels were quantified for voxels within the brain using LCModel for the volunteers. Metabolite ratios included in the analysis were those with Cramer-Rao lower bounds (CRLB) lower than 10% for tCho, tCr and NAA, and 20% for the others. To evaluate the accuracy of each reduced k-space sampling and calibration scheme, the fully sampled data was reconstructed as a gold standard and regression plots of all brain voxels were used to compare metabolite peak heights and ratios as shown in the diagram in (Figure 6.23).

k-space Sampling Pattern Strategies (structured vs random) The design of an optimal sampling pattern (for a given acceleration factor and coil geometry) must take into account two different objectives: the k-space samples must contain as much information about the sampled image as possible and the inevitable subsampling artifacts in the reconstruction should be as small as possible. These are complementary but not identical aims. Intuitively we are suggesting one should acquire predominantly those coefficients of the image which have the largest magnitude. Of course, this is one of the reasons for the good performance of variable density sampling; central frequencies, where the energy of images is concentrated, are more densely sampled than the outer frequencies. Figure 6.24 shows an example of where these large magnitudes are located in k-space for two coil-array configurations (8- and 32-channel). Given a reference or calibration image, we took the magnitude of its Fourier transform of each individual channel. These maps then served as density maps

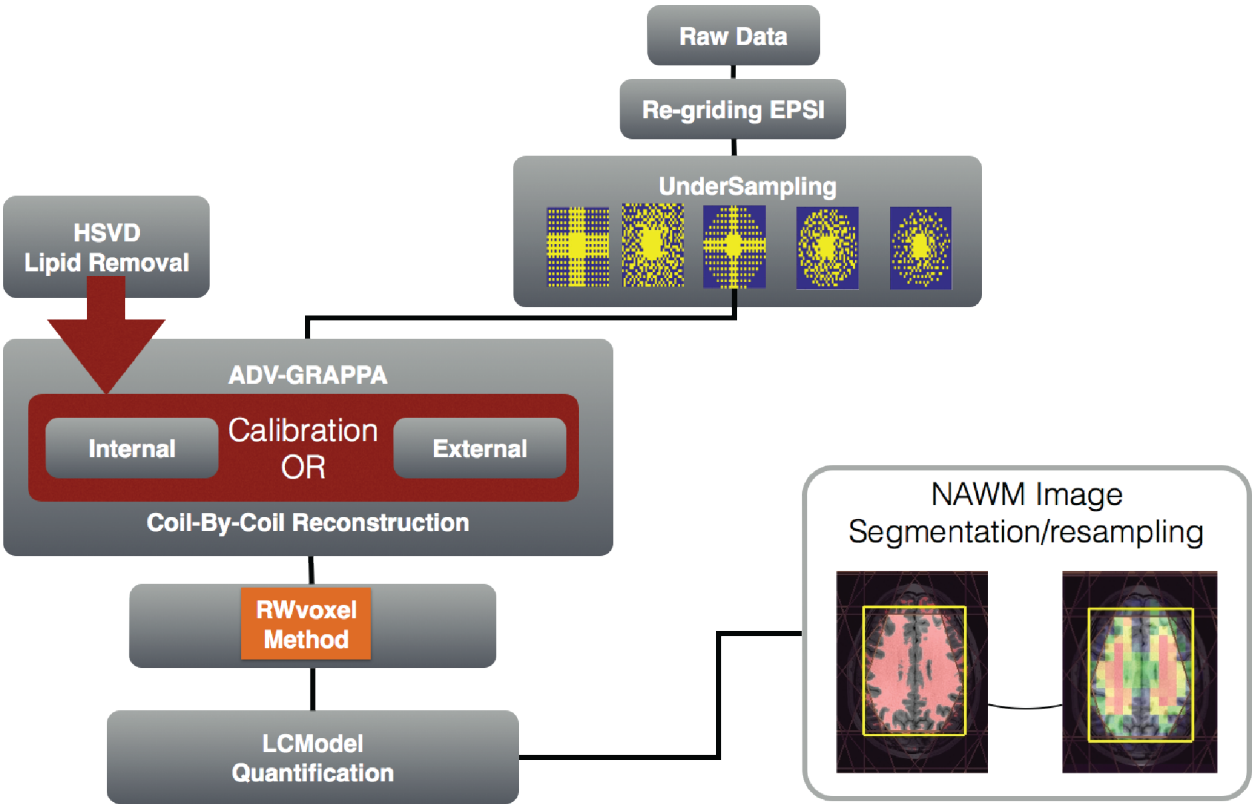

Figure 6.23: Data processing flow chart of AVD-GRAPPA reconstruction for 3D-EPSI per slice.

on a Cartesian grid in k-space, defined by the desired resolution. The density maps of the 8-channel array coil are very similar among the individual channels due to the symmetric geometry of the head coil. The large k-space variability in the individual channels of the 32-channel array coil suggests that optimized sampling patterns covering influential regions will have more impact on the higher coil arrays due to their anti-symmetric geometries. Therefore, for higher acceleration factors, the k-space sampling pattern (specially the location of the calibration region) needs to be adaptive and smart in regards to the coil configuration and the relative position of the acquisition region to each individual channel. Based on our observation, since good reconstruction of each individual channel strongly depends on capturing regions that have higher magnitude coefficients during undersampling, the various sampling patterns were generated from a Poisson-Disc distribution to ensure certain number of points within a given region and then manually modified to cover the important regions of all the channels. Our observation is that a template taken from any of these calibration scans that cover the whole-brain will give good results. It is important to note, the way that we implemented these randomized sampling trajectories on the MRI-scanner for accelerated MRSI (Chapter 5) gives complete freedom to choose any sample point in the 2D phase encode plane easily.

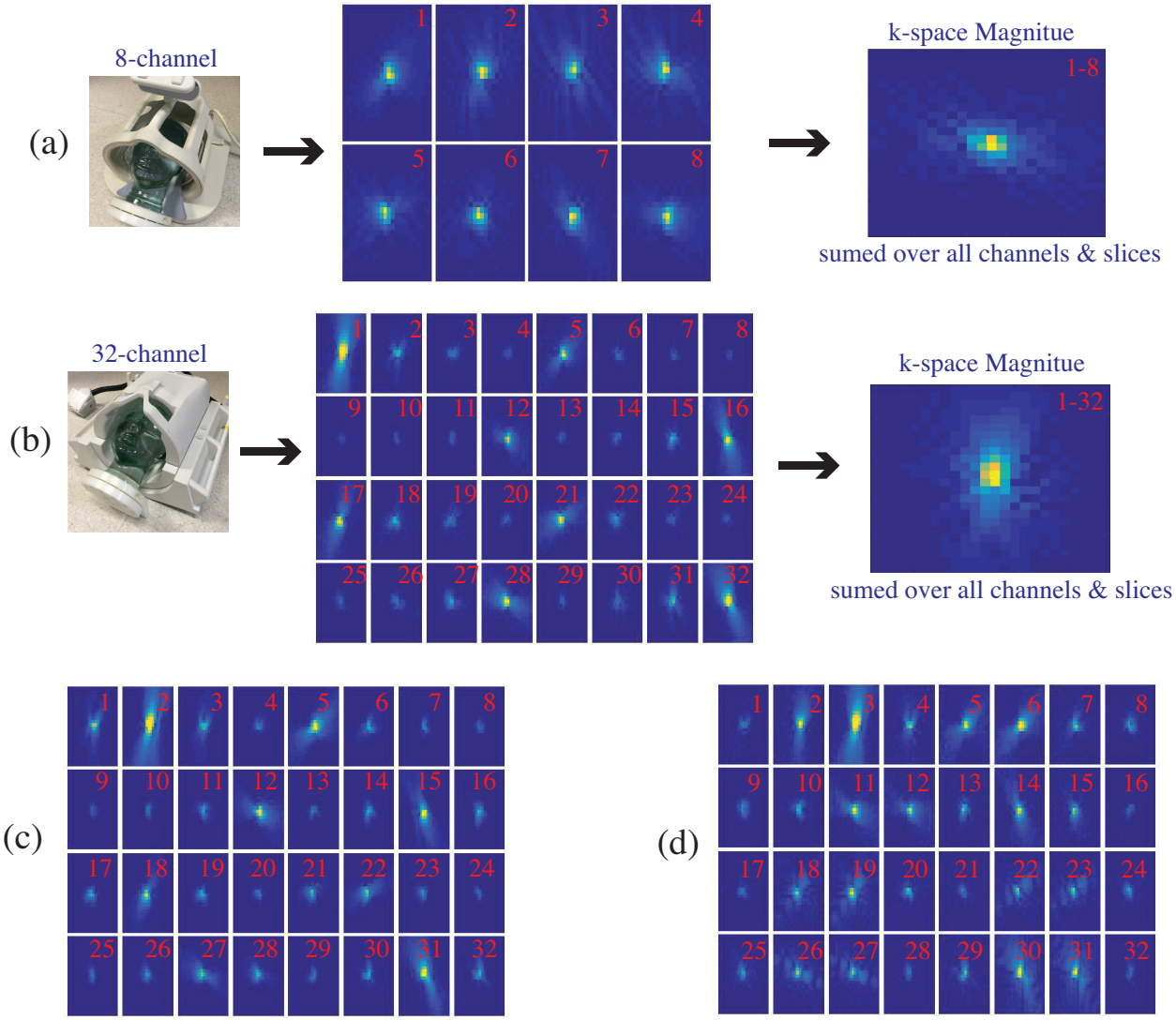

Figure 6.24: Fourier Transform of the reference or calibration image used for the sensitivity information. (a) 8-channel array coil: k-space magnitude for individual coils while has been summed over all the slices. (b) 32-channel array coil: k-space magnitude for individual coils while has been summed over the all the slices. (c) 32-channel array coil: individual channels for slice 8. (d) 32-channel array coil: individual channels for slice 11. It is clearly seen that the largest k-space magnitude for the slice 8 and 11 are observed in different regions in different channels. The sampling pattern imposed included all of these regions to improve reconstruction performance.

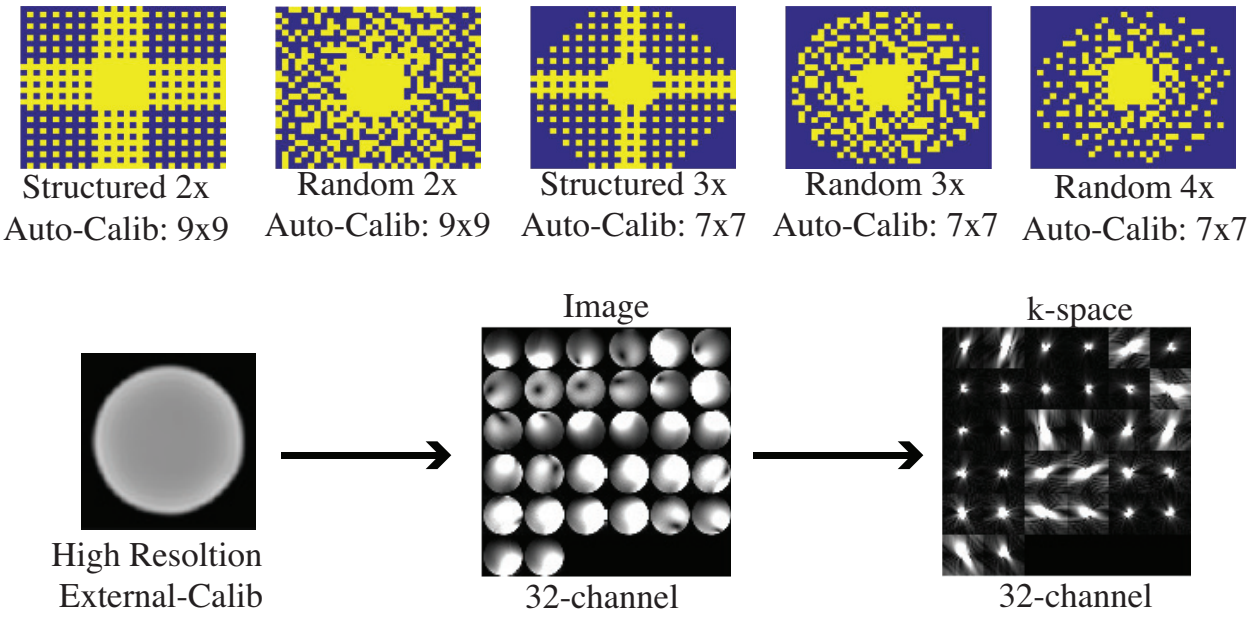

Figure 6.25: Phantom: Matrix $24 \times 24 \times 16$, Res:0.56cc. Spin-Echo Calibration with TR/TE= $1300/35ms$ and Matrix $64 \times 64 \times 32$

Lipid Contamination Artifacts: The large brain coverage of conventional low resolution MRSI data suffers from lipid contamination in terms of fat signals bleeding into nearby voxels due to its inherit point spread function. When whole brain coverage is necessary, many of the lipid suppression methods face severe limitations in the presence of strong $\mathbf{B_1}$ and $\mathbf{B_0}$ inhomogeneities and fail to suppress the fat signals optimally. When it comes to accelerated MRSI data, these artifacts are expressed in much larger scale degrading the performance of the traditional MRSI parallel imaging techniques especially with higher acceleration factors. Since these bleeding fat signals usually have a different phase from the metabolites in the contaminated voxels, the traditional PI reconstructions cannot always fully unfold the aliasing of cranial lipids which can severely compromise the final spectral quality inside the brain, in particular the quantification of NAA can be severely compromised. In these cases, the random sampling patterns have the added benefit that the aliased lipid signals are incoherent and noise-like, and thus amenable to removal during reconstruction. The undesirable lipid signal is then removed from each channel prior to GRAPPA reconstruction using non-iterative time-domain fitting with the Lanczos-based version of HSVD to filter out signals from 1.8 to -1.0 ppm (35).

Calibration Region and Size: The stability and integrity of the estimated kernel weights are compromised due to the limited spatial frequency of the MRSI and the lipid contamination which leads to inaccuracy of the spectral reconstruction of the metabolites under investigation. We believe in accelerated MRSI, using an external calibration region (with

higher resolution and matching the spectroscopic imaging sequence) as ACS data to construct the calibration matrix and to estimate the kernel weights will improve the reconstruction outcome by increasing the spatial frequency and minimizing the effect of lipid contamination. It is important that the matched imaging sequence mimics the first FID point of the MRSI data as closely as possible. In our case a spin-echo (SE) MRI sequence with the same TE and TR is used as a reference sequence. If the same point spread function and the same phase evolution of MRSI becomes necessary in our reconstruction, an additional fat suppression module is implemented on top of the calibration sequence to further suppress the effect of the fat signals. While the size of the internal calibration region (central k-space) are very limited in MRSI (in order of $[9 \times 9]$, $[7 \times 7]$, $[5 \times 5]$ due to the lengthly acquisition times), the large external calibration region (in order of $[64 \times 64]$, $[32 \times 32]$) provides the flexibility of experimenting with various kernel sizes and their impacts on the AVD-GRAPPA reconstruction.

Interpolation Kernel Size: The MRSI data were processed in the following way: each data set was reconstructed several times, using AVD-GRAPPA, each time with a different kernel size ($[3 \times 3]$, $[5 \times 5]$, $[7 \times 7]$ and $[9 \times 9]$). The AVD-GRAPPA kernels were calibrated for each unique local sampling pattern set. Overall, the reconstruction is insensitive to the kernel size, achieving similar results, with slightly more accurate results for smaller kernel sizes. Larger kernel sizes propagate the aliased lipid signals more throughout the brain. The total number of correlated k-space points (as a result of the multi-channel coils) were estimated empirically for the 32-channel array coil from the 3D-PSF of the acquired "sensitivity" maps that had been summed over all channels and all slices. The number of k-space points greater than 50% of the maximum signal in the 3D-PSF, the full-volume at half maximum (FVHM) corresponded to $[3 \times 3]$ kernel size, greater than 75% corresponded to $[5 \times 5]$, greater than 90% corresponded to $[7 \times 7]$. Although the kernel size $[7 \times 7]$ utilized almost all the correlated k-space points, the kernel size $[3 \times 3]$ gave the best performance.

Number of FID Points: The MRSI-GRAPPA technique in (32–34) reconstructs each FID time point independently assuming the temporal information is uncoupled from spatial information in PEPSI acquisition due to its high bandwidth in readout. Rueckert et al (33) shows the best GRAPPA performance for the calibration method that used either every FID time point or every group of consecutive sections of the FID time points of the fully sampled non water suppressed (NWS) data. Unfortunately, in our experiments we weren't able to utilize all of the 712 FID time points due to the limited memory available in the current proof-of-concept implementation of AVD-GRAPPA in MATLAB. The calibration matrix denoted by W, is constructed from all the ACS portion of the acquired data (from all the channels and FID points). The row of W is constructed by sliding a window throughout the ACS data, taking each block inside of the ACS region to be a row in the matrix. The columns of W are shifted versions of the ACS area, leading to a matrix structure known as Block-Hankel (regularized least-square problem with regularization). For one slice, for all 712 FID time points, the $W^T W$ matrix becomes as large as 313 GB, for 100 points as large as 7 GB and for

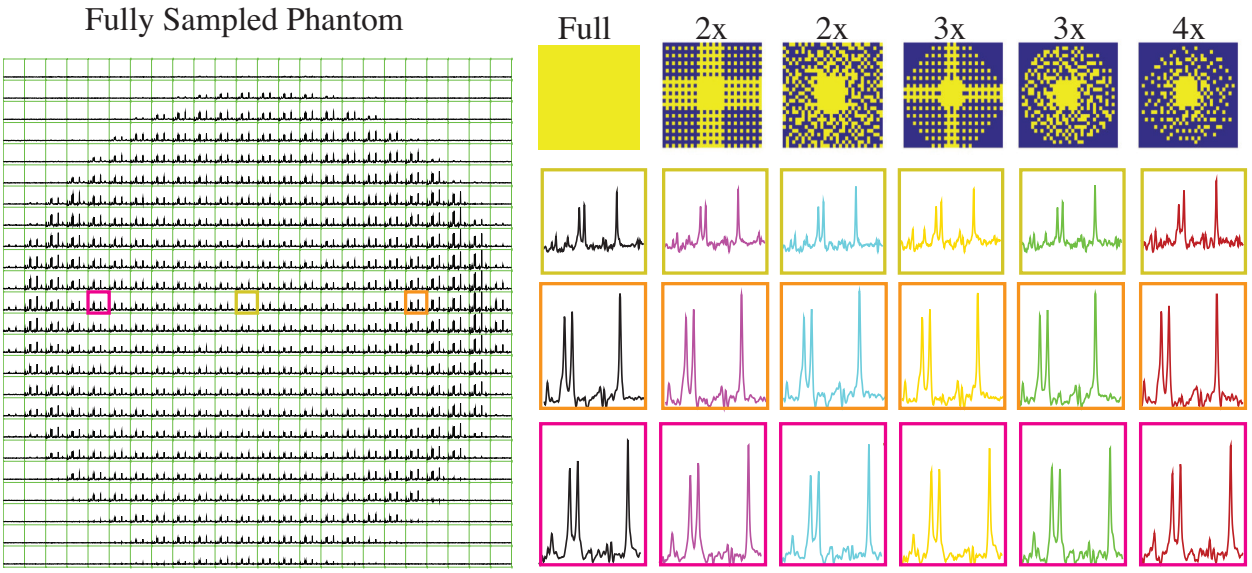

Figure 6.26: Reconstructed phantom for full k-space with individual voxels highlighting the AVD-GRAPPA reconstruction for 5 different sampling patterns using internal calibration region of sizes $[9 \times 9]$ and $[7 \times 7]$ with kernel size of $[3 \times 3]$.

50 points as large as 1.7 GB, therefore, computationally infeasible. However, we were able to construct the calibration matrix several times, using the first FID point, the first and second FID points, the first 10, 20 and 25 FID points for one of the NWS dataset. Each time the AVD-GRAPPA kernel weights were estimated for those points and the mean of kernel weights were applied to the rest of the FID points. Following the AVD-GRAPPA reconstruction of each scenario, it was observed that the quality of the synthesized missing points degraded as more FID points were added to the calibration matrix. This result suggests that, for our sequence the temporal information is coupled with the spatial information and the columns of the calibration matrix become linearly dependent as more FID points are added.

Phantom: Initially we were able to improve the conditioning and quality of the calibration matrix only by implementing the Tikhonov regularization into AVD-GRAPPA (Figure 6.26), however the greater improvement was achieved by using a fully-sampled PD image as calibration region along with Tikhonov factor (Figure 6.27). Figure 6.27 shows the regression plots that compare results of the spectral fitting of all metabolites (tNAA, tCho, tCr, glx, and mi+gly) for AVD-GRAPPA and full k-space data for all voxels within the phantom using random undersampling pattern with 2x acceleration, $[3 \times 3]$ kernel size and external calibration. Figure 6.27(a,b,c,d,e) shows the metabolites from AVD-GRAPPA data plotted against those obtained from full k-space data using an internal calibration matrix and Figure6.27(f,g,h,m,n) shows the metabolites from GRAPPA data plotted against those obtained from full k-space data using an external calibration matrix.

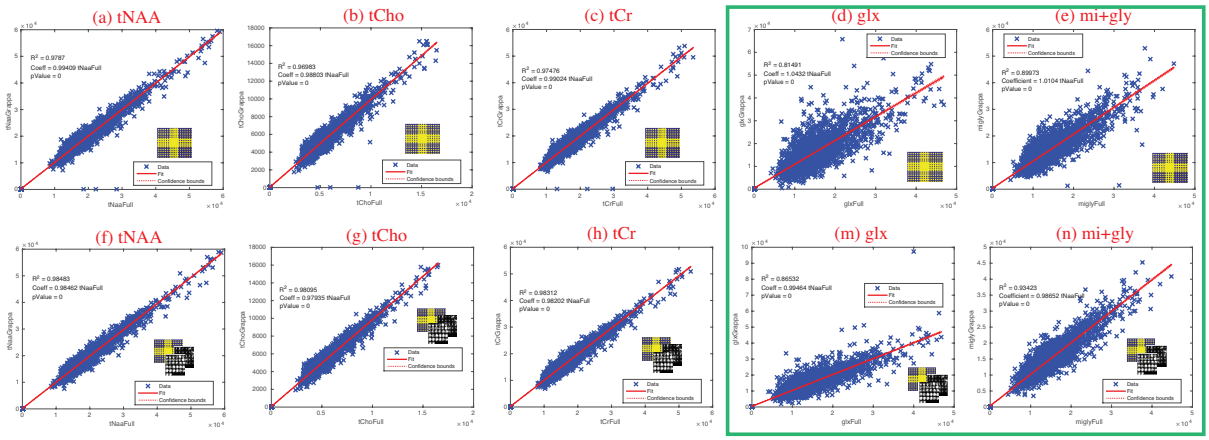

Figure 6.27: Regression plot of individual metabolites' concentration (tNAA, tCho, tCr, glx and mi+gly) for structured pattern 2x acceleration (a,b,c,d,e): AVD-GRAPPA are plotted against their Full k-space using internal calibration region of size 9x9. (f,g,h,m,n): AVD-GRAPPA are plotted against their Full k-space using high-resolution external calibration region of PD image.

Linear regression shows a strong correlation between AVD-GRAPPA and the gold standard, with correlation coefficient of $R^2_{tNAA} = 0.98$, $R^2_{tCho} = 0.97$, $R^2_{tCr} = 0.97$, $R^2_{glx} = 0.81$, and $R^2_{mi+gly} = 0.90$ for internal calibration and $R^2_{tNAA} = 0.98$, $R^2_{tCho} = 0.98$, $R^2_{tCr} = 0.98$, $R^2_{glx} = 0.87$, and $R^2_{mi+gly} = 0.93$ for external calibration. The slight difference between

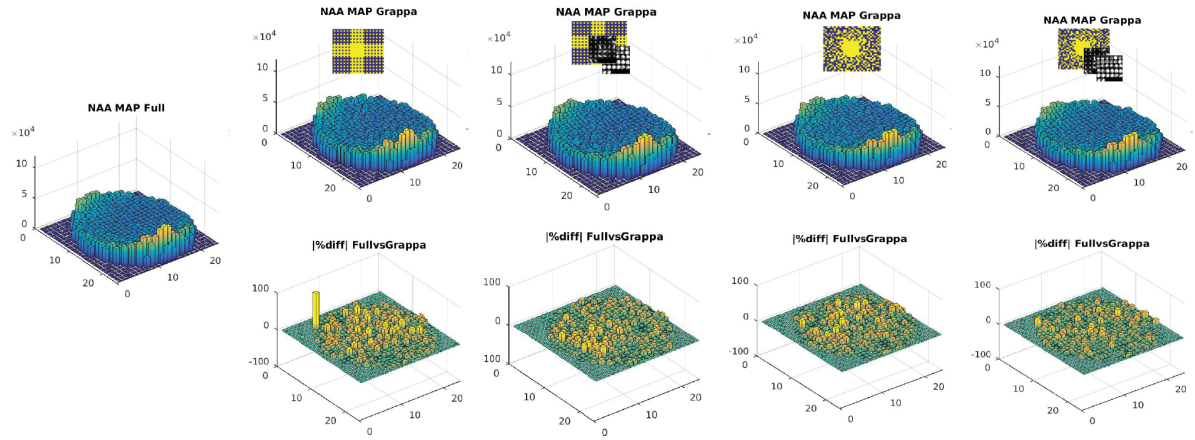

Figure 6.28: Aliasing artifacts for NAA map for random vs structured sampling pattern for 2x acceleration for both internal and external calibration

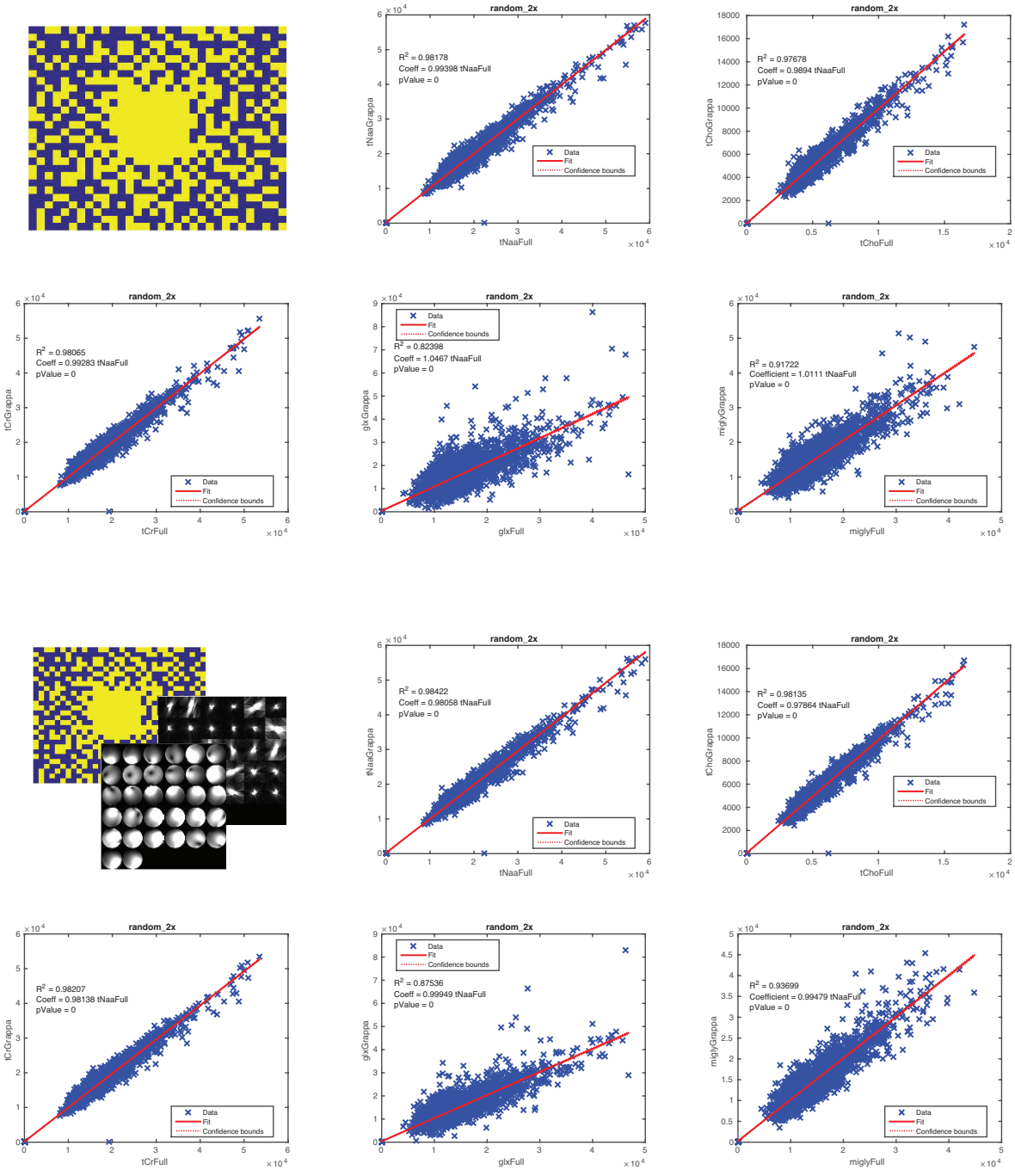

Figure 6.29: Voxel metabolites from the whole-phantom from GRAPPA-EPSI plotted against those obtained with full k-space EPSI for tNAA, tCho, tCr, glx, and mi+gly using both internal or external calibration techniques.

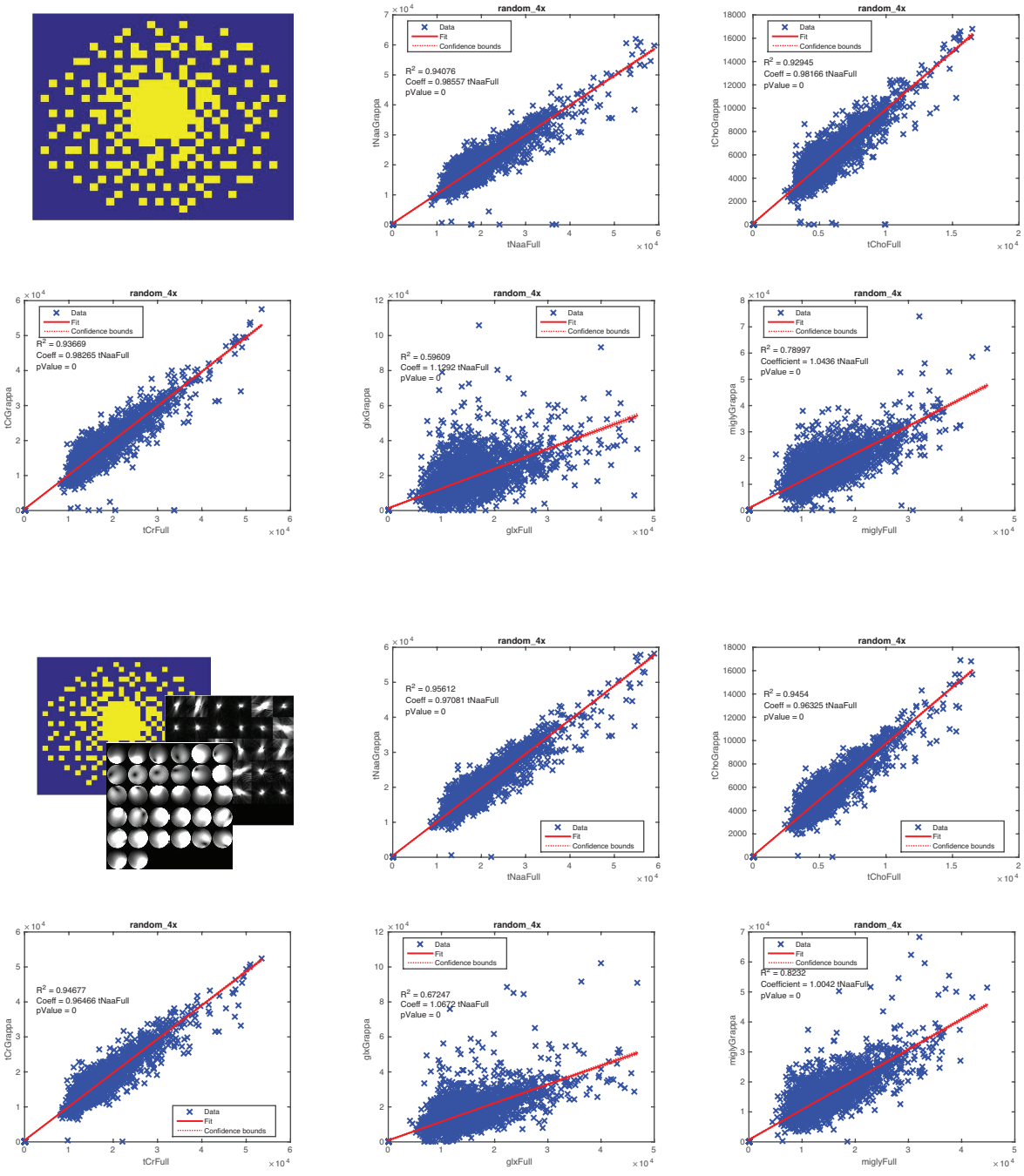

Figure 6.30: Voxel metabolites from the whole-phantom from GRAPPA-EPSI plotted against those obtained with full k-space EPSI for tNAA, tCho, tCr, glx, and mi+gly using both internal or external calibration techniques.

these two options (using internal or external calibration) is observed in tighter fit for smaller peaks (such as glx or mi+gly) favorable towards external calibration . Similar results were observed for other sampling patterns and accelerations in Figures 6.29 and 6.30. To compare the aliasing artifacts of the structured vs random sampling pattern, Figure 6.28 shows the tNAA maps for fully sampled and AVD-GRAPPA reconstruction for 2x acceleration with both internal and external calibration options. The % difference maps illustrate that AVD-GRAPPA with external calibration performs slightly better. The % mean-difference of metabolites maps decreases from 6.8% to 2.5%.

Volunteers: We have shown that in highly accelerated in-vivo MRSI, using random sampling patterns, and an external calibration image (higher resolution with matching parameters to spectroscopy), to construct the calibration matrix to estimate the kernel weights will enhance the reconstruction outcome by minimizing the effect of lipid contamination. Further improvement is achieved by removing the lipid from each channel prior to applying the kernel weights to the neighboring points. Figure 6.31 shows an example of an in-vivo whole-brain short-echo 3D MRSI from a volunteer using AVD-GRAPPA algorithm. The AVD-GRAPPA reconstruction used high-resolution external calibration with kernel size of $[3 \times 3]$ for 3 random sampling patterns (acceleration 2, 3, and 4x) with and without HSVD as pre-processing step. Figure 6.31(a) shows the fully sampled data. Figure 6.31(b,c,d) shows 2, 3, and 4x acceleration without lipid removal prior to AVD-GRAPPA. Lipid contamination increases as the acceleration factor increases, especially in anterior and posterior regions. Figure 6.31(e,f,g) shows 2, 3, and 4x acceleration with HSVD lipid removal prior to AVD-GRAPPA. The complete lipid behavior can be observed in Figure 6.31, while Figure 6.32 illustrates the several enlarged voxels.

Tabel 6.5 shows the percent mean-difference maps of tNAA and Cho/NAA (a.k.a % mean error) for AVD-GRAPPA with external calibration with and without HSVD for acceleration 2, 3 and 4x. As acceleration factor increases, the percent mean-difference of metabolites maps remains around 13% (a reasonable range) only when HSVD is used to remove the contaminated lipid.

	w/o HSVD			w/ HSVD (Lipid remvoal)	
%Error	NAA	Cho/NAA	%Error	NAA	Cho/NAA
Random 2x	13.3 ± 12.6	15.1 ± 13.5	Random 2x	13.1 ± 11.8	15.3 ± 13.3
Random 3x	16.7 ± 17.9	17.8 ± 16.4	Random 3x	15.2 ± 14.1	16.7 ± 15.7
Random 4x	18.6 ± 17.0	21.2 ± 20.1	Random 4x	13.1 ± 11.8	15.4 ± 13.3

Table 6.5: Mean of the percent difference between the metabolites maps from fully sampled data and AVD-GRAPPA for 3 random sampling pattering of acceleration 2x,3x and 4x.

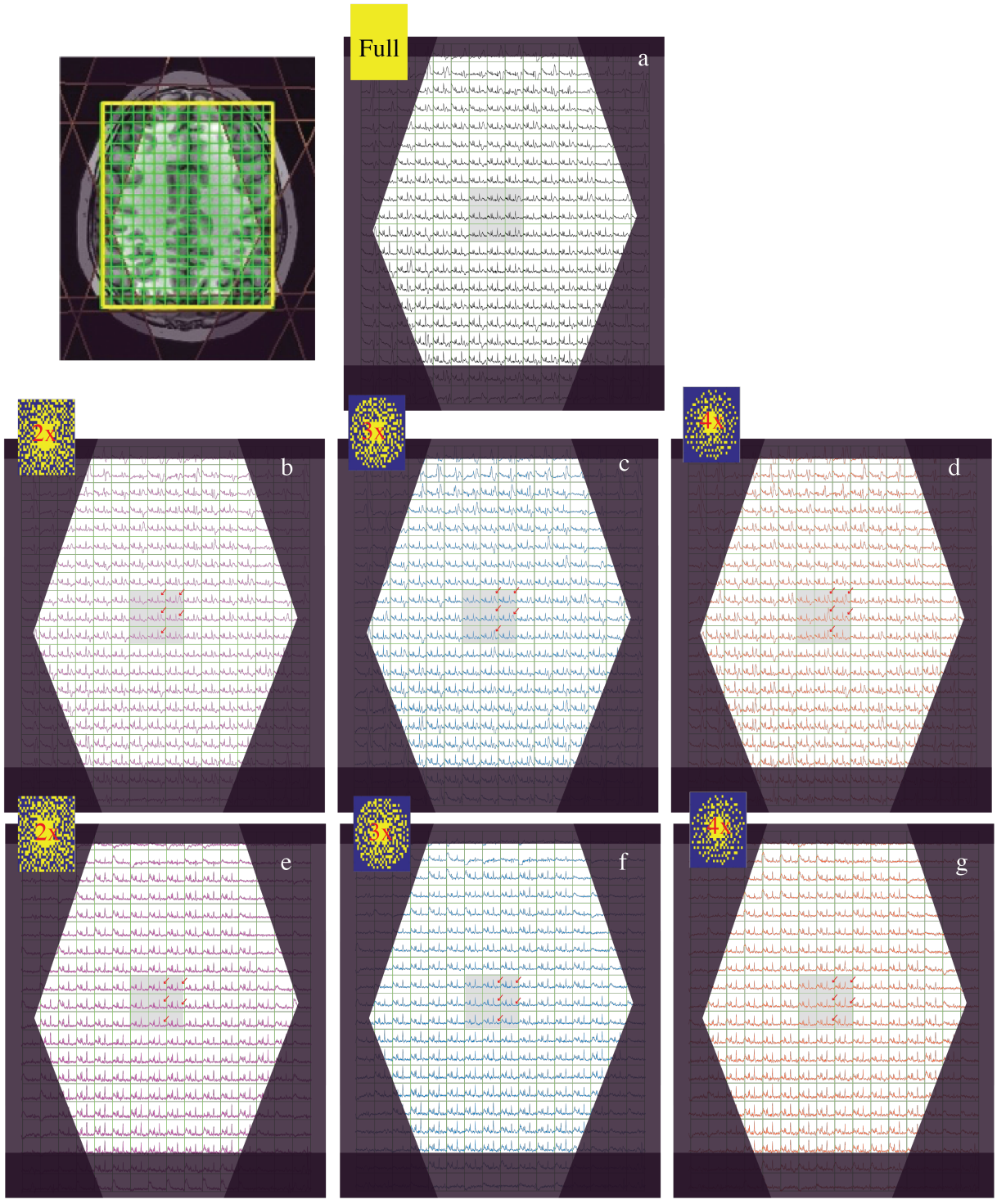

Figure 6.31: The AVD-GRAPPA reconstruction used high-resolution external calibration with kernel size of $[3 \times 3]$ for 3 random sampling patterns w/o HSVD. (a): Full k-space recon (b,c,d): 2,3,4x sub-sample recon without lipid removal prior to AVD-GRAPPA. (e,f,g) 2,3,4x sub-sample recon with HSVD lipid removal prior to AVD-GRAPPA.

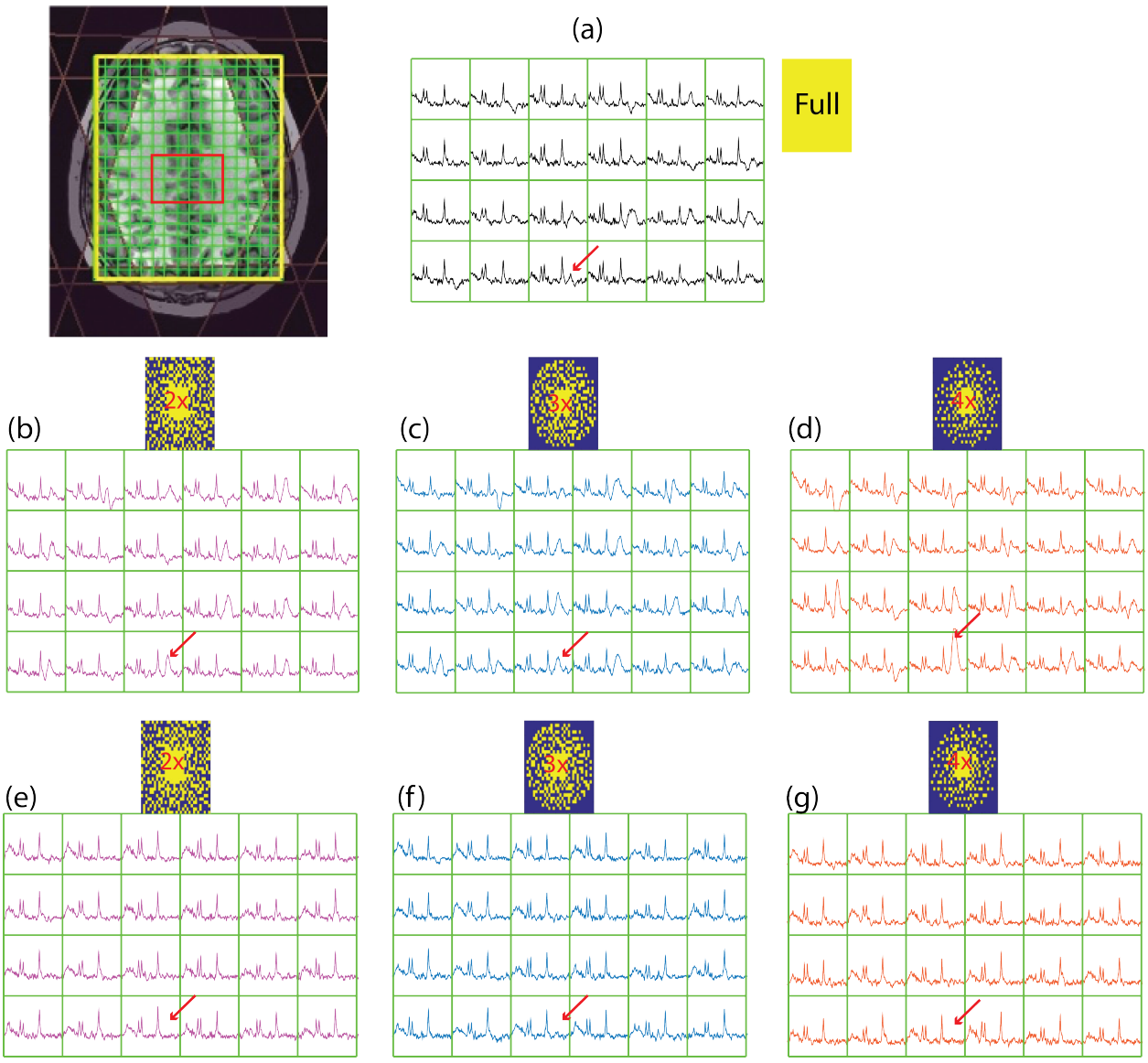

Figure 6.32: T_1-weighted MRI with in-vivo whole-brain 3D MRSI from a volunteer. The AVD-GRAPPA reconstruction used high-resolution external calibration with kernel size of $[3 \times 3]$ for 3 random sampling patterns (acceleration 2, 3, and 4x) with and without HSVD as pre-processing step. (a): Full k-space recon (b,c,d): 2, 3, 4x sub-sample recon without lipid removal prior to AVD-GRAPPA. Lipid contamination increases as the acceleration factor increases specially in anterior and posterior regions. (e,f,g) 2, 3, 4x sub-sample recon with HSVD lipid removal prior to AVD-GRAPPA.

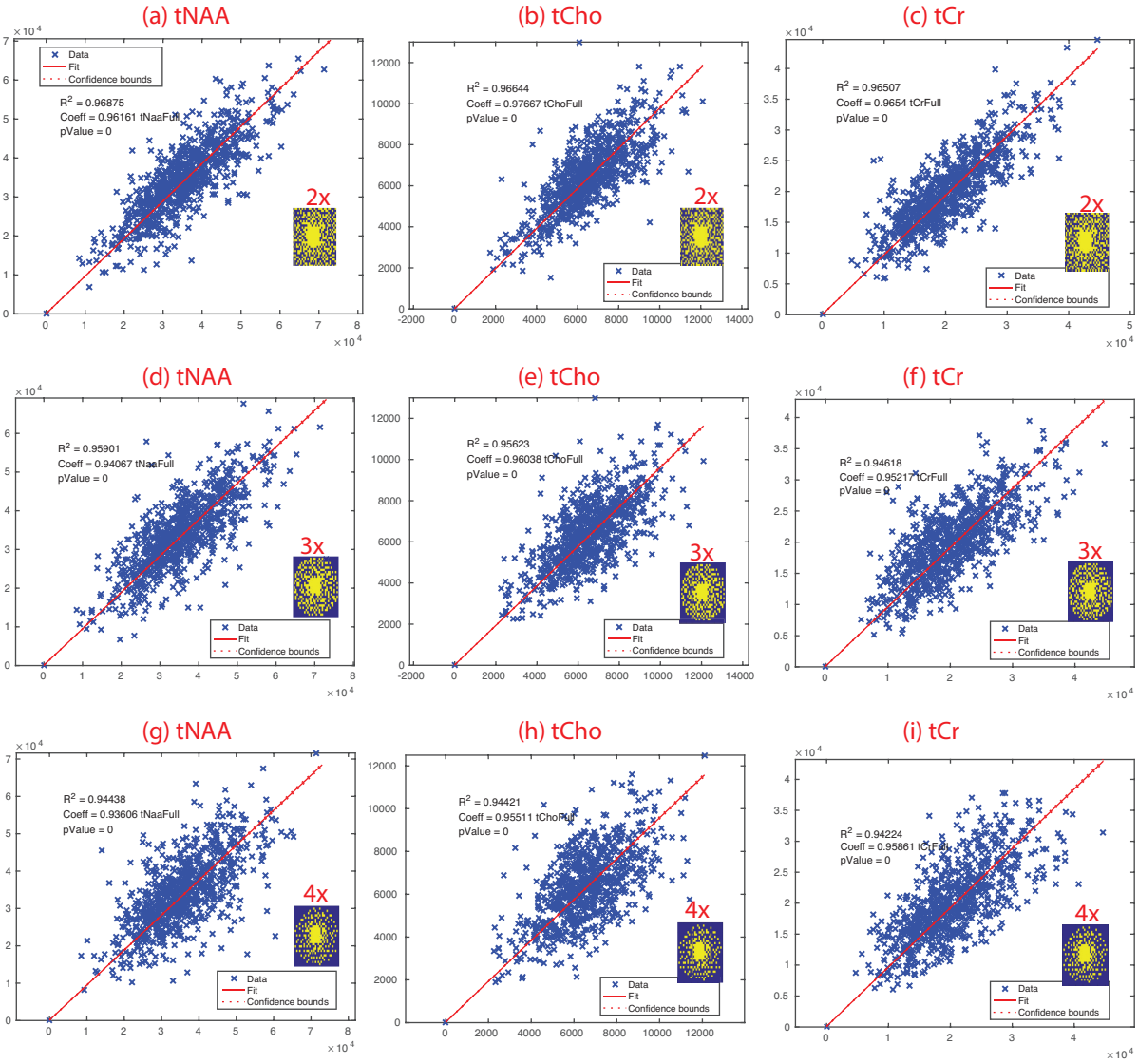

Figure 6.33: Regression plot of individual metabolites' concentration (tNAA, tCho, tCr) for random sampling pattern 2x acceleration (a,b,c), 3x acceleration (d,e,f), and 4x acceleration (g,h,i) respectively. AVD-GRAPPA are plotted against their Full k-space using high-resolution external calibration region of PD image.

The AVD-GRAPPA reconstruction has improved the condition number of constructed calibration matrix by ≈ 6 orders of magnitude using external calibration and an additional ≈ 60 fold using regularization. Figure 6.33 shows the regression plots that compare results of the spectral fitting for all acquired AVD-GRAPPA data and full k-space data for voxels within the brain using random undersampling pattern with acceleration factor of 2, 3, 4x and kernel size of 3×3. Figure 6.33(a,b,c) shows the metabolite (tNAA, tCho, tCr) from AVD-GRAPPA data plotted against those obtained from full k-space data using a high-resolution external calibration matrix for acceleration 2x. Figure 6.33(d,e,f) shows the metabolites (tNAA, tCho, tCr) from AVD-GRAPPA data plotted against those obtained from full k-space data using high-resolution external calibration matrix for a 3x acceleration. Figure 6.33(g,h,i) shows the metabolites (tNAA, tCho, tCr) from AVD-GRAPPA data plotted against those obtained from full k-space data using a high-resolution external calibration matrix for a 4x acceleration. Linear regression shows a strong correlation between AVD-GRAPPA and the gold standard, with correlation coefficient of $R^2_{tNAA} = 0.97$, $R^2_{tCho} = 0.97$, $R^2_{tCr} = 0.93$ for acceleration factor of 2x, $R^2_{tNAA} = 0.95$, $R^2_{tCho} = 0.98$, $R^2_{tCr} = 0.94$ for an acceleration factor of 3x, and $R^2_{tNAA} = 0.94$, $R^2_{tCho} = 0.93$, $R^2_{tCr} = 0.93$, for an acceleration factor of 4x.

As demonstrated the whole-brain 3D-MRSI at 3T with 32 channel coil can be accelerated up to 4-fold to provide high quality spectra in under 6 min with a voxel resolution of $0.56cc$ in a phantom and volunteers using AVD-GRAPPA enabled EPSI. With typical MRSI datasets, the limited matrix can provide a challenge for obtaining accurate estimates for reconstruction, however, using a high-resolution external calibration enhances the performance and reduces the severe ill-conditioning of calibration matrix. The finite extent of the encoded MRSI k-space (hence PSF) suggests that variable random sampling (compared to structured undersampling) will benefit the parallel imaging reconstruction of MRSI data sets with higher lipid contamination. Having the flexibility and capability of using various sampling patterns in acquisition and reconstruction processes allows one to control the spatial aliasing and artifacts of the reconstruction more intelligently. Furthermore, the size of the interpolation filter kernel and calibration region need to be optimized for specific applications. Although AVD-GRAPPA reconstruction strongly depends on the k-space subsets (calibration region), it is insensitive to the kernel size.

6.6 Summary and Conclusion

This chapter summarizes some of the existing auto-calibration methods and their properties for MRI application. The various methods all have differences in their theoretical and practical performances, especially in which kinds of coil sensitivity information is needed and how this information is acquired and applied.

Furthermore, the implementation of GRAPPA, POCS SPIRiT, and POCS ℓ_1-SPIRiT were modified in a manner so they can be applied to MRSI applications. The challenges for

clinical usage of these methods were discussed and some solutions were given in each MRSI application. This chapter should give the reader a good idea of which methods are best utilized in particular applications of brain MRSI. This work also introduces a new approach called AVD-GRAPPA that can robustly reconstruct the whole-brain 3D-MRSI that was accelerated up to 4-fold to provide high quality spectra in under 6 min with a voxel resolution of $0.56cc$ in a phantom and volunteers.

Although SPIRiT-based reconstruction appeared to perform well for 8-channel MRSI data, ℓ_1-SPIRiT became completely infeasible for 32-channel data in terms of memory usage and computation time. Performance of SPIRiT-based reconstruction is very sensitive to the number of channels. As an iterative reconstruction, the computational complexity of SPIRiT can be more intensive than direct reconstruction. The cartesian POCS algorithm requires that in each iteration an operation occurs similar to a single GRAPPA reconstruction. The current SPIRiT and GRAPPA implementation exploit parallelism from multiple slices and channels among multiple CPU cores. The future parallelization should exploit voxel-wise parallelism, while leveraging the channel-wise and slice-wise parallelism across multiple CPU cores.

While optimizing sampling patterns, sampling rate, calibration region, calibration's condition number, and kernel size are common between SPIRiT and GRAPPA, the additional parameters such as thresholding, stopping criteria, tolerable error measure (objective function and its residual), number of iterations and convergence need to be addressed for SPIRiT-based reconstruction. Although the SPIRiT-based approach is very flexible and has better noise performance, there are too many parameters to optimize for large MRSI matrices with a large number of individual coils, while dealing with long processing time. The SPIRiT approach has an advantage of using highly non-uniform sampling patterns while the traditional-GRAPPA has a much more accurate, faster, and more stable reconstruction.

The key feature of the AVD-GRAPPA reconstruction scheme is imitating the SPIRiT's arbitrary cartesian sampling patterns with an add-on option of using high-resolution external sensitivity information for calibration (GRAPPA meets SENSE meets random sampling). This is an encouraging step forward in accurate and robust GRAPPA-based MRSI reconstructions for clinical purposes. Since some of the parameters have been optimized for AVD-GRAPPA reconstruction in certain datasets, this knowledge can be incorporated into improving the performance of SPIRiT reconstruction by optimizing its remaining parameters in those same date sets. Additionally, this allows for a fair comparison between these two techniques while leveraging all the advantages that are unique to a particular algorithm. Future work will include evaluation of the performance of this technique in whole-brain MRSI data sets for brain tumor patients. Further studies will consider increased acceleration factors and larger acquisition matrices.

6.7 References

1. J. Carlson, "An algorithm for NMR imaging reconstruction based on multiple RF receiver coils," *Journal of Magnetic Resonance (1969)*, 1987.

2. J. Carlson, "Mri data acquisition and image reconstruction from multiple, non-interacting receiver coils," *Engineering in Medicine and Biology Society*, 1989.

3. J. W. Carlson and T. Minemura, "Imaging time reduction through multiple receiver coil data acquisition and image reconstruction.," *Magnetic Resonance in Medicine*, vol. 29, pp. 681–687, May 1993.

4. J. R. Kelton, R. L. Magin, and S. M. Wright, "An algorithm for rapid image acquisition using multiple receiver coils," in *Proceedings of the SMRM 8th annual meeting, Amsterdam*, p. 1172, 1989.

5. M. Hutchinson and U. Raff, "Fast MRI data acquisition using multiple detectors.," *Magnetic Resonance in Medicine*, vol. 6, pp. 87–91, Jan. 1988.

6. D. Kwiat, S. Einav, and G. Navon, "A decoupled coil detector array for fast image acquisition in magnetic resonance imaging," *Medical Physics*, 1991.

7. J. B. Ra and C. Y. Rim, "Fast imaging using subencoding data sets from multiple detectors.," *Magnetic Resonance in Medicine*, vol. 30, pp. 142–145, July 1993.

8. D. K. Sodickson and W. J. Manning, "Simultaneous acquisition of spatial harmonics (SMASH): fast imaging with radiofrequency coil arrays.," *Magnetic Resonance in Medicine*, vol. 38, pp. 591–603, Oct. 1997.

9. K. Pruessmann, M. Weiger, and M. Scheidegger, "SENSE: sensitivity encoding for fast MRI," *Magnetic Resonance in Medicine*, 1999.

10. E. N. Yeh, C. A. McKenzie, M. A. Ohliger, and D. K. Sodickson, "3Parallel magnetic resonance imaging with adaptive radius ink-space (PARS): Constrained image reconstruction usingk-space locality in radiofrequency coil encoded data," *Magnetic Resonance in Medicine*, vol. 53, no. 6, pp. 1383–1392, 2005.

11. C. Liu, R. Bammer, and M. E. Moseley, "Parallel imaging reconstruction for arbitrary trajectories usingk-space sparse matrices (kSPA)," *Magnetic Resonance in Medicine*, vol. 58, no. 6, pp. 1171–1181, 2007.

12. D. Sodickson, "AUTO-SMASH: A self-calibrating technique for SMASH imaging," *Magnetic Resonance Materials in Physics*, 1998.

13. M. A. Griswold, P. M. Jakob, M. Nittka, J. W. Goldfarb, and A. Haase, "Partially parallel imaging with localized sensitivities (PILS).," *Magnetic Resonance in Medicine*, vol. 44, pp. 602–609, Oct. 2000.

14. M. A. Griswold, P. M. Jakob, R. M. Heidemann, M. Nittka, V. Jellus, J. Wang, B. Kiefer, and A. Haase, "Generalized autocalibrating partially parallel acquisitions (GRAPPA).," *Magnetic Resonance in Medicine*, vol. 47, pp. 1202–1210, June 2002.

15. M. Lustig and J. Pauly, "SPIRiT: Iterative selfconsistent parallel imaging reconstruction from arbitrary kspace," *Magnetic Resonance in Medicine*, 2010.

16. W. E. Kyriakos, L. P. Panych, D. F. Kacher, C. F. Westin, S. M. Bao, R. V. Mulkern, and F. A. Jolesz, "Sensitivity profiles from an array of coils for encoding and reconstruction in parallel (SPACE RIP).," *Magnetic Resonance in Medicine*, vol. 44, pp. 301–308, Aug. 2000.

17. D. K. Sodickson and C. A. McKenzie, "A generalized approach to parallel magnetic resonance imaging," *Medical Physics*, vol. 28, no. 8, p. 1629, 2001.

18. M. Bydder, D. J. Larkman, and J. V. Hajnal, "Generalized SMASH imaging," *Magnetic Resonance in Medicine*, vol. 47, pp. 160–170, Dec. 2001.

19. K. P. Pruessmann, M. Weiger, P. Bornert, and P. Boesiger, "Advances in sensitivity encoding with arbitrary k-space trajectories.," *Magnetic Resonance in Medicine*, vol. 46, pp. 638–651, Sept. 2001.

20. J. Goldfarb and M. Shinnar, "Field-of-view restrictions for artifact-free SENSE imaging," in *Proceedings of the 10th Annual Meeting of the ISMRM. 2002.*, 2002.

21. O. Dietrich, K. Nikolaou, and B. Wintersperger, "iPAT: applications for fast and cardiovascular MR imaging," *ELECTROMEDICA-ERLANGEN*, vol. 70, pp. 133–146, 2002.

22. P. B. Roemer, W. A. Edelstein, C. E. Hayes, S. P. Souza, and O. M. Mueller, "The NMR phased array.," *Magnetic Resonance in Medicine*, vol. 16, pp. 192–225, Nov. 1990.

23. M. A. Griswold, S. Kannengiesser, R. M. Heidemann, J. Wang, and P. M. Jakob, "Field-of-view limitations in parallel imaging," *Magnetic Resonance in Medicine*, vol. 52, pp. 1118–1126, Nov. 2004.

24. M. M. Murphy, M. M. Alley, J. J. Demmel, K. K. Keutzer, S. S. Vasanawala, and M. M. Lustig, "Fast l-SPIRiT compressed sensing parallel imaging MRI: scalable parallel implementation and clinically feasible runtime.," *IEEE transactions on medical imaging*, vol. 31, pp. 1250–1262, June 2012.

25. J. H. Ardenkjaer-Larsen, B. Fridlund, A. Gram, G. Hansson, L. Hansson, M. H. Lerche, R. Servin, M. Thaning, and K. Golman, "Increase in signal-to-noise ratio of ¿ 10,000 times in liquid-state NMR.," *Proceedings of the National Academy of Sciences of the United States of America*, vol. 100, pp. 10158–10163, Sept. 2003.

26. J. Wolber, F. Ellner, B. Fridlund, A. Gram, H. Jóhannesson, G. Hansson, L. H. Hansson, M. H. Lerche, S. Månsson, R. Servin, M. Thaning, K. Golman, and J. H. Ardenkjaer-Larsen, "Generating highly polarized nuclear spins in solution using dynamic nuclear polarization," *Nuclear Instruments and Methods in Physics Research Section A: Accelerators, Spectrometers, Detectors and Associated Equipment*, vol. 526, pp. 173–181, June 2004.

27. U. Dydak, M. Weiger, K. P. Pruessmann, D. Meier, and P. Boesiger, "Sensitivity-encoded spectroscopic imaging.," *Magnetic Resonance in Medicine*, vol. 46, pp. 713–722, Oct. 2001.

28. A. Ebel and A. A. Maudsley, "Improved spectral quality for 3D MR spectroscopic imaging using a high spatial resolution acquisition strategy," *Magnetic Resonance Imaging*, vol. 21, pp. 113–120, Feb. 2003.

29. X. P. Zhu, K. Young, A. Ebel, B. J. Soher, L. Kaiser, G. Matson, W. M. Weiner, and N. Schuff, "Robust analysis of short echo time H-1 MRSI of human brain," *Magnetic Resonance in Medicine*, vol. 55, pp. 706–711, Mar. 2006.

30. S. Banerjee, E. Ozturk-Isik, and S. Nelson, "Fast magnetic resonance spectroscopic imaging at 3 Tesla using autocalibrating parallel technique," *EMBS*, 2006.

31. S. Banerjee, E. Ozturk-Isik, and e. al, "Elliptical magnetic resonance spectroscopic imaging with GRAPPA for imaging brain tumors at 3 T," *Magnet Reson Imaging*, 2009.

32. X. Zhu, A. Ebel, J. X. Ji, and N. Schuff, "Spectral phase-corrected GRAPPA reconstruction of three-dimensional echo-planar spectroscopic imaging (3D-EPSI)," *Magnetic Resonance in Medicine*, vol. 57, no. 5, pp. 815–820, 2007.

33. M. Rueckert, R. Otazo, and S. Posse, "GRAPPA Reconstruction of Sensitivity Encoded 2D and 3D Proton Echo Planar Spectroscopic Imaging (PEPSI) with SNR Adaptive Recalibrating," *Proceeding of the 14th Annual Scientific Meeting of the ISMRM*, pp. 1–1, Dec. 2006.

34. M. Sabati, J. Zhan, V. Govind, K. L. Arheart, and A. A. Maudsley, "Impact of reduced k-space acquisition on pathologic detectability for volumetric MR spectroscopic imaging," *Journal of Magnetic Resonance Imaging*, vol. 39, Apr. 2013.

35. W. W. F. Pijnappel, A. van den Boogaart, R. DeBeer, and D. Van Ormondt, "SVD-based quantification of magnetic resonance signals," *Journal of Magnetic Resonance*, vol. 97, pp. 122–134, Jan. 1992.

Chapter 7

Summary

Magnetic resonance spectroscopic imaging (MRSI) is a valuable modality for diagnosis and evaluation of brain tumors. The three major difficulties that are encountered in using MRSI in a clinical setting are limited coverage, coarse spatial resolution and long data acquisition time. The unifying goal of the projects in this dissertation work was to develop new means of acquiring and reconstructing faster MR spectroscopic data and to automate the post-processing routines for a clinical setting. This dissertation puts forth four major themes toward the advancement of this goal (Figure 7.1). These branches are interlaced and will affect the reconstruction performance.

In implementing and optimizing compressed sensing and parallel imaging reconstruction techniques for 3D whole-brain MRSI data, to accelerate the acquisition time, increase coverage of the brain or resolution while ensuring high quality data without loss of information,

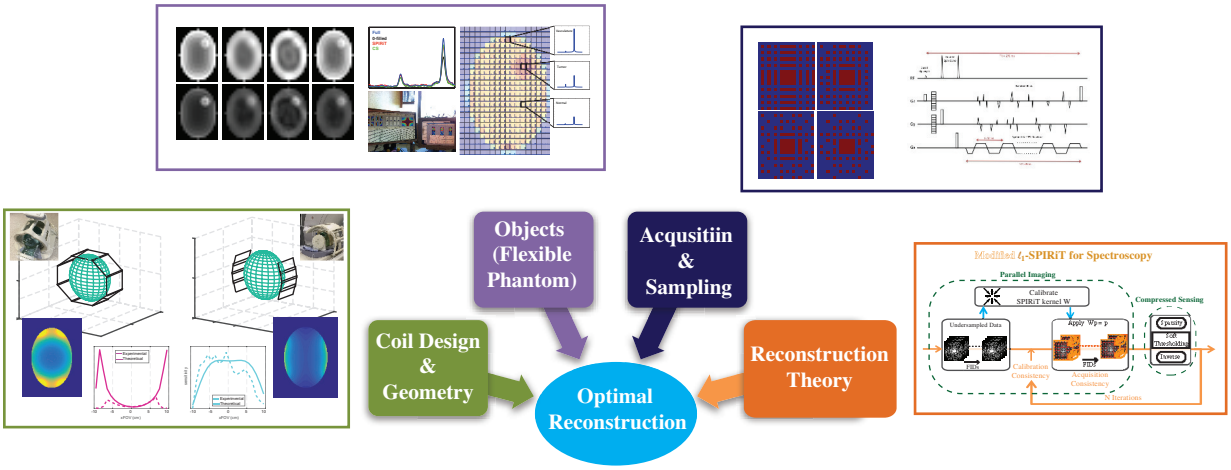

Figure 7.1: Framework for optimizing reconstruction

all aspects of imaging should be considered. Accuracy of reconstruction in k-space strongly depends on selection of the k-space subset and reconstruction kernel. The optimal k-space subset depends on coil sensitivities, coil placement, and the object itself. Chapter 3 focused on simulating coil profiles and geometries in addition to flexible numerical phantoms. The simulation tools have been used to investigate how different size coils and arrangements would influence the reconstruction and the sensitivity profile of the combined data. The ability to optimize the geometry and number of elements for specific regions of interest prior to coil construction will be critical for future studies. Chapter 4 compared several coil combination techniques and presented the most robust algorithm for phase sensitive coil combination of multi-channel, multi-voxel MRSI data for clinical applications in the brain.

The increased encoding capabilities of many-element coil arrays have enabled the use of alternative k-space undersampling patterns that are not feasible with standard few-element coil arrays. There are many possible ways to undersample a 3D MRSI experiment, however, the aliasing patterns of these different schemes will not necessarily be identical and each will affect the reconstruction in its own way. One of the key design challenges in implementing compressed sensing for specific MRSI applications is the development of pulse sequences and acquisition schemes that incorporate "incoherent" sampling, which is achieved by pseudo-random undersampling. Chapter 5 focused on compressed sensing theory with three different non-linear reconstruction techniques and presented an initial design of a pulse sequence to adapt compressed sensing rapid imaging in human clinical studies of MRSI.

Many different parallel imaging reconstructions are possible. As described in Chapter 6, the various methods all have differences in their theoretical and practical performances, especially in which kinds of coil sensitivity information is needed and how this information is acquired. A method should be selected based on the relative advantages or disadvantages for the specific application for which it is used. The research presented in Chapter 6 demonstrated the feasibility of SPIRiT, ℓ_1-SPIRiT and traditional-GRAPPA in various MRSI applications. This work optimized various parameters in each algorithm and finally it introduced a new approach called AVD-GRAPPA that is typically more robust and computationally manageable in a clinical setting.

In short, throughout this dissertation, I developed techniques and algorithms for acquisition, reconstruction, and quantitative analysis of high-field multi-channel MRSI with the goal of improving the speed, sensitivity and specificity of the data obtained for the management of patients with brain tumor in clinical setting. I designed and implemented an automated scheme for MRI machines to simplify the MRSI pulse sequence developments to support the variety of complex reconstruction techniques for the purpose of expediting MRSI acquisition time. I designed, simulated, optimized and implemented MRSI sampling patterns, and the corresponding linear and non-linear iterative reconstruction techniques in MATLAB to speed up the MRSI acquisition by 4-5 times using novel approaches in compressed sensing and parallel imaging. I Automated the MRSI post-processing pipeline with new

reconstruction techniques and quantification. I developed a MATLAB code to theoretically simulate configurable multi-channel RF receive coils with MRSI numeral phantoms to study and explore design parameters before prototyping. I investigated and implemented several MRSI coil combination algorithms in MATLAB and validated their performances with Monte Carlo simulations of phantoms, healthy volunteers and large population of patients. I built 2-channel quadrature traveling wave MR receiver coil using a circularly polarized micro-strip resonators and experimented with accelerated acquisition and reconstruction.

In conclusion, MR spectroscopic imaging is an important tool in brain tumor diagnosis, treatment planning, and monitoring the effects of therapy. This work has contributed in enabling future research in accelerating MRSI acquisition and reconstruction by detailing the important obstacles and challenges in using certain parallel imaging and compressed sensing algorithms, characterizing their influential parameters and identifying their bottlenecks. The results of this dissertation can be utilized to acquire more accurate and faster spectroscopic data and improve tumor characterization.